DESIGN & IMPLEMENTATION OF COMPLEX-VALUED FIR DIGITAL FILTERS WITH APPLICATION TO MIGRATION OF SEISMIC DATA

By

Wail Abdul-Hakim Mousa

Submitted in accordance with the requirements
for the degree of Doctor of Philosophy

The University of Leeds
School of Electronic and Electrical Engineering

April 2006

The candidate confirms that the work submitted is his own and that appropriate credit has been given where reference has been made to the work of others.

The copy has been supplied on the understanding that it is copyright material and that no quotation from the thesis may be published without proper acknowledgement.

Dedicated to

My dearly beloved father, mother, wife

and

my daughters Dana & Juwana

Acknowledgments

In the name of Allah, the Most Gracious and the Most Merciful

Firstly, all praise and glory goes to Allah the Almighty, the Most Gracious and the Most Merciful who gave me the courage and patience to carry out this work and said in the Holy Quran: **Another of His signs is that He created the Heavens and Earth, the diversity of your languages and colours. There truly are signs in this for those who know**. The Byzantines chapter, verse no. 22. Secondly, peace and blessing be upon His messenger the last Prophet Mohammad (p.b.u.h.) who said: **Whoever does not thank people does not thank Allah**, (Al-Tirmidhi Sunan, vol. 4 p. 339 and Abu-Dawud Sunan, vol. 5 p. 157-158). Also, peace and blessings on all the Prophet Mohammad's Companions (may Allah be pleased with them).

Acknowledgments and deep appreciation are due to Schlumberger Dhahran Carbonate Research, Dhahran, Saudi Arabia, for fully sponsoring and supporting my PhD studies at the School of Electronic & Electrical Engineering, University of Leeds, United Kingdom.

My deep appreciation and gratitude goes to my first supervisor Dr Said Boussakta, second supervisor Dr Desmond McLernon, and third supervisor Dr Mirko Van-der-Baan for their constant endeavour, guidance and the numerous moments of attention they devoted throughout the course of this PhD research work. Their valuable guidance made it possible for me to finish this work.

For their assistance and support, I would like to thank all my fellow students and staff: academic or non-academic members of the School of Electronic & Electrical Engineering, Leeds University, specially Moyra Culbert and Dona Fletcher.

I extend my deepest gratitude to Dr Kamal Babour, former director of Schlumberger Dhahran Carbonate Research, who always provided me with full encouragement as well as valuable recommendations since I joined the research centre. Also, I would like to express my deep appreciation

to my PhD programme mentor Dr Claudio Bagaini and to Dr Ali Özbek, Schlumberger Cambridge Research, for their valuable suggestions and comments with respect to my PhD research. I would like to thank as well all my friends and colleagues back home in Saudi Arabia at King Fahd University of Petroleum & Minerals (KFUPM) and at Schlumberger Middle East, S.A.

I would like thank to Dr Jan Thorbecke, Cray Company, for passing me a copy of his PhD thesis. Thanks are also due to Dr R. Ferguson, Department of Geological Sciences, University of Texas at Austin, USA for providing me with the SEG/EAGE data set.

Special thanks are also due to Dr Mohammad Y. Aziz, Mr. Basem S. Samman, Dr Fahad I. Al-Dobiyan, Dr Abdul-Hakim Al-Matroudi, Mr. Mansour Dhabab, Mr. Nehad Shkair, Mr. Salah Salamah, Mr. Ahmad Abdul-Aall, Mr. Mohammad Abdul-Aall, Mr. Yousef Abdoh, Mr. Abdul-Elah Abual-Elaa, Mr. Magdi Elyas and all the people who supported me during my studies at Leeds and made my work and stay at Leeds very pleasant and joyful.

Last but not least, sympathetic thanks are extended to my father Professor Abdul-Hakim Mousa and my Mother Liyla Shaker, who both blessed me with their prayers, support, and love. I ask Allah the Almighty to bless them with constant happiness and health, and keep them alive for a long time. In addition, I want to thank my sisters Alaa and Dr Manar, and my brothers Abdullah and Mohammed for their constant support and love. I want to pass my deep appreciations to my beloved wife Roba and daughter Dana whose love, patience and support have kept alive my enthusiasm to finish this work. Also, special thanks are due to my brothers-in-law, my father and mother-in-law, and the rest of the family for their prayers and encouragements. To my grandfathers Mohammad Khttab Shaker, Mousa, my grandmother A'mena, and to the rest of family, friends, and everyone I know who has passed away- may their souls rest in peace and may they earn a high place in paradise, (Amen)

Abstract

One-dimensional (1-D) and two-dimensional (2-D) frequency-space seismic migration FIR digital filter coefficients are of complex values when such filters require special space domain as well as wavenumber domain characteristics. In this thesis, such FIR digital filters are designed using Vector Space Projection Methods (VSPMs), which can satisfy the desired predefined filters' properties, for 2-D and three-dimensional (3-D) seismic data sets, respectively. More precisely, the pure and the relaxed projection algorithms, which are part of the VSPM theory, are derived. Simulation results show that the relaxed version of the pure algorithm can introduce significant savings in terms of the number of iterations required. Also, due to some undesirable background artifacts on migrated sections, a modified version of the pure algorithm was used to eliminate such effects. This modification has also led to a significant reduction in the number of computations when compared to both the pure and relaxed algorithms. We further propose a generalization of the 1-D (real/complex-valued) pure algorithm to multi-dimensional (m-D) complex-valued FIR digital filters, where the resulting frequency responses possess an approximate equiripple nature. Superior designs are obtained when compared with other previously reported methods. In addition, we also propose a new scheme for implementing the predesigned 2-D migration FIR filters. This realization is based on Singular Value Decomposition (SVD). Unlike the existing realization methods which are used for this geophysical application, this cheap realization via SVD, compared with the true 2-D convolution, results in satisfactory wavenumber responses. Finally, an application to seismic migration of 2-D and 3-D synthetic sections is shown to confirm our theoretical conclusions. The proposed resulting migration FIR filters are applied also to the challenging SEG/EAGE Salt model data. The migrated section (image) outperformed images obtained using other FIR filters and with other standard migration techniques where difficult structures contained in such a challenging model are imaged clearly.

Contents

Acknowledgments ii

Abstract iv

List of Figures ix

List of Tables xviii

List of Abbreviations and Maths Symbols xx

1 Introduction 1

1.1 Introduction 1

1.2 Thesis Organization 8

2 Background 10

2.1 Introduction 10

2.2 Seismic Acquisition 14

2.3 Seismic Record and Seismic Data Processing 15

2.3.1 Seismic Data Processing 16

2.3.2 Seismic Data and Noise 19

2.4 Migration 21

2.4.1 Huygens' Principle and Basic Migration Principles 22

2.4.2 Migration Kinds 26

2.4.3 Migration as a Filtering Process 28

2.4.4 Frequency-Wavenumber Migration Techniques 33

2.4.5 The Explicit Frequency-Space Migration Technique 35
2.4.6 The Frequency-Space Depth Post-Stack Migration and its Imaging Principle 39
2.5 Conclusion 42

3 One-Dimensional Migration Complex-Valued FIR Digital Filter Design Using Vector Space Projection Methods 43
3.1 Introduction 43
3.2 Vector Space Projection Methods Background 46
3.3 The Design of 1-D Complex-Valued FIR Migration Filters Using Vector Space Projection Methods 49
3.3.1 The constraint set C_1 51
3.3.2 The constraint set C_2 53
3.3.3 The constraint sets C_3, C_4, and C_5 57
3.4 The Pure Projection Design Algorithm for 1-D Migration Complex-Valued FIR Filters 62
3.5 The Relaxed Projection Design Algorithm for 1-D Migration Complex-Valued FIR Filters 64
3.5.1 Relaxed Projection for C_3 65
3.5.2 Relaxed Projection for C_2 68
3.6 The Modified Projection Design Algorithm for 1-D Migration Complex-Valued FIR Filters 68
3.7 Simulation Results 70
3.7.1 1-D Migration FIR Filter Design Using Vector Space Projection Methods Simulations 71
3.7.2 2-D Seismic Migration Synthetic Experiments 78
3.8 Discussion 83
3.9 Conclusion 84

4 Two-Dimensional Migration Complex-Valued FIR Digital Filter Design Using Vector Space Projection Methods **86**

4.1 Introduction 86

4.2 2-D Migration FIR Filters for 3-D Seismic Data 88

4.3 The Design of 2-D Migration Complex-Valued FIR Filters via McClellan Transformations 89

4.4 The Pure Projection Design Algorithm for 2-D Migration Complex-Valued FIR Filters 92

4.5 The Relaxed Projection Design Algorithm for 2-D Migration Complex-Valued FIR Filters 94

4.6 The Modified Projection Design Algorithm for 2-D Migration Complex-Valued FIR Filters 95

4.7 Simulation Results 96

4.7.1 2-D Migration FIR Filter Design Using Vector Space Projection Methods 96

4.7.2 3-D Seismic Migration Synthetic Experiments 102

4.8 Discussion 107

4.9 Conclusion 108

5 The Design of Multi-Dimensional Complex-Valued FIR Digital Filters by the Method of Pure Projections **109**

5.1 Introduction 109

5.2 Complex-valued FIR Filter Design using the Pure Projection Method . . . 111

5.2.1 The constraint set C_1 112

5.2.2 The constraint set C_2 113

5.2.3 The constraint sets C_3, C_4 and C_5 113

5.3 The Pure Projection Design Algorithm for m-D Complex-Valued FIR Filters 115

5.4 Simulation Results 116

5.4.1 Low Delay Single Passband Filters 117

5.4.2 Seismic Migration Filters 118

5.5 Discussion 124
5.6 Conclusion 124

6 Realization of 2-D Migration FIR Digital Filters for 3-D Seismic Volumes Via Singular Value Decomposition 126

6.1 Introduction 126
6.2 Singular Value Decomposition Realization for the 2-D Migration FIR Impulse Response 130
6.2.1 Singular Value Decomposition & FIR Filters Realization 130
6.2.2 Singular Value Decomposition Realization of Migration FIR Filters 132
6.3 Error Analysis 136
6.4 Simulation Results 138
6.4.1 Accuracy of the 2-D Migration FIR Digital Filters Realized Via SVD 138
6.4.2 3-D Seismic Migration Impulse Response Tests 145
6.5 Discussion 156
6.6 Conclusion 157

7 Migration Experiments on the Two-Dimensional SEG/EAGE Salt Model 158

7.1 Introduction 158
7.2 Post-Stack Migration of the 2-D SEG/EAGE Salt Model 160
7.2.1 Accuracy of the 1-D Seismic Migration FIR Filters 160
7.2.2 2-D Impulse Responses 161
7.2.3 2-D Dip Accuracy and Stability 164
7.2.4 Application to the SEG/EAGE Salt Model 165
7.3 Discussion & Conclusion 175

8 Conclusion and Further Work 176

List of Publications 180

References 182

List of Figures

2.1 Geophysical survey methods where seismic reflection is considered to be the mostly used and well-known surveying method. 10

2.2 A single seismic trace. 11

2.3 Convolution seismic data model. A seismic pulse is convolved with the reflection coefficient log (reflectivity function) to get a seismic trace. . . . 12

2.4 A typical example for a noisy seismic section (courtesy of [1]). 13

2.5 Analogue receiver array acquisition technique. 14

2.6 An example of a single sensor recorder (courtesy of www.slb.com). . . . 15

2.7 Point-receiver array acquisition technique. 15

2.8 One-sided shot gather (CSG) configuration. In this example, 6 receivers respond to one shot from one side of the receiver array. 16

2.9 Two-sided shot gather (CSG) configuration where 6 receivers from both sides of the shot respond. 16

2.10 Common mid-point gather (CMP) configuration. We see that each of the shot-receiver combinations is centered around the same mid-point. 16

2.11 Examples of (a) a CSG record with responses due to 3 shots and (b) a CMP gather with responses due to 3 shots. Both are courtesy of [2]. . . . 17

2.12 A CMP stacked section example (courtesy of [2]). 18

2.13 General classification of techniques for filtering seismic data. 21

2.14 The beach example for illustrating Huygens' principle. 22

2.15 This figure shows how the approaching waves with semi-circular wavefronts generated by Huygens' secondary source from the beach example (Figure 2.14) are recorded as hyperbolas in time. 23

2.16 (a) A point scatterer (acting as Huygens' secondary source), and (b) a curved reflector which is produced based on the point scatterer. 24

2.17 (a) An array of point scatterers positioned at different locations, and (b) its resultant curved reflectors interfering with each other. 25

2.18 Migration principles. The apparent reflector with a dip angle β in the time section when migrated is moved up-dip, steepened (to an angle θ), shortened, and mapped on its true subsurface location. 26

2.19 This is another migration classification which depends on how much physics one puts into the migration algorithm. 27

2.20 Migration types as a function of computational complexity and lateral velocity variations. The most accurate and most expensive migration kind is the pre-stack depth migration. 28

2.21 Earth model of an upward propagating seismic wavefield. 29

2.22 A hypothetical earth model showing vertically varying velocities due to homogeneous media within each earth layer. 34

2.23 1-D Seismic migration FIR filter requirements. 37

2.24 Diagram illustrating the explicit depth $\omega - x$ post-stack migration process. 41

3.1 Geometric interpretation of the relaxed projection operator T_c in Eq. (3.3). 48

3.2 1-D Seismic migration FIR filters (see section 3.7.1.1) designed using the proposed pure, relaxed, and modified projection algorithms with $N = 39$, $k_{c_p} = 0.25$, $\delta_p = \delta_s = 10^{-3}$, and $\epsilon = 10^{-12}$ (a) Magnitude response, (b) Phase response, and (c) Phase response error between the ideal and designed filters. 72

3.3 The impulse response for the designed filters (see section 3.7.1.1) using the proposed pure, relaxed, and modified projection algorithms with $N = 39$, $k_{c_p} = 0.25$, $\delta_p = \delta_s = 10^{-3}$, and $\epsilon = 10^{-12}$. (a) The real part, and (b) the imaginary part. 74

3.4 The mean-square error between $\mathbf{h}_{k+1}$ and $\mathbf{h}_k$ versus the number of iterations for the designed (see section 3.7.1.1) 1-D seismic migration filter using the proposed pure, relaxed, and modified projection algorithms with $N = 39$, $k_{c_p} = 0.25$, $\delta_p = \delta_s = 10^{-3}$, and $\epsilon = 10^{-12}$. 75

3.5 The ideal and designed filter's phase responses (see section 3.7.1.2) using the proposed modified projection algorithm in section 3.6 with $\delta_p = \delta_s = 10^{-3}$, and $\epsilon = 10^{-12}$ for $N = 39$. These filters are designed with cut-off's at (a) $k_{c_p} = 0.2$, (b) $k_{c_p} = 0.25$, (c) $k_{c_p} = 0.3$, and (d) $k_{c_p} = 0.35$. 76

3.6 1-D seismic migration FIR filters designed (see section 3.7.1.3) using the proposed modified projection, the modified Taylor series, and the complex Remez exchange algorithms with $N = 29$, and $k_{c_p} = 0.25$. (a) Magnitude response, (b) Magnitude response error within the passband, (c) Phase response, and (d) Phase response error within the passband. . . 78

3.7 2-D Migrated synthetic sections (see section 3.7.2.1) using the proposed modified projectors with $\Delta z = 2$ meters, $\Delta x = 10$ meters, $\Delta t = 4$ msec, $c = 1000$ meters/sec, and up to a maximum frequency of 80 Hz. The filters parameters are $\delta_p = \delta_s = 10^{-3}$, and $\epsilon = 10^{-12}$ for (a) $N = 19$ with an approximate resulting dip angle of 60°, (b) $N = 29$ with an approximate resulting dip angle of 69°, and (c) $N = 39$ with an approximate resulting dip angle of 73°. 80

3.8 2-D Migrated synthetic sections (see section 3.7.2.1) with $\Delta z = 2$ meters, $\Delta x = 10$ meters, $\Delta t = 4$ msec, $c = 1000$ meters/sec, and up to a maximum frequency of 80 Hz where the filters' parameters are $\delta_p = \delta_s = 10^{-3}$, $\epsilon = 10^{-12}$ and $M = 512$ for $N = 29$ with an approximate resulting dip angle of 69° using (a) the proposed relaxed projection algorithm, (b) the proposed modified projection algorithm and for (c) the modified Taylor series algorithm where $N = 29$ with an approximate resulting dip angle of 56°. 81

3.9 (a) A 2-D synthetic time-space section containing dipping events with angles $0^o, 30^o, 50^o, 60^o, 70^o$ and 80°. This section is constructed based on a Ricker wavelet input with a dominant frequency of 15 Hz and with a time duration of 0.2 seconds. 2-D Migrated synthetic sections (see section 3.7.2.2) containing dipping events with angles $0^o, 30^o, 50^o, 60^o, 70^o$ and 80° for (b) the modified projection algorithm with $N = 29$, and (c) the modified Taylor series method with $N = 29$. 82

4.1 Chebyshev structure for designing/realizing 2-D FIR digital filters based on 1-D odd length impulse responses having even symmetry. 90

4.2 Contour plots for comparing exact and approximation of circularly symmetrical filters using (a) the original McClellan transformation, and (b) the improved McClellan transformation. 91

4.3 (a) Magnitude response of the pure projector designed 2-D seismic migration filter, (b) Phase response of the pure projector designed 2-D seismic migration filter with $N = 25$, $k_{c_p} = 0.25$, $k_{c_s} = 0.3841$, $\delta_p = \delta_s = 10^{-3}$, and $\epsilon = 10^{-14}$ (see section 4.7.1.1). 99

4.4 (a) Magnitude response of the relaxed projector designed 2-D seismic migration filter, (b) Phase response of the relaxed projector designed 2-D seismic migration filter with $N = 25$, $k_{c_p} = 0.25$, $k_{c_s} = 0.3841$, $\delta_p = \delta_s = 10^{-3}$, and $\epsilon = 10^{-14}$ (see section 4.7.1.1). 100

4.5 (a) Magnitude response of the modified projector designed 2-D seismic migration filter, (b) Phase response of the modified projector designed 2-D seismic migration filter with $N = 25$, $k_{c_p} = 0.25$, $k_{c_s} = 0.401$, $\delta_p = \delta_s = 10^{-3}$, and $\epsilon = 10^{-14}$ (see section 4.7.1.1). 101

4.6 The mean-square error between $\mathbf{h}_{k+1}$ and $\mathbf{h}_k$ versus the number of iterations for the designed 2-D seismic migration filter using the proposed pure, relaxed, and modified projection algorithms with $N = 25$, $k_{c_p} = 0.25$, $\delta_p = \delta_s = 10^{-3}$, and $\epsilon = 10^{-14}$ (see section 4.7.1.1). 102

4.7 (a) Magnitude response of the McClellan designed 2-D seismic migration filter, (b) Phase response of the McClellan designed 2-D seismic migration filter with $N = 25$, $k_{c_p} = 0.25$, $k_{c_s} = 0.401$, $\delta_p = \delta_s = 10^{-3}$, and $\epsilon = 10^{-14}$ (see section 4.7.1.2). 104

4.8 (a) Magnitude response of the improved McClellan designed 2-D seismic migration filter, (b) Phase response of the improved McClellan designed 2-D seismic migration filter with $N = 25$, $k_{c_p} = 0.25$, $k_{c_s} = 0.401$, $\delta_p = \delta_s = 10^{-3}$, and $\epsilon = 10^{-14}$ (see section 4.7.1.2). 105

4.9 $N = 25$, 3-D Seismic migration impulse response 2-D slice (see section 4.7.2) using (a) true 2-D filters designed using the modified projections with an approximate resulting dip angle of 65°, (b) the McClellan transformation method, and (c) the improved McClellan transformation method. 106

5.1 Low-pass filter design specifications. 117

5.2 A 1-D complex-valued low delay FIR low-pass filter (see section 5.4.1.1) with $N = 31$, $M = 310$, $\omega_{p_1} = -0.1\pi$, $\omega_{p_2} = 0.3\pi$, $\omega_{s_1} = -0.2\pi$, $\omega_{s_2} = 0.4\pi$ $\delta_p = 0.00025$, $\delta_s = 0.025$, and $\epsilon = 10^{-5}$: (a) magnitude response in dB (pure projection: solid line and Complex Remez: dash-dot line), (b) passband group delay (pure projection (POCS): solid line, Complex Remez: dash-dot line and the Desired Group Delay: dash line), and (c) convergence of the 1-D complex-valued low delay FIR low-pass filter design using pure projection distance error curve. 119

5.3 The magnitude response in dB of a 2-D complex-valued low delay (a delay of 9 samples) shifted circularly symmetric FIR filter designed using pure projection (see section 5.4.1.2) with $N = 19 \times 19$, $M = 190 \times 190$, centred at $(-0.1\pi, 0.1\pi)$ with passband radius of 0.3π, stopband radius of 0.5π, $\delta_p = \delta_s = 25 \times 10^{-3}$, and $\epsilon = 5 \times 10^{-5}$. 120

5.4 A 1-D complex-valued seismic migration FIR filter (see section 5.4.2.1) with $N = 35$, $M = 350$, $\omega_p = 0.5\pi$, $\omega_s = 0.6\pi$, $\delta_p = 10^{-3}$, $\delta_s = 0.0025$, and $\epsilon = 5 \times 10^{-5}$: (a) its magnitude response in dB (pure projection: solid line and Complex Remez: dash-dot line), (b) its passband phase response (pure projection (POCS): solid line, Complex Remez: dash-dot line and the Desired Passband Phase Response: dash line), and (c) convergence of the 1-D complex-valued seismic migration FIR filter design using pure projection distance error curve. 122

5.5 The (a) magnitude response in dB and (b) the passband phase response of a 2-D complex-valued seismic migration FIR filter designed using pure projection with $N = 25 \times 25$, $M = 250 \times 250$, with passband radius of 0.5π, stopband radius of 0.7π, $\delta_p = \delta_s = 10^{-3}$, and $\epsilon = 5 \times 10^{-5}$ (see section 5.4.2.2). 123

6.1 SVD based realization structure for a pre-designed 2-D complex-valued migration FIR digital filter. Each branch represents a 2-D sub-filter of which is composed of two cascaded 1-D FIR digital filters. 131

6.2 A 25×25 2-D seismic migration FIR digital filter (see section 6.4.1.1) with a cut-off $k_{c_p} = 0.25$. (a) Pre-designed magnitude spectrum, and (b) Pre-designed phase spectrum. 140

6.3 Singular values of the matrix $\mathbf{B}_1$ (see equation Eq. (6.16)) for the pre-designed 25×25 2-D seismic migration FIR digital filter (see section 6.4.1.1). We see that most of the filter energy is concentrated in the first four or five singular values. 141

6.4 Maximum absolute wavenumber error bounds and within the passband and the stopband for the SVD realized pre-designed 25×25 2-D seismic migration FIR digital filter (see section 6.4.1.1) with respect to the number of parallel sections used. 142

6.5 Maximum and root-mean-squared phase errors within the passband for the SVD realized pre-designed 25×25 2-D seismic migration FIR digital filter (see section 6.4.1.1) with respect to the number of parallel sections used as well as the total used energy. 143

6.6 A 25×25 2-D seismic migration FIR digital filter (see sections 6.4.1.1 and 6.4.1.2) (with a cut-off $k_{c_p} = 0.25$) showing contour plots of the magnitude spectrum for the (a) Pre-designed, (b) SVD realized with $K = 4$, (c) SVD realized with $K = 5$, (d) Original McClellan transformation method, and (e) Improved McClellan transformation method. 148

6.7 A 25×25 2-D seismic migration FIR digital filter (see sections 6.4.1.1 and 6.4.1.2) (with a cut-off $k_{c_p} = 0.25$) showing contour plots of the phase spectrum for the (a) Pre-designed, (b) SVD realized with $K = 4$, (c) SVD realized with $K = 5$, (d) Original McClellan transformation method, and (e) Improved McClellan transformation method. 149

6.8 A 25×25 2-D seismic migration FIR digital filter (see section 6.4.1.1) with a cut-off $k_{c_p} = 0.25$. (a) SVD realized magnitude spectrum ($K = 3$), and (b) SVD realized phase spectrum ($K = 3$). 150

6.9 A 25×25 2-D seismic migration FIR digital filter (see section 6.4.1.1) with a cut-off $k_{c_p} = 0.25$. (a) SVD realized magnitude spectrum ($K = 4$), and (b) SVD realized phase spectrum ($K = 4$). 151

6.10 A 25×25 2-D seismic migration FIR digital filter (see section 6.4.1.1) with a cut-off $k_{c_p} = 0.25$. (a) SVD realized magnitude spectrum ($K = 5$), and (b) SVD realized phase spectrum ($K = 5$). 152

6.11 Diagram illustrating the explicit depth 3-D $\omega - x - y$ post-stack migration process which is based on using the 2-D FIR filters realized (implemented) via SVD (see section 6.4.2). 153

6.12 3-D Seismic migration impulse response 2-D slice (see section 6.4.2) using (a) direct convolution, and our proposed SVD realization scheme with (b) $K = 3$ and SNR= -0.8722 dB (c) $K = 4$ and SNR= 4.9115 dB, and (d) $K = 5$ and SNR= 11.1296 dB. 154

6.13 3-D Seismic migration impulse response 2-D slice (see section 6.4.2) using (a) direct convolution (b) our proposed SVD realization scheme with $K = 5$ and SNR= 11.1296 dB (c) the original McClellan transformation method with SNR= -2.8654 dB and (d) the improved McClellan transformation method with and SNR= -3.4829 dB. 155

7.1 This is a 3-D perspective of the SEG/EAGE Salt Model. The model contains various challenging geological structures such as sand bodies, salt sill, different faults, etc. 160

7.2 The designed 1-D migration FIR filters (see section 7.2.1) using the modified projections (solid-line), the modified Taylor series (dash-dotted line), and the complex Remez exchange (dashed line) algorithms with $N = 25$, and $k_{c_p} = 0.25$, (a) Magnitude response error within the passband, and (b) Phase response error within the passband. 162

7.3 2-D Impulse response sections (see section 7.2.2) with $\Delta z = 4$ meters, $\Delta x = 20$ meters, $\Delta t = 2$ msec, $c = 750$ meters/sec, and we have used a maximum frequency of 80 Hz using (a) the modified projections algorithm where the filter's parameters are $\delta_p = \delta_s = 10^{-3}$, and $\epsilon = 10^{-15}$ for $N = 25$ with an approximate resulting dip angle of 70°, (b) the modified Taylor series method where $N = 25$ with an approximate resulting dip angle of 45°, and (c) the complex Remez method where $N = 25$ with an approximate resulting dip angle of 70°. 164

7.4 (a) A 2-D synthetic time-space section containing dipping events with angles $0^o, 30^o, 50^o, 60^o, 70^o$ and 80° (see section 7.2.3). Migration of the 2-D synthetic time-space section containing dipping events with angles $0^o, 30^o, 50^o, 60^o, 70^o$ and 80° using (b) the modified projections algorithm with $N = 25$, and (c) the modified Taylor series method with $N = 25$. . . 166

7.5 SEG/EAGE Salt velocity Model (see section 7.2.4). 167

7.6 The time-space zero-offset section of the SEG/EAGE Salt Model which is generated based on finite differences (see section 7.2.4). This data set serves to assess the structural migration capabilities of different post-stack migration algorithms (see for example [3]). 168

7.7 Migrated SEG/EAGE Salt model (see section 7.2.4) via (a) the modified projections method, and (b) the modified Taylor series method. 170

7.8 Migrated SEG/EAGE Salt model (see section 7.2.4) via (a) the Split-Step method, and (b) the PSPI method. 171

7.9 Zoom-in on an area with different dips (see section 7.2.4): (lateral position 7500 : 9750 m, and depth 1200 : 1800 m) via (a) the modified projections technique, (b) the modified Taylor series method, (c) the Split-Step Fourier method, and (d) the PSPI method. 172

7.10 Zoom-in on an area with steep dips (see section 7.2.4): left flank of the salt model (lateral position 6000 : 8000 m, and depth 1800 : 2800 m)via the (a) modified projections technique, (b) the modified Taylor series method, (c) the split-step Fourier method, and (d) the PSPI method. 173

7.11 Zoom-in on a structurally challenging sub-salt area (see section 7.2.4) (lateral position 6500 : 8500 m, and depth 3400 : 4000 m) via the (a) modified projections technique, (b) the modified Taylor series method, (c) the split-step Fourier method, and (d) the PSPI method. 174

List of Tables

3.1 Running time comparisons (see section 3.7.1.3) for the modified Projection, modified Taylor Series, and the Complex Remez exchange algorithms using MATLAB on a Pentium 4 of speed 2.6 GHz PC with RAM=1GB. 77

3.2 FIR filter coefficients (see section 3.7.2.1) lengths for the proposed modified projectors showing the accuracy of migration up to certain dip angles. 79

6.1 Comparison of the mean and maximum absolute errors within the passband and stopband wavenumber responses (see section 6.4.1.2) between the pre-designed 2-D Seismic Migration FIR filter and: its realized version using the original McClellan transformation, the improved McClellan transformation, and our proposed SVD realization with $N = 25$. . . . 144

6.2 Comparison between the number of multiplications per output sample required to realize a 2-D complex-valued FIR seismic migration filter (see section 6.4.1.2) using the direct 2-D convolution with quadrantal symmetry, the original McClellan transformation, the improved McClellan transformation, and our proposed SVD realization with $N = 25$. 145

6.3 Comparison between the number of additions per output sample required to realize a 2-D complex-valued FIR seismic migration filter (see section 6.4.1.2) using the direct 2-D convolution with quadrantal symmetry, the original McClellan transformation, the improved McClellan transformation, and our proposed SVD realization with $N = 25$. 146

7.1 Comparison of CPU design time (see section 7.2.1) for designing a 25-tap 1-D seismic migration FIR filters (wavefield extrapolators) with a normalized wavenumber cut-off of $k_{c_p} = 0.25$ using the modified projections (with $\epsilon = 10^{-15}$), the complex Remez (with a passband weight of 80) and the modified Taylor series methods (8 derivative terms). 163

7.2 Comparison of computational cost (number of complex multiplications and additions) (see section 7.2.4) for each angular frequency at a depth slice for migrating the 2-D zero-offset SEG/EAGE salt model using 25-tap 1-D seismic migration FIR filters (wavefield extrapolators), the Split-Step Fourier method and the PSPI method (with 4 reference velocities and 2048 FFT points). 169

List of Abbreviations and Maths Symbols

Abbreviations

1-D	One-Dimensional
2-D	Two-Dimensional
3-D	Three-Dimensional
m-D	Multi-Dimensional
FIR	Finite Impulse Response
FFT	Fast Fourier Transform
DSFT	Discrete Space Fourier Transform
DTFT	Discrete Time Fourier Transform
VSPM	Vector Space Projection Method
POCS	Projections onto Convex Sets
CSG	Common Shot Gather
CMP	Common Mid-Point Gather
NMO	Normal Move-out Correction
SNR	Signal-to-Noise Ratio
PDE	Partial Differential Equation
LSI	Linear Shift-Invariant
MSE	Mean-Squared Error
RMS	Root-Mean-Squared Error
SVD	Singular Value Decomposition

SEG	Society of Exploration Geophysicists
EAGE	European Association of Geoscientists and Engineers

Mathematical Symbols

N	FIR digital filter length
$h[n]$	1-D impulse response of an FIR digital filter
$h[n_1, n_2]$	2-D impulse response of an FIR digital filter
$H_d(e^{j\omega})$	Desired 1-D frequency response of an FIR digital filter
$H_d(e^{jk_x})$	Desired 1-D wavenumber response of an FIR digital filter
$H_d(e^{j\omega_1}, e^{j\omega_2})$	Desired 2-D frequency response of an FIR digital filter
$H_d(e^{jk_x}, e^{jk_y})$	Desired 2-D wavenumber response of an FIR digital filter
$H(e^{j\omega})$	1-D frequency response of an FIR digital filter
$H(e^{jk_x})$	1-D wavenumber response of an FIR digital filter
$H(e^{j\omega_1}, e^{j\omega_2})$	2-D frequency response of an FIR digital filter
$H(e^{jk_x}, e^{k_y})$	2-D wavenumber response of an FIR digital filter
δ_p	Maximum allowable passband tolerance
δ_s	Maximum allowable stopband tolerance
ω_p	FIR filter passband frequency cut-off
ω_s	FIR filter stopband frequency cut-off
k_{c_p}	FIR filter passband wavenumber cut-off
k_{c_s}	FIR filter stopband wavenumber cut-off
$\mathbf{S}$	m-D finite extent support
$\mathbf{\Omega}_p$	m-D passband region
$\mathbf{\Omega}_s$	m-D stopband region
$\mathbb{R}$	Set of real numbers
$\mathbb{R}^M$	Set of M-dimensional real numbers
$\mathbb{C}$	Set of complex numbers
$\mathbb{C}^M$	Set of M-dimensional complex numbers
$\mathbb{Z}$	Set of integers

t	Time in seconds
z	Depth in meters
f	Temporal frequency in Hertz
ω	Digital angular frequency in radians
Ω_t	Analogue angular/temporal frequency in radians
x	In-line offset (axis) in meters
k_x	Digital spatial frequency (wavenumber) with respect to x-axis in m^{-1}
K_x	Analogue spatial frequency (wavenumber) with respect to x-axis in m^{-1}
y	Cross-line offset (axis) in meters
k_y	Digital spatial frequency (wavenumber) with respect to y-axis in m^{-1}
K_y	Analogue spatial frequency (wavenumber) with respect to y-axis in m^{-1}
c	Velocity of travelling acoustic seismic waves in m/s
θ	Angle to the vertical for a travelling seismic wave with a given velocity
$u(x,t,z)$	Acoustic seismic wavefield
$U(K_x,\Omega_t,z)$	2-D Fourier transform of $u(x,t,z)$
Δt	Temporal sampling interval
Δx	In-line spatial sampling interval
Δy	Cross-line spatial sampling interval
Δz	Vertical (depth) spatial sampling interval
$u(x_i,t_l,z_k)$	Sampled form of $u(x,t,z)$
ω_o	A fixed angular frequency
c_o	A fixed velocity
$\mathbf{h}$	Impulse response vector
$\mathbf{H}$	Hilbert space
C	a given constraint set
P_{C_i}	Projection operator onto a convex set C_i
T_{C_i}	Relaxed projection operator onto a convex set C_i
λ_i	Relaxation parameter of T_{C_i}
I	Identity operator on $\mathbf{H}$

$\|\cdot\|$	Euclidean or L_2 norm
$\Re\{.\}$	Real part for a given complex number
$\Im\{.\}$	Imaginary part for a given complex number
C_o	Solution set (intersection set of all constraint sets)
ϵ	A given threshold
$\leftrightarrow$	Fourier transform pair
$\mathbf{I}$	Identity matrix
$\mathbf{J}$	Contra-identity matrix
$\mathbf{A}$	2-D FIR impulse response matrix
$\mathbf{A}_K$	2-D FIR approximated impulse response matrix via SVD
K	Number of parallel sections used in the SVD implementation
r	The rank of a given matrix
$\mathbf{U}$	A unitary matrix related to the SVD decomposition
$\mathbf{u}_k$	The kth column vectors of $\mathbf{U}$
$\mathbf{v}_k$	The kth column vectors of $\mathbf{V}$
$\mathbf{V}$	A unitary matrix related to the SVD decomposition
$\mathbf{\Sigma}$	A diagonal matrix containing the singular values of a given matrix
σ_k	The kth singular value of a given decomposed matrix
$*$	The complex conjugate transpose of a given matrix

Chapter 1

Introduction

1.1 Introduction

Oil, gas, coal, and minerals are extremely important natural resources for human beings. Such resources are buried in deep land or marine sub-earth structures. The oil exploration process, in particular, finds possible drilling locations where the actual drilling of an oil well is used to test the geological hypothesis of oil and gas. But in order to produce oil, we need first to determine the sub-earth structure, i.e., get a clear and an accurate image of the subsurface [1, 2, 3, 4]. This can be done by the method known as reflection seismology. This geophysical technique relies on the generation of artificial seismic waves and the recording of their reflections from different geological layers. However, such acquired seismic data does not reveal an accurate image of the sub-earth unless we use appropriate *Digital Signal Processing (DSP)* techniques [1, 5, 4].

DSP has played an important role in many applications of both science and engineering disciplines. Some examples are seismology, sonar, radar, medical, communications, etc [6, 7]. The actual application of DSP theory in seismology began with the work of the Geophysical Analysis Group at the Massachusetts Institute of Technology (MIT) between 1960 and 1965 where it was one of the great historical milestones in seismic data processing [8].

Among the various important and necessary seismic DSP steps is the so called *Seismic Migration* or simply *Migration*. It seeks to determine the structure of the interior of the earth from the data obtained at the surface. Due to wave propagation within the sub-earth layers, the data is geometrically affected. For example, wave diffractions will appear whenever a discontinuity faces the propagating waves. Also, layer dips are mispositioned and need to be shortened. Improper correction of such undesirable geometrical effects leads to false interpretation and, therefore, oil/gas wells may be damaged or even lost.

A propagating acoustic seismic wave is governed by a hyperbolic wave equation which can be represented as a partial differential equation (PDE). *Seismic Migration filters* may simply be considered as a clever way of solving this PDE [6]. These filters, also known as phase filters or wavefield extrapolators, are able to correct for undesirable geometrical effects and improve the resolution of such data. From the signal processing point of view, these filters are basically non-causal complex-valued Finite Impulse Response (FIR) filters with phases possessing even symmetry- i.e., non-linear phases [9, 7, 6, 10].

There exist many migration (extrapolation) methods. One migration method known as the Frequency-Wavenumber (or $\omega - k_x$) technique [1, 11, 12]. This migration technique requires the data to be Fourier transformed from the time-space ($t - x$) domain to the $\omega - k_x$ domain. Then, at each frequency sample, the seismic migration complex-valued FIR filters are applied in the wavenumber response domain. The main advantage of this migration method is that the process could be preformed in the $\omega - k_x$ domain by simply transforming the data from the $t - x$ domain into the $\omega - k_x$ domain and then multiplying by the $\omega - k_x$ response of the filters. However, this is limited to earth layer structures that have materials which change as the wave propagates in deeper layers (homogeneous medium per layer)- in other words, where the velocities of the propagating seismic waves are vertically varying. Also, when performing migration in the $\omega - k_x$ domain, one needs to take into account the sampling artifacts (aliasing) which might be introduced in the

migrated sections with respect to spatial axes.

On the other hand, there exist an other attractive migration technique called the Frequency-Space (or $\omega - x$). For this technique, the data is only Fourier transformed with respect to time to the frequency domain. Then, at each frequency sample, the migration is applied using the seismic migration complex-valued FIR filters in the space domain via convolution [13, 12, 1, 14]. By using convolution, each designed filter output sample can be computed independently, or in parallel with other output samples. Also, it is considered to be a simple method since it is likely to be implemented more effectively on various computer architectures such as parallel processors [1, 15, 16, 17]. In addition, it can be extended for use in 3-D depth migration either via splitting or filter transformation [11, 10]. Finally, and most importantly, it can be accurately used for migration of one-way wavefields through strongly laterally varying media, i.e., for material that is also changing horizontally (heterogeneous media).

However, as we shall see later in this thesis, the frequency-space migration requires special FIR filter design characteristics in order to ultimately achieve stable and accurate seismic migrated sections (images). Stable migration of seismic data (one-way wavefields) through strongly laterally inhomogeneous media is considered to be a challenge. The problem arises since we need short FIR filter lengths to handle strong lateral variations in velocities accurately but long FIR filter lengths to correct for steep dips. Short length FIR filters are also desirable because computation times are proportional to chosen operator lengths. In addition, the accuracy of the $\omega - x$ migration over large distances may quickly deteriorate due to operator instability [12, 14].

Many attempts were carried out in order to properly design the seismic migration $\omega - x$ FIR filters [13, 12, 18, 19, 20, 14]. However, there is still a need for improving the design of such FIR digital filters used for this important geophysical DSP step. In consequence, better sub-earth images can be obtained and, therefore, reduce the oil exploration

risks. One of the mathematical techniques where we can fulfil such design characteristics is known as Vector Space Projection Methods (VSPM)s. Due to its attractive properties, this method has been used for designing other FIR filters [21, 22, 23]. However, they were restricted to real-valued FIR filter coefficients.

Therefore, this thesis mainly deals with the design of complex-valued FIR digital filters for seismic data frequency-space migration using the method of VSPMs or more precisely its subset, projections onto convex sets (POCS). The idea discussed in this thesis is to extend the work done on designing real-valued FIR digital filters using VSPMs to the more general class which is the class of complex-valued FIR filters. The design of complex-valued seismic migration FIR digital filters based on the one-dimensional (1-D) migration filter desired specifications by using VSPMs is important for such an application. Therefore, in this thesis, complex-valued FIR digital filter design for seismic migration application using the method of VSPMs or more precisely using the pure projection algorithm is derived. Moreover, the relaxed version of the complex-valued seismic migration FIR digital filter's pure projection design algorithm is also derived where the speed of convergence is significantly increased [24, 25, 26]. In addition, for practical reasons, a simple modification of the derived pure projector is introduced to further enhance the migrated sections and reduce the number of iterations required to achieve convergence [27, 26]. The use of such seismic migration FIR digital filters designed using the pure, the relaxed, and the modified projections are suitable for laterally varying geological structure media. They result in stable migration images as well as accommodating high propagation angles with short length filters and with less numerical background artifacts on migrated sections when compared with other previously reported migration FIR filters.

In order to subjectively quantify our proposed migration FIR filters designed using VSPM, we applied these filters to the challenging two-dimensional (2-D) Society of Exploration Geophysicists/European Association of Geoscientist and Engineers (SEG/EAGE) Salt model data. This model works as a standard data set to evaluate any new migration

technique. The migrated result is then compared with images obtained via migration FIR filters based on the modified Taylor series [12], and with other standard migration techniques such as the Phase Shift Plus Interpolation (PSPI) [28] and the Split-Step Fourier [29] methods. The VSPM algorithm provides very stable depth filters. The resulting migrated section using VSPM is of comparable quality to the expensive PSPI result, and visibly outperforms the other two techniques. Both strong dips and sub-salt structures are imaged clearly [30, 31], and so, a better interpretation can be performed with the use of our proposed FIR digital filters. Hence, the oil/gas exploration risks are much reduced.

Although seismic data prospecting started around 1910, it remained almost exclusively a 2-D problem until the middle of 1980's [32]. Three-dimensional (3-D) acquisition techniques were experimented with as early as 1940, however, they did not progress far until digital signal processing became common in the 1970's. The percentage of the current worldwide seismic effort is growing rapidly [32, 8]. Acquiring 3-D seismic data volumes has many advantages over acquiring 2-D data sets and all ultimately result in a better interpretation of such data. As a consequence, the oil/gas exploration risks are reduced [32]. An example of a new digital seismic acquisition system is the Schlumberger Q-Land acquisition system, which can digitally acquire massive 3-D seismic data volumes [33, 34, 35, 23].

2-D migration FIR filters (extrapolators), that are used for 3-D (frequency-space $\omega - x - y$) migration, are quadrantally symmetric FIR digital filters where their magnitude and phase wavenumber spectra are of circular symmetry [11, 10, 1, 36]. There were two important factors which prevented the use of such true 2-D migration FIR digital filters. The first factor was the computing/storage facilities which nowadays have become less important due to recent technological advances. Secondly, most of the present 1-D migration FIR digital filter (and filters in general) design algorithms cannot be extended to the 2-D case- e.g., the Remez algorithm [19, 21]. Hence, for both reasons, researchers were using approximations of 2-D migration FIR filters based on pre-designed 1-D fil-

ters. For example, if we assume that the true 2-D migration FIR digital filter is separable, then such migration FIR filters can be designed, as is the case in [6]. Another way is by using the McClellan transformation, which takes into account the circular symmetry of the filter's wavenumber response, as in [37, 38, 10, 11, 39, 40, 6]. Although such filters designed via approximations are cheap to design and to implement, these approximations come with a price, i.e., they give errors in migrated sections [11], as will be highlighted later on in this thesis.

As a result, there is a need to accurately design 2-D $\omega - x - y$ migration FIR digital filters. Hence, the 1-D migration FIR filter algorithms that we derived for 2-D seismic data sets are then extended to the design of 2-D migration FIR filters that are used for 3-D seismic data sets. In this case, such filters eliminate errors introduced by approximating such 1-D FIR filters for the migration application [24, 36, 31]. In other words, migration can be performed based on true 2-D migration FIR digital filters and, therefore, more accurate sub-earth volumes are obtained.

The $\omega - x - y$ migration (filtering) process is carried out over all frequencies and so it is considered to be an expensive process [9, 10]. Different approaches have been proposed to mitigate such a computationally expensive 3-D migration process that relies so heavily on direct convolution with a 2-D complex-valued FIR filter impulse response [9]. However, these approaches suffer from noticeable wavenumber response errors. Singular Value Decomposition (SVD) for 2-D FIR filter realization has drawn the attention of DSP researchers in many image processing applications [6, 40]. However, such an SVD realization was based on realizing real-valued FIR filters.

So in this thesis, the mathematical development of realizing (implementing) 2-D complex-valued quadrantal symmetrical migration FIR filters (for the 3-D $\omega - x - y$ migration) using SVD, is presented. In order to simplify the SVD computations for such impulse response structure (i.e., quadrantal symmetry), we apply a special matrix transformation similar to

the one reported in [41] on the migration filter impulse response, which guarantees that no distortion of the wavenumber phase response occurs and the magnitude responses result in stable migration. Also, this results in less numerical SVD computational errors. We exploit the existence of insignificant singular values and discard them so that we reduce the computational complexity of the expensive 3-D $\omega - x - y$ migration problem at the expense of almost negligible errors. As a result, our proposed realization method for such geophysical application overcomes the problems of other previously reported and heavily used realization schemes in terms of computational complexity, stable migrated images, and circularly symmetrical wavenumber responses [42, 43, 44]. Therefore, a better 3-D geophysical interpretation of such migrated volumes is obtained.

In addition to the migration FIR digital filters mentioned earlier, there exist other examples of FIR filters with complex coefficients such as low delay single passband filters which are used in communications [45, 20]. A number of algorithms have been proposed for the design of complex-valued FIR filters [46, 19, 20, 47]. However, many design algorithms are either expensive in terms of the design complexity [46, 47] or cannot be extended to higher dimensions greater than 1 unless using filter transformations if possible [21, 22]. Such transformations result in suboptimal designs [48, 49].

Therefore, by adjusting the pure design algorithm that we proposed for the design of the migration FIR filters, it can be used for designing any complex-valued FIR digital filter with a predefined fixed phase [50, 51]. Hence, the design of m-D complex-valued FIR digital filters using the method of pure projections is shown. That is, the work carried out for designing 1-D real-valued FIR digital filters using pure projections (as reported in [22]) is extended to the more general class of m-D complex-valued FIR filters which are important in the many applications stated earlier. This extension to the m-D case is possible due to the existence of m-D type FFT algorithms [50, 51, 52, 53].

1.2 Thesis Organization

To start with, necessary and sufficient background is given about seismic data and seismic data acquisition and processing . Migration principles, types, filtering, etc., are also given. More specifically, the explicit depth frequency-space method for post-stacked data is explained. All are included in chapter 2.

Chapter 3 of this thesis starts by introducing the VSPM and stating the fundamental theory of projections. The mathematical development necessary for designing migration filters is then shown. Based on this, the design algorithms of 1-D complex-valued seismic migration FIR digital filters using the pure, the relaxed, and the modified projections algorithms will be given. Simulation results of designed filters and synthetic seismic data is also shown based on the VSPM design algorithms and compared with other well known filters used in the geophysics community.

Then, chapter 4 extends the derived 1-D design algorithms (which are shown in chapter 3) using the pure, the relaxed, and the modified projections to the 2-D case. For the sake of clarity and comparisons, the standard McClellan filter transformation and its improved version for filter design is also briefly described. 2-D filters are designed using the pure, the relaxed, and the modified projection design algorithms and compared with those designed using the McClellan and its improved version design methods. 3-D synthetic seismic data are used to validate and compare the modified projection filters applied to it and compared with those migrated using both McClellan transformations.

In chapter 5, with a proper adjustment to one of the constraint sets, the 1-D pure design algorithm is then extended to the design of general m-D complex-valued FIR filters. Simulation results on complex-valued FIR digital filters including the seismic migration filters are shown and compared with the complex Remez exchange technique reported in [19, 20].

Chapter 6 is organized as follows. An introduction to the concept of SVD realization for 2-D FIR digital filters is given. Also, the mathematical development for realizing 2-D quadrantally symmetrical complex-valued FIR seismic migration digital filters using SVD is presented. Error analysis, relating to the SVD realization of migration filters is then shown. Simulation results are performed for 2-D seismic migration FIR filters realized by using the proposed SVD scheme. An application of the proposed implementation method to 3-D synthetic seismic data is shown and compared with other standard implementation methods.

In chapter 7, the explicit depth extrapolation migration FIR filters designed using the modified projection method are applied to the challenging SEG/EAGE salt model. This is performed to test the derived migration FIR filters and to show that such proposed design algorithms result in robust designs which compete with other migration FIR filters and other standard migration methods. We compare our results with other $\omega - x$ migration design techniques as well as other standard migration methods.

Finally, chapter 8 concludes with a summary that highlights the major contributions of this thesis. This will include suggestions for possible ideas that would be used in further research work.

Chapter 2

Background

2.1 Introduction

Among many geophysical surveying techniques, seismic reflection is the most widely used and well-known geophysical technique (Figure 2.1). Seismic reflection acquired data can be produced to reveal details of geological structures on scales from the top tens of meters of drift to the whole lithosphere [5, 1]. Part of its success lies in the fact that the raw seismic data is processed to produce seismic sections which are images of the sub-surface structure. A geologist can then make an informed interpretation by understanding

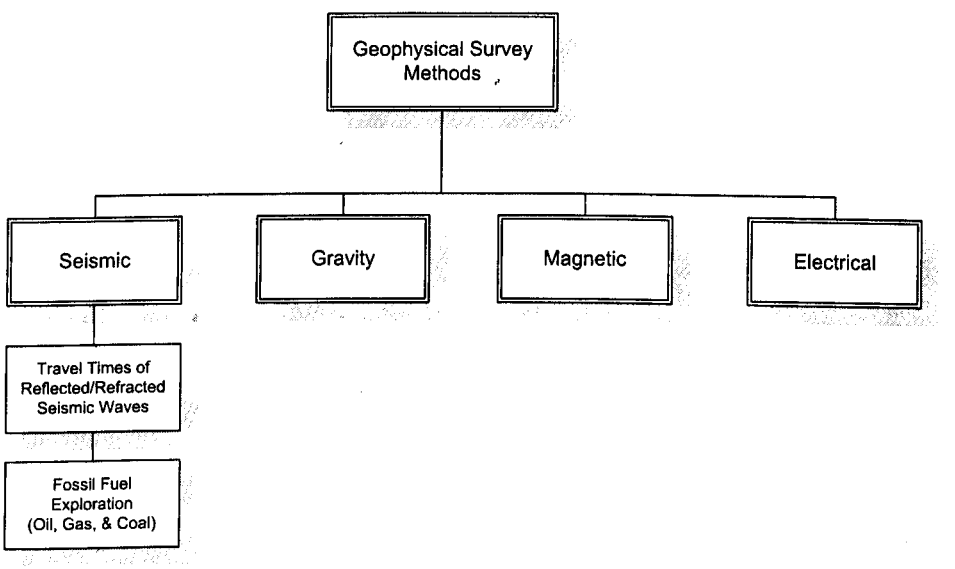

Figure 2.1: Geophysical survey methods where seismic reflection is considered to be the mostly used and well-known surveying method.

how the reflection method is used and seismic sections are created. The analysis of seismic data is performed for many applications such as petroleum exploration, determination of the earth's core structure, monitoring earthquakes, etc. [54, 1].

Seismic signals are generated at a source (transmitter), such as an explosion which propagates through earth layers. Some of these signals will be reflected, some will be refracted and some might neither be reflected nor refracted (simply lost due to attenuation). At the surface, the reflected signals are then recorded at a receiver (acquisition step) at acoustic impedance contrasts. The strength of this impedance contrast is defined as reflectivity. In summary, a seismic analysis scenario involves collection of data by an array of receivers (seismometers), transmission over a narrow band channel, and storage of data for analysis, processing, and interpretation [5, 1, 8].

A seismic trace (Figure 2.2) represents a combined response of a layered ground and a recording system to a seismic pulse. Any display of a collection of one or more seismic traces is termed a *seismogram*. Assuming that the pulse shape remains unchanged as it propagates through such a layered ground, the resultant seismic trace may be regarded as the convolution of the input impulse with a time series known as a *Reflectivity function*,

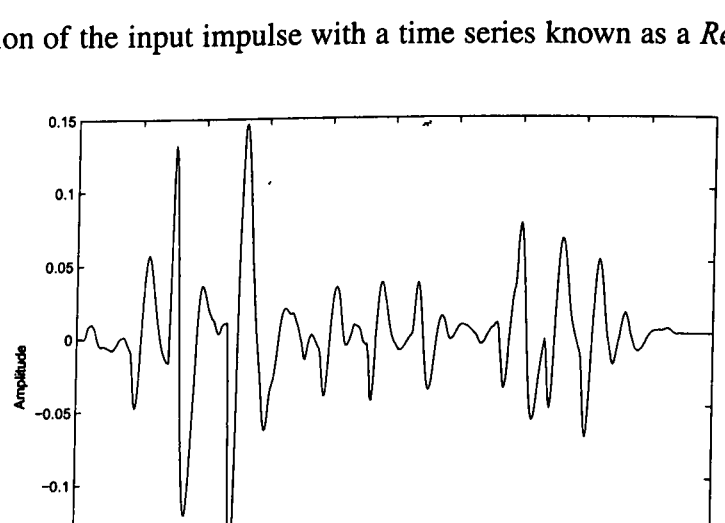

Figure 2.2: A single seismic trace.

which is composed of spikes (delta functions). Each spike has an amplitude related to the reflection coefficient of a boundary and a travel time equivalent to the two-way reflection time for that boundary. Furthermore, the time series represents the impulse response of the layered ground, which is basically the output for a spike input. Since the pulse has a finite length, individual reflections from closely-spaced boundaries are seen to overlap in time on the resultant seismogram. Figure 2.3 represents a typical seismic convolution model [5].

Due to storm, traffic, heavy industry, unwanted waves such as surface waves, etc, seismic records are highly corrupted with noise (unwanted energy). This unwanted energy could be sort of incoherent noise such as instrument signals and/or coherent noise like the ground-roll noise during the acquisition. A typical example for a noisy seismic section is shown in Figure 2.4.

As a consequence of the above effects, seismic traces generally have a complex appearance and reflection events are often not recognized without the application of suitable

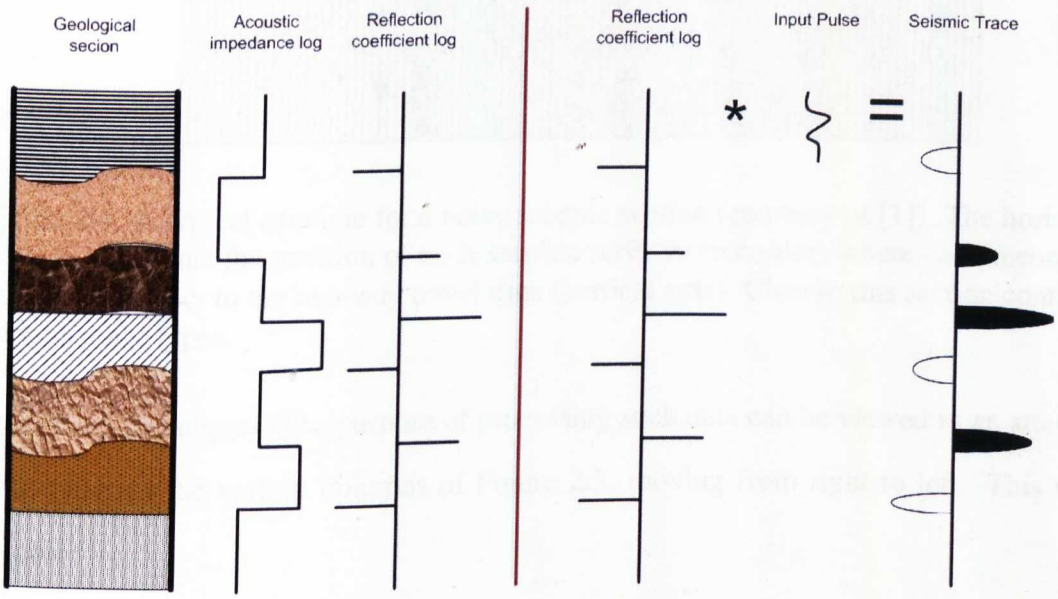

Figure 2.3: Convolution seismic data model. A seismic pulse is convolved with the reflection coefficient log (reflectivity function) to get a seismic trace. The reflection coefficient log is related to the geological section of the sub-earth through the reflection coefficient of each geological boundary and the two-way travel time which takes the seismic signal to forward and backward propagate through the sub-earth.

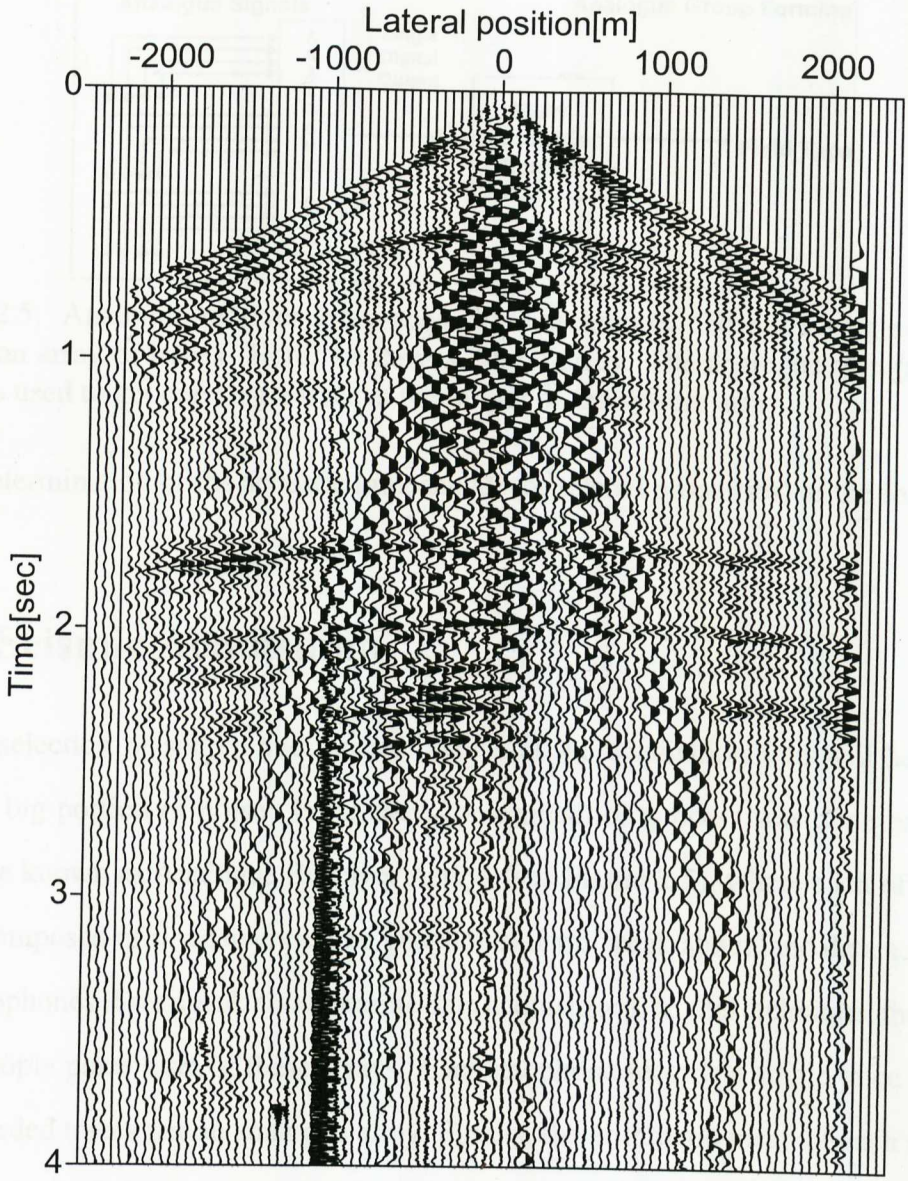

Figure 2.4: A typical example for a noisy seismic section (courtesy of [1]). The horizontal axis represents the position of each seismic receiver (recorder) where each records a trace with respect to the two-way travel time (vertical axis). Clearly, this section contains various noise types.

processing techniques. The purpose of processing such data can be viewed as an attempt to reconstruct the various columns of Figure 2.3, moving from right to left. This will involve:

- removing noise,
- determining the input pulse and removing that to give the reflectivity function,
- determining the velocity function to allow conversion from time to depth axis, and

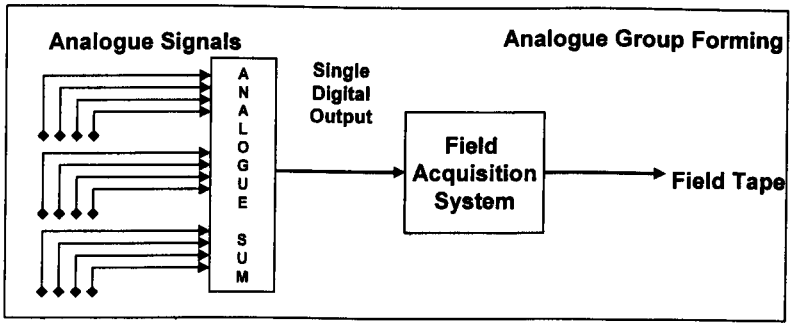

Figure 2.5: Analogue receiver array acquisition technique. To get a single trace, we require an array of traces. Here, we have a 3 by 4 array. The analogue sum (arithmetic mean) is used to get one single trace at the output of the system array.

- determination of the acoustic impedances (or related properties) of the formations.

2.2 Seismic Acquisition

Careful selection of source and receiver arrays at the acquisition step will help eliminating a big portion of noise. Previously, the acquisition process was done based on a technique known as Analogue Receiver Arrays (see Figure 2.5), where each of these arrays is composed of n receivers called geophones if we speak about land data acquisition (or hydrophones if we speak about marine data acquisition). In this technique, the seismic cruise people place a set of these arrays. Each geophone records a single trace resulting in n recorded traces per an analogue array. Finally, the arithmetic mean of each analogue array (average of all traces recorded in such array) is given as an output of that array and considered as a single trace [1]. This helps in reducing noise during acquisition [1, 5].

Schlumberger has recently developed a new recording system known as the Q-land, with a view to replacing the analogue receiver array with one single geophone (Figure 2.6). Q-Land Single-sensor recording (www.slb.com) is basically an integrated acquisition and processing system which provides superior data quality through the efficient recording and processing of up to 30,000 live single-sensor channels. The system yields denser digital spatial sampling of the wavefield. Composition of the single geophone records by digital array forming, provides almost a noise-free system and a high resolution per seismic trace (see Figure 2.7) [33, 34]. It also yields better noise attenuation and sig-

Figure 2.6: An example of a single sensor recorder (courtesy of www.slb.com).

nal preservation. Single receiver recordings have the advantage that better noise-rejection filters can be designed. The filters can be either time-invariant or adaptive [55, 56].

2.3 Seismic Record and Seismic Data Processing

A collection of traces with the response of several geophones to the energy from one shot is termed a *Common Shot Gather* (CSG) - see Figure 2.8 and Figure 2.9. A collection of traces where all shot-receiver combinations are centered around one surface mid-point is termed a *Common Mid-point Gather* (CMP) [1, 5] as in Figure 2.10. In CSGs and CMPs, seismic traces are plotted side-by-side in their correct relative positions and records are commonly displayed with their time axis arranged vertically down. An example of a CSG record and a CMP record are both shown in Figure 2.11 (a) and (b), respectively.

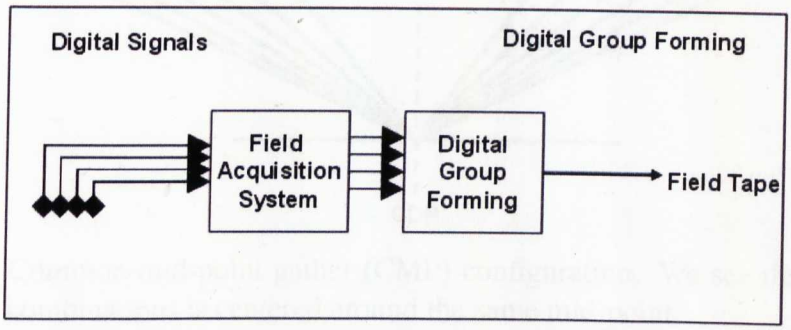

Figure 2.7: Point-receiver array acquisition technique. Unlike to the analogue receiver array technique, each receiver records only one trace. Here, 4 receivers record 4 seismic traces.

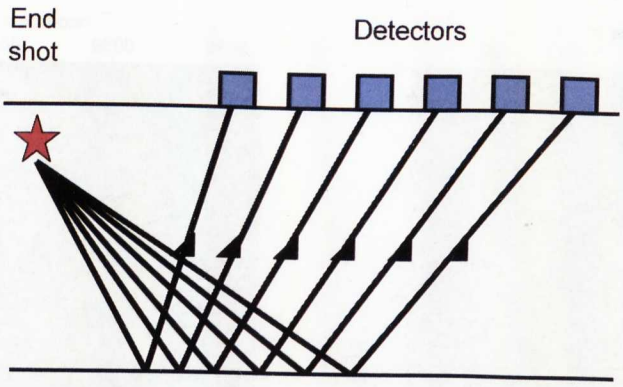

Figure 2.8: One-sided shot gather (CSG) configuration. In this example, 6 receivers respond to one shot from one side of the receiver array.

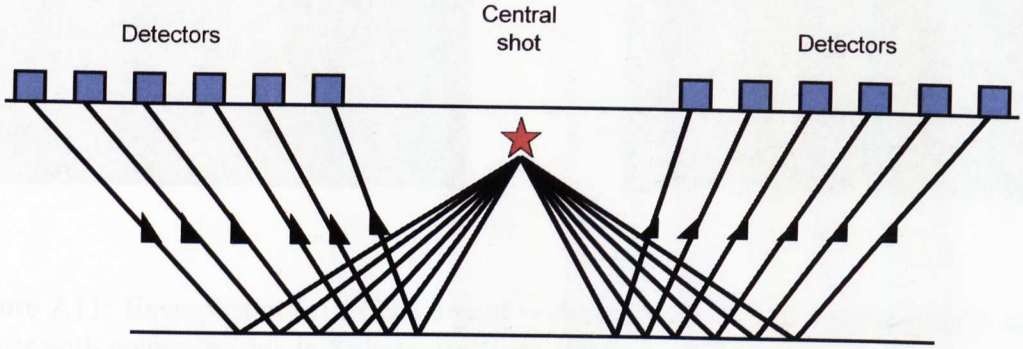

Figure 2.9: Two-sided shot gather (CSG) configuration where 6 receivers from both sides of the shot respond.

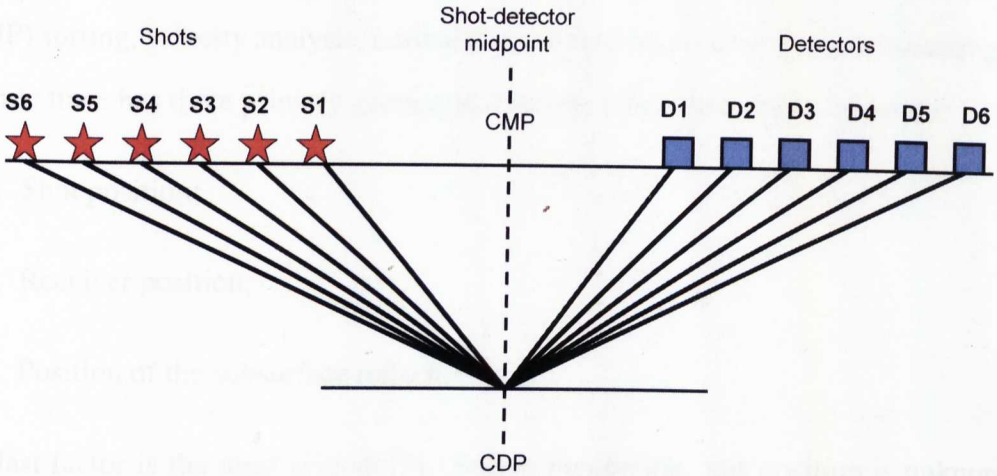

Figure 2.10: Common mid-point gather (CMP) configuration. We see that each of the shot-receiver combinations is centered around the same mid-point.

2.3.1 Seismic Data Processing

Seismic data processing can be considered as a sequence of cascaded operations that attenuate/remove noise accompanying seismic data as well as making geometrical corrections such that the final image will truly show a map (seismic image) of the subsurface.

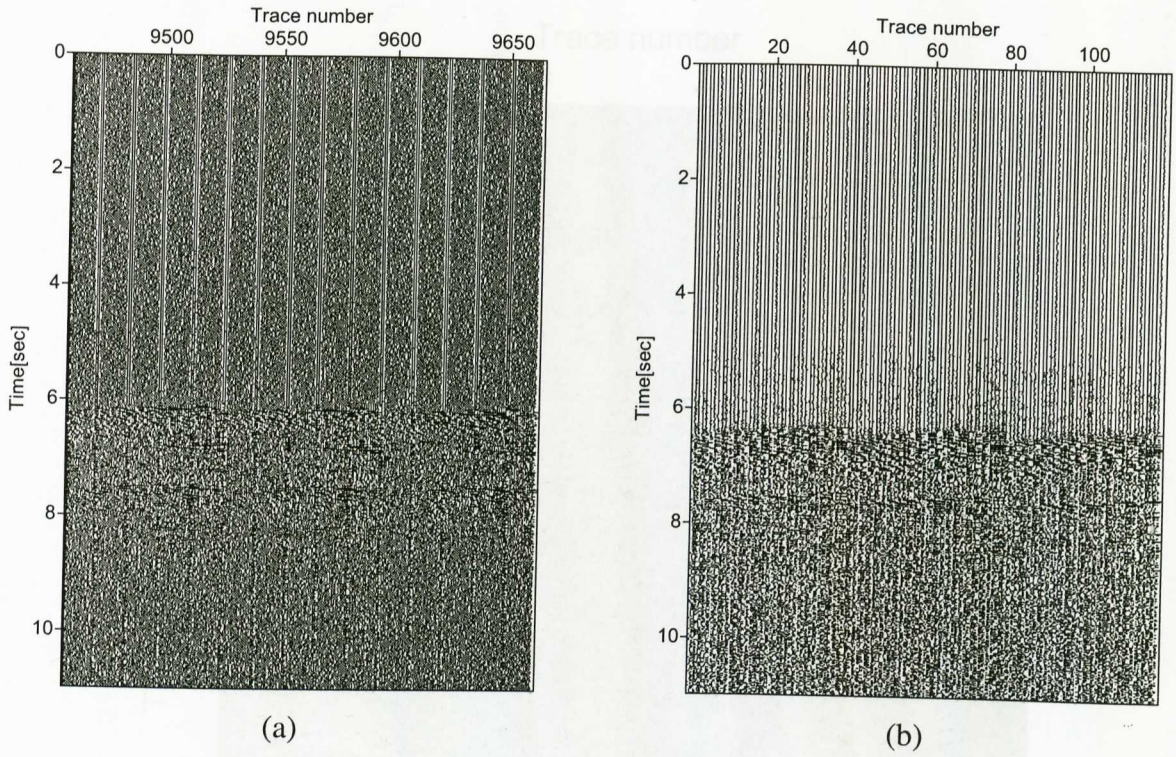

Figure 2.11: Examples of (a) a CSG record with responses due to 3 shots and (b) a CMP gather with responses due to 3 shots. Both are courtesy of [2].

Processing of seismic data includes, but is not limited to: filtering, common mid-point (CMP) sorting, velocity analysis, normal move-out (NMO) correction, and stacking. Each seismic trace has three primary geometrical factors which determine its nature:

1. Shot position;

2. Receiver position;

3. Position of the subsurface reflection point.

The last factor is the most critical [5]. Before processing, this position is unknown but a good approximation can be made by assuming that this reflection point lies vertically under the position on the surface mid-way between the shot and the receiver for that particular trace. This point is referred to as *mid-point* or *depth-point* (CDP) (Figure 2.10). The CMP gather is important for seismic processing because the subsurface velocity can be easily derived. In general, the reflection seismic energy is very weak and it is essential to increase the signal-to-noise ratio (SNR) of most data. Once the velocity is known, the

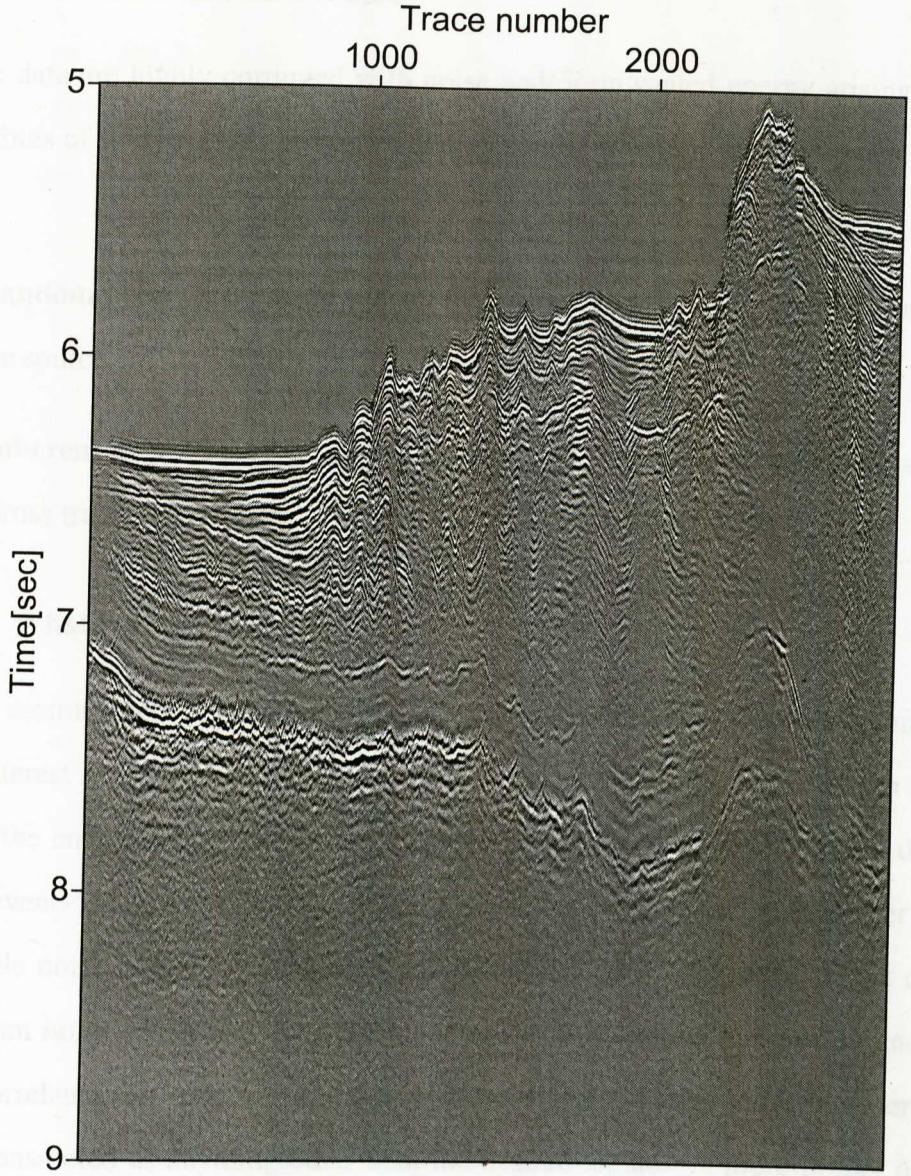

Figure 2.12: A CMP stacked section example (courtesy of [2]).

traces in CMP gathers can be corrected for NMO, which is basically a way of correcting for time differences which occur due to offset in a CMP gather, i.e., to get the equivalent of a *zero-offset* trace. This implies that all traces will have the same reflected pulses at the same time, but with different random and coherent noise. So combining all the traces in a CMP gather will average out noise and the SNR increases. This process is known as stacking. An example of a stacked CMP gather section is shown in Figure 2.12.

2.3.2 Seismic Data and Noise

Seismic data are highly corrupted with noise and/or unwanted energy arising from different kinds of sources. This unwanted energy can be classified into two main categories [1]:

- **Random noise (incoherent noise)**: This type of added energy is not generated by the source.
- **Coherent noise**: This type is usually generated by the source itself and is coherent across traces and gathers.

2.3.2.1 What is noise?

Noise in seismic records is variable in both time and space [57]. One can define the signal of interest as the energy which is coherent from trace to trace. Noise, on the other hand, is the energy that is incoherent from trace to trace [58]. Furthermore, data from seismic events is correlated and its energy is generally concentrated at the lower frequencies, while noise is more uncorrelated and broadband [54]. However, this is only true for random noise. Spatially coherent noise is the most troublesome noise and can be highly correlated and sometimes aliased with the signal [58] and [55]. In general, noise can be considered as anything other than the desired signal. A more proper definition of noise contaminating seismic signals can be stated by defining the type of signals we are interested in. The authors in [58] defined the signal of interest as the energy that is most coherent and desirable for geophysical interpretation of primarily reflected arrivals. Anything other than that is considered to be unwanted energy, i.e., noise.

2.3.2.2 Random noise

Disturbances in seismic data which lack phase coherency between adjacent traces are considered to be random noise. Unlike coherent noise energy, such energy is usually not related to the source that generates the seismic signals. In land seismic records, wind, rain, and instrument noise are examples of random noise. Based on the assumption that

random noise is an additive white Gaussian noise (AWGN) [1, 59], it can be removed easily in several different ways such as frequency filtering, deconvolution, stacking [1, 5], wavelet denoising [60, 61, 62], filtering using Gabor representation [63] and many other methods. However, due to the advances in acquisition technology systems as described previously, the issue of random noise removal is becoming less important when compared to the issue of removing coherent noise.

2.3.2.3 Coherent noise

Spatially coherent noise is the energy which is generated by the source. It is an undesirable energy that is added to the primary signals. Such energy shows consistent phase from trace to trace. Examples of such a type in land seismic records are [1]: multiple reflections (called multiples), surface waves like ground roll and air waves, coherent scattered waves, vibroseis truck noise, dynamite ghosts, etc. Improper removal of coherent noise can affect nearly all the processing techniques and complicates interpretation of geological structures (see [1], [5], and [64]). There exist loads of techniques which deal with the problem of suppressing/attenuating coherent noise that contaminates seismic data [1, 65, 64, 66, 67, 39, 68, 69, 70]. A schematic diagram can be seen in Figure 2.13, which shows various methods for seismic data filtering depending upon the type of noise corrupting the recorded data. The filtering process is an important step in order to proceed further with the other seismic DSP steps such as migration that will help geophysicists to better analyze and interpret the acquired data. The reader can examine into references [1] and [8] for more information about seismic data filtering and noise suppression.

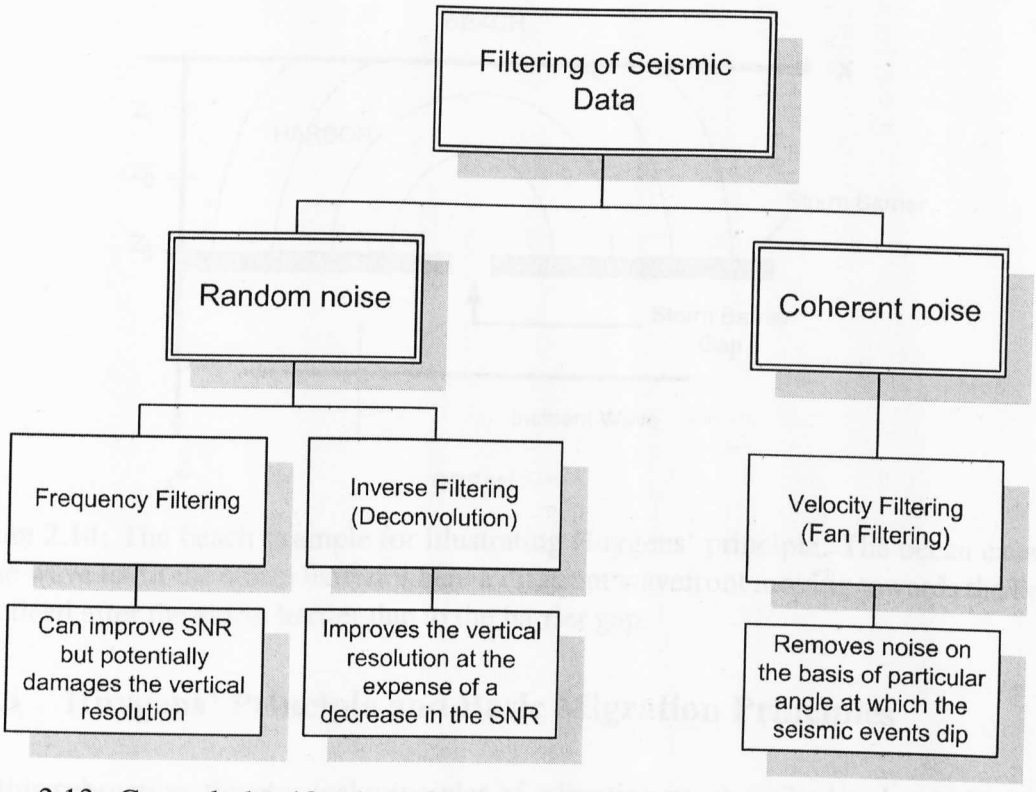

Figure 2.13: General classification of techniques for filtering seismic data. This classification is based on the type of noise that contaminates the data, namely, random and coherent noise.

2.4 Migration

After performing the necessary different filtering processes on the data, it can be very misleading to think of such data as a cross-section of the earth. This is because the actual reflection points are unknown. We need to take wave propagation effects into account to correctly determine the reflection points of the subsurface structure [71]. This is done using a process known as *Seismic Migration*. Migration can be defined as the process of reconstructing a seismic section so that the reflection events are repositioned under their correct surface location at their correct vertical reflection time or depth location [5, 1]. Basically, migration removes the distorting effects of dipping reflectors from seismic sections. It also removes the diffracted arrivals resulting from sharp lateral discontinuities [9, 7, 6, 10].

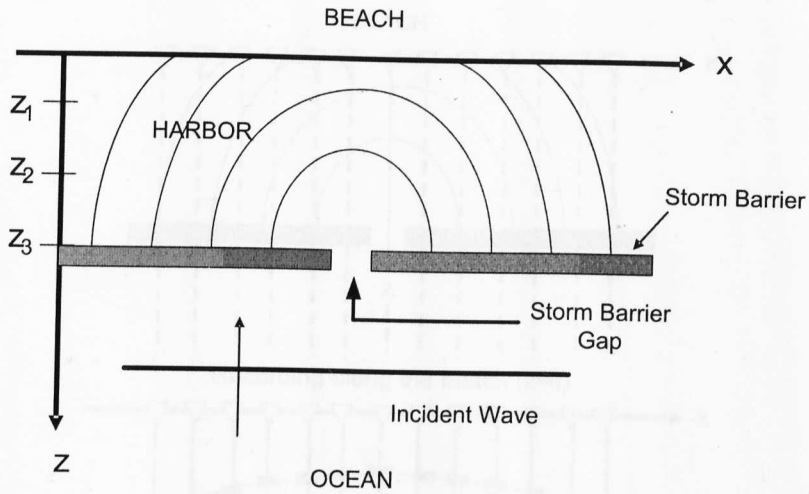

Figure 2.14: The beach example for illustrating Huygens' principle. The ocean causes a plane wave to hit the storm barrier where a different wavefront moving towards the beach is noticed after the storm barrier due to the barrier gap.

2.4.1 Huygens' Principle and Basic Migration Principles

For this subsection, the physical principles of migration are described and we will follow [1, 72, 73]. Huygens' principle is the basis of migration. Consider the harbour example shown in Figure 2.14. Let us assume that a storm barrier exists at some distance z_3 from the beach and that there is a gap in the barrier. Now, also imagine that a calm afternoon breeze that comes from the ocean causes a plane incident water wave to hit the barrier. Its wavefront is parallel to the storm barrier. As we walk along the beach line, we notice a different wavefront from the incoming plane wave. The gap on the storm barrier has acted as a secondary source and generated the semicircular wavefront that is propagating towards the beach. Now, assume that we did not know about the storm barrier and the gap. We may want to lay out a receiver cable along the beach to record in time the approaching waves. Figure 2.15 illustrates this idea of recording in time the approaching waves with semicircular wavefronts. So the gap in the storm barrier acts as a Huygens' secondary source.

We can apply this principle to reflection seismology by imagining that each point on a reflector (geological interface) generates a secondary source in response to the incident wavefield. This is known as the *exploding reflector model* [72]. Consider a single point

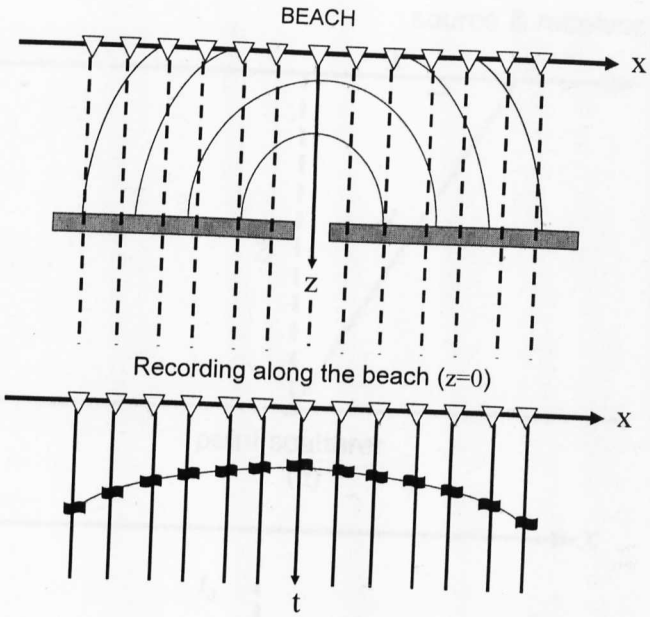

Figure 2.15: This figure shows how the approaching waves with semi-circular wavefronts generated by Huygens' secondary source from the beach example (Figure 2.14) are recorded as hyperbolas in time.

scatterer in a medium as shown in Figure 2.16 (a). The minimum travel time is given by:

$$t_0 = \frac{2z}{c} \tag{2.1}$$

where z is the depth of the scatter and c is the velocity of the propagating wave (which we assume to be constant). Also, assume that the source and the receiver are co-located (zero-offset) as in Figure 2.16 (a). The travel time as a function of distance, x, is given by [73]:

$$t(x) = \frac{2\sqrt{x^2 + z^2}}{c}. \tag{2.2}$$

By squaring, rearranging, and using Eq. (2.1) then Eq. (2.2) can be expressed as:

$$\frac{t(x)^2}{t_0^2} - \frac{4x^2}{c^2 t_0^2} = 1. \tag{2.3}$$

This shows us that the travel time curve for the scattered arrival has the form of a hyperbola with the apex directly above the scattering point (our secondary source) as seen in Figure 2.16 (b).

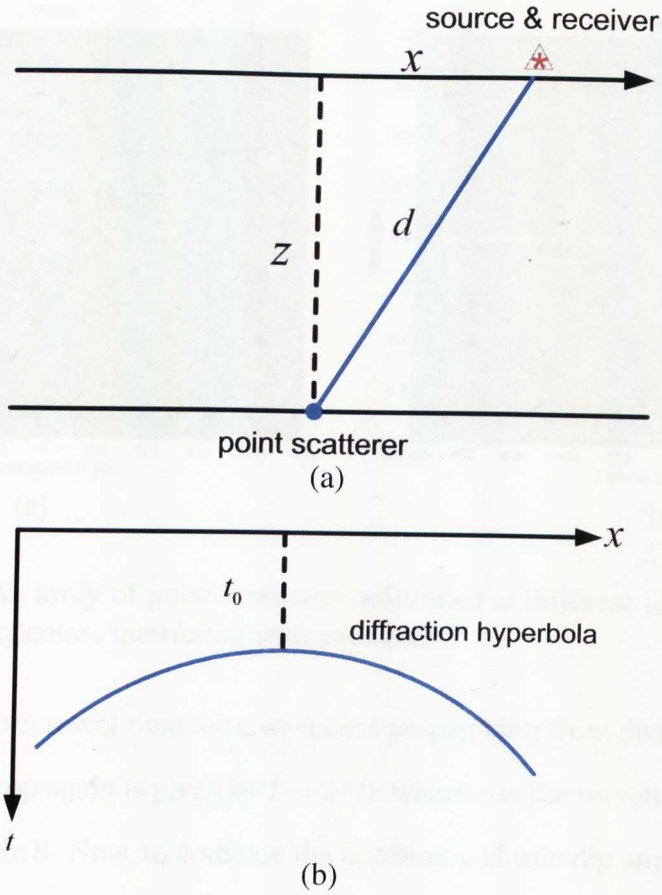

Figure 2.16: (a) A point scatterer (acting as Huygens' secondary source), and (b) a curved reflector which is produced based on the point scatterer.

Now, consider a horizontal reflector (Figure 2.17 (a)) that is composed of a series of point scatterers (gaps), each one of which generates a diffraction hyperbola in a zero-offset section as in Figure 2.17 (b). Following Huygens' principle, these hyperbolas sum coherently only at the time of the reflection while the later contributions cancel out (Figure 2.17 (b)). However, if the reflector vanishes at some point, then there will be a diffracted arrival from the endpoint that will show up in zero-offset data. This creates an artifact in the section that might be falsely interpreted as structure. We need to migrate such sections in order to remove such artifacts.

Another principle goal of migration is to map the apparent dip that is seen on the zero-offset sections into true dip [1, 72, 74, 71]. True dip angle is always greater than apparent dip angle. Consider a reflector dipping at an angle of θ in the true earth as in Figure

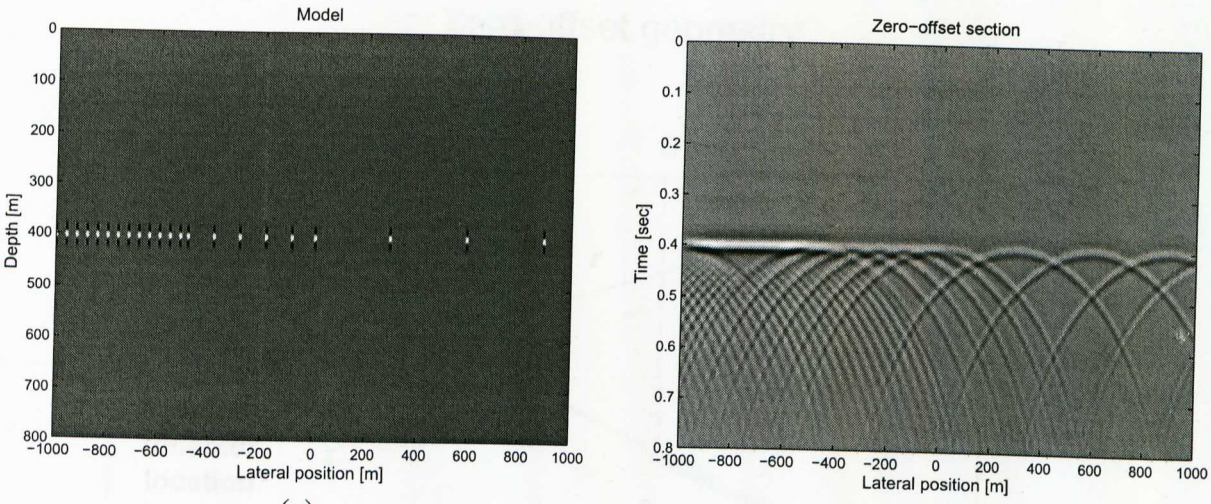

(a) (b)

Figure 2.17: (a) An array of point scatterers positioned at different locations, and (b) its resultant curved reflectors interfering with each other.

2.18. The zero-offset travel time for a wavefield propagating from distance x down to the reflector and back up again is given by $t = 2r/c$ where r is the wavefield path length and is equal to $r = x \sin\theta$. Now, to compare the apparent and true dip angles, the travel time must be converted to depth via Eq. (2.1) and, therefore, in the unmigrated depth section $z = x \sin\theta$. By definition, the slope of this event is the tangent of the apparent dip angle, say β. Therefore, we have:

$$\tan\beta = \sin\theta. \tag{2.4}$$

Equation (2.4) shows clearly that the apparent dip angle is always less than true dip angle. Again in Figure 2.18 the events associated with the two zero-offset wavefields drawn from the dipping reflector to the two receivers will appear on the unmigrated section at the position locations associated with the two receivers [1]. Therefore, migration moves the energy horizontal, i.e., up dip the energy. In addition, from the same figure, the length of the reflector in the geological section is shorter than in the time section. Thus, migration also shorten reflectors. In summary, migration focuses energy by collapsing diffractions as well as it correctly steepens, shortens, and moves reflectors up-dip.

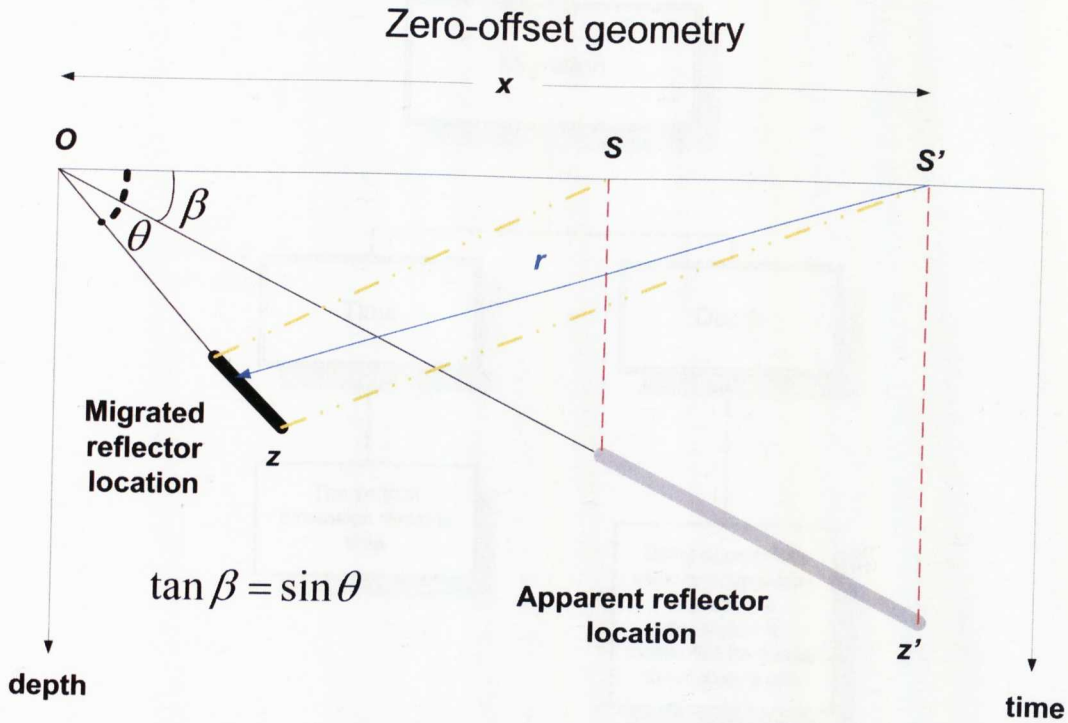

Figure 2.18: Migration principles. The apparent reflector with a dip angle β in the time section when migrated is moved up-dip, steepened (to an angle θ), shortened, and mapped on its true subsurface location.

2.4.2 Migration Kinds

Migration can be implemented based on different techniques. It is an important and expensive process that is applied to reflection seismic data before it is interpreted. Since it is the last major process applied to the data, it is likely to be blamed for all sorts of things like inconsistent amplitudes and lack of structural details even though these problems may arise from acquisition or earlier processing steps [32]. Therefore, it is important to know what type of migration to use.

Migration can be classified as *Pre-stack* migration or *Post-stack* migration. For the former, migration is performed on pre-stacked data either on CSGs or on CMPs. For large surveys, it will require massive computer storage and days, maybe even weeks, of CPU time on a super computer [32]. For the later case, the migration is applied on the stacked CMP data. It is much less expensive than pre-stack migration but it is also less accurate in complicated areas of the sub-earth. Finally, it can be accomplished on work-

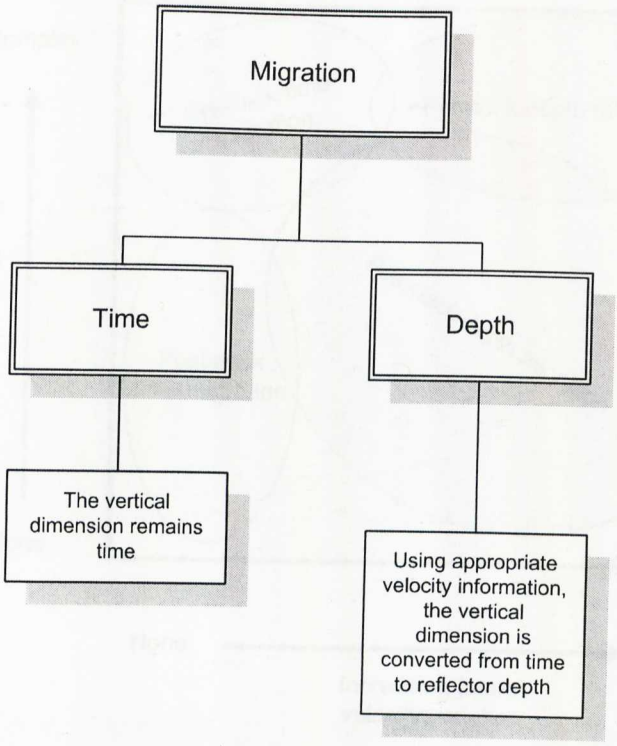

Figure 2.19: This is another migration classification which depends on how much physics one puts into the migration algorithm.

station class machines.

Moreover, migration can be classified in terms of how much physics we put into the algorithm, specifically for handling velocity variations. This type of classification is based on time migration versus depth migration (see Fig 2.19). Note that any migration (pre-stack or post-stack) can be output in time or depth. In areas of strong velocity variations, depth migration is used and the output is given as a depth section. Geological examples of strong lateral velocity variations include salt overhangs, sub-salt areas, or combinations of such features [32]. The main difference between time and depth migration is mostly for ease of interpretation afterwards where one can make more simplifications in time migration than for depth migration. Figure 2.20 illustrates schematically were pre/post stack time/depth migration is employed.

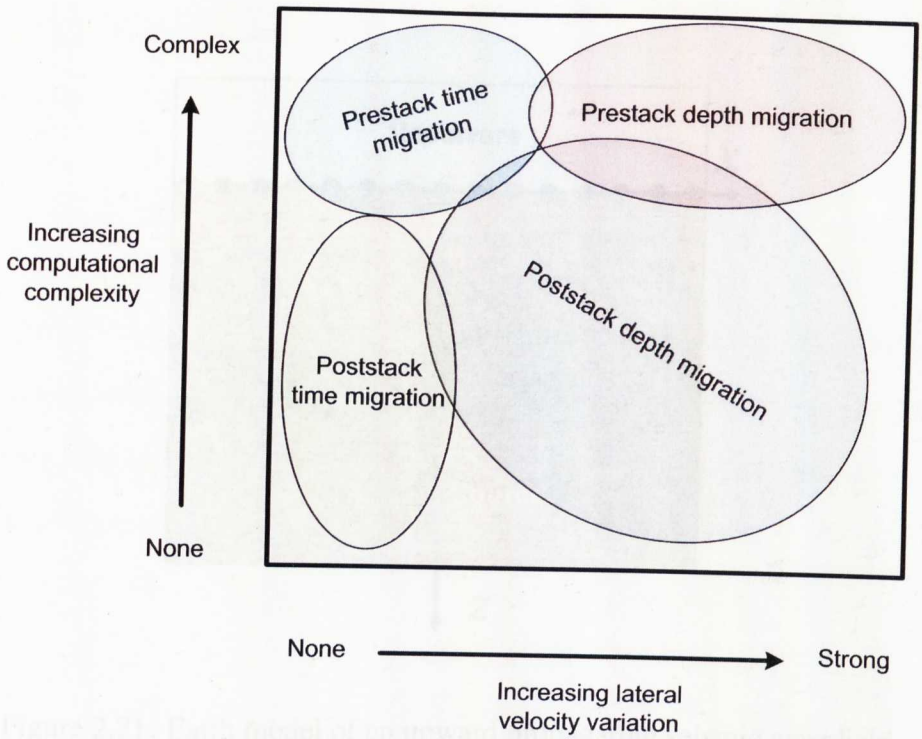

Figure 2.20: Migration types as a function of computational complexity and lateral velocity variations. The most accurate and most expensive migration kind is the pre-stack depth migration.

2.4.3 Migration as a Filtering Process

This subsection describes the migration as a filtering process and shows the complex-valued seismic migration filter's origins. Here, the migration is based on the concept that a wavefield (acquired seismic data) which is measured at the earth's surface, $u(x, t, z = 0)$, represents the boundary values of the wavefield $u(x, t, z)$ reflected in the sub-earth. The main objective of this migration is to determine the true position of the reflectors by downward continuation of the wavefield that is measured at the surface. This can mathematically be explained through the wave equation and its solution where over here we deal with the 2-D case.

Let us assume that an acoustic seismic wave propagates upwards through the earth (Figure 2.21). For simplicity we assume that the wave propagates in a homogeneous medium with constant velocity c. This wave can be described by the following 2-D hy-

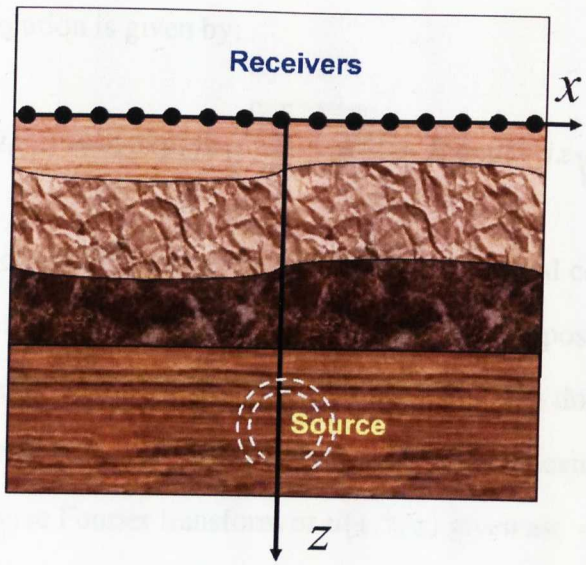

Figure 2.21: Earth model of an upward propagating seismic wavefield.

perbolic wave equation [1, 75]:

$$\frac{\partial^2 u}{\partial x^2} + \frac{\partial^2 u}{\partial z^2} = \frac{1}{c^2}\frac{\partial^2 u}{\partial t^2}. \tag{2.5}$$

where $u(x, t, z)$ is the propagating wavefield (displacement), t stands for the time variable, x represents the lateral spatial axis, and z denotes the depth axis. Now, define $j = \sqrt{-1}$ and let $U(K_x, \Omega_t, z)$ be the 2-D Fourier transform of $u(x, t, z)$ with respect to the variables x and t as given by:

$$U(K_x, \Omega_t, z) = \int_{-\infty}^{\infty}\int_{-\infty}^{\infty} u(x, t, z)e^{j(K_x x - \Omega_t t)}dxdt. \tag{2.6}$$

Note that K_x and Ω_t are the analogue wavenumber and analogue angular frequency. Taking the Fourier transform of both sides of Eq. (2.5) and carrying out the necessary rearrangement gives:

$$\frac{\partial^2 U(K_x, \Omega_t, z)}{\partial z^2} = (\frac{\Omega_t^2}{c^2} - K_x^2)U(K_x, \Omega_t, z). \tag{2.7}$$

Equation (2.7) is a second-order ordinary differential equation with respect to the variable z. Its well-known solution is given by:

$$U(K_x, \Omega_t, z) = A\exp(jz\sqrt{\frac{\Omega_t^2}{c^2} - K_x^2}) + B\exp(-jz\sqrt{\frac{\Omega_t^2}{c^2} - K_x^2}) \tag{2.8}$$

where A and B are constants that can be found using the initial conditions related to the differential equation. Following the sign convention of [6], the positive exponent refers to an up-going propagation while the negative solution refers to a down-going propagation. Since it is assumed that the wave is propagating upwards, one can set $B = 0$. To find A, consider the 2-D inverse Fourier transform of $u(x, t, z)$ given as:

$$u(x, t, z) = \int_{-\infty}^{\infty}\int_{-\infty}^{\infty} U(K_x, \Omega_t, z)e^{-j(K_x x - \Omega_t t)}dK_x d\Omega_t. \tag{2.9}$$

Substituting Eq. (2.8) (with $B = 0$) into Eq. (2.9) yields:

$$u(x, t, z) = \int_{-\infty}^{\infty}\int_{-\infty}^{\infty} A\exp(jz\sqrt{\frac{\Omega_t^2}{c^2} - K_x^2})e^{-j(K_x x - \Omega_t t)}dK_x d\Omega_t. \tag{2.10}$$

Now, by putting $z = 0$, it can be clearly seen from Eq. (2.9) and Eq. (2.10) that the boundary condition $A = U(K_x, \Omega_t, 0)$ and, therefore Eq. (2.8) becomes:

$$U(K_x, \Omega_t, z) = \begin{cases} U(K_x, \Omega_t, 0)\exp(jz\sqrt{\frac{\Omega_t^2}{c^2} - K_x^2}) & \text{if } |\Omega_t| > c|K_x| \\ U(K_x, \Omega_t, 0)\exp(-z\sqrt{K_x^2 - \frac{\Omega_t^2}{c^2}}) & \text{if } |\Omega_t| \leq c|K_x| \end{cases} \tag{2.11}$$

where $U(K_x, \Omega_t, 0) = \mathcal{F}\{u(x, t, 0)\}$ represents the boundary condition for the differential equation given in Eq. (2.7). Then the record $u(x, t, z)$ will be $u(x, t, z) = \mathcal{F}^{-1}\{U(K_x, \Omega_t, z)\}$. Note that $\mathcal{F}$ and $\mathcal{F}^{-1}$ are the forward and inverse Fourier transform operators, respectively. In general, at $z = z_o + \Delta z$ and given the initial condition at $z = z_o$, the general solution in terms of boundaries at a width equal to Δz is given by:

$$U(K_x, \Omega_t, z_o + \Delta z) = \begin{cases} U(K_x, \Omega_t, z_o)\exp(j\Delta z\sqrt{\frac{\Omega_t^2}{c^2} - K_x^2}) & \text{if } |\Omega_t| > c|K_x| \\ U(K_x, \Omega_t, z_o)\exp(-\Delta z\sqrt{K_x^2 - \frac{\Omega_t^2}{c^2}}) & \text{if } |\Omega_t| \leq c|K_x|. \end{cases} \tag{2.12}$$

Clearly, Eq. (2.12) can be rewritten as:

$$U(K_x, \Omega_t, z_o + \Delta z) = U(K_x, \Omega_t, z_o) H_d(K_x, \Omega_t) \tag{2.13}$$

where

$$H_d(K_x, \Omega_t) = \begin{cases} \exp(j\Delta z\sqrt{\frac{\Omega_t^2}{c^2} - K_x^2}) & \text{if } |\Omega_t| > c|K_x| \\ \exp(-\Delta z\sqrt{K_x^2 - \frac{\Omega_t^2}{c^2}}) & \text{if } |\Omega_t| \leq c|K_x|. \end{cases} \tag{2.14}$$

Equation (2.14) can be seen as the wavenumber-angular frequency response of a space-time linear-shift invariant (LSI) analogue filter [75, 6, 10] and it is known as a *Seismic Migration Filter* [7]. In the geophysics community, this filter is known as the extrapolation operator since one extrapolates the previous depth seismic section to the next one [1, 14, 9].

To explain more, let us reconsider the harbour example in Figure 2.15. Moving the receiver cable from the beach into the water closer to the barrier is like moving the recording receiver cable from the surface down into the earth close to the reflectors. Recall that the gap of the barrier can be thought of as a point scatterer on the reflection geological interface causing the diffraction hyperbola. Now, start with the wavefield recorded at the surface (at $z = 0$) and move the receivers down to depth levels at finite intervals. The wavefield extrapolation as in Eq. (2.13) of up-going wavefields at the surface can be considered in this case as equivalent to lowering the receivers into the earth. The recording cable is the storm barrier. Also, the arrival from the gap occurs at $t = 0$. As the cable moves into the ocean and records closer to the barrier, the recorded diffraction hyperbola arrives earlier, and become shorter and more compressed. Furthermore, it collapses to a point when the receivers coincide with the storm barrier over which the source point forms a gap. This is how we link Huygens' principle with migration or wavefield extrapolation [1].

To carry on, the wavefield in practice is presented in sampled form so let us define Δt to be the temporal sampling interval, Δx to be the horizontal spatial (trace) sampling

interval, and Δz as the depth sampling interval. Then, the discrete version of the acoustic wavefield $u(x,t,z)$ is $u(x_i, t_l, z_k)$ where $x_i = i\Delta x$, $t_l = l\Delta t$, and $z_k = k\Delta z$ for all $i, l, k \in \mathbb{Z}$ with $\mathbb{Z}$ the set of integers. Also, define k_x as the digital wavenumber counterpart of K_x and ω as the digital angular frequency counterpart of Ω_t. The migration operation is performed using a digital filter (derived from its analogue counterpart in Eq. (2.14) [1, 75, 12]) whose frequency-wavenumber ($\omega - k_x$) response is given by:

$$H_d(e^{jk_x}, e^{j\omega}) = \exp(j\frac{\Delta z}{\Delta x}\sqrt{\frac{\Delta x^2}{\Delta t^2}\frac{\omega^2}{c^2} - k_x^2}). \tag{2.15}$$

This is the ideal frequency-wavenumber response of an all-pass filter with non-linear phase. For a single angular frequency ω_o, Eq. (2.15) becomes a 1-D digital filter given by:

$$H_d(e^{jk_x}, e^{j\omega_o}) := H_d(e^{jk_x}) = \exp(j\frac{\Delta z}{\Delta x}\sqrt{\frac{\Delta x^2}{\Delta t^2}\frac{\omega_o^2}{c^2} - k_x^2}). \tag{2.16}$$

From the signal processing point of view, Eq. (2.16) shows that $H_d(e^{jk_x})$ is a complex-valued even function with $H_d(e^{jk_x}) = H_d(e^{-jk_x})$. Also, it was shown in [75] that the migration (extrapolation) process cannot be obtained by a causal filter since its response is defined for negative values of the variable t. Therefore, Eq. (2.16) can be approximated by a non-causal even symmetric FIR digital filter of length N (N is odd) [1, 12, 10]. That is,

$$H_d(e^{jk_x}) = h[0] + 2\sum_{n=1}^{\frac{N+1}{2}-1} h[n]\cos(nk_x). \tag{2.17}$$

where $h[n] \in \mathbb{C}$ ($\mathbb{C}$ is the set of complex numbers), i.e., the FIR filter coefficients are complex-valued. Now, the filter response cut-off is given by the wavenumber k_c where:

$$k_x = k_c = \frac{\Delta x}{\Delta t}\frac{\omega_o}{c} \tag{2.18}$$

where the approximation needs only to be accurate for $|k_x| < |k_c|$ since this corresponds to the wavenumbers k_x for which the waves are propagating [1, 12]. Finally, let $b =$

$\Delta z/\Delta x$, and then the 1-D migration filter simply becomes:

$$H_d(e^{jk_x}) = \exp(jb\sqrt{k_c^2 - k_x^2}). \tag{2.19}$$

Then, for each frequency sample we can extrapolate a spatially sampled seismic wavefield $u(x_i, e^{j\omega_o}, z_k)$ from say depth z_k to $z_{k+1} = z_k + \Delta z$ using:

$$U(e^{jk_x}, e^{j\omega_o}, z_o + \Delta z) = U(e^{jk_x}, e^{j\omega_o}, z_o)H_d(e^{jk_x}, e^{j\omega_o}) \tag{2.20}$$

where $U(e^{jk_x}, e^{j\omega_o}, z_o + \Delta z)$ is equal to the discrete-space Fourier transform (DSFT) of $u(x_i, e^{j\omega_o}, z_k)$ with respect to x_i.

2.4.4 Frequency-Wavenumber Migration Techniques

Equation (2.20) informs us that the propagating wavefield on the z_kth layer to the next layer at z_{k+1} is easily accomplished in the $\omega - k_x$ domain. This type of extrapolation is called the phase shift method and was first introduced by Gazdag [76] for performing post-stack migration. His migration algorithm starts with Fourier transforming the input traces from their $t-x$ domain to the $\omega-k_x$ domain and then using the extrapolation form given in Eq. (2.20). This method is accurate up to dip angles of 90° [1]. In addition, this method is accurate when a constant velocity is used for each extrapolation step Δz. However, the velocity may vary for each depth step size. In this case, an accurate migration is allowed when the velocities vary only with depth as illustrated in Figure 2.22, i.e., when the velocities are vertically varying. This is justified when using small depth sampling intervals Δz [76, 1]. More details, as well as other variations of the $\omega - k_x$ technique like the Stolt method, can be found in [77, 78, 79, 1].

To overcome the limitation of the $\omega - k_x$ extrapolation method, Gazdag and Sguazzero [28] developed a method called the Phase Shift plus interpolation (PSPI) migration technique which can handle horizontal velocity variations. It migrates a Fourier transformed wavefield just as the phase shift migration does. However, in the PSPI technique, the

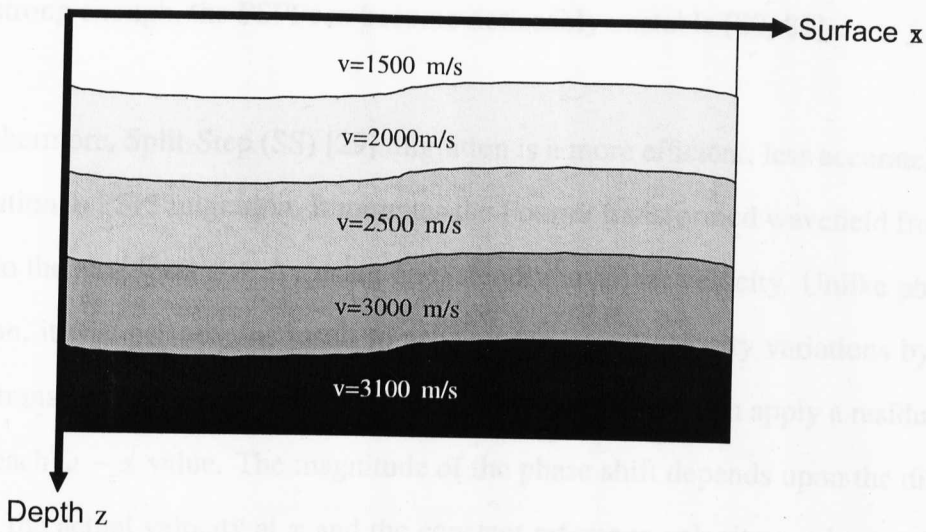

Figure 2.22: A hypothetical earth model showing vertically varying velocities due to homogeneous media within each earth layer. These types of subsurface structures can be easily migrated in the frequency-wavenumber $\omega - k_x$ domain, i.e., using the phase-shift technique.

migration from depth z to $z + \Delta z$ is done multiple times, for a range of reference velocities. Now, each of these wavefields is inverse Fourier transformed to the $\omega - x$ domain. A single wavefield at the depth $z + \Delta z$ is then constructed by interpolating between the available constant-velocity extrapolations, using the velocity at each spatial location x to guide the interpolation. This single combined wavefield is then transformed back to wavenumber, and the migration continues. The more velocities used in the phase shift migration, the greater the accuracy of the PSPI method will be. Although, the PSPI technique is a very accurate depth migration method, but it is also very expensive. At a single angular frequency in a depth slice, the PSPI method costs [28]:

$$COST_{PSPI} = (n_{ref} + 2)\frac{3N_{FFT}}{2}\log_2 N_{FFT} \tag{2.21}$$

complex multiplications and additions. Here, n_{ref} stands for the number of used reference velocities and N_{FFT} is the number of FFT points used in the algorithm to transform the trace spatial samples to wavenumber domain and vice versa. In addition, patching together constant velocity solutions is still an approximation. If the lateral velocity varia-

tion is strong enough, the PSPI can become noticeably unstable [80, 81].

Furthermore, Split-Step (SS) [29] migration is a more efficient, less accurate, alternative solution to PSPI migration. It migrates the Fourier transformed wavefield from depth level z to the next level $z + \Delta z$ using one laterally invariant velocity. Unlike phase shift migration, it will perturb this result to account for lateral velocity variations by inverse Fourier transforming the wavefield to space. After that, it will then apply a residual phase shift at each $\omega - x$ value. The magnitude of the phase shift depends upon the difference between the actual velocity at x and the constant reference velocity used to perform the migration. It completes the split-step extrapolation from z to $z + \Delta z$ by Fourier transforming the perturbed wavefield back to the wavenumber domain again. According to [3], the computational cost of the SS method for single angular frequency at a depth slice is approximately one-half of that for the PSPI given in Eq. (2.21). For more details see [29, 81, 3].

2.4.5 The Explicit Frequency-Space Migration Technique

Another way of accurately migrating laterally varying materials, is by using the N-length FIR digital filter coefficients that appeared in Eq. (2.17). This is known to be the frequency-space ($\omega - x$) wavefield extrapolation where the extrapolation of a spatially sampled seismic wavefield $u(x_i, e^{j\omega_o}, z_k)$ from depth z_k to $z_{k+1} = z_k + \Delta z$ may be performed independently for each frequency ω_o, by a spatial convolution with a predesigned 1-D migration digital filter $h[n]$ (see Eq. (2.17)) using [12]:

$$u(x_i, e^{j\omega_o}, z_{k+1}) = \sum_{n=(-N+1)/2}^{(N-1)/2} h[n] u(x_{i-n}, e^{j\omega_o}, z_k). \tag{2.22}$$

In this case, the variation of velocities can be handled by letting the coefficients of the migration filter $h[n]$ vary as the velocity changes with the spatial coordinates x_i and z_k [12, 1, 13]. This is also known as the explicit finite-difference method [13, 1] since we start from the actual acoustic wave equation and then approximately solve it. The ap-

proximation is necessary to avoid unstable migrated sections. Such a technique is much less expensive when compared with the PSPI or SS methods and can also handle lateral velocity variations. The total computational cost of the explicit depth $\omega - x$ migration for a given angular frequency at one depth slice is:

$$COST_{\omega-x} = n_x \frac{3N-1}{2} \tag{2.23}$$

complex multiplications and additions, where N is the FIR filter length and n_x is the total number of spatial samples (number of traces).

2.4.5.1 Problem Definition

In order to properly migrate (extrapolate) seismic wavefields, there are special filter requirements that are needed for using this attractive method. Firstly, the spatial convolution filter coefficients, $h[n]$, must perform migration of wavefields for high propagation angles in heterogeneous media. This, however, implies that the spatial length of the filters must be large enough to contain those angles. On the other hand, migration in heterogeneous media requires a short spatial filter length to handle the lateral variations accurately. Furthermore, the amplitude of the magnitude wavenumber response of the filter given by Eq. (2.19) should neither be much greater than one nor be much smaller than one within the passband. That is, if the amplitude is much greater than one, say by 10^{-2}, and one is using 500 migration steps, then this leads to unstable migration results, since this small amplitude amplifies due to the migration recursive operation by $1.01^{500} \approx 144.77$ [1, 14]. Similarly, if the amplitude is much less than one, then this will attenuate the wavefield during migration. Also, within the stopband region, the magnitude spectrum must exponentially decay towards zero. Lastly, but not least, the phase wavenumber response of the designed filter must be accurate for the whole range of angles for which the filter is designed, i.e., it must be accurate within the filter's prescribed passband. Figure 2.23 summarizes the 1-D $\omega - x$ seismic migration FIR digital filter requirements. It is worth mentioning that unlike the $\omega - k_x$ technique there is a limit to the maximum possible angle of wavefield propagation for the $\omega - x$ wavefield extrapolation method. The maximum

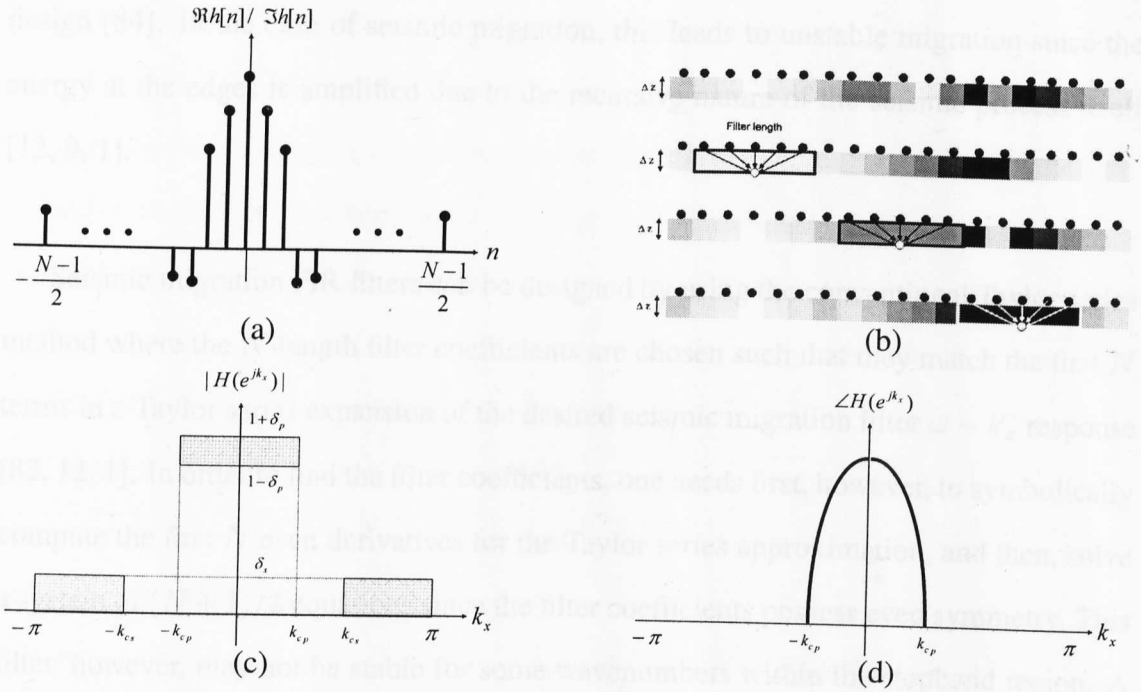

Figure 2.23: 1-D Seismic migration FIR filter requirements. (a) A non-causal spatial operator with even symmetry, and (b) a short length $\omega - x$ migration filter for accuracy. In other words, due to heterogeneous media within a layer, the velocity will also vary horizontally. At every lateral position, a new filter is used to perform migration on the data from one depth level to another one. Within the filter length, the medium is assumed to be homogeneous. Finally, (c) is an accurate magnitude wavenumber response, and (d) an accurate passband phase response.

possible angle of propagation for the $\omega - x$ migration method depends on the success in properly designing such digital filters that fulfil the requirements illustrated in Figure 2.23 [82, 1, 14, 81].

2.4.5.2 Previous Work

Designing FIR seismic migration filters is still an important and a challenging area of research. Researchers have proposed and used several techniques to design complex-valued FIR seismic migration digital filters [14, 12, 11, 9, 10, 1]. In general, most of the techniques were proposed to satisfy either the time (space)-domain constraints or the frequency (wavenumber)-domain constraints [7, 83, 21]. For example, an impulse response windowing technique is a simple technique for designing general FIR filters [84, 7]. However, since all frequency(wavenumber)-selective filters are ideally discontinuous at their band edges, simple truncation of the impulse response often yields an unacceptable FIR

LEEDS UNIVERSITY LIBRARY

design [84]. In the case of seismic migration, this leads to unstable migration since the energy at the edges is amplified due to the recursive nature of the seismic process itself [12, 9, 1].

Seismic migration FIR filters can be designed by using the conventional Taylor series method where the N-length filter coefficients are chosen such that they match the first N terms in a Taylor series expansion of the desired seismic migration filter $\omega - k_x$ response [82, 12, 1]. In order to find the filter coefficients, one needs first, however, to symbolically compute the first N even derivatives for the Taylor series approximation, and then, solve a system of $(N+1)/2$ equations since the filter coefficients possess even symmetry. This filter, however, may not be stable for some wavenumbers within the stopband region. A modified version of this method was proposed by Hale [12] in 1991. Stability is guaranteed to exist where this modification forces the spectrum of such filters to be zero within the stopband region. However, designed seismic migration FIR filters using this modified method require long filter lengths to include high dip angles [12].

Moreover, it may be preferable to employ a design technique that is based on constraining the frequency(wavenumber)-domain to match certain specifications, like the case for these migration filters. While there exist many optimization techniques to meet such design specifications, the most widely used approach is the Parks-McClellan equiripple (Remez) filter design method [84, 7]. These filters are optimal in the min-max sense, meaning that, for a set of specifications, the largest error is always minimized. Such a technique was adopted by Soubaras [18] for designing 1-D migration FIR filters where both the real and imaginary parts of the filter are optimized in the min-max sense. Due to the ripply nature of its magnitude response, the filters can result in numerical background artifacts on migrated sections [14]. Moreover, since this method is based on polynomial factorization [21, 40, 22], it cannot be easily extended to the multi-dimensional (m-D) filter design case. This would limit the use of methods like the Parks-McClellan filter design for m-D filters. In addition, the Parks-McClellan design algorithm cannot incor-

porate additional constraints placed on the filter design [22].

In another development, Karam and McClellan [19] have extended the Parks-McClellan algorithm to FIR filters with complex coefficients. Under certain conditions [19], the designed filter will be optimal in the min-max sense for the set of extremal points. If not, it will be optimal with respect to a subset of the whole defined set of extremal points. The optimal design algorithm was shown by the same authors in [20]. Simulation results in both papers proved that this algorithm is efficient in terms of memory and speed of convergence. Unless we use a filter transformation like the one reported in [12, 10], it is not easy to extend this algorithm to the two-dimensional (2-D) FIR filter design, and the m-D will be even more complicated and difficult to achieve [21]. In addition, more constraints cannot be added to the design. Finally, the designed seismic migration FIR filter results using this method are practically undesirable since they lead to the introduction of numerical artifacts in migrated sections [14] as well as possessing unacceptable phase errors as we will see later on in simulation results.

Thorbecke *et al.* [85, 14], have used the L_2-norm and called it the weighted least-square (WLSQ) method as an alternative to the optimization criterion used for designing the migration FIR filters with the Remez exchange technique. Such a design technique is suitable for designing 2-D FIR filters that are used for the three-dimensional (3-D) seismic migration and the filters are comparable with those reported in [18]. However, such an optimization method lacks simplicity as well as requires matrix inversion [14].

2.4.6 The Frequency-Space Depth Post-Stack Migration and its Imaging Principle

Let us consider the shape of the wavefield at observation time $t = 0$ generated by a geological interface. Since no time has elapsed and, thus, no propagation has occurred, the wavefront shape must be the same as the reflector shape that generated the wavefront [72, 74, 1]. The fact that the wavefront shape at $t = 0$ corresponds to the reflector shape is

called the *imaging principle* which is performed after carrying out migration from depth z_k to depth z_{k+1} as given in Eq. (2.22) [1, 82, 72, 74]. We now need to extract our image from the extrapolated wavefield. In the case of the post-stack $\omega - x$ (or even the post-stack $\omega - k_x$) migration, the imaging principle is met by summing over all the angular frequencies ω_l's (l is the frequency index) [1, 82], i.e.,

$$u(x_i, t = 0, z_k) = \sum_l u(x_i, e^{j\omega_l}, z_k). \tag{2.24}$$

Now, we are ready to describe the explicit depth $\omega - x$ post-stack migration algorithm that is going to be used in this thesis. Firstly, after designing the 1-D seismic migration FIR digital filters, we store them in a look-up table. For each designed filter, we only store half of the filter coefficients (half of $h[n]$) due to the even symmetry of our explicit depth migration FIR digital filters as shown in Eq. (2.17). The explicit depth $\omega - x$ migration algorithm starts by transforming the stacked seismic section (which approximates the zero-offset section of the originally acquired data) from the $t - x$ domain to the $\omega - x$ domain. The migration of post-stacked seismic data based on the explicit depth migration is then given as follows:

1. We start at the first depth slice which works as the outer loop for the algorithm.
2. At the current depth slice, we start from the first frequency wavefield sample (inner loop).
3. Depending up on the current frequency-velocity values, calculate the wavenumber cut-off k_c using Eq. (2.18) and select the proper 1-D filter.
4. Perform the migration convolution given by Eq. (2.22).
5. Once we finish all the angular frequencies of the current depth slice, we proceed to the next depth slice.

If we reach the maximum number of depth slices, we stop the iterations, apply the imaging principle in Eq. (2.24), and write to a disc our final sub-earth $z - x$ image. Otherwise, go to the next depth slice and repeat steps $2 - 5$. Figure 2.24 shows a simple flow chart for

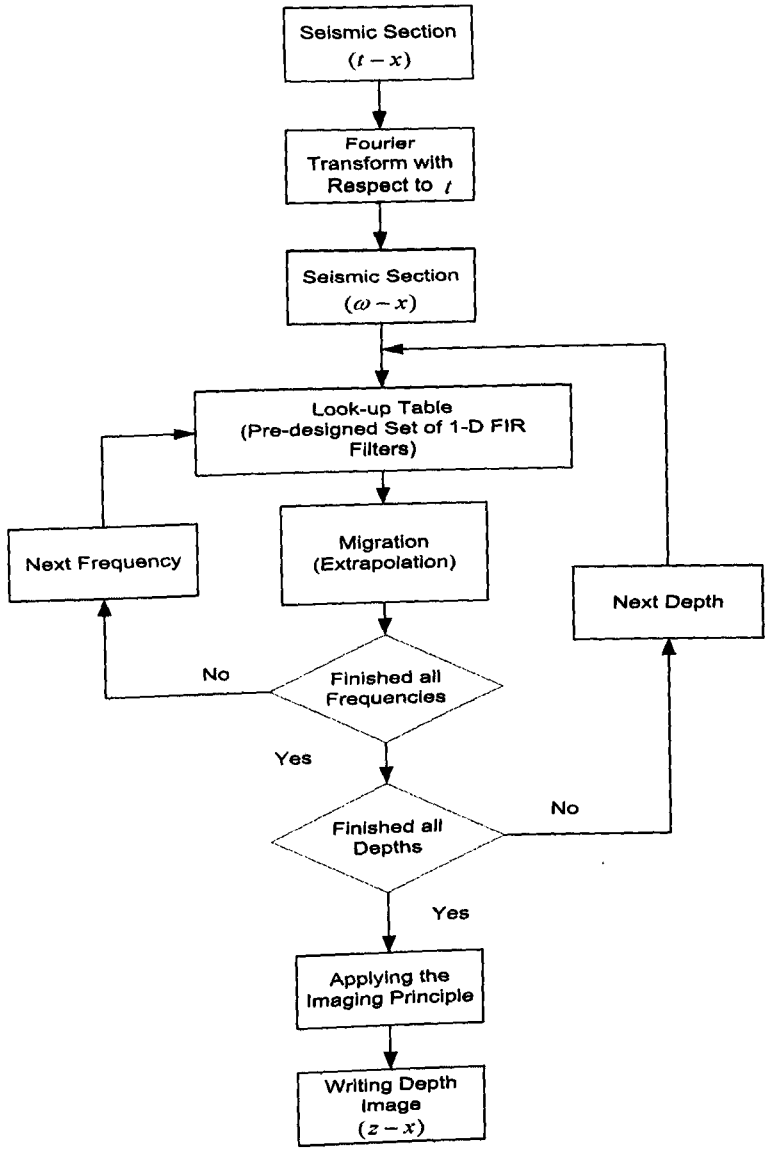

Figure 2.24: Diagram illustrating the explicit depth $\omega - x$ post-stack migration process. We start first by transforming the seismic section from the $t - x$ domain to the $\omega - x$ domain and then begin the iterations. Within each depth loop, we perform the extrapolation depending on the inner frequency loop and the current velocity value. Once all frequencies within the inner loop are finished we proceed to the next depth. Finally, we stop the outer depth loop once we reach the maximum number of depth slices, apply the imaging principle, and then store the migrated image on a disc.

a typical post-stack $\omega - x$ migration process. It is worth mentioning that since within a depth loop the angular frequencies are independent, we can parallelize this algorithm by preforming the extrapolation for each angular frequency on different processors [15, 16, 17].

2.5 Conclusion

In this chapter, a brief overview of seismic data acquisition and processing was shown. Great emphasis was put on the main scope of the thesis, namely, seismic migration. This material represents a necessary and sufficient background for the subsequent chapters for those who are unfamiliar with seismic data and seismic data processing. However, anyone who is interested in more details about seismology and its applications, processing methods, etc., is strongly recommended to look into Yilmaz's book on the subject [1].

More importantly, in order to have an accurate geological interpretation, it is necessary to perform seismic migration. Among the various types of migration, the explicit depth $\omega - x$ wavefield extrapolation serves as a promising migration technique. That is, if the FIR filters are properly designed according to the specifications in Figure 2.23, they result in accurate images of complicated subsurface structures. This comes with less computations when compared with other expensive and accurate methods such as the PSPI or the SS method. Also, keeping in mind that we can reduce the migration time using parallel processing, then this is another reason that makes the explicit depth $\omega - x$ migration technique advantageous among others. We talked in this chapter about 1-D $\omega - x$ migration FIR digital filters that are used for 2-D migration, but the same concepts and algorithm apply to the 2-D frequency-inline-crossline ($\omega - x - y$) migration FIR digital filters which are used for migrating 3-D seismic data volumes. We will explicitly describe this case in chapter 4.

Finally, as mentioned earlier, the focus of this thesis will be on explicit depth $\omega - x$ migration of CMP stacked sections, i.e., post-stack depth migration based on the frequency-space strategy. However, this does not limit the $\omega - x$ filters (that will be presented in the coming chapters) from being used for other types of migration such as the pre-stack time/depth migration or post-stack time migration. In other words, the post-stack explicit depth $\omega - x$ migration that will be presented in this thesis acts as a kernel for pre-stack time/depth migration or the post-stack time migration.

Chapter 3

One-Dimensional Migration Complex-Valued FIR Digital Filter Design Using Vector Space Projection Methods

3.1 Introduction

FIR Digital filters are important in various applications, including seismology, radar, sonar, medical, etc [83, 6, 7]. There exist many FIR digital filter design algorithms such as those reported in [83, 84, 40]. Vector Space Projection Methods (VSPMs), developed by Bregman [86] and Gubin [87], were introduced as a better choice for designing zero/linear phase (real-valued) m-D FIR filters [21, 22, 23]. The idea of employing VSPMs for FIR filter design (where part of the theory is known as *Projection onto convex sets (POCS)* or *Pure Projectors*), was first introduced by A. Çetin *et al.* in 1997 [21]. They presented an iterative design based on two Fast Fourier Transforms (FFT) (one forward and one inverse) to design zero-phase FIR filters where the algorithm alternately satisfies both the frequency (wavenumber) domain constraints on the magnitude response bounds as well as the time (space) domain constraints on the impulse response support [21]. Also, Özbek

et al., [23] have applied the theory of pure projections for designing 3-D finite length filters with zero-phase frequency-wavenumber response for hexagonal grids. In addition, Hermanowicz *et al.* [88] have extended the work of Çetin *et al.*, [21] to the design of complex FIR digital filters. In all cases, the design algorithms came with no proof to guarantee that such heuristic iterative algorithms always lead to the required solution (filter). In addition, the heuristic nature of such approaches does not obviously lend itself to the design of filters with other possible constraints [22, 89].

Recently in 2000, K. Haddad *et al.* [22] presented a more rigorous mathematical use of VSPMs for designing real-valued FIR digital filters. The designed filters are feasible in the sense that they satisfy all the filters' known properties which are formulated as constraint sets. For the pure projections theory, to guarantee convergence and unique projection points, these constraint sets must be closed and convex in a suitable Hilbert space [22, 89]. By using the M-dimensional Euclidean space, i.e., $\mathbb{R}^M$, which is a Hilbert space, real-valued FIR filters can be designed as shown in [22]. In general, VSPMs are attractive for FIR digital filter design since the design method can be easily extended to the design of m-D filters, which is difficult to achieve for other methods such as Karam-McClellan [22, 23, 21, 19]. In addition, the VSPMs can handle any number of constraints including linear, convex, and non-convex types. For example, if the constraint sets which describe the requirements of the designed quantity are not convex, then there exist solutions for such problems which still make VSPM an attractive approach [89, 22]. Also, the convergence of such algorithms can be speeded up by using what is known as *Relaxed Projectors* [89]. Moreover, they are able to find solutions satisfying all constraints, i.e., feasible solutions rather than optimal ones. In general, feasible solutions are simpler and less computationally expensive, as well as being perfectly acceptable for designing many filters [22]. Finally, for the case of designing FIR digital filters, the VSPMs requires the computation of two FFTs per iteration only [21].

As was shown in chapter 2, seismic migration FIR digital filter coefficients are of complex values and require special space domain as well as wavenumber domain characteristics where many methods were proposed to properly design such FIR filters. This chapter deals with the design of explicit depth $\omega - x$ one-dimensional (1-D) seismic migration FIR filters using the theory of Vector Space Projection Methods (VSPM) (or simply the Projections onto Convex Sets (POCS)) for two-dimensional (2-D) seismic data sets. The idea of designing complex-valued FIR filters using VSPMs stems from the fact that the VSPM theory can satisfy the desired pre-defined filters' properties. More precisely, the pure and the relaxed projection algorithms, which are part of the VSPM theory, are derived. Simulation results show that by using the relaxed version of the basic derived VSPM designed seismic migration filter, we can save up to 86.46% of the iterations. Also, due to some undesirable background artifacts on migrated sections, a modified version of the basic VSPM was used to eliminate such effects. This modification has also led to a significant reduction in the number of computations, i.e., requiring only 5.18% as many when compared to the basic derived VSPM design algorithm and only 38.36% when compared to the relaxed VSPM design algorithm.

Here, we evaluate and compare our proposed design algorithms with the well known techniques for designing such FIR filters. The use of our seismic migration FIR digital filters designed using the pure, the relaxed, and the modified projections, where they are suitable for laterally varying geological structure media, result in stable migration images. Also, they accommodate high propagation angles with short length filters and with less numerical background artifacts on migrated sections [24, 25, 27, 26]. This, in effect, helps in reducing the geophysical interpretation errors of sub-earth maps.

The chapter is organized as follows. Section 3.2 introduces some background on VSPMs, or more precisely the Pure and Relaxed Projectors, stating the fundamental theorem of POCS for both the relaxed and the pure projectors. Section 3.3 deals with the design of such filters using VSPMs by setting up the required constraint sets and deriving

their associated projection operators. The design algorithm for the 1-D pure projection method is presented in section 3.4. The relaxed version of this design algorithm is given in section 3.5 while the modification of the pure projector is shown in section 3.6. Section 3.7 presents some FIR filter design results which can be used for the 2-D seismic migration processes. Also, these designed seismic migration FIR filters were applied on synthetic seismic data sources. A discussion of some practical aspects of the proposed design algorithms is given in section 3.8. Finally, the main contributions and conclusions of this chapter are summarized in section 3.9.

3.2 Vector Space Projection Methods Background

The approach of Vector Space Projection Methods (VSPM)s has recently been used in a number of applications [90, 91, 92, 93, 94, 95]. However, for the sake of clarity, this section introduces the mathematical background needed to design complex-valued FIR seismic migration digital filters using pure and relaxed projection algorithms and we broadly follow [89]. To start with, let all the filters of interest be elements of a Hilbert space $\mathbf{H}$ and consider a closed convex set $C \subset \mathbf{H}$. Then, for any vector $\mathbf{h} \in \mathbf{H}$, the projection of $\mathbf{h}$ onto C is the nearest neighbor element in C to $\mathbf{h}$, where this nearest neighbor is unique, and is determined by:

$$\|\mathbf{h} - P_C\mathbf{h}\| = \min_{\mathbf{y}\in C}\|\mathbf{h} - \mathbf{y}\| \tag{3.1}$$

where P_C is the pure projector operator and $\|\cdot\|$ is the Euclidean norm for a given Hilbert space $\mathbf{H}$ [96]. One can refer to more properties of the projector P_C in [89]. Note that Eq. (3.1) gives the implicit form of the projection of an arbitrary point onto a closed convex set. Practically, it is desired to explicitly derive the projection of an arbitrary point for a given closed convex set.

Sometimes depending upon the application the convergence speed of the pure projection algorithm needs to be increased. For this reason, the *Relaxed Projector* T_C, which is an extension to the pure projector P_C, will be introduced. For each constant λ, one can

define an operator T_C as follows:

$$T_C = I + \lambda(P_C - I) \tag{3.2}$$

where I is the identity operator on $\mathbf{H}$ and $0 < \lambda < 2$. For each $\mathbf{h} \in \mathbf{H}$, the operator T_C acts in the following fashion:

$$\begin{aligned} T_C\mathbf{h} &= \mathbf{h} + \lambda(P_C\mathbf{h} - \mathbf{h}) \\ &= (1-\lambda)\mathbf{h} + \lambda P_C\mathbf{h}. \end{aligned} \tag{3.3}$$

Clearly, when $\lambda = 1$, T_C is simply the projector P_C. Note that if $\mathbf{h} \notin C$, then Eq. (3.3) has the following instructive geometric interpretation as shown in Figure 3.1:

1. When λ varies form 0 to 2, $T_C\mathbf{h}$ traces out the line segment from $\mathbf{h}$ to the point $\mathbf{h} + 2(P_C\mathbf{h} - \mathbf{h})$;

2. For each $\lambda \in (0, 2)$, the vector $T_C\mathbf{h} - \mathbf{h}$ always points in the same direction as that of the projection;

3. $T_C\mathbf{h}$ is always closer to the set C than to the point $\mathbf{h}$ itself.

Furthermore, from Eq. (3.3) we can see that when $\lambda \in (0, 1)$, the point $T_C\mathbf{h}$ lies in between the point $\mathbf{h}$ and its projection $P_C\mathbf{h}$. This implies that $T_C\mathbf{h}$ lies outside the set C. For such a case T_C seems to under-project $\mathbf{h}$ toward C. On the other hand, when $\lambda > 1$, the point $T_C\mathbf{h}$ lies farther away from the point $\mathbf{h}$ than the projection $P_C\mathbf{h}$. In this case, the operator T_C seems to over-project the point $\mathbf{h}$ towards the set C. Due to this behavior, the operator T_C is called the *Relaxed Projector* for the set C. Note this λ is known as the *Relaxation Parameter*. Despite its name, however, the relaxed projector T_C is not a projector unless $\lambda = 1$. But one can utilize such a projector to speed up the convergence of projection-type algorithms [89].

The basic idea of VSPMs, or more specifically, the basic idea of pure projections is as follows. Every known property of the unknown $\mathbf{h} \in \mathbf{H}$ will restrict $\mathbf{h}$ to lie in a closed

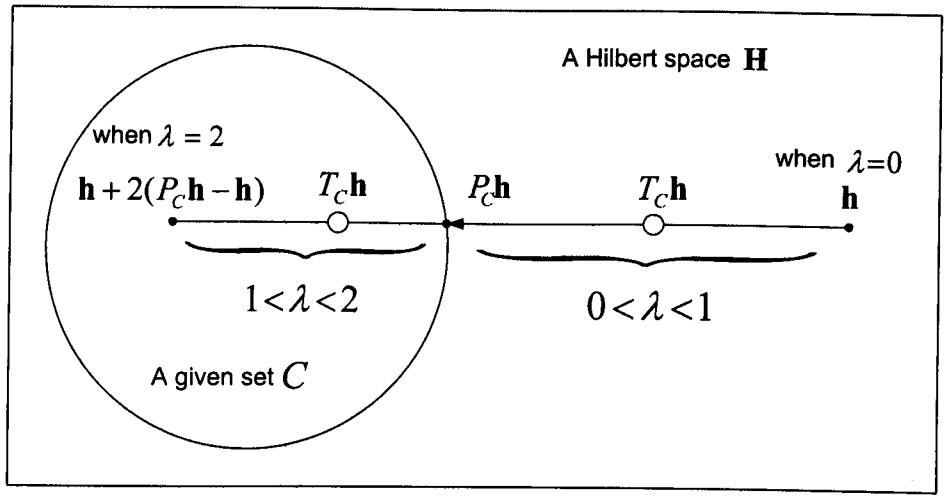

Figure 3.1: Geometric interpretation of the relaxed projection operator T_c in Eq. (3.3). Note that when $\lambda = 1$, the relaxed projector T_C simply becomes the pure projector P_C. Also, when $0 < \lambda < 1$, T_C under-projects $\mathbf{h}$ toward C and when $1 < \lambda < 2$, T_C over-projects $\mathbf{h}$ towards C.

convex set, say $C_i \in \mathbf{H}$. Thus, for m known properties, there are m closed convex sets $C_1, C_2, \cdots, C_m$ and $\mathbf{h} \in C_o$ where C_o denotes their intersection set given by:

$$C_o = \bigcap_{i=1}^{m} C_i. \tag{3.4}$$

The set C_o, which is considered as the solution set, will contain elements that satisfy all constraint sets and, therefore, represents feasible solutions. For each $i = 1, 2, \cdots, m$, let P_{C_i} denote the projection operator onto the set C_i and let I be an identity operator, then the corresponding relaxed projector T_{C_i} is given by:

$$T_{C_i} = I + \lambda_i (P_{C_i} - I) \tag{3.5}$$

for $\lambda_i \in (0, 2)$. Also, let T refer to the concatenation of all these relaxed projectors, that is,

$$T = T_{C_m} T_{C_{m-1}} \cdots T_{C_1}. \tag{3.6}$$

Then, the Fundamental Theorem of POCS is given as follows:

Theorem 1 *Assume that C_o is non-empty. Then for every $\mathbf{h} \in \mathbf{H}$ and for every $\lambda_i \in (0,2)$, $i = 1, 2, \cdots, m$, the iterates $\{\mathbf{h}_k\}$ generated (with an arbitrary starting point $\mathbf{h}_0$) by*

$$\mathbf{h}_{k+1} = T_{C_m} T_{C_{m-1}} \cdots T_{C_1} \mathbf{h}_k \tag{3.7}$$

will converge weakly to a point of C_o [89].

Since our Hilbert space is of finite dimension, the algorithm will strongly converge to a point of C_o [96]. This algorithm is generally referred to as the *Relaxed Projection*. In particular, when the projector P_{C_i} is used instead of T_{C_i} for each set in Eq. (3.7), then the algorithm reduces to:

$$\mathbf{h}_{k+1} = P_{C_m} P_{C_{m-1}} \cdots P_{C_1} \mathbf{h}_k. \tag{3.8}$$

This is usually referred to as the *Pure Projection* algorithm or simply POCS [89].

Two important issues related to the practical use of VSPM methods are: the choice of the initial starting point of the iteration (initial filter coefficients) and the choice of the relaxed parameters in the relaxed projectors, if they are used. For the case of FIR filter design, it is preferable to start with the ideal (desired) filter coefficients as shown in [21, 22]. For the relaxation parameters, section 3.5 will discuss the case for FIR seismic migration filter design. For more details and some illustration examples, the reader can refer to [91, 89].

3.3 The Design of 1-D Complex-Valued FIR Migration Filters Using Vector Space Projection Methods

Since our seismic migration N-length FIR digital filter coefficients are complex-valued, this implies that our Hilbert space must be the set of complex-valued M-dimensional vectors, i.e., $\mathbf{H} = \mathbb{C}^M$ where $M \gg N$. To properly design such filters using VSPMs, the required characteristics of seismic migration FIR digital filters must be formulated as closed convex sets that belong to $\mathbb{C}^M$. The remaining material in this section will be to

derive the unique projections onto these formulated constraint sets.

In other words, the designed seismic migration filters must satisfy both the space and also the wavenumber domains' requirements (refer to Figure 2.23) in which these requirements are put in proper sets that are both closed and convex. These properties are summarized as [6, 9, 7, 10]:

1. An acceptable N-length FIR filter which must be short enough to validate the assumption of having homogeneous material within the filter length and long enough to accommodate high propagation angles. These coefficients must be complex-valued and have even symmetry, which implies that N must be odd.

2. In addition, its magnitude response must be almost equal to one in the passband. In other words, the magnitude spectrum within the passband of its discrete space Fourier transform (DSFT) must be upper and lower bounded by $1 + \delta_p$ and $1 - \delta_p$, respectively, for small δ_p's. Moreover, the stopband magnitude spectrum of its DSFT must be bounded by δ_s.

3. Finally, its phase response should be accurate for the whole range of wavenumbers, i.e., it must be even symmetrical with respect to the $k_x = 0$ axis which is equal to the defined phase in Eq. (2.19).

The proposed constraint sets which describe the above required characteristics of our 1-D migration FIR digital filters are defined as:

1. $C_1 = \{\mathbf{h} \in \mathbb{C}^M : h[n] = h[-n]$ for $n \in S$ and $h[n] = 0$ for $n \in S^c\}$ where $S = \{-\frac{N-1}{2}, -\frac{N-1}{2}+1, \cdots, 0, \cdots, \frac{N-1}{2}-1, \frac{N-1}{2}\}$, N is odd, and S^c is the complement of S. In words, C_1 is the set of all complex-valued sequences (vectors) of length M with at most N odd non-zero members (filter coefficients) that are non-causal and even symmetric.

2. $C_2 = \{\mathbf{h} \in \mathbb{C}^M$ with $h[n] \leftrightarrow H(e^{jk_x}) : \phi(k_x) = \angle H(e^{jk_x}) = b\sqrt{k_{c_p}^2 - k_x^2}\}$ where k_{c_p} is the cut-off wavenumber. That is, C_2 is simply the set of all sequences which

are complex-valued and whose DSFT argument (phase response) is constrained to be equal to $b\sqrt{k_{c_p}^2 - k_x^2}$.

3. $C_3 = \{\mathbf{h} \in \mathbb{C}^M$ with $h[n] \leftrightarrow H(e^{jk_x}) : |H(e^{jk_x})| \geq 1 - \delta_p$ for $k_x \in k_{x_p}\}$ where k_{x_p} is the passband interval which is equal to $[-k_{c_p}, k_{c_p}]$ and δ_p is the maximum passband allowable tolerance. C_3 is the set of complex-valued sequences whose DSFT magnitude spectrum is lower bounded by $1 - \delta_p$ in the passband.

4. $C_4 = \{\mathbf{h} \in \mathbb{C}^M$ with $h[n] \leftrightarrow H(e^{jk_x}) : |H(e^{jk_x})| \leq 1 + \delta_p$ for $k_x \in k_{x_p}\}$. That is, C_4 is the set of complex-valued sequences whose DSFT magnitude should not exceed the limit $1 + \delta_p$ in the passband.

5. $C_5 = \{\mathbf{h} \in \mathbb{C}^M$ with $h[n] \leftrightarrow H(e^{jk_x}) : |H(e^{jk_x})| \leq \delta_s$ for $k_x \in k_{x_s}\}$ where $k_{x_s} = [-\pi, -k_{c_s}) \cap (k_{c_s}, \pi]$. k_{c_s} is the stopband cut-off wavenumber frequency and δ_s is the maximum allowable stopband tolerance. Essentially, C_5 is the set of all sequences which are complex-valued and whose DSFT magnitude is limited to a maximum of δ_s in the stopband k_{x_s}.

The remaining part of this section is devoted to show that such defined constraint sets are indeed closed and convex, and also to derive their associated projection operators.

3.3.1 The constraint set C_1

The constraint set C_1 represents all the seismic migration FIR filters that are of the specified fixed length N. We need to show that this set is a closed convex set. Also, we will show that based on this set, we will indeed limit the migration FIR filter to the specified length.

Convexity of C_1: Let $\mathbf{h}_1, \mathbf{h}_2 \in C_1$, then by the definition of convexity, $\mathbf{h}_3 = \mu\mathbf{h}_1 + (1 - \mu)\mathbf{h}_2$ where $0 \leq \mu \leq 1$. Then for $n \in S$, $h_3[n] = \mu h_1[n] + (1 - \mu)h_2[n]$ which in turns makes $h_3[n]$ equal to $\mu h_1[-n] + (1 - \mu)h_2[-n]$. Hence, $h_3[n] = h_3[-n]$ and, therefore, C_1 is convex.

Closure of C_1: To show that C_1 is a closed set, let $\{\mathbf{h}_n\}$ be a convergent sequence in C_1 where it converges to $\hat{\mathbf{h}}$. We want to show that $\hat{\mathbf{h}} \in C_1$ also. Let the support S^c be the complement of the support S defined earlier. Then

$$\begin{aligned} \|\mathbf{h}_n - \hat{\mathbf{h}}\|^2 &= \sum_{i \in S} |h_n[i] - \hat{h}[i]|^2 + \sum_{i \in S^c} |h_n[i] - \hat{h}[i]|^2 \\ &\geq \sum_{i \in S} |h_n[i] - \hat{h}[i]|^2. \end{aligned} \tag{3.9}$$

Now by taking the limit as $n \longrightarrow \infty$, one can obtain $\sum_{i \in S} |h_n[i] - \hat{h}[i]|^2 = 0$ which is logically equivalent to saying that:

$$h_n[i] = \hat{h}[i] \text{ for } i \in S. \tag{3.10}$$

Hence, $\hat{\mathbf{h}} \in C_1$ and C_1 is closed.

Projection onto C_1: Since C_1 is closed and convex, then we can derive the projection of an arbitrary vector, which belongs to the Hilbert space, onto C_1. According to Eq. (3.1), the projection will be unique. Let $\mathbf{x} \in \mathbb{C}^M$, which is an arbitrary vector in the Hilbert space $\mathbb{C}^M$ and $\mathbf{x} \notin C_1$. Let the support S^c be the complement of the support S. Then for $\mathbf{x} \notin C_1$ and $\mathbf{h} \in C_1$:

$$\begin{aligned} \|\mathbf{x} - \mathbf{h}\|^2 &= \sum_{i \in S} |x[i] - h[i]|^2 + \sum_{i \in S^c} |x[i] - h[i]|^2 \\ &= \sum_{i \in S} |x[i] - h[i]|^2 + \sum_{i \in S^c} |x[i]|^2 \\ &= \sum_{i \in S} |x[i] - h[-i]|^2 + \sum_{i \in S^c} |x[i]|^2. \end{aligned} \tag{3.11}$$

However, $\|\mathbf{x} - \mathbf{h}\|$ is minimized with respect to $\mathbf{h}$ if

$$\begin{aligned} h[n] &= x[n] \text{ for } n = 0, 1, \cdots, (N-1)/2 \\ &= x[-n] \text{ for } n = -(N-1)/2, -(N-1)/2 + 1, \cdots, -1. \end{aligned} \tag{3.12}$$

Therefore, the projection onto C_1, i.e., P_{C_1} can be given by the following equation:

$$P_{C_1}\mathbf{x} = \begin{cases} x[n], \text{ for } |n| \leq (N-1)/2 \\ 0, \text{ otherwise.} \end{cases} \tag{3.13}$$

3.3.2 The constraint set C_2

C_2 represents the set of all seismic migration FIR filters with the pre-defined phase response. In the following, we show that this proposed set is indeed closed and convex as well as we will derive its unique projection operator.

Convexity of C_2: Let $\mathbf{h}_1, \mathbf{h}_2 \in C_2$ where $H_1(e^{jk_x})$ and $H_2(e^{jk_x})$ are the DSFT of $\mathbf{h}_1$ and $\mathbf{h}_2$, respectively. Note that from the definition of C_2, $H_1(e^{jk_x})$ and $H_2(e^{jk_x})$ will have the same phase, say $\phi(k_x) = b\sqrt{k_{c_p}^2 - k_x^2}$. Using the definition of convexity, let $\mathbf{h}_3 = \mu\mathbf{h}_1 + (1-\mu)\mathbf{h}_2$ where $0 \leq \mu \leq 1$. In the DSFT domain, this is equivalent to $H_3(e^{jk_x}) = \mu H_1(e^{jk_x}) + (1-\mu)H_2(e^{jk_x})$. But one can write $H_3(e^{jk_x})$ as:

$$\begin{aligned} H_3(e^{jk_x}) &= \mu|H_1(e^{jk_x})|\exp(j\phi(k_x)) + (1-\mu)|H_2(e^{jk_x})|\exp(j\phi(k_x)) \\ &= [\mu|H_1(e^{jk_x})| + (1-\mu)|H_2(e^{jk_x})|]\exp(j\phi(k_x)) \\ &= |H_3(e^{jk_x})|\exp(j\phi(k_x)). \end{aligned} \tag{3.14}$$

Hence, $\mathbf{h}_3 \in C_2$. Therefore, C_2 is convex.

Closure of C_2: Let $\{\mathbf{h}_n\}$ be a convergent sequence in C_2 where it converges to $\hat{\mathbf{h}}$. Denote $H_n(e^{jk_x})$ and $\hat{H}(e^{jk_x})$ as the DSFT of $\mathbf{h}_n$ and $\hat{\mathbf{h}}$, respectively. We want to show that also $\hat{\mathbf{h}} \in C_2$. Denote the phase of $H_n(e^{jk_x})$ by $\phi(k_x) = b\sqrt{k_{c_p}^2 - k_x^2}$ and also denote the phase

of $\hat{H}(e^{jk_x})$ by $\psi(k_x)$. Then,

$$\begin{aligned} \|\mathbf{h}_n - \hat{\mathbf{h}}\|^2 &= \frac{1}{2\pi}\int_{-\pi}^{\pi} |H_n(e^{jk_x}) - \hat{H}(e^{jk_x})|^2 dk_x \\ &= \frac{1}{2\pi}\int_{-\pi}^{\pi} ||H_n(e^{jk_x})| \exp(j\phi(k_x)) \\ &\quad -|\hat{H}(e^{jk_x})| \exp(j\psi(k_x))|^2 dk_x. \end{aligned} \tag{3.15}$$

Now, using the fact that [89]

$$\begin{aligned} &||H_n(e^{jk_x})| \exp(j\phi(k_x)) - |\hat{H}(e^{jk_x})| \exp(j\psi(k_x))|^2 \\ &\qquad \geq |\hat{H}(e^{jk_x})|^2 \sin^2(\phi(k_x) - \psi(k_x)) \end{aligned} \tag{3.16}$$

then

$$\|\mathbf{h}_n - \hat{\mathbf{h}}\|^2 \geq \frac{1}{2\pi}\int_{-\pi}^{\pi} |\hat{H}(e^{jk_x})|^2 \sin^2(\phi(k_x) - \psi(k_x)) dk_x. \tag{3.17}$$

When $n \longrightarrow \infty$, we obtain

$$\frac{1}{2\pi}\int_{-\pi}^{\pi} |\hat{H}(e^{jk_x})|^2 \sin^2(\phi(k_x) - \psi(k_x)) dk_x = 0. \tag{3.18}$$

Hence, either $\hat{H}(e^{jk_x}) = 0$, which contradicts the fact that it is a member of C_2, or $\sin^2(\phi(k_x) - \psi(k_x)) = 0$. In this case, $\phi(k_x) - \psi(k_x) = m\pi$ or $\phi(k_x) = \psi(k_x) + m\pi$ where $m \in \mathbb{Z}$. However, m must be even since $\mathbf{h}_n \longrightarrow \hat{\mathbf{h}}$. Therefore, $\hat{\mathbf{h}} \in C_2$ and C_2 is closed.

Projection onto C_2: Since C_2 is a closed and convex set, we are left with deriving the projection of an arbitrary vector $\mathbf{x} \in \mathbb{C}^M$ ($\mathbf{x} \notin C_2$) onto C_2. Based on the definition of the constraint set C_2, we need to minimize the following equation:

$$J(H(e^{jk_x})) = \|X(e^{jk_x}) - H(e^{jk_x})\|^2 \tag{3.19}$$

with respect to $H(e^{jk_x})$ and subject to $\phi(k_x) = \angle H(e^{jk_x}) = b\sqrt{k_{c_p}^2 - k_x^2}$, where $X(e^{jk_x})$ is the DSFT of x. Note that $\|\cdot\|$ is now the L_2 norm with respect to continuous functions. Construct the following Lagrangian [97] equation in the DSFT domain:

$$J(H(e^{jk_x})) = \|X(e^{jk_x}) - H(e^{jk_x})\|^2 - \lambda[\arctan \frac{\Im\{H(e^{jk_x})\}}{\Re\{H(e^{jk_x})\}} - \phi(k_x)] \tag{3.20}$$

where $\Re\{.\}$ and $\Im\{.\}$ denote the real and imaginary parts for a given complex number. Now, let $X_r = \Re\{X(e^{jk_x})\}$, $X_i = \Im\{X(e^{jk_x})\}$, $H_r = \Re\{H(e^{jk_x})\}$, and $H_i = \Im\{H(e^{jk_x})\}$. Then, Eq. (3.20) can be rewritten as

$$J(H_r, H_i) = (X_r - H_r)^2 + (X_i - H_i)^2 - \lambda[\arctan \frac{H_i}{H_r} - \phi(k_x)]. \tag{3.21}$$

The first order conditions are:

$$\frac{\partial J(H_r, H_i)}{\partial H_r} = -2X_r + 2H_r + \lambda \frac{H_i}{H_r^2 + H_i^2} = 0 \tag{3.22}$$

and

$$\frac{\partial J(H_r, H_i)}{\partial H_i} = -2X_i + 2H_i - \lambda \frac{H_r}{H_r^2 + H_i^2} = 0 \tag{3.23}$$

and the constraint is

$$\frac{H_i}{H_r} = \tan(\phi(k_x)). \tag{3.24}$$

From Eq. (3.22), solve for λ to obtain:

$$\lambda = \frac{2(X_r - H_r)(H_r^2 + H_i^2)}{H_i}. \tag{3.25}$$

Similarly, using Eq. (3.23), solve for λ to get:

$$\lambda = \frac{-2(X_i - H_i)(H_r^2 + H_i^2)}{H_r}. \tag{3.26}$$

Now, equating Eq. (3.25) and Eq. (3.26), gives:

$$\frac{(X_r - H_r)}{(X_i - H_i)} = -\tan\phi(k_x). \tag{3.27}$$

Substituting Eq. (3.24) into Eq. (3.27) gives:

$$\frac{(X_r - H_r)}{(X_i - H_i)} = -\frac{H_i}{H_r} \tag{3.28}$$

which is equivalent to:

$$(H_r^2 + H_i^2) = X_r H_r + X_i H_i. \tag{3.29}$$

Since $X_r = |X(e^{jk_x})|\cos\theta_x$ and $X_i = |X(e^{jk_x})|\sin\theta_x$ where $\theta_x = \arctan\frac{X_i}{X_r}$, and $H_r = |H(e^{jk_x})|\cos\phi(k_x)$, $H_i = |H(e^{jk_x})|\sin\phi(k_x)$ and $|H(e^{jk_x})|^2 = H_r^2 + H_i^2$, then Eq. (3.29) can be rewritten as:

$$\begin{aligned} |H(e^{jk_x})| &= |X(e^{jk_x})|(\cos\theta_x\cos\phi(k_x) + \sin\theta_x\sin\phi(k_x)) \\ &= |X(e^{jk_x})|\cos(\theta_x - \phi(k_x)). \end{aligned} \tag{3.30}$$

However, Eq. (3.30) will only be true if $\theta_x - \phi(k_x) \in [-\pi/2 + n\pi, \pi/2 + n\pi]$ where n is an even integer. Hence, in this case we have two possibilities:

- If $\theta_x - \phi(k_x) \in [-\pi/2 + n\pi, \pi/2 + n\pi]$ where n is an even integer, then $\cos(\theta_x - \phi(k_x)) \geq 0$, and hence, $H(e^{jk_x}) = |X(e^{jk_x})|\cos(\theta_x - \phi(k_x))\exp(j\phi(k_x))$.
- If $\theta_x - \phi(k_x) \in [-\pi/2 + l\pi, \pi/2 + l\pi]$ where l is an odd integer, then $\cos(\theta_x - \phi(k_x)) < 0$, and hence, $H(e^{jk_x}) = -|X(e^{jk_x})|\cos(\theta_x - \phi(k_x))\exp(j\phi(k_x))$ since $|H(e^{jk_x})| \geq 0$.

Therefore, the projection onto C_2, i.e., P_{C_2} can be given by the following equation:

$$P_{C_2}\mathbf{x} \leftrightarrow \begin{cases} |X(e^{jk_x})|\cos(\theta_x - \phi(k_x))\exp(j\phi(k_x)), \text{ if } \cos(\theta_x - \phi(k_x)) \geq 0 \\ -|X(e^{jk_x})|\cos(\theta_x - \phi(k_x))\exp(j\phi(k_x)), \text{ if } \cos(\theta_x - \phi(k_x)) < 0 \end{cases} \tag{3.31}$$

where $\leftrightarrow$ stands for the Fourier transform pair notation.

3.3.3 The constraint sets C_3, C_4, and C_5

Following the same methodology for the constraint set C_1 and C_2, we can easily show that C_3, C_4, C_5 are closed convex sets in $\mathbb{C}^M$. Recall that C_3 and C_4 represents the constraint sets whose wavenumber magnitude responses are respectively upper and lower limited to δ_p within the passband region. Also, recall that C_5 contains all the seismic migration FIR filters whose stopband wavenumber magnitude responses are limited to δ_s. The projection operators are derived as follows:

Projection onto C_3: Our aim is find the minimum projection with respect to $\mathbf{h}$ subject to the constraint given in C_3 for an arbitrary $\mathbf{x} \in \mathbb{C}^M$, where $\mathbf{x} \notin C_3$. That is:

$$\min_{\mathbf{h} \in C_3} J(H(e^{jk_x})) = \|X(e^{jk_x}) - H(e^{jk_x})\|^2 \tag{3.32}$$

subject to $|H(e^{jk_x})| \geq (1 - \delta_p)$ where $X(e^{jk_x})$ is the DSFT of $\mathbf{x}$. For simplicity, denote the $1 - \delta_p$ as β. The following Lagrangian equation in the DSFT domain is:

$$J(H(e^{jk_x})) = \|X(e^{jk_x}) - H(e^{jk_x})\|^2 + \lambda[|H(e^{jk_x})|^2 - \beta^2]. \tag{3.33}$$

Again, let $X_r = \Re\{X(e^{jk_x})\}$, $X_i = \Im\{X(e^{jk_x})\}$, $H_r = \Re\{H(e^{jk_x})\}$, and $H_i = \Im\{H(e^{jk_x})\}$. Then, Eq. (3.33) can be rewritten as

$$J(H_r, H_i) = (X_r - H_r)^2 + (X_i - H_i)^2 + \lambda[H_r^2 + H_i^2 - \beta^2]. \tag{3.34}$$

The Kuhn-Tuker conditions are [97]:

$$\begin{aligned} \frac{\partial J(H_r, H_i)}{\partial H_r} &= -2X_r + 2H_r + 2\lambda H_r \\ &= 0 \end{aligned} \tag{3.35}$$

$$\begin{aligned}\frac{\partial J(H_r, H_i)}{\partial H_i} &= -2X_i + 2H_i + 2\lambda H_i \\ &= 0 \end{aligned} \tag{3.36}$$

and the constraint is

$$H_r^2 + H_i^2 \geq \beta^2; \lambda \geq 0 \tag{3.37}$$

$$\lambda(\beta^2 - H_r^2 - H_i^2) = 0. \tag{3.38}$$

The derivation is now performed case by case:

- **Case 1:** $H_r^2 + H_i^2 = \beta^2$

  From Eq. (3.35), we will solve for H_r to get

$$H_r = \frac{X_r}{1+\lambda}. \tag{3.39}$$

  Similarly, we can use Eq. (3.36) to obtain H_i:

$$H_i = \frac{X_i}{1+\lambda}. \tag{3.40}$$

  By substituting Eq. (3.39) and Eq. (3.40) into $H_r^2 + H_i^2 = \beta^2$ and solving for λ, where $\lambda \geq 0$, we obtain:

$$1 + \lambda = \sqrt{\frac{X_r^2 + X_i^2}{\beta^2}}. \tag{3.41}$$

  Therefore, substituting Eq. (3.41) into Eq. (3.39) and Eq. (3.40), respectively:

$$H_r = \beta \frac{X_r}{\sqrt{X_r^2 + X_i^2}} \tag{3.42}$$

  and

$$H_i = \beta \frac{X_i}{\sqrt{X_r^2 + X_i^2}}. \tag{3.43}$$

Hence, for $|X(e^{jk_x})| \leq \beta$:

$$H(e^{jk_x}) = \beta \frac{X(e^{jk_x})}{|X(e^{jk_x})|} \tag{3.44}$$

or

$$H(e^{jk_x}) = \beta \exp(j\angle X(e^{jk_x})). \tag{3.45}$$

- **Case 2:** $H_r^2 + H_i^2 > \beta^2$

  In this case, $\lambda = 0$ and from Eq. (3.35), $H_r = X_r$ while from Eq. (3.36), $H_i = X_i$. Therefore, for $|X(e^{jk_x})| > \beta$,

$$H(e^{jk_x}) = X(e^{jk_x}). \tag{3.46}$$

Therefore, the projection onto C_3, i.e, P_{C_3} can be given by the following equation:

$$P_{C_3}\mathbf{x} \leftrightarrow \begin{cases} X(e^{jk_x}), \text{ if } |X(e^{jk_x})| > (1-\delta_p) \text{ for } k_x \in k_{x_p} \\ (1-\delta_p)\exp(j\angle X(e^{jk_x})), \text{ if } |X(e^{jk_x})| \leq (1-\delta_p) \text{ for } k_x \in k_{x_p} \\ X(e^{jk_x}), \text{ otherwise.} \end{cases} \tag{3.47}$$

Projection onto C_4: Our objective is to find the minimum projection with respect to $\mathbf{h}$ subject to the constraint given in C_4 for an arbitrary $\mathbf{x} \in \mathbb{C}^M$, where $\mathbf{x} \notin C_4$. That is:

$$\min_{\mathbf{h} \in C_4} J(H(e^{jk_x})) = \|X(e^{jk_x}) - H(e^{jk_x})\|^2 \tag{3.48}$$

subject to $|H(e^{jk_x})| \leq (1+\delta_p)$ where $X(e^{jk_x})$ is the DSFT of $\mathbf{x}$. For simplicity, denote the $1+\delta_p$ as α. The following Lagrangian equation in the DSFT domain is:

$$J(H(e^{jk_x})) = \|X(e^{jk_x}) - H(e^{jk_x})\|^2 - \lambda[|H(e^{jk_x})|^2 - \alpha^2]. \tag{3.49}$$

Again, let $X_r = \Re\{X(e^{jk_x})\}$, $X_i = \Im\{X(e^{jk_x})\}$, $H_r = \Re\{H(e^{jk_x})\}$, and $H_i = \Im\{H(e^{jk_x})\}$. Then, Eq. (3.49) can be rewritten as

$$J(H_r, H_i) = (X_r - H_r)^2 + (X_i - H_i)^2 - \lambda[H_r^2 + H_i^2 - \alpha^2]. \tag{3.50}$$

The Kuhn-Tuker conditions are [97]:

$$\begin{aligned} \frac{\partial J(H_r, H_i)}{\partial H_r} &= -2X_r + 2H_r - 2\lambda H_r \\ &= 0 \end{aligned} \tag{3.51}$$

$$\begin{aligned} \frac{\partial J(H_r, H_i)}{\partial H_i} &= -2X_i + 2H_i - 2\lambda H_i \\ &= 0 \end{aligned} \tag{3.52}$$

and the constraint is

$$H_r^2 + H_i^2 \leq \alpha^2; \lambda \geq 0 \tag{3.53}$$

$$\lambda(H_r^2 + H_i^2 - \alpha^2) = 0. \tag{3.54}$$

Once again we have two cases:

- **Case 1:** $H_r^2 + H_i^2 = \alpha^2$

  From Eq. (3.51), we will solve for H_r to get

$$H_r = \frac{X_r}{1 - \lambda}. \tag{3.55}$$

  Similarly, we can use Eq. (3.52) to obtain H_i:

$$H_i = \frac{X_i}{1 - \lambda}. \tag{3.56}$$

By substituting Eq. (3.55) and Eq. (3.56) into $H_r^2 + H_i^2 = \alpha^2$ and solving for λ, where $\lambda \geq 0$, we get:

$$1 - \lambda = -\sqrt{\frac{X_r^2 + X_i^2}{\alpha^2}}. \tag{3.57}$$

Therefore, by substituting Eq. (3.57) into Eq. (3.55) and Eq. (3.56), respectively:

$$H_r = -\alpha \frac{X_r}{\sqrt{X_r^2 + X_i^2}} \tag{3.58}$$

and

$$H_i = -\alpha \frac{X_i}{\sqrt{X_r^2 + X_i^2}}. \tag{3.59}$$

Hence, for $|X(e^{jk_x})| \geq \alpha$:

$$H(e^{jk_x}) = -\alpha \frac{X(e^{jk_x})}{|X(e^{jk_x})|} \tag{3.60}$$

or

$$H(e^{jk_x}) = -\alpha \exp(j\angle X(e^{jk_x})). \tag{3.61}$$

- **Case 2:** $H_r^2 + H_i^2 < \alpha^2$

  In this case, $\lambda = 0$ and from Eq. (3.51), $H_r = X_r$ while from Eq. (3.52), $H_i = X_i$. Therefore, for $|X(e^{jk_x})| < \alpha$,

$$H(e^{jk_x}) = X(e^{jk_x}). \tag{3.62}$$

Therefore, the projection onto C_4, i.e, P_{C_4} can be given by the following equation:

$$P_{C_4}\mathbf{x} \leftrightarrow \begin{cases} X(e^{jk_x}), \text{ if } |X(e^{jk_x})| < (1+\delta_p) \text{ for } k_x \in k_{x_p} \\ -(1+\delta_p)\exp(j\angle X(e^{jk_x})), \text{ if } |X(e^{jk_x})| \geq (1+\delta_p) \text{ for } k_x \in k_{x_p} \\ X(e^{jk_x}), \text{ otherwise.} \end{cases} \tag{3.63}$$

By the same argument given for the constraint set C_4, it can be shown that the projection of an arbitrary vector $\mathbf{x} \in \mathbb{C}^M$, where $\mathbf{x} \notin C_5$ is given by

$$P_{C_5}\mathbf{x} \leftrightarrow \begin{cases} X(e^{jk_x}), \text{ if } |X(e^{jk_x})| < \delta_s \text{ for } k_x \in k_{x_s} \\ -\delta_s \exp(j\angle X(e^{jk_x})), \text{ if } |X(e^{jk_x})| \geq \delta_s \text{ for } k_x \in k_{x_s} \\ X(e^{jk_x}), \text{ otherwise.} \end{cases} \tag{3.64}$$

By considering each of the above projection operators, namely, P_{C_i} where $i = 1, \cdots, 5$, we can see that they are consistent with our desired feasible solution (required migration FIR digital filter characteristics). For example, P_{C_1} will truncate over the impulse response to be of a length of N. Also, during the iterations, P_{C_4} for example will limit the upper bound of the migration FIR filter with a magnitude response greater than $1 + \delta_p$. The same will apply for the remaining operators.

3.4 The Pure Projection Design Algorithm for 1-D Migration Complex-Valued FIR Filters

Based on Eq. (3.8) given in theorem 1, the pure projection design algorithm for designing 1-D seismic migration complex-valued FIR digital filters is given by

$$\mathbf{h}_{k+1} = P_{C_1}P_{C_2}P_{C_3}P_{C_4}P_{C_5}\mathbf{h}_k \tag{3.65}$$

where P_{C_1}, P_{C_2}, P_{C_3}, P_{C_4} and P_{C_5} are given in Eqs. (3.13), (3.31), (3.47), (3.63) and (3.64) respectively. More explicitly, the design algorithm can be described as follows. Start with an arbitrary complex-valued vector $\mathbf{h}_0$ of dimension M . Then for the kth iteration perform the following steps:

1. Using Eq. (3.64), project $\mathbf{h}_k$ onto C_5, that is

$$\mathbf{g}_{1,k} = P_{C_5}\mathbf{h}_k \leftrightarrow \begin{cases} H_k(e^{jk_x}), \text{ if } |H_k(e^{jk_x})| < \delta_s \text{ for } k_x \in k_{x_s} \\ -\delta_s \exp(j\angle H_k(e^{jk_x})), \text{ if } |H_k(e^{jk_x})| \geq \delta_s \text{ for } k_x \in k_{x_s} \\ H_k(e^{jk_x}), \text{ otherwise.} \end{cases} \tag{3.66}$$

2. Project $\mathbf{g}_{1,k}$ onto C_4 using Eq. (3.63)

$$\mathbf{g}_{2,k} = P_{C_4}\mathbf{g}_{1,k} \leftrightarrow \begin{cases} G_{1,k}(e^{jk_x}), \text{ if } |G_{1,k}(e^{jk_x})| < (1+\delta_p) \text{ for } k_x \in k_{x_p} \\ -(1+\delta_p)\exp(j\angle G_{1,k}(e^{jk_x})), \\ \text{if } |G_{1,k}(e^{jk_x})| \geq (1+\delta_p) \text{ for } k_x \in k_{x_p} \\ G_{1,k}(e^{jk_x}), \text{ otherwise.} \end{cases} \tag{3.67}$$

3. Project $\mathbf{g}_{2,k}$ onto C_3 using Eq. (3.47)

$$\mathbf{g}_{3,k} = P_{C_3}\mathbf{g}_{2,k} \leftrightarrow \begin{cases} G_{2,k}(e^{jk_x}), \text{ if } |G_{2,k}(e^{jk_x})| > (1-\delta_p) \text{ for } k_x \in k_{x_p} \\ (1-\delta_p)\exp(j\angle G_{2,k}(e^{jk_x})), \\ \text{if } |G_{2,k}(e^{jk_x})| \leq (1-\delta_p) \text{ for } k_x \in k_{x_p} \\ G_{2,k}(e^{jk_x}), \text{ otherwise.} \end{cases} \tag{3.68}$$

4. Project $\mathbf{g}_{3,k}$ onto C_2 using Eq. (3.31)

$$\mathbf{g}_{4,k} = P_{C_2}\mathbf{g}_{3,k} \leftrightarrow \begin{cases} |G_{3,k}(e^{jk_x})|\cos(\theta_{G_{3,k}} - \phi(k_x))\exp(j\phi(k_x)), \\ \text{if } \cos(\theta_{G_{3,k}} - \phi(k_x)) \geq 0 \\ -|G_{3,k}(e^{jk_x})|\cos(\theta_{G_{3,k}} - \phi(k_x))\exp(j\phi(k_x)), \\ \text{if } \cos(\theta_{G_{3,k}} - \phi(k_x)) < 0. \end{cases} \tag{3.69}$$

5. Finally, project $\mathbf{g}_{4,k}$ onto C_1 using Eq. (3.13)

$$\mathbf{h}_{k+1} = P_{C_1}\mathbf{g}_{4,k} = \begin{cases} \mathbf{g}_{4,k}[n], \text{ for } |n| \leq (N-1)/2 \\ 0, \text{ otherwise.} \end{cases} \tag{3.70}$$

If the mean-square error between $\mathbf{h}_{k+1}$ and $\mathbf{h}_k$ is less than or equal to a pre-defined threshold ϵ, then stop the algorithm. Otherwise, repeat steps $1-5$.

3.5 The Relaxed Projection Design Algorithm for 1-D Migration Complex-Valued FIR Filters

We can speed up the convergence of the pure projector algorithm by using the relaxed projector operator given in Eq. (3.5) and the algorithm given in Eq. (3.7) in theorem 1. In addition, recall that when the relaxation parameter λ_i for the constraint set C_i is equal to 1, the relaxed projector simply becomes the pure projector. Note also that λ_i must be in the set interval $(0, 2)$. It is reported that the relaxation parameters for more than two constraint sets cannot be determined except heuristically [91, 90, 98, 89]. Based on the derived pure projectors, however, for each projection operator we can examine how the choice of relaxation parameters can affect the convergence of iterations within the interval $(0, 2)$ [89].

For all previously derived projectors, these intervals were determined and after several experiments, it turns out that the most important projectors which significantly reduce the number of iterations for designing our 1-D seismic migration FIR digital filters are the constraint sets C_2 and C_3. By fixing $\lambda_1 = \lambda_4 = \lambda_5 = 1$, and varying λ_2 and λ_3 with respect to their determined intervals, we can expect to achieve faster convergence with the relaxed projection algorithm than with the pure projection algorithm that was given in Eq. (3.65). Therefore, the following is the relaxed algorithm of Eq. (3.65):

$$\mathbf{h}_{k+1} = P_{C_1} T_{C_2} T_{C_3} P_{C_4} P_{C_5} \mathbf{h}_k \tag{3.71}$$

where T_{C_2} and T_{C_3} are the relaxed projectors associated with C_2 and C_3, respectively. The following subsections will mathematically find the intervals for both λ_3 and λ_2 for which

the algorithm in Eq. (3.71) is expected to converge faster than the algorithm given in Eq. (3.65):

3.5.1 Relaxed Projection for C_3

We can relax Eq. (3.47) to get

$$T_{C_3}\mathbf{x} \leftrightarrow \begin{cases} X(e^{jk_x}), \text{ if } |X(e^{jk_x})| > (1-\delta_p) \text{ and } k_x \in k_{x_p} \\ (1-\lambda_3)X(e^{jk_x}) + \lambda_3(1-\delta_p)\exp(j\angle X(e^{jk_x})), \\ \quad \text{if } |X(e^{jk_x})| \leq (1-\delta_p) \text{ and } k_x \in k_{x_p} \\ X(e^{jk_x}), \text{ otherwise.} \end{cases} \tag{3.72}$$

Now, we are left to show what bounds should be placed on the relaxation parameter λ_3. We can rewrite the real part of the relaxed projection in Eq. (3.72) as:

$$(1-\lambda_3)X_r + \lambda_3(1-\delta_p)\cos(\theta_X) \tag{3.73}$$

and the imaginary part as:

$$(1-\lambda_3)X_i + \lambda_3(1-\delta_p)\sin(\theta_X) \tag{3.74}$$

where $X_r = \Re X(e^{jk_x})$, $X_i = \Im X(e^{jk_x})$, and $\theta_X = \angle X(e^{jk_x})$. Recall that $0 < \delta_p < 1$, which implies that $0 < 1 - \delta_p < 1$.

Case 1:

$$0 < \lambda_3 < 1 \tag{3.75}$$

which implies

$$0 < 1 - \lambda_3 < 1. \tag{3.76}$$

For X_r, if $X_r > 0 \Rightarrow \cos(\theta_X) > 0$, then multiplying Eq. (3.76) by X_r gives

$$0 < (1-\lambda_3)X_r < X_r \tag{3.77}$$

and multiplying Eq. (3.75) by $(1-\delta_p)\cos(\theta_X)$:

$$0 < \lambda_3(1-\delta_p)\cos(\theta_X) < (1-\delta_p)\cos(\theta_X). \tag{3.78}$$

Now, using Eq. (3.77) and Eq. (3.78), we get:

$$(1-\lambda_3)X_r + \lambda_3(1-\delta_p)\cos(\theta_X) > (1-\delta_p)\cos(\theta_X). \tag{3.79}$$

On the other hand, if $X_r < 0 \Rightarrow \cos(\theta_X) < 0$, then multiplying Eq. (3.76) by $-X_r$ gives:

$$-X_r < -(1-\lambda_3)X_r < 0 \tag{3.80}$$

and multiplying Eq. (3.75) by $-(1-\delta_p)\cos(\theta_X)$ gives:

$$-(1-\delta_p)\cos(\theta_X) < -\lambda_3(1-\delta_p)\cos(\theta_X) < 0. \tag{3.81}$$

Using Eq. (3.80) and Eq. (3.81), we will have:

$$-(1-\lambda_3)X_r - \lambda_3(1-\delta_p)\cos(\theta_X) > -(1-\delta_p)\cos(\theta_X). \tag{3.82}$$

Similarly, for X_i, we can show that if $X_i' > 0 \Rightarrow \sin(\theta_X) > 0$, giving

$$(1-\lambda_3)X_i + \lambda_3(1-\delta_p)\sin(\theta_X) > (1-\delta_p)\sin(\theta_X). \tag{3.83}$$

If $X_i < 0 \Rightarrow \sin(\theta_X) < 0$, then

$$-(1-\lambda_3)X_i - \lambda_3(1-\delta_p)\sin(\theta_X) > -(1-\delta_p)\sin(\theta_X). \tag{3.84}$$

Hence, Eq. (3.79), Eq. (3.82), Eq. (3.83), Eq. (3.84) indicate that the pure projector P_{C_3} will converge faster than the relaxed projector T_{C_3} if $0 < \lambda_3 < 1$.

Case 2:

$$1 < \lambda_3 < 2. \tag{3.85}$$

This implies

$$-1 < 1 - \lambda_3 < 0. \tag{3.86}$$

For X_r, if $X_r > 0 \Rightarrow \cos(\theta_X) > 0$, then multiplying Eq. (3.86) by X_r gives

$$-X_r < (1 - \lambda_3)X_r < 0 \tag{3.87}$$

and multiplying Eq. (3.85) by $(1 - \delta_p)\cos(\theta_X)$ yields:

$$(1 - \delta_p)\cos(\theta_X) < \lambda_3(1 - \delta_p)\cos(\theta_X) < 2(1 - \delta_p)\cos(\theta_X). \tag{3.88}$$

Now, using Eq. (3.87) and Eq. (3.88) gives:

$$(1 - \lambda_3)X_r + \lambda_3(1 - \delta_p)\cos(\theta_X) < (1 - \delta_p)\cos(\theta_X). \tag{3.89}$$

On the other hand, if $X_r < 0 \Rightarrow \cos(\theta_X) < 0$, then multiplying Eq. (3.86) by $-X_r$ yields

$$0 < -(1 - \lambda_3)X_r < X_r \tag{3.90}$$

and multiplying Eq. (3.85) by $-(1 - \delta_p)\cos(\theta_X)$ gives

$$-2(1 - \delta_p)\cos(\theta_X) < -\lambda_3(1 - \delta_p)\cos(\theta_X) < -(1 - \delta_p)\cos(\theta_X). \tag{3.91}$$

Using Eq. (3.90) and Eq. (3.91) gives:

$$-(1 - \lambda_3)X_r - \lambda_3(1 - \delta_p)\cos(\theta_X) < -(1 - \delta_p)\cos(\theta_X). \tag{3.92}$$

Similarly, for X_i, we can show that if $X_i > 0 \Rightarrow \sin(\theta_X) > 0$, then

$$(1 - \lambda_3)X_i + \lambda_3(1 - \delta_p)\sin(\theta_X) < (1 - \delta_p)\sin(\theta_X) \tag{3.93}$$

and if $X_i < 0 \Rightarrow \sin(\theta_X) < 0$, then

$$-(1-\lambda_3)X_i - \lambda_3(1-\delta_p)\sin(\theta_X) < -(1-\delta_p)\sin(\theta_X). \tag{3.94}$$

According to Eq. (3.90), Eq. (3.92), Eq. (3.93), and Eq. (3.94) then if $\lambda_3 \in (1,2)$, the relaxed algorithm converges faster than the pure one.

3.5.2 Relaxed Projection for C_2

Similarly, the relaxed version of the projection in Eq. (3.31) can be written as:

$$T_{C_2}\mathbf{x} \leftrightarrow \begin{cases} (1-\lambda_2)X(e^{jk_x}) + \lambda_2|X(e^{jk_x})|\cos(\theta_x - \phi(k_x))\exp(j\phi(k_x)), \\ \quad \text{if } \cos(\theta_x - \phi(k_x)) \geq 0 \\ (1-\lambda_2)X(e^{jk_x}) - \lambda_2|X(e^{jk_x})|\cos(\theta_x - \phi(k_x))\exp(j\phi(k_x)), \\ \quad \text{if } \cos(\theta_x - \phi(k_x)) < 0. \end{cases} \tag{3.95}$$

Following similar steps to obtain the relaxation parameter λ_3 for the relaxed projector T_{C_3}, it can be shown that for $\cos(\theta_x - \phi(k_x)) \geq 0$, λ_2 will lie within $(0,1)$ if $\cos(\phi(k_x)) \geq 0$ or $\sin(\phi(k_x)) \geq 0$. Otherwise, $\lambda_2 = 1$. On the other hand, for $\cos(\theta_x - \phi(k_x)) < 0$, it can be shown that if $\cos(\phi(k_x)) \leq 0$ or $\sin(\phi(k_x)) \leq 0$, then $\lambda_3 \in (0,1)$. Otherwise, $\lambda_2 = 1$.

3.6 The Modified Projection Design Algorithm for 1-D Migration Complex-Valued FIR Filters

It was empirically shown [21, 23, 22] that the pure projection algorithm for real-valued FIR filter design results in an approximate equiripple frequency (wavenumber) response. Furthermore, the results of migrating synthetic seismic sections using the Remez exchange filters like the one shown in [14], yields migrated images containing background artifacts. It is claimed that these little background artifacts are due to the passband magnitude spectrum ripple of the designed filters [14]. Therefore, it is expected that migration

results using the pure or the relaxed projection algorithms given in Eq. (3.65), and Eq. (3.71), respectively, will also contain such undesirable artifacts. Moreover, we can see that P_{C_1} is simply a truncation process on the output of the previous projections, where we have implicitly applied a rectangular window. We can solve such problems by modifying the projection onto C_1 where we employ one of the standard space/time-domain windows like Hamming, Hanning, or Kaiser windows that ultimately eliminate this effect. It can be shown that by employing a window for the projection onto the constraint set C_1, C_1 will remain closed and convex. That is because after applying the window (the new projection), the projection still results in a finite extent vector of dimension M with at most N non-zero values that are of even symmetry with respect to the $n = 0$ axis.

In our case, the Kaiser window will be used since it is considered to be optimal in the sense that it has the largest energy in the main lobe for a given peak side lobe level, and we can easily control the passband and evanescent ripples [84, 83, 99, 100]. Also, the Kaiser window can be considered as a more general window that includes other windows (as special) such as rectangular, Hamming, and others, depending on its shape parameter defined below [84]. The simulation results on synthetic seismic sections will show the non-existence of such artifacts and will also show that the number of iterations for designing such filters will be reduced with a number even smaller than the relaxed projector case.

This reduction in the number of design iterations can be explained since the window applied in the space domain has significantly reduced the energy in its side lobes in the wavenumber domain. This means that we will achieve the desired minimum ripple within the operator wavenumber passband in a reduced number of iterations, i.e., it will be closer to the desired seismic migration filter and, therefore, will speed up the algorithm. Mathematically, Eq. (3.13) can be rewritten as:

$$P_{C_1}\mathbf{x} = W_R\mathbf{x} \tag{3.96}$$

where the rectangular (or boxcar) window is defined as:

$$W_R = \begin{cases} 1, \text{ for } |n| \leq (N-1)/2 \\ 0, \text{ otherwise.} \end{cases} \tag{3.97}$$

But rather than using Eq. (3.97) for the projection onto C_1, we will use:

$$W_K = \begin{cases} \frac{I_o[\beta\sqrt{1-(\frac{2n}{N-1})^2}]}{I_o[\beta]}, \text{ for } |n| \leq (N-1)/2 \\ 0, \text{ otherwise} \end{cases} \tag{3.98}$$

where $I_o[\cdot]$ is the modified zero-order Bessel function of the first kind, β is the shape parameter which determines the trade-off between the main-lobe and peak side-lobe level [83, 84]. The value of β can be found using [83, 84]:

$$\beta = \begin{cases} 0.1102(A-8.7), \text{ for } A > 50 \\ 0.5842(A-21)^{0.4} + 0.07886(A-21), \text{ for } 21 \leq A \leq 50 \\ 0, \text{ for } A < 21 \end{cases} \tag{3.99}$$

where $A = -20\log_{10}\delta_s$. Hence, the new projection onto C_1 will be:

$$P_{C_1}\mathbf{x} = \begin{cases} x[n]\frac{I_o[\beta\sqrt{1-(\frac{2n}{N-1})^2}]}{I_o[\beta]}, \text{ for } |n| \leq (N-1)/2 \\ 0, \text{ otherwise.} \end{cases} \tag{3.100}$$

3.7 Simulation Results

This section is divided into two main subsections. The first subsection deals with designing 1-D seismic migration FIR digital filters. The second section shows an application of the proposed VSPM 1-D seismic migration FIR filter design algorithms to 2-D synthetic seismic sections. Perhaps it is worth mentioning that the results obtained in all our simulations are not restricted to the filters' chosen parameters, but can apply to all cases. Finally, note that all the simulations are preformed in MATLAB which is installed on a Pentium 4 machine with a speed of 2.6 GHz and with a RAM of 1GB.

3.7.1 1-D Migration FIR Filter Design Using Vector Space Projection Methods Simulations

For the 1-D seismic migration filters, we will show several investigated simulations for filters designed using the pure projections given in Eq. (3.65), the relaxed projections given in Eq. (3.71), and the modified projection algorithm given in section 3.6. This will include some comparisons with other reported 1-D complex-valued seismic migration FIR filters. For the wavenumber response figures, only half the spectrum will need to be shown since the filters are even symmetrical with respect to the $k_x = 0$ axis. Also, note that all designed filters which are shown in the following subsections are designed based on normalized wavenumbers.

3.7.1.1 Simulation 1:1-D Migration Filter Design Using Pure, Relaxed, and Modified Projections Comparisons

The objective of this experiment is to compare the 1-D complex-valued seismic migration FIR digital filter designed using the pure, the relaxed, and the modified projection algorithms previously derived and discussed in sections 3.4, 3.5, and 3.6, respectively. Also, we want to show that all designs satisfy our migration FIR filter requirements (see Figure 2.23).

The filter parameters were chosen based on [10, 14] as follows: $k_{c_p} = 0.25$, $k_{c_s} = 0.3347$ for both the pure and relaxed projectors, $k_{c_s} = 0.3429$ for the modified projector, $\delta_p = \delta_s = 10^{-3}$, an odd length of $N = 39$ and a Hilbert space dimension of (number of FFT points) $M = 256$. Figure 3.2 (a) shows the magnitude response for designed filters where all the designs satisfy constraint sets C_3, C_4, and C_5. We can also observe that, when compared to the designed filters using the pure and relaxed projectors, the modified projection designed filter possesses a larger transition bandwidth as would be expected due to usage of the Kaiser window given in Eq. (3.98). Figure 3.2 (b) shows the phase spectrum within the passband for the three designed filters where they satisfy the constraint set C_2. The phase difference error between the desired and designed filters in the

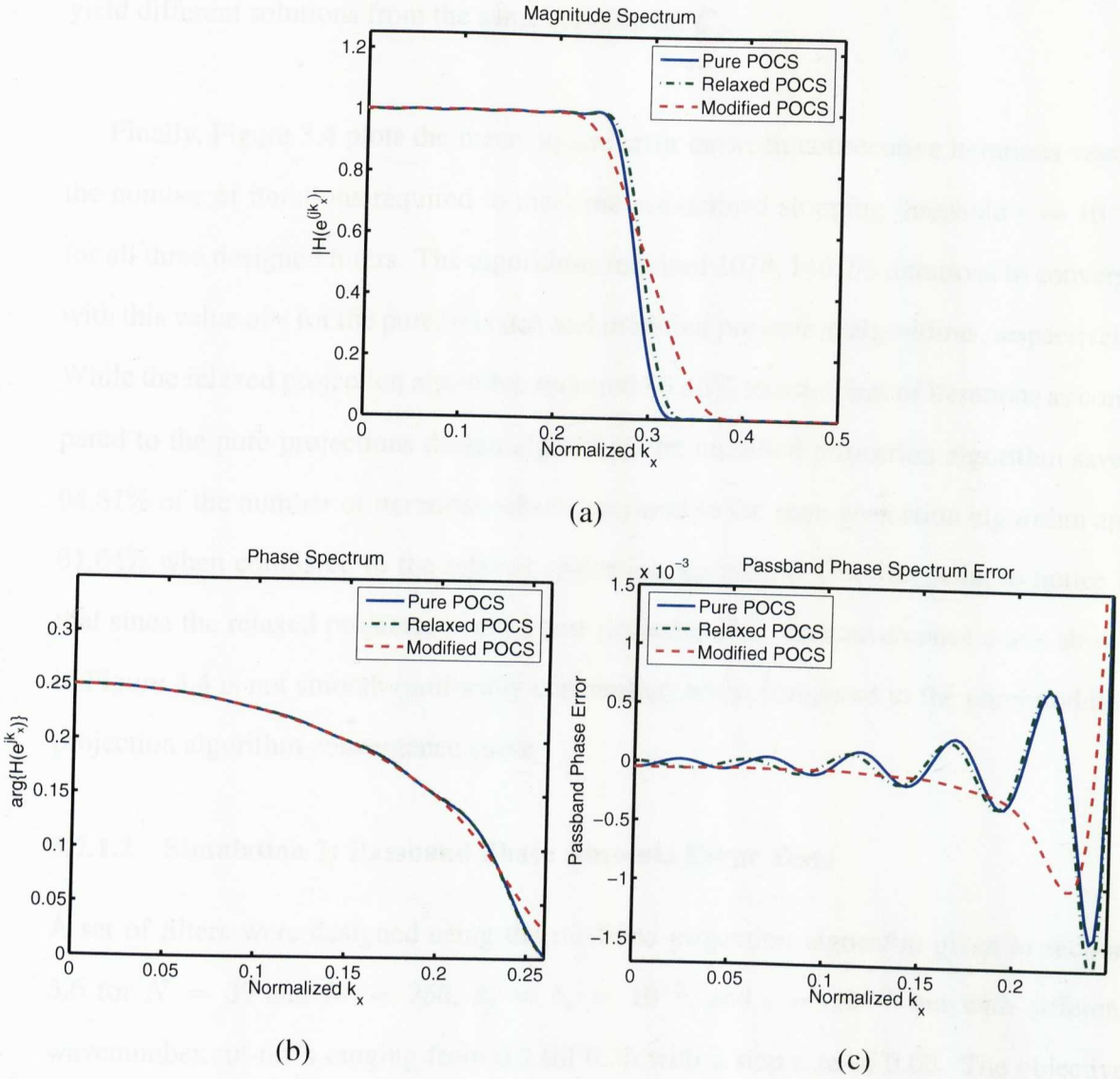

Figure 3.2: 1-D Seismic migration FIR filters (see section 3.7.1.1) designed using the proposed pure, relaxed, and modified projection algorithms with $N = 39$, $k_{c_p} = 0.25$, $\delta_p = \delta_s = 10^{-3}$, and $\epsilon = 10^{-12}$ (a) Magnitude response, (b) Phase response, and (c) Phase response error between the ideal and designed filters. Clearly, all designs satisfy the 1-D seismic migration FIR filter requirements in C_2, C_3, C_4, and C_5.

passband is shown in Figure 3.2 (c) where the pure as well as the relaxed passband phase results possess an oscillatory nature, unlike the modified design approach.

The real and imaginary parts of the impulse response given in Figure 3.3 (a) and Figure 3.3 (b) (for all three filters) show that they satisfy the space domain constraint C_1. However, the filter coefficients (solutions) are not identical but satisfy the wavenumber response constraint sets as well as being of finite length equal to 39, i.e., all the designs

yield different solutions from the same solution set C_o.

Finally, Figure 3.4 plots the mean-square error between consecutive iterations versus the number of iterations required to meet the pre-defined stopping threshold $\epsilon = 10^{-12}$ for all three designed filters. The algorithms required 1078, 146, 56 iterations to converge with this value of ϵ for the pure, relaxed, and modified projection algorithms, respectively. While the relaxed projection algorithm required 86.46% less number of iterations as compared to the pure projections design algorithm, the modified projection algorithm saved 94.81% of the number of iterations when compared to the pure projection algorithm and 61.64% when compared to the relaxed projection algorithm. One last point to notice is that since the relaxed projector is not a true projector [22], its convergence curve shown in Figure 3.4 is not smooth (uniformly converging) when compared to the pure/modified projection algorithm convergence curve.

3.7.1.2 Simulation 2: Passband Phase Absolute Error Tests

A set of filters were designed using the modified projection algorithm given in section 3.6 for $N = 39$ and $M = 256$, $\delta_p = \delta_s = 10^{-3}$, and $\epsilon = 10^{-12}$ but with different wavenumber cut-off's ranging from 0.2 till 0.35 with a step size of 0.05. The objective of this experiment is to show the effect of varying the filter bandwidth on the filter's phase spectrum and the mean absolute passband phase errors between the desired and designed filters. For each phase, this error is calculated in two regions as illustrated in Figure 3.5. The left hand side (LHS) of the vertical solid line is the error up to 88% of the passband width while the right hand side (RHS) of the vertical solid line is the error for the remaining passband width. This is to show how much phase error exists near the cut-off wavenumber. These errors are displayed on the phase response figures as shown in Figure 3.5. The LHS error will be always smaller than the RHS. Also, one can notice that the error will approach zero as the cut-off approaches 0.5, i.e., as the filter becomes an all pass filter.

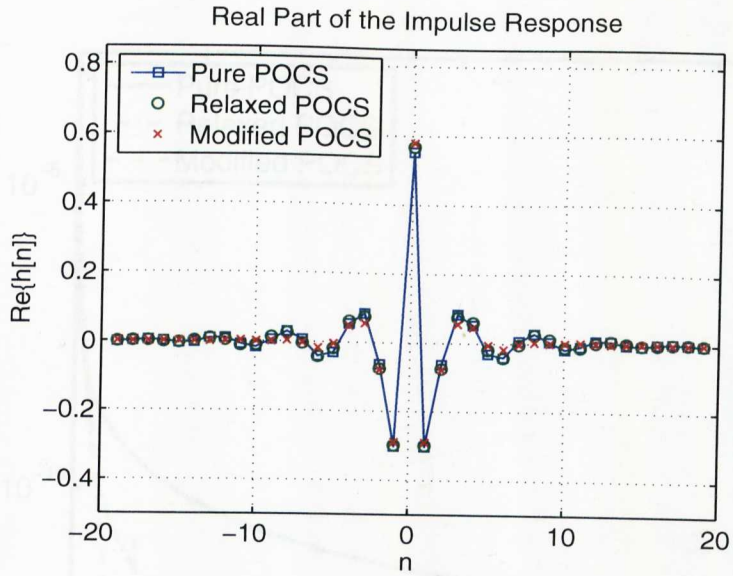

(a)

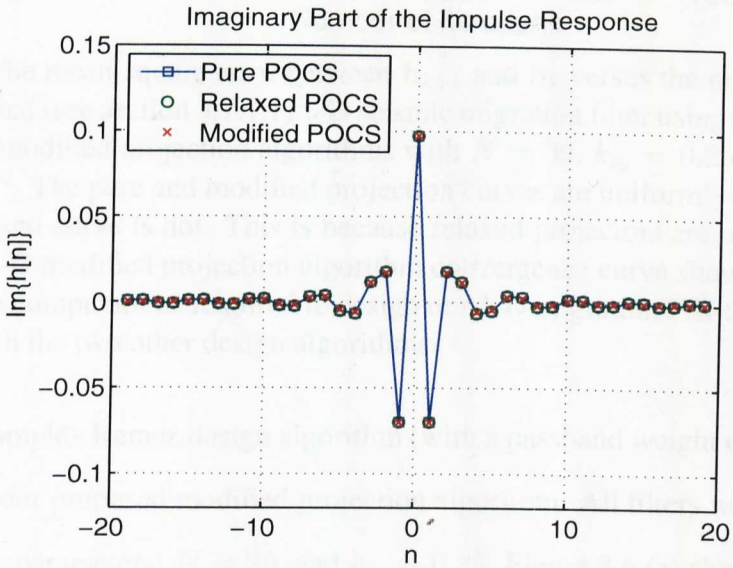

(b)

Figure 3.3: The impulse response for the designed filters (see section 3.7.1.1) using the proposed pure, relaxed, and modified projection algorithms with $N = 39$, $k_{c_p} = 0.25$, $\delta_p = \delta_s = 10^{-3}$, and $\epsilon = 10^{-12}$. (a) The real part, and (b) the imaginary part. The designs satisfy the 1-D seismic migration FIR filter requirement in C_1.

3.7.1.3 Simulation 3: Comparisons with Previously Reported 1-D Migration FIR Filters

In order to evaluate the proposed algorithms, 1-D seismic migration FIR digital filters have been designed using the modified Taylor series method (with 8 derivatives)[1] reported

[1] We have reproduced the modified Taylor series design algorithm.

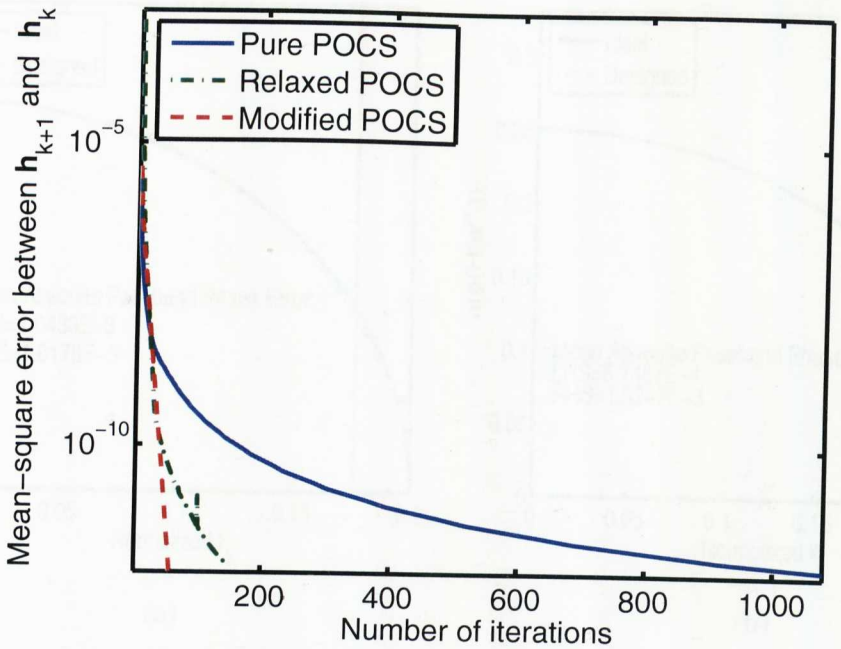

Figure 3.4: The mean-square error between $\mathbf{h}_{k+1}$ and $\mathbf{h}_k$ versus the number of iterations for the designed (see section 3.7.1.1) 1-D seismic migration filter using the proposed pure, relaxed, and modified projection algorithms with $N = 39$, $k_{c_p} = 0.25$, $\delta_p = \delta_s = 10^{-3}$, and $\epsilon = 10^{-12}$. The pure and modified projection curves are uniformly converging. However, the relaxed curve is not. This is because relaxed projectors are not true projectors. Finally, the 1-D modified projection algorithm convergence curve shows a significant reduction in the computations required to design our 1-D migration FIR digital filters when compared with the two other design algorithms.

in [12], the complex Remez design algorithm (with a passband weight of 60)[2] reported in [19, 20], and our proposed modified projection algorithm. All filters were designed with the same filter parameters: $N = 29$, and $k_{c_p} = 0.25$. Figure 3.6 (a) shows the magnitude response for these filters. Clearly, the magnitude response for both the modified Taylor series method and the modified projection algorithm have a flatter magnitude response within the passband and are smoothly decaying to zero within the stopband as compared to the complex Remez exchange algorithm. This can be seen clearly in Figure 3.6 (b) where the passband magnitude response error for the modified projection and modified Taylor series methods are very close to zero whereas the error is oscillating between -0.005 and 0.01 for the complex Remez exchange algorithm designed filter. Unlike the complex Remez exchange algorithm, this results in more stable migration images using both the modified projection algorithm as well as the modified Taylor series method. However,

[2]For this method, we used the built-in MATLAB function called CFIRPM.

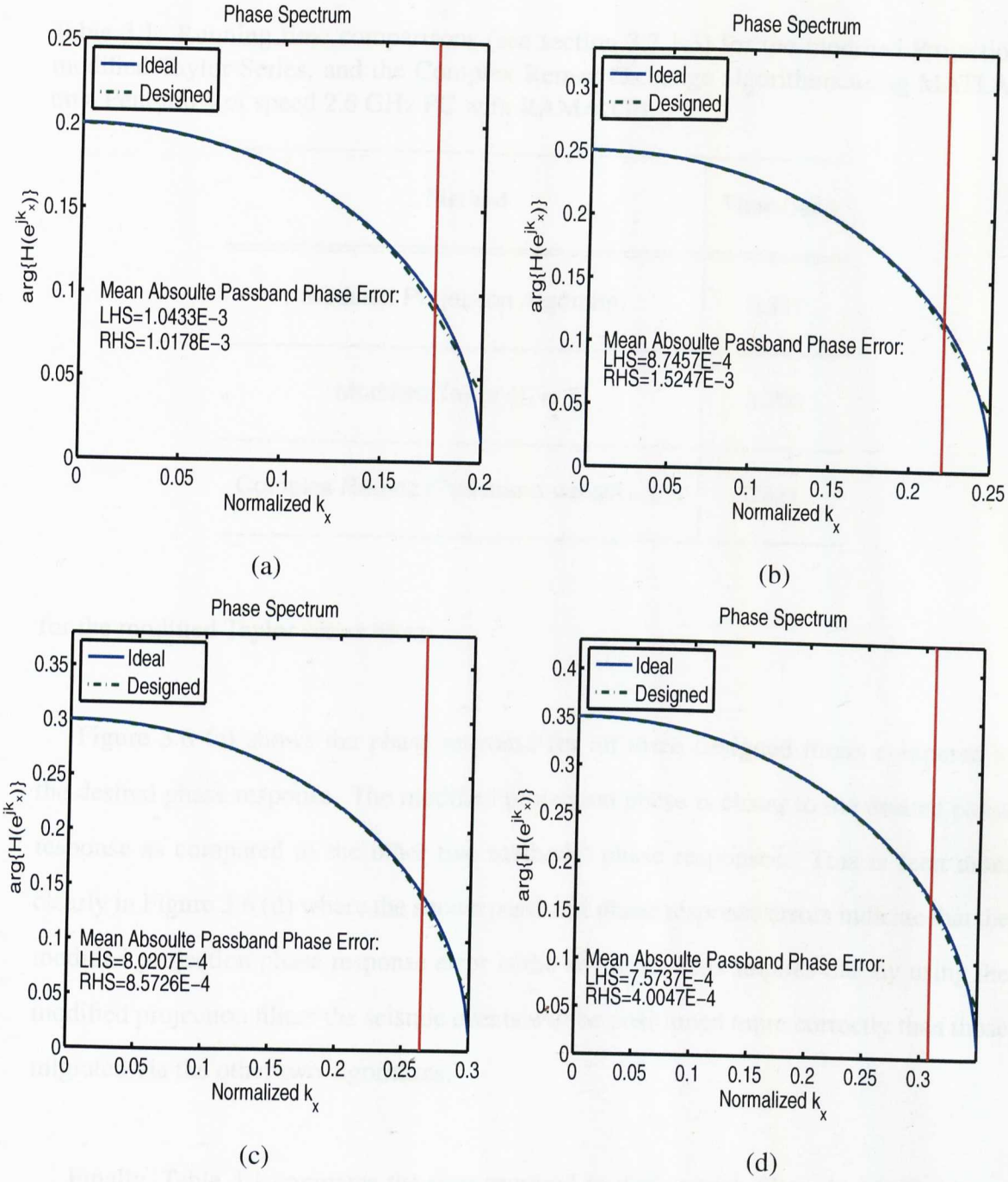

Figure 3.5: The ideal and designed filter's phase responses (see section 3.7.1.2) using the proposed modified projection algorithm in section 3.6 with $\delta_p = \delta_s = 10^{-3}$, and $\epsilon = 10^{-12}$ for $N = 39$. LHS and RHS denote the mean absolute passband phase error in the region to the left and to the right of the vertical solid line that is positioned at $0.88k_{c_p}$, respectively. These filters are designed with cut-off's at (a) $k_{c_p} = 0.2$, (b) $k_{c_p} = 0.25$, (c) $k_{c_p} = 0.3$, and (d) $k_{c_p} = 0.35$. The error decreases as the filter becomes an all-pass.

from Figure 3.6 (b) the modified projection filter accommodates higher propagating angles. This is because it starts to attenuate signals at wavenumber values higher than those

Table 3.1: Running time comparisons (see section 3.7.1.3) for the modified Projection, modified Taylor Series, and the Complex Remez exchange algorithms using MATLAB on a Pentium 4 of speed 2.6 GHz PC with RAM=1GB.

Method	**Time (sec.)**
Modified Projection Algorithm	0.327
Modified Taylor ($L = 8$)	3.705
Complex Remez (Passband weight= 60)	0.321

for the modified Taylor series filter.

Figure 3.6 (c) shows the phase response for all three designed filters compared to the desired phase response. The modified projection phase is closer to the desired phase response as compared to the other two methods' phase responses. This is seen more clearly in Figure 3.6 (d) where the shown passband phase response errors indicate that the modified projection phase response error is the smallest. This implies that by using the modified projection filters the seismic events will be positioned more correctly than those migrated via the other two algorithms.

Finally, Table 3.1 compares the time required to design such filters in MATLAB on a Pentium 4 of speed 2.6 GHz PC with RAM=1GB. It can be seen that, for the aforementioned filter specifications, the complex Remez algorithm is the fastest (0.321 seconds) as compared to the other two methods while the modified Taylor series method is the slowest (3.705 seconds). This is because the modified Taylor series method required $(L = 8) \leq ((N + 1)/2 = 15)$ symbolic derivatives for having such a desired response [12]. The modified projection required 0.327 seconds, which is acceptable due to its overall out-performing response when compared to the other two methods.

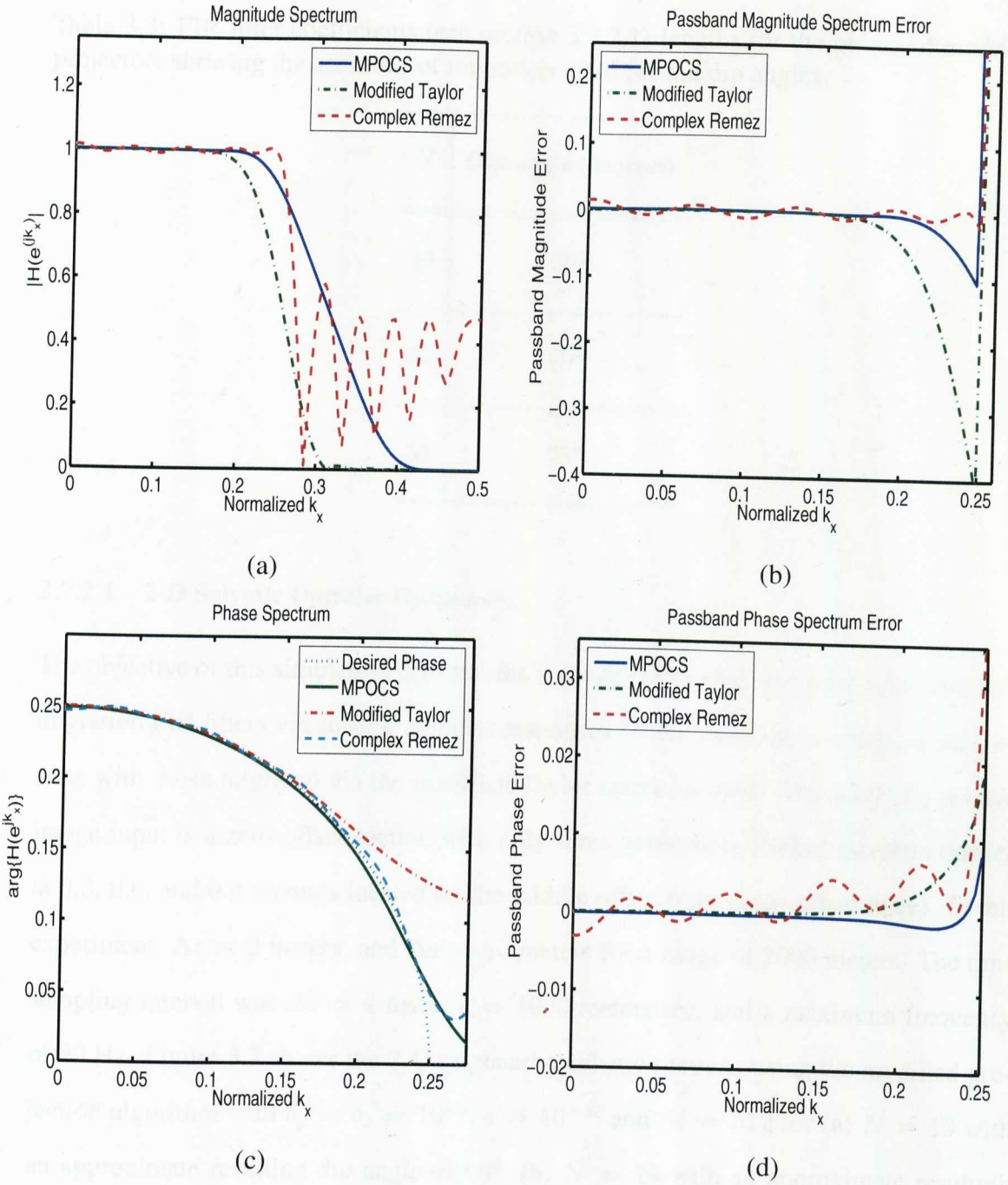

Figure 3.6: 1-D seismic migration FIR filters designed (see section 3.7.1.3) using the proposed modified projection, the modified Taylor series, and the complex Remez exchange algorithms with $N = 29$, and $k_{c_p} = 0.25$. (a) Magnitude response, (b) Magnitude response error within the passband, (c) Phase response, and (d) Phase response error within the passband.

3.7.2 2-D Seismic Migration Synthetic Experiments

Here we present two basic experiments on synthetic seismic data in order to test our proposed modified projection FIR filters where we also compare them with the stable modified Taylor series method [12].

Table 3.2: FIR filter coefficients (see section 3.7.2.1) lengths for the proposed modified projectors showing the accuracy of migration up to certain dip angles.

N	**Dip-angle (degrees)**
19	60°
29	69°
39	73°

3.7.2.1 2-D Seismic Impulse Responses

The objective of this simulation is to test the accuracy of our modified projection seismic migration FIR filters via seismic impulse responses. Also, we want to compare such results with those migrated via the modified Taylor series method. The synthetic seismic image input is a zero-offset section with only three zero-phase Ricker wavelets centred at 0.3, 0.6, and 0.9 seconds located on the middle offset trace (zero-offset trace). In this experiment, $\Delta z = 2$ meters, and $\Delta x = 10$ meters for a range of 2000 meters. The time sampling interval was $\Delta t = 4$ msec, $c = 1000$ meters/sec, and a maximum frequency of 80 Hz. Figure 3.7 shows the 2-D migrated synthetic sections using the modified projection algorithm with $\delta_p = \delta_s = 10^{-3}$, $\epsilon = 10^{-12}$ and $M = 512$ for (a) $N = 19$ with an approximate resulting dip angle of 60°, (b) $N = 29$ with an approximate resulting dip angle of 69°, (c) $N = 39$ with an approximate resulting dip angle of 73°. Table 3.2 summarises the relationship between the dip angles and the filter length.

For the same zero-offset experiment mentioned above, the relaxed projection design algorithm (see section 3.5) and the Taylor series method where used to migrate such a synthetic seismic section for $N = 29$. Figure 3.8 (a) shows the 2-D migrated synthetic section using the relaxed projection algorithm for $N = 29$. Figure 3.8 (b) shows again the 2-D migrated synthetic section using the modified projection algorithm for $N = 29$ and

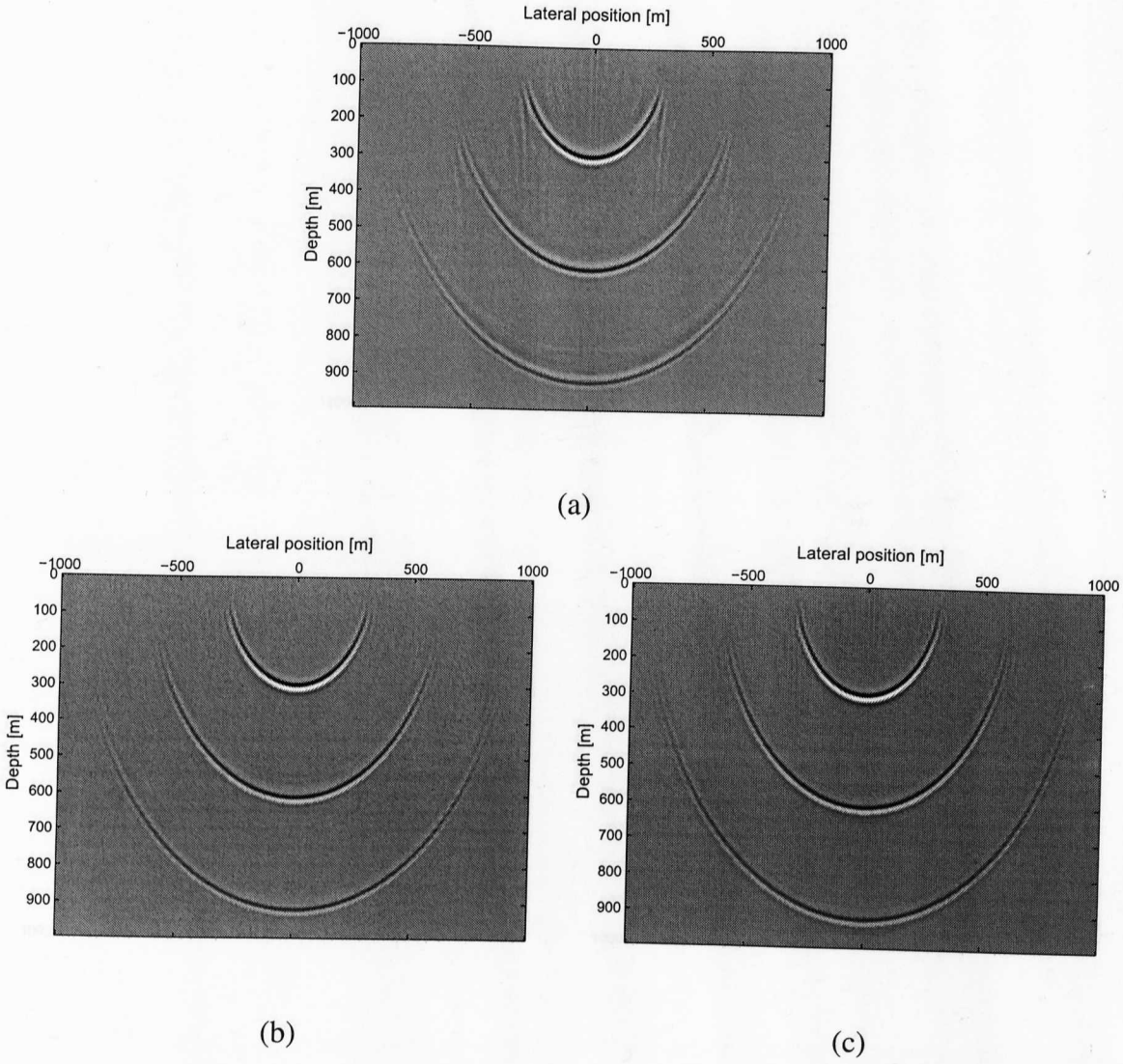

Figure 3.7: 2-D Migrated synthetic sections (see section 3.7.2.1) using the proposed modified projectors with $\Delta z = 2$ meters, $\Delta x = 10$ meters, $\Delta t = 4$ msec, $c = 1000$ meters/sec, and up to a maximum frequency of 80 Hz. The filters parameters are $\delta_p = \delta_s = 10^{-3}$, and $\epsilon = 10^{-12}$ for (a) $N = 19$ with an approximate resulting dip angle of 60°, (b) $N = 29$ with an approximate resulting dip angle of 69°, and (c) $N = 39$ with an approximate resulting dip angle of 73°.

Figure 3.8 (c) shows the 2-D migrated synthetic section using the modified Taylor series algorithm [12]. Note that a nonlinear gray scale mapping is used to highlight the background artifacts for all migration impulse response images. Clearly, the modified Taylor series method attenuates propagating waves having angles more than approximately 56°, unlike the case for the proposed relaxed and the proposed modified projection methods where they accommodate propagation angles up to approximately 69° for the same filter length. However, the migration impulse response using the relaxed (or the pure) pro-

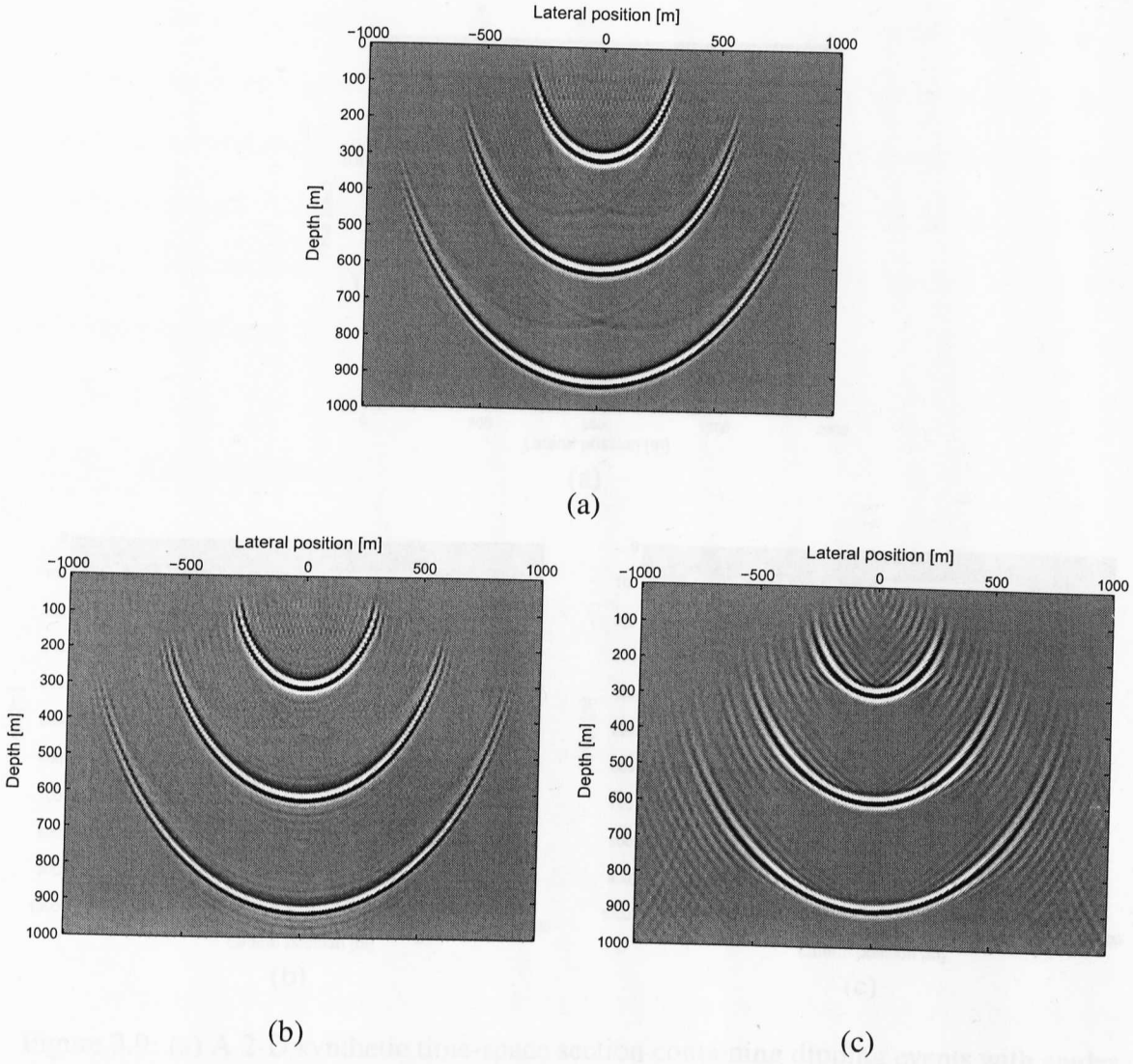

Figure 3.8: 2-D Migrated synthetic sections (see section 3.7.2.1) with $\Delta z = 2$ meters, $\Delta x = 10$ meters, $\Delta t = 4$ msec, $c = 1000$ meters/sec, and up to a maximum frequency of 80 Hz where the filters' parameters are $\delta_p = \delta_s = 10^{-3}$, $\epsilon = 10^{-12}$ and $M = 512$ for $N = 29$ with an approximate resulting dip angle of 69° using (a) the proposed relaxed projection algorithm, (b) the proposed modified projection algorithm and for (c) the modified Taylor series algorithm where $N = 29$ with an approximate resulting dip angle of 56°.

jections contains undesirable artifacts as described in section 3.6 as well as requiring a greater number of FFT computations to design the same migration filters when compared with the modified projection algorithm. Thus, using the modified projection design algorithm for designing the explicit depth wavefield extrapolators resulted in the best image when compared to the other two methods, and also with less computational effort.

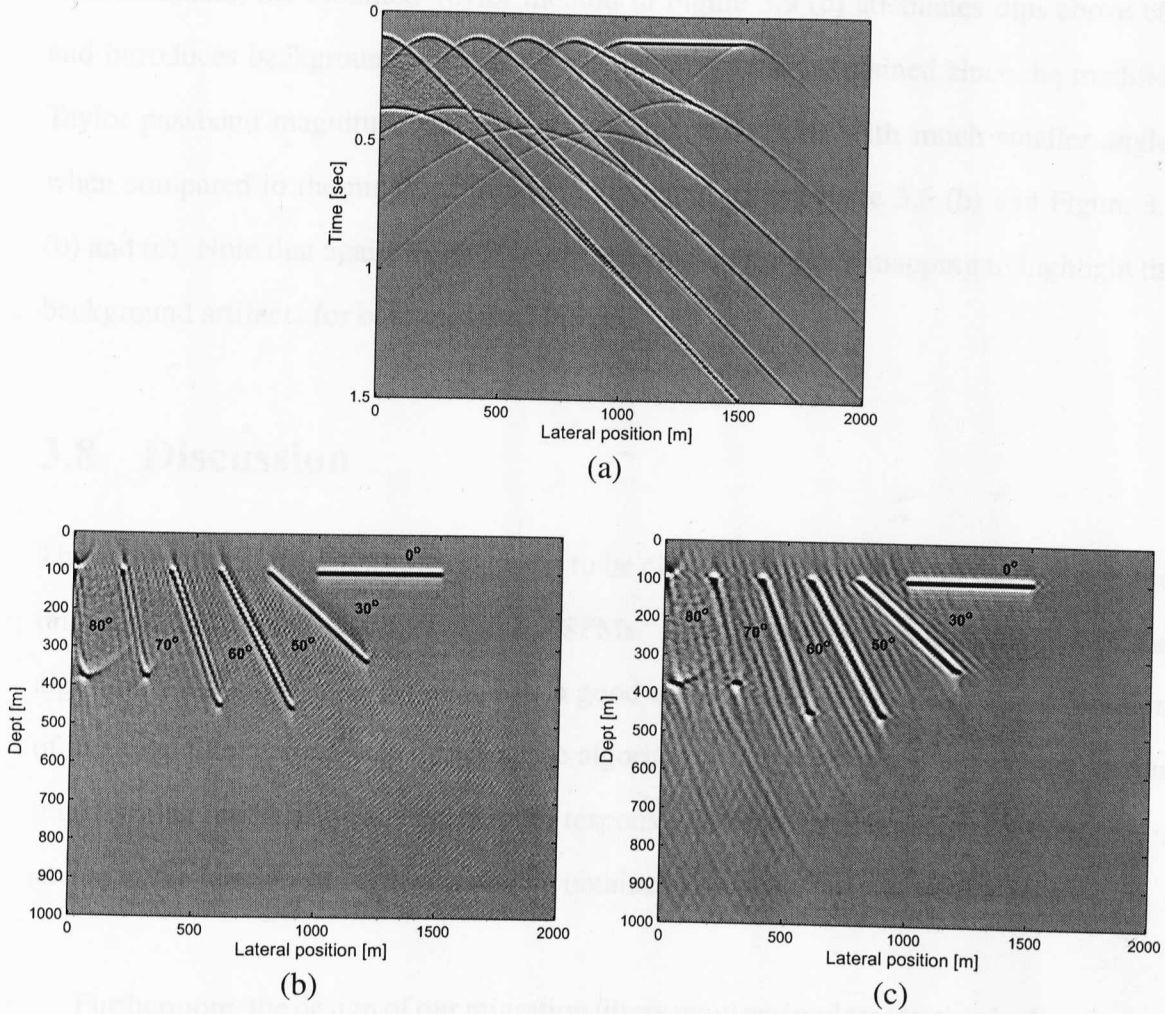

Figure 3.9: (a) A 2-D synthetic time-space section containing dipping events with angles $0^o, 30^o, 50^o, 60^o, 70^o$ and 80°. This section is constructed based on a Ricker wavelet input with a dominant frequency of 15 Hz and with a time duration of 0.2 seconds. 2-D Migrated synthetic sections (see section 3.7.2.2) containing dipping events with angles $0^o, 30^o, 50^o, 60^o, 70^o$ and 80° for (b) the modified projection algorithm with $N = 29$, and (c) the modified Taylor series method with $N = 29$.

3.7.2.2 2-D Seismic Extrapolation on Synthetic Data Containing Dip Events

The same set of filters designed using the modified projection algorithm and the modified Taylor series method for the impulse response experiments in the previous subsection are used to migrated a synthetic time-space seismic section shown in Figure 3.9 (a). This section contains dips with angles: $0^o, 30^o, 50^o, 60^o, 70^o$ and 80° and is constructed based on a Ricker wavelet input with a dominant frequency of 40 Hz and with a time duration of 0.2 seconds. Figure 3.9 (b) shows the migrated section using the modified projection algorithm which clearly has accommodated dips up to 70° and a little of the 80° dip. On

the other hand, the modified Taylor method in Figure 3.9 (c) attenuates dips above 60° and introduces background artifacts. These results can be explained since the modified Taylor passband magnitude response propagates wavefields with much smaller angles when compared to the modified projection operator as in Figure 3.6 (b) and Figure 3.8 (b) and (c). Note that again we have used a nonlinear gray scale mapping to highlight the background artifacts for both migrated images.

3.8 Discussion

There are many practical issues that need to be clarified for the design of the 1-D seismic migration FIR digital filters using the VSPMs. One of these is the initialization of the algorithm. As reported in [89, 91, 21], a good choice is to start with an approximation of the ideal filter response to initialize the algorithm. This is obtained by inverse Fourier transforming the ideal filter wavenumber response into the space domain. By doing so, a saving in the number of iterations will be obtained [89, 91].

Furthermore, the design of our migration filters requires implementation in the wavenumber domain of the constraint sets C_i, where $i = 2, \cdots, 5$. Ideally, they should be implemented (realized) on a discrete wavenumber grid via the Discrete Space Fourier Transform (DSFT). An M-length DSFT is implemented using the FFT algorithm for which M is much greater than the FIR filter spatial length N. The choice of $M \geq 10 \times N$ (M is a power of 2 for the FFT algorithm) results in satisfactory designs so that a we have an M discrete wavenumber values over the normalized wavenumber interval.

In addition, for the pure and relaxed design algorithms in sections 3.4 and 3.5, respectively, the stopband cut-off wavenumbers are chosen based on the transition bandwidth calculation of a low pass filter given in [21, 7] which can be computed essentially using:

$$\Delta k_c = \frac{-20 \log_{10} \sqrt{\delta_p \delta_s} - 13}{(N-1)14.6} \tag{3.101}$$

where $k_{c_s} = k_{c_p} + \Delta k_c$. This is because we need to have, for a given filter length N, a limit for our maximum allowable passband and stopband tolerances, i.e., δ_p and δ_s, respectively, to achieve stable migrated images of the sub-earth. Similarly, for the modified projection algorithm in section 3.6, the stopband cut-off wavenumbers are chosen based on the transition bandwidth calculation of a low pass filter for the Kaiser window given in [84] which equals:

$$\Delta k_c = \frac{-20\log_{10}\delta_s - 7.95}{14.36N}. \tag{3.102}$$

Finally, for the relaxation parameters in section 3.5, we have used an ad hoc way of adaptively changing the relaxation parameters λ_2 and λ_3. To be more specific, for λ_2 and depending upon the conditions shown in subsection 3.5.2, we used:

$$\lambda_2(k) = 0.8 - \frac{1}{k} \tag{3.103}$$

where the iteration value $k = 2, 3, \cdots$. So this will let λ_2 starts at a value less than one and continue to decrease till zero. Similarly, for λ_3 defined in subsection 3.5.1, we used:

$$\lambda_3(k) = 1.2 + \frac{1}{k} \tag{3.104}$$

where $k = 2, 3, \cdots$ and, in this case, the relaxation parameter λ_3 will start with at a value greater than 1 and continue to increase with the number of iterations. In both cases, several experiments were implemented based on the relaxed projection algorithm in section 3.5 with many relaxation parameters. The values of filter lengths and their corresponding used relaxation parameters were recorded. Finally, in each case, we used curve fitting to obtain Eqs. (3.103) and (3.104).

3.9 Conclusion

The pure and relaxed projectors have been derived and used to design 1-D complex-valued seismic migration FIR filters where two FFT computations per iteration are required for the design. The proposed relaxed projection algorithm has significantly reduced the num-

ber of iterations by 86.46% as compared to the proposed pure projection algorithm for the same filter parameters and for the same stopping threshold. Also, the modified version of the pure projection has been proposed and used to eliminate the undesirable background artifacts on migrated sections. This modification also has led to a significant reduction in the number of FFT computations by 94.81% when compared to the basic derived VSPM design algorithm and by 61.64% when compared to the relaxed VSPM design algorithm.

The designed filters satisfy all the frequency-space seismic migration FIR filter requirements. In other words, using such robust filter designs, we achieved stable migration sections for the $\omega - x$ migration method, which is used for laterally varying media. Also, such designed filters accommodate high propagation angles when compared to other reported methods, such as the modified Taylor series method, and with less numerical background artifacts. As an example, 2-D seismic migration experiments show that one can use a 1-D seismic migration FIR filter designed using the modified projection algorithm of 29 taps to accommodate dip angles up to 69°. Finally, as will be shown in chapter 4, these algorithms can be extended to 2-D seismic migration FIR filters which can be used for the migration of 3-D seismic volumes.

Chapter 4

Two-Dimensional Migration Complex-Valued FIR Digital Filter Design Using Vector Space Projection Methods

4.1 Introduction

There exist plenty of 1-D seismic migration FIR filter design techniques [14]. Unless using a filter transformation, however, it is difficult to extend most of those design algorithms to the design of 2-D seismic migration FIR filters (see [24, 36, 26] and section 2.4.5.2). The VSPM theory was proposed for designing 2-D zero-phase/linear-phase (real-valued) finite length FIR filters responses on rectangular grids [21],[22] as well as on hexagonal grids [23].

In the previous chapter, we proposed new 1-D seismic migration FIR filter design algorithms based on the VSPMs theory. Such FIR filters met all the required migration (extrapolation) characteristics and are suitable for the migration of 2-D seismic sections. But since earth is 3-D and due to the advances in computing technology, we are in need to

design true 2-D seismic migration FIR filters for the migration of 3-D seismic volumes. Seismic volumes which are migrated based on true 2-D migration FIR filters are expected to result in superior sub-earth volumes and the exploration risks are therefore reduced.

In this chapter, we extend the design algorithm of frequency-space explicit depth migration FIR digital filters using the method of VSPM which was reported in chapter 3 for the migration of 3-D seismic volumes. In addition to the explicit depth migration required characteristics defined previously (Figure 2.23), these 2-D FIR filters must possess circular symmetry with respect to their wavenumber responses. Simulation results show that by using the 2-D relaxed version of the basic derived 2-D pure algorithm for designing such 2-D FIR filters, we can save up to 56.45% of the design iterations- i.e., number of FFT computations. The 2-D modified version of the 2-D pure design algorithm saves 95.72% of the number of 2-D FFT computations used to design the same 2-D migration FIR filters using the 2-D pure design algorithm and 90.18% with the one designed using the 2-D relaxed projection design algorithm. The use of such seismic migration FIR digital filters designed using the pure, the relaxed, and the modified projections, where they are suitable for laterally varying velocities, result in stable migration images. Also, they accommodate high propagation angles with short length filters and with less numerical background artifacts on migrated sections. The filters, in addition, possess circular symmetry with respect to their wavenumber responses when compared with the standard techniques used in the geophysics community for designing/implementing such FIR filters, namely, the McClellan transformations [12, 1]. 3-D migration impulse responses show that 2-D filters of 25×25 taps designed using the proposed 2-D modified projection design algorithm accommodate dip angles up to 65°. Such responses result in less numerical artifacts and possess perfect circular symmetry when compared with those migrated via the McClellan transformations [36, 26].

In this chapter, the 2-D migration FIR filter for 3-D Seismic data is introduced in section 4.2. In section 4.3, the most widely used approach for designing 2-D seismic mi-

gration FIR digital filters, i.e., the McClellan transformation and its improved version are briefly presented. After that, sections 4.4, 4.5, and 4.6 state the pure, relaxed, and modified projection design algorithms for designing the 2-D complex-valued seismic migration FIR digital filters. Simulation results are given in section 4.7. After that, a discussion is given in 4.8 and, finally, section 4.9 summarizes the main contributions of this chapter.

4.2 2-D Migration FIR Filters for 3-D Seismic Data

Similarly to the 2-D migration (extrapolation) process presented in section 2.4.5, 3-D depth extrapolation is performed, one angular frequency ω_o at a time, using 2-D migration filters. The wavenumber response $H_d(e^{jk_x}, e^{jk_y})$ can easily be obtained from the 1-D migration wavenumber response $H_d(e^{jk_x})$ based on [12, 1]:

$$H_d(e^{jk_x}, e^{jk_y}, e^{j\omega_o}) := H_d(e^{jk_x}, e^{jk_y}) = \exp[j\frac{\Delta z}{\Delta x}\sqrt{\frac{\Delta x^2}{\Delta t^2}\frac{\omega_o^2}{c_o^2} - (k_x^2 + \frac{\Delta x^2}{\Delta y^2}k_y^2)}] \quad (4.1)$$

where k_x is the in-line wavenumber and k_y is the cross-line wavenumber, Δx and Δy are the in-line and cross-line spatial sampling intervals, respectively, Δz is the migration depth step size, Δt is the time sampling interval, and, finally, c_o is the velocity of the geological material. Assuming that $\Delta x = \Delta y$, the 2-D migration filter $H_d(e^{jk_x}, e^{jk_y})$ presented by Eq. (4.1) can be rewritten as:

$$H_d(e^{jk_x}, e^{jk_y}) = \exp[jb\sqrt{k_{c_p}^2 - (k_x^2 + k_y^2)}] \quad (4.2)$$

where $b = \Delta z/\Delta x$ and $k_{c_p} = \frac{\Delta x}{\Delta t}\frac{\omega_o}{c_o}$ is the cut-off wavenumber. Clearly, the desired 2-D wavenumber response is of circularly symmetry in the magnitude as well as for the phase response and is non-linear.

To handle lateral variations, the frequency-space or the $\omega - x - y$ migration of a spatially sampled seismic wavefield $u(x_i, y_j, e^{j\omega_l}, z_k)$ from depth z_k to $z_{k+1} = z_k + \Delta z$ is performed independently for each frequency ω_l, by a direct 2-D spatial convolution with

a designed 2-D non-causal quadrantally symmetrical $N \times N$ (N is odd) complex-valued migration filter impulse response $h[n_1, n_2]$ using [1, 13, 12, 14, 75]:

$$u(x_i, y_j, e^{j\omega_l}, z_{k+1}) = \sum_{n_1=(-N+1)/2}^{(N-1)/2} \sum_{n_2=(-N+1)/2}^{(N-1)/2} h[n_1, n_2] u(x_{i-n_1}, y_{j-n_2}, e^{j\omega_l}, z_k). \quad (4.3)$$

4.3 The Design of 2-D Migration Complex-Valued FIR Filters via McClellan Transformations

McClellan and Chen [38, 40] have shown that a 1-D FIR filter which is of odd length and possessing even symmetry (which is the same for the seismic migration FIR filter impulse response Eq. (2.17)) can be represented by:

$$H_d(e^{jk}) = h[0] + 2 \sum_{n=1}^{\frac{N+1}{2}-1} h[n] C_n(\cos(nk)) \quad (4.4)$$

where $C_n(x)$ is the nth order Chebyshev polynomial in x and k is a wavenumber (or frequency) axis. Define the McClellan transformation as [38, 37, 101, 40]:

$$\begin{aligned} \cos(nk) &= A\cos(nk_x) + B\cos(nk_y) + C\cos(nk_x)\cos(nk_y) + D \\ &= F(e^{jk_x}, e^{jk_y}). \end{aligned} \quad (4.5)$$

A, B, C and D are the filter transformation parameters. Now, by applying the McClellan transformation in Eq. (4.5) to equation Eq. (4.4), we obtain:

$$H_d(e^{jk_x}, e^{jk_y}) = h[0] + 2 \sum_{n=1}^{\frac{N+1}{2}-1} h[n] C_n(F(e^{jk_x}, e^{jk_y})) \quad (4.6)$$

where

$$C_n(F) = 2FC_{n-1}(F) - C_{n-2}(F), \text{for } n \geq 2 \quad (4.7)$$

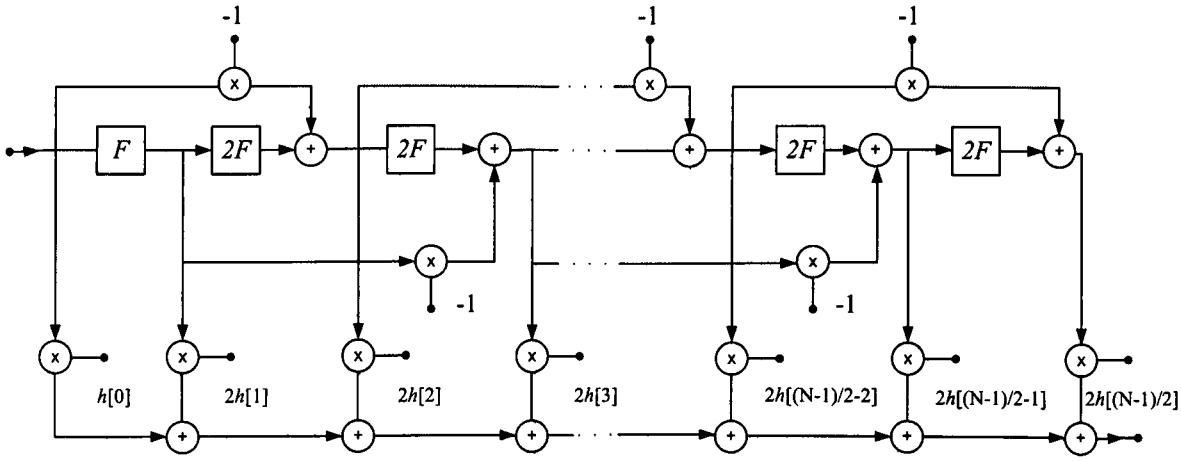

Figure 4.1: Chebyshev structure for designing/realizing 2-D FIR digital filters based on 1-D odd length impulse responses having even symmetry.

and $C_1 = F$ and $C_0 = 1$. That is, 1-D FIR filters are needed to be pre-designed and then used in Eq. (4.6) to obtain the corresponding 2-D FIR filters.

As was shown in Eq. (4.2), ideally the 2-D migration filters are of circular symmetry. Such filters may be designed and implemented by replacing $\cos(nk)$ with $F(e^{jk_x}, e^{jk_y}) = \cos(n\sqrt{k_x^2 + k_y^2})$ [38, 37, 101, 40, 10]. In general, an exact representation of $F(e^{jk_x}, e^{jk_y})$ in the Chebyshev filter structure as shown in Figure 4.1 would result in a very high computational cost [38]. Therefore, McClellan and Chen in [38] have suggested the approximation in Eq. (4.5) where $A = B = C = -D = \frac{1}{2}$ are used for circularly symmetrical wavenumber (frequency) response filters, i.e.,

$$F(e^{jk_x}, e^{jk_y}) = -1 + \frac{1}{2}(1 + \cos(nk_x))(1 + \cos(nk_y)). \tag{4.8}$$

This approximation is exact for $k_x = 0$ or $k_y = 0$ and is the DSFT of the compact 2-D FIR filter:

$$\begin{bmatrix} 1/8 & 1/4 & 1/8 \\ 1/4 & -1/2 & 1/4 \\ 1/8 & 1/4 & 1/8 \end{bmatrix}. \tag{4.9}$$

Now, using such a 2-D FIR filter in Figure 4.1, any 1-D FIR filter can be transformed to a 2-D filter with approximate circular symmetry. Figure 4.2 (a) represents a contour plot

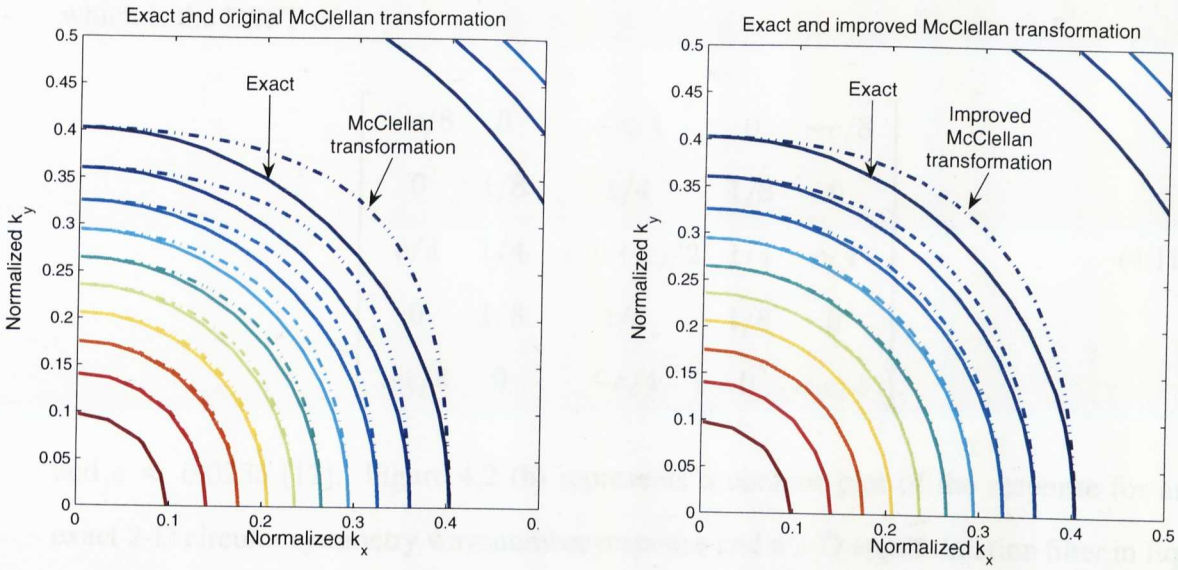

(a) (b)

Figure 4.2: Contour plots for comparing exact (solid contour lines) and approximation (dash dotted contour lines) of circularly symmetrical filters using (a) the original McClellan transformation, and (b) the improved McClellan transformation. Clearly, the error increases along the line $k_x \approx k_y$.

of the response for an exact 2-D circular symmetry wavenumber response and the 2-D approximation filter in Eq. (4.8). It indicates that such a transformation for both magnitude and phase responses are exact for $k_x = 0$ or $k_y = 0$. However, the approximation exhibits increasing error with increasing k for $k_x \approx k_y$. Hale [12], who first introduced the McClellan transformation to the geophysics community, has suggested an increase in the size of the 2-D transformation filter given in Eq. (4.9) by adding extra terms to the approximation in Eq. (4.8). That is,

$$F(e^{jk_x}, e^{jk_y}) = -1 + \frac{1}{2}(1+\cos(nk_x))(1+\cos(nk_y)) - \frac{c}{2}(1-\cos(2nk_x))(1-\cos(2nk_y)) \tag{4.10}$$

which is the DSFT of:

$$\begin{bmatrix} -c/8 & 0 & -c/4 & 0 & -c/8 \\ 0 & 1/8 & 1/4 & 1/8 & 0 \\ c/4 & 1/4 & -(1+c)/2 & 1/4 & c/4 \\ 0 & 1/8 & 1/4 & 1/8 & 0 \\ -c/8 & 0 & -c/4 & 0 & -c/8 \end{bmatrix} \tag{4.11}$$

and $c \approx 0.0255$ [12]. Figure 4.2 (b) represents a contour plot of the response for an exact 2-D circular symmetry wavenumber response and a 2-D approximation filter in Eq. (4.10). Again, such a transformation for both magnitude and phase responses are exact for $k_x = 0$ or $k_y = 0$ but they still exhibit increasing error with increasing k for $k_x \approx k_y$. This error, however, has been reduced when compared to the original transformation via Eq. (4.9). Neither design, however, results in the perfectly circular symmetrical response required by Eq. (4.2).

4.4 The Pure Projection Design Algorithm for 2-D Migration Complex-Valued FIR Filters

The 1-D design algorithm for designing migration FIR digital filters (see section 3.4) is extended here to the 2-D case which is given as follows. Note that for more details about the constraint sets C_i that describe the required migration FIR filter characteristics and their associated projection operators P_{C_i}, where $i = 1, \cdots, 5$, refer to the previous chapter in section 3.3. Now, assuming that we are interested in designing such filters for rectangular grids, let k_s and k_p respectively be the stopband (evanescent) and passband regions and denote the exact phase response as $\phi(k_x, k_y) = b\sqrt{k_{c_p}^2 - (k_x^2 + k_y^2)}$ where k_{c_p} is the passband cutoff. Also, denote k_{c_s} as the stopband cutoff. Finally, let δ_p and δ_s respectively be the maximum allowable passband and stopband regions' tolerances. Now, start with an arbitrary complex-valued vector $\mathbf{h}_0$ of dimension $M \times M$ (M is the number

of FFT samples), which is much greater than the spatial operator length $N \times N$. Then for the kth iteration

1. Project $\mathbf{h}_k$ onto C_5, that is

$$\mathbf{g}_{1,k} = P_{C_5}\mathbf{h}_k \leftrightarrow \begin{cases} H_k(e^{jk_x}, e^{jk_y}), \text{ if } A_{C_5} \\ -\delta_s \exp(j\angle H_k(e^{jk_x}, e^{jk_y})), \text{ if } B_{C_5} \\ H_k(e^{jk_x}, e^{jk_y}), \text{ otherwise} \end{cases} \tag{4.12}$$

where A_{C_5} is $|H_k(e^{jk_x}, e^{jk_y})| < \delta_s$, B_{C_5} is $|H_k(e^{jk_x}, e^{jk_y})| \geq \delta_s$ and $k_x, k_y \in k_s$.

2. Project $\mathbf{g}_{1,k}$ onto C_4 using

$$\mathbf{g}_{2,k} = P_{C_4}\mathbf{g}_{1,k} \leftrightarrow \begin{cases} G_{1,k}(e^{jk_x}, e^{jk_y}), \text{ if } A_{C_4} \\ -(1+\delta_p) \exp(j\angle G_{1,k}(e^{jk_x}, e^{jk_y})), \text{ if } B_{C_4} \\ G_{1,k}(e^{jk_x}, e^{jk_y}), \text{ otherwise} \end{cases} \tag{4.13}$$

where A_{C_4} is $|G_{1,k}(e^{jk_x}, e^{jk_y})| < (1+\delta_p)$, B_{C_5} is $|G_{1,k}(e^{jk_x}, e^{jk_y})| \geq (1+\delta_p)$, and $k_x, k_y \in k_p$.

3. Project $\mathbf{g}_{2,k}$ onto C_3 using

$$\mathbf{g}_{3,k} = P_{C_3}\mathbf{g}_{2,k} \leftrightarrow \begin{cases} G_{2,k}(e^{jk_x}, e^{jk_y}), \text{ if } A_{C_3} \\ (1-\delta_p) \exp(j\angle G_{2,k}(e^{jk_x}, e^{jk_y})), \text{ if } B_{C_3} \\ G_{2,k}(e^{jk_x}, e^{jk_y}), \text{ otherwise} \end{cases} \tag{4.14}$$

where A_{C_3} is $|G_{2,k}(e^{jk_x}, e^{jk_y})| > (1-\delta_p)$, B_{C_3} is $|G_{2,k}(e^{jk_x}, e^{jk_y})| \leq (1-\delta_p)$ and $k_x, k_y \in k_p$.

4. Project $\mathbf{g}_{3,k}$ onto C_2 using

$$\mathbf{g}_{4,k} = P_{C_2}\mathbf{g}_{3,k} \leftrightarrow \begin{cases} |G_{3,k}(e^{jk_x}, e^{jk_y})| \\ \cos\left(\theta_{G_{3,k}} - \phi(k_x, k_y)\right)\exp(j\phi(k_x, k_y,)), \text{ if } A_{C_2} \\ -|G_{3,k}(e^{jk_x}, e^{jk_y})| \\ \cos\left(\theta_{G_{3,k}} - \phi(k_x, k_y)\right)\exp(j\phi(k_x, k_y)), \text{ if } B_{C_2} \end{cases} \tag{4.15}$$

where $\theta_{G_{3,k}} = \angle G_{3,k}(e^{jk_x, jk_y})$, A_{C_2} is $\cos\left(\theta_{G_{3,k}} - \phi(k_x, k_y)\right) \geq 0$, and B_{C_2} is $\cos\left(\theta_{G_{3,k}} - \phi(k_x, k_y)\right) < 0$.

5. Finally, project $\mathbf{g}_{4,k}$ onto C_1 by

$$\mathbf{h}_{k+1} = P_{C_1}\mathbf{g}_{4,k} = \begin{cases} g_{4,k}[n_1, n_2], \text{ for } |n_1, n_2| \leq (N-1)/2 \\ 0, \text{ otherwise.} \end{cases} \tag{4.16}$$

Now, if the mean-square error between $\mathbf{h}_k$ and $\mathbf{h}_{k+1}$ is less than or equal to a pre-defined threshold ϵ, then stop the algorithm. Otherwise, repeat steps 1-5.

4.5 The Relaxed Projection Design Algorithm for 2-D Migration Complex-Valued FIR Filters

Similar to the 1-D case (see chapter 3, section 3.5), we can expect to achieve faster convergence with the 2-D relaxed projection algorithm than with the 2-D pure projection algorithm by fixing the relaxation parameters $\lambda_1 = \lambda_4 = \lambda_5 = 1$, and varying λ_2 and λ_3 with respect to their pre-determined intervals. That is, we relax P_{C_2} as T_{C_2} and P_{C_3} as T_{C_3}. Therefore, the above 2-D pure projection design algorithm for 2-D migration complex-valued FIR filters is used except for replacing step number 3 with :

$$\mathbf{g}_{3,k} = T_{C_3}\mathbf{g}_{2,k} \leftrightarrow \begin{cases} G_{2,k}(e^{jk_x}, e^{jk_y}) \text{ if } A_{C_3} \\ (1-\lambda_3)G_{2,k}(e^{jk_x}, e^{jk_y}) + \lambda_3(1-\delta_p)\exp(j\angle G_{2,k}(e^{jk_x}, e^{jk_y})) \text{ if } B_{C_3} \\ G_{2,k}(e^{jk_x}, e^{jk_y}), \text{ otherwise} \end{cases} \tag{4.17}$$

for $\lambda_3 \in (1,2)$ where A_{C_3} is $|G_{2,k}(e^{jk_x}, e^{jk_y})| > (1-\delta_p)$, B_{C_3} is $|G_{2,k}(e^{jk_x}, e^{jk_y})| \leq (1-\delta_p)$ and $k_x, k_y \in k_p$. Also, step number 4 is replaced with:

$$\mathbf{g}_{4,k} = T_{C_2}\mathbf{g}_{3,k} \leftrightarrow \begin{cases} (1-\lambda_2)G_{3,k}(e^{jk_x}, e^{jk_y}) \\ +\lambda_2|G_{3,k}(e^{jk_x}, e^{jk_y})|\cos(\theta_{G_{3,k}} - \phi(k_x,k_y))\exp(j\phi(k_x,k_y,)), \text{ if } A_{C_2} \\ (1-\lambda_2)G_{3,k}(e^{jk_x}, e^{jk_y}) \\ -\lambda_2|G_{3,k}(e^{jk_x}, e^{jk_y})|\cos(\theta_{G_{3,k}} - \phi(k_x,k_y))\exp(j\phi(k_x,k_y)), \text{ if } B_{C_2} \end{cases} \tag{4.18}$$

where A_{C_2} is $\cos(\theta_{G_{3,k}} - \phi(k_x,k_y)) \geq 0$, and B_{C_2} is $\cos(\theta_{G_{3,k}} - \phi(k_x,k_y)) < 0$. For $\cos(\theta_{G_{3,k}} - \phi(k_x,k_y)) \geq 0$, λ_2 will be within $(0,1)$ if $\cos(\phi(k_x,k_y)) \geq 0$ or $\sin(\phi(k_x,k_y)) \geq 0$. Otherwise, $\lambda_2 = 1$. On the other hand, for $\cos(\theta_{G_{3,k}} - \phi(k_x,k_y)) < 0$, and if $\cos(\phi(k_x,k_y)) \leq 0$ or $\sin(\phi(k_x,k_y)) \leq 0$, then $\lambda_3 \in (0,1)$. Otherwise, $\lambda_2 = 1$.

4.6 The Modified Projection Design Algorithm for 2-D Migration Complex-Valued FIR Filters

For the modified design algorithm, the 2-D pure design algorithm prestated in section 4.4 is used except that the projection of $\mathbf{g}_{4,k}$ onto C_1 is replaced by:

$$\mathbf{h}_{k+1} = P_{C_1}\mathbf{g}_{4,k} = \begin{cases} g_{4,k}[n_1,n_2]\frac{I_o[\beta\sqrt{1-(\frac{2n_1}{N-1})^2}]I_o[\beta\sqrt{1-(\frac{2n_2}{N-1})^2}]}{I_o[\beta]^2}, \text{ for } |n_1,n_2| \leq (N-1)/2 \\ 0, \text{ otherwise} \end{cases} \tag{4.19}$$

where $I_o[\cdot]$ is the modified zero-order Bessel function of the first kind, and β is the shape parameter which determines the trade-off between the main-lobe and peak side-lobe level (see [40] for more details).

4.7 Simulation Results

This section is divided into two main parts. The first subsection deals with designing 2-D migration filters using the pure, relaxed and modified algorithms in sections 4.4, 4.5, and 4.6, respectively. These designed filters are compared with those designed via the McClellan and the improved McClellan (McClellan-Hale) transformations. The second section shows an application of the proposed VSPM seismic migration FIR filter design algorithms to 2-D synthetic seismic sections. Note that the results obtained in all our simulations can apply to all cases and are not restricted to the filters' parameters chosen. In addition, all the designed filters which are shown in the following subsections are displayed with respect to their normalized wavenumbers. Finally, all the simulations are preformed in MATLAB which is installed on a Pentium 4 machine with a speed of 2.6 GHz and with a RAM of 1GB.

4.7.1 2-D Migration FIR Filter Design Using Vector Space Projection Methods

In this subsection, we want to compare the accuracy of the 2-D migration FIR digital filters designed with the three extended projection algorithms given earlier. Also, we want to compare those with the one designed by using the McClellan and the improved McClellan transformations.

4.7.1.1 Simulation 1: 2-D Migration FIR Digital Filter Design Using the Pure, Relaxed, and Modified Projections Comparisons

A 25×25 2-D migration FIR filter is designed using the pure projection algorithm. The filter parameters are as follows: $k_{c_p} = 0.25$, $k_{c_s} = 0.3841$, and $\delta_p = \delta_s = 10^{-3}$. Figure

4.3 (a) shows the magnitude spectrum of such a filter which meets the filter magnitude spectrum constrains, i.e, C_3, C_4, and C_5. Moreover, Figure 4.3 (b) shows the phase spectrum in the passband for this designed filter where the phase in the passband is meeting the constraint C_2 requirements, i.e, being of circular symmetry. The design took 1286 iterations to converge with respect to $\epsilon = 10^{-14}$.

Similarly to the designed 2-D migration FIR filter using pure projectors, a 25×25 2-D seismic migration FIR filter is designed using the relaxed projection algorithm with the same design parameters. The designed filter was obtained with 560 iterations and Figure 4.4 shows a similar result to Figure 4.3. This is an expected result since both filters (solutions) are coming from the same solution set, which contains all possible filters satisfying the same filter parameters.

Also, a 25×25 2-D migration FIR filter is designed using the modified projection algorithm with the same parameters except for the stopband cut-off wavenumber which is in this case $k_{c_s} = 0.401$. The 2-D modified projection algorithm took only 55 iterations to converge with respect to $\epsilon = 10^{-14}$. The obtained filter possesses a flatter magnitude response as is clearly seen in Figure 4.5 (a) when compared with Figure 4.3 (a) and Figure 4.4 (a), respectively. The ripply effect has been removed even with respect to the phase response as can be seen in Figure 4.5 (b) and when compared with Figure 4.3 (b) and Figure 4.4 (b), respectively, resulting in a reduced phase error response. It should also be noticed that the 2-D magnitude response of the modified projection algorithm possesses a better circularly symmetrical shape when compared to those designed with the pure and the relaxed projection algorithms.

Finally, Figure 4.6 plots the mean-square error versus the number of iterations required to meet the pre-defined $\epsilon = 10^{-14}$. Note that all curves shows a uniform convergence of the three proposed design algorithms. When compared to the 2-D filter designed using the pure projection algorithm, the relaxed projection algorithms has saved (in this case)

56.45% of the FFT computations. Also, the modified projection algorithm has saved (in this case) 95.72% of the FFT computations when compared with the pure design algorithm, while it has saved 90.18% FFT computations when compared to the relaxed projection algorithm 2-D designed seismic migration filter. Thus, as in the case for the 1-D modified projection algorithm, the 2-D modified projection algorithm serves as a good choice for migrating 3-D seismic volumes. This is due to the reduced computations of the design, the circular symmetrical wavenumber response, and its magnitude response, which is expected to result in stable migration volumes.

4.7.1.2 Simulation 2: Comparisons With the McClellan Transformations

In Figures 4.7 and 4.8 the same 2-D filters were obtained but this time with the McClellan transformation and its improved version (refer to section 4.3). The 1-D filters used to design these filters via the transformation were designed using the 1-D modified projection algorithm in section 3.6 with $N = 25$, $k_{c_p} = 0.25$, and $\delta_p = \delta_s = 10^{-3}$. Clearly, the magnitude response of the improved McClellan transformation in Figure 4.8 (a) shows an improvement in the design when compared to the original McClellan transformation magnitude response in Figure 4.7 (a). Also, since the pre-designed 1-D migration filters satisfied the migration FIR filter characteristics, it is expected that these designs result in stable migration volumes. However, both designs are approximations to the true 2-D design and, hence, will not result in perfect circular symmetry of migrated sections when compared to the 2-D filters designed via the modified projection algorithm, as will be shown in the next subsection. Nevertheless, such transformations are much cheaper to design even when compared with the 2-D modified projection algorithm. Note that such cheap design (implementation) techniques were proposed for migrating 3-D volumes to speed up the migration process. That was at the time where the capabilities of computing facilities were limited compared with today's.

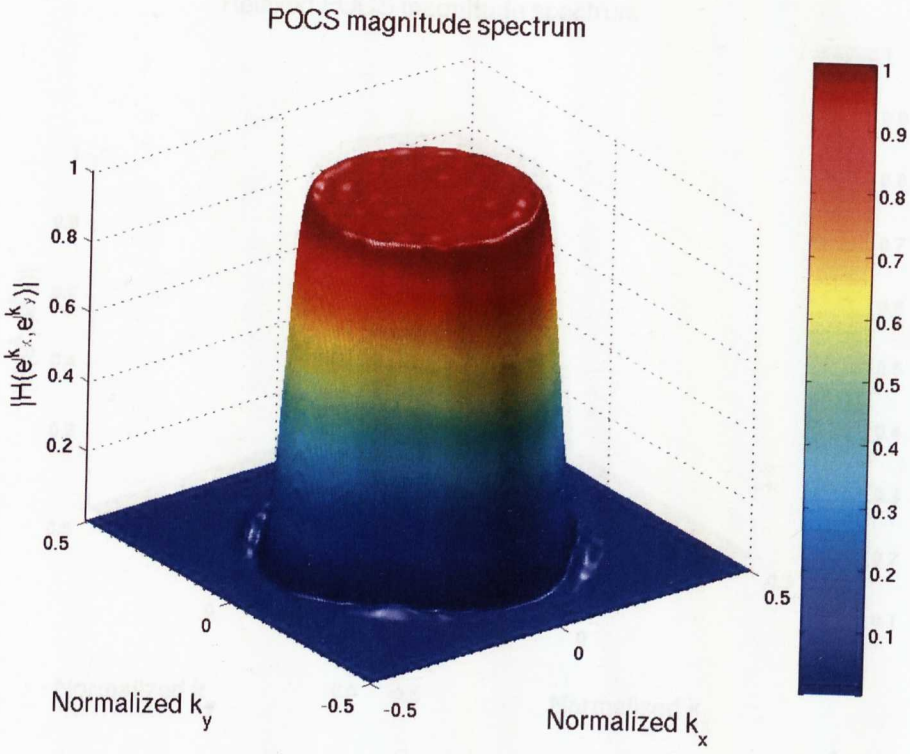

(a)

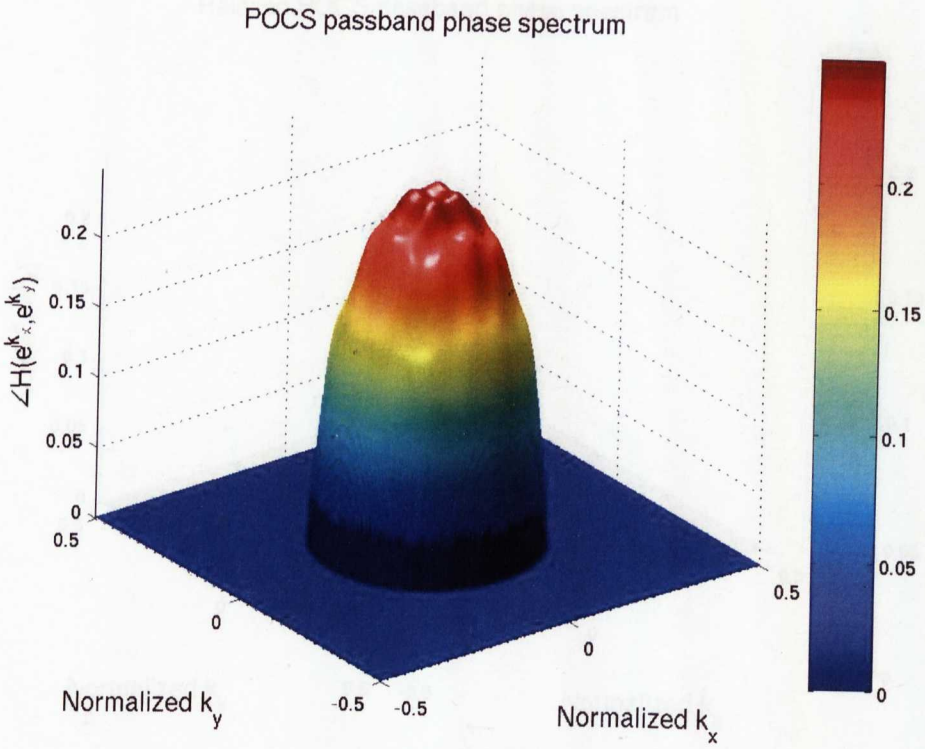

(b)

Figure 4.3: (a) Magnitude response of the pure projector designed 2-D seismic migration filter, (b) Phase response of the pure projector designed 2-D seismic migration filter with $N = 25$, $k_{c_p} = 0.25$, $k_{c_s} = 0.3841$, $\delta_p = \delta_s = 10^{-3}$, and $\epsilon = 10^{-14}$ (see section 4.7.1.1).

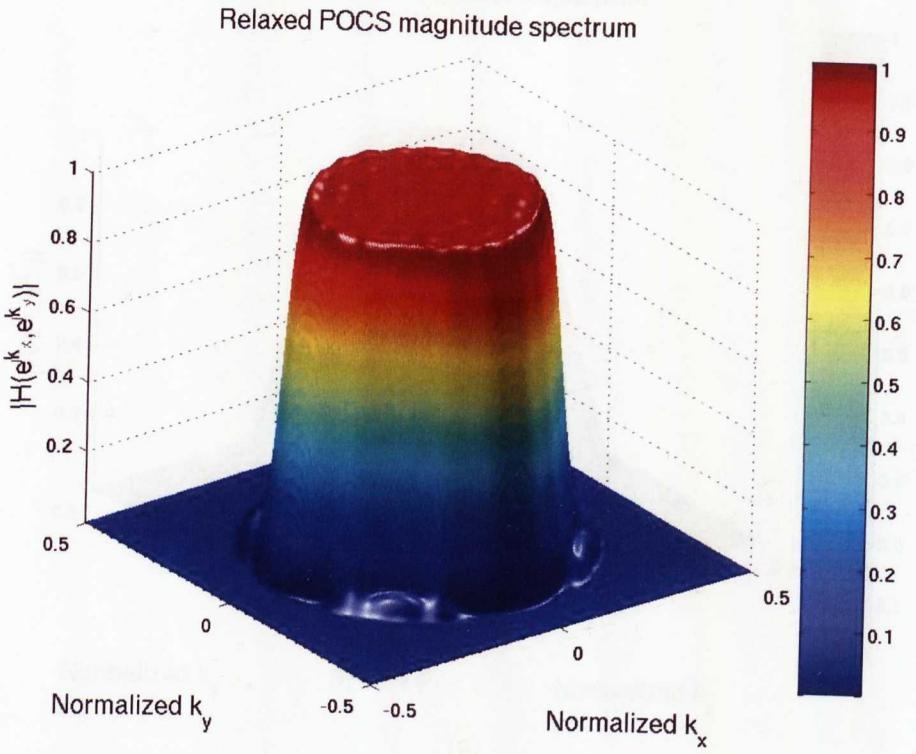

(a)

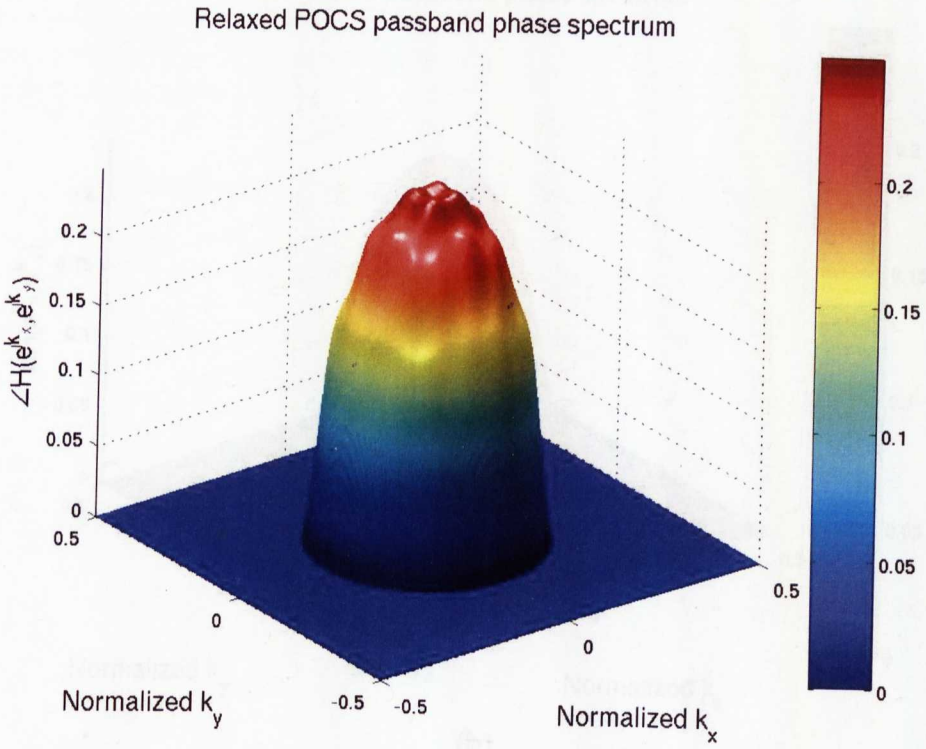

(b)

Figure 4.4: (a) Magnitude response of the relaxed projector designed 2-D seismic migration filter, (b) Phase response of the relaxed projector designed 2-D seismic migration filter with $N = 25$, $k_{c_p} = 0.25$, $k_{c_s} = 0.3841$, $\delta_p = \delta_s = 10^{-3}$, and $\epsilon = 10^{-14}$ (see section 4.7.1.1).

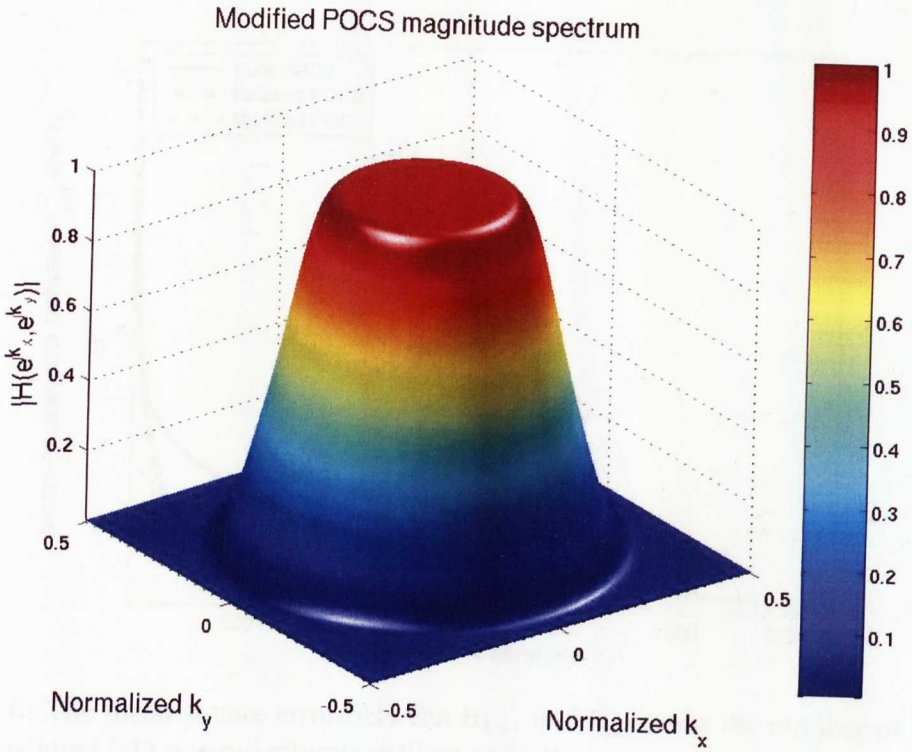

(a)

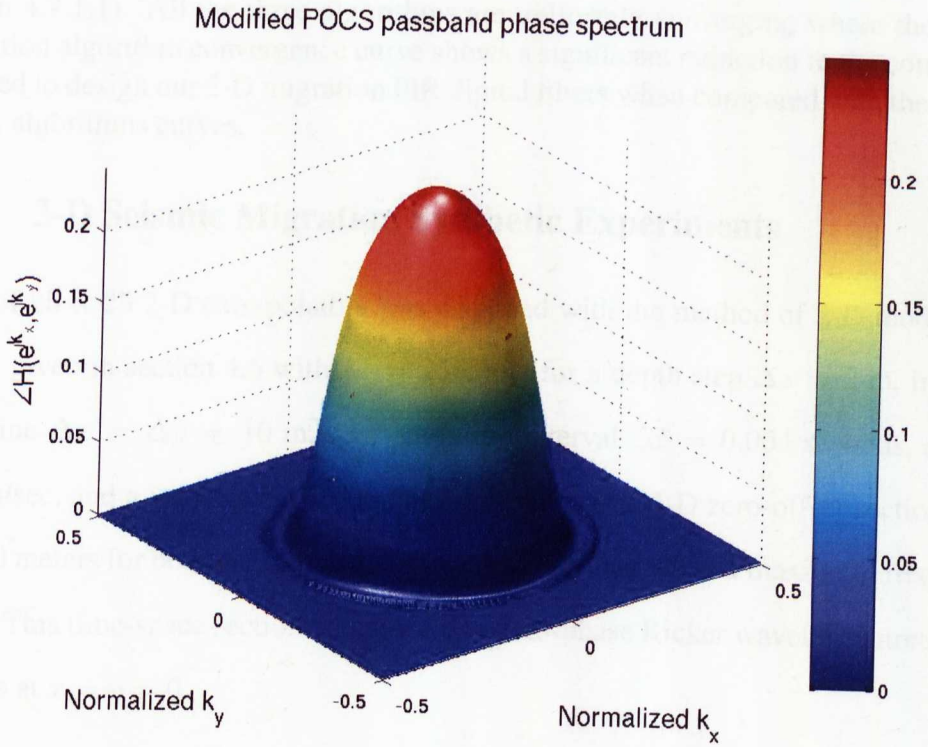

(b)

Figure 4.5: (a) Magnitude response of the modified projector designed 2-D seismic migration filter, (b) Phase response of the modified projector designed 2-D seismic migration filter with $N = 25$, $k_{c_p} = 0.25$, $k_{c_s} = 0.401$, $\delta_p = \delta_s = 10^{-3}$, and $\epsilon = 10^{-14}$ (see section 4.7.1.1). Note that the 2-D modified projection algorithm resulted in better magnitude as well as phase wavenumber responses when compared with the 2-D pure design algorithm result in Figure 4.3 and the 2-D relaxed design algorithm result in Figure 4.4.

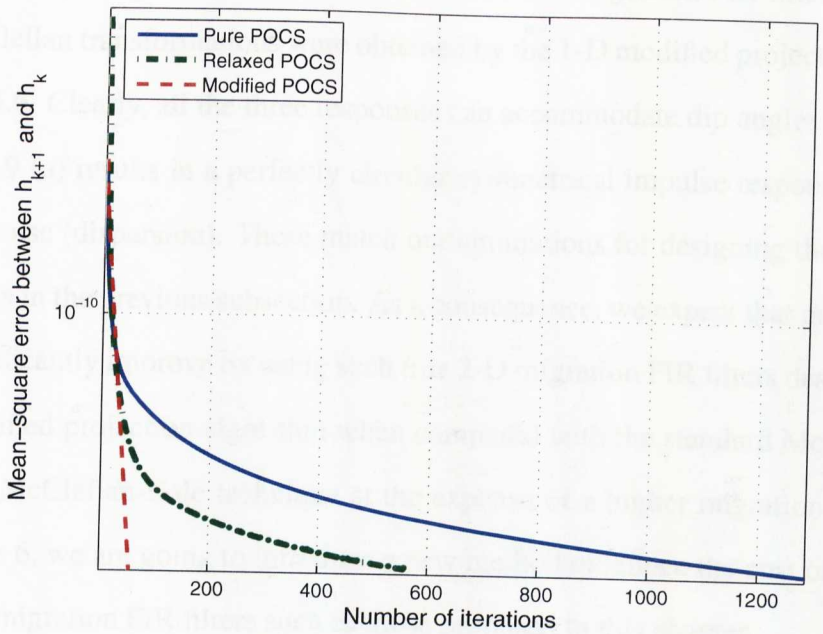

Figure 4.6: The mean-square error between $\mathbf{h}_{k+1}$ and $\mathbf{h}_k$ versus the number of iterations for the designed 2-D seismic migration filter using the proposed pure, relaxed, and modified projection algorithms with $N = 25$, $k_{c_p} = 0.25$, $\delta_p = \delta_s = 10^{-3}$, and $\epsilon = 10^{-14}$ (see section 4.7.1.1). All the three algorithms are uniformly converging where the modified projection algorithm convergence curve shows a significant reduction in the computations required to design our 2-D migration FIR digital filters when compared with the other two design algorithms curves.

4.7.2 3-D Seismic Migration Synthetic Experiments

A set of 25×25 2-D extrapolators was designed with the method of 2-D modified projection given in section 4.6 with $M = 256$, and for a depth step $\Delta z = 2$ m, in-line and cross-line $\Delta x = \Delta y = 10$ m, time sampling interval $\Delta t = 0.004$ seconds, $\omega = 50\pi$ radians/sec, and a velocity $c = 1000$ m/s. We migrated a 3-D zero-offset section a range of 1100 meters for both the in-line and cross-line sections, up to a maximum frequency of 45 Hz. This time-space section contained one zero-phase Ricker wavelet centred at 0.512 seconds at $x = y = 0$.

A 2-D slice at depth $z = 220$ m of the migrated 3-D volume is shown in Figure 4.9 (a) using the proposed 2-D modified projection FIR filter design algorithm. In Figure 4.9 (b) and (c), respectively, we see 2-D depth slices at $z = 220$ m of the same 3-D seismic volume using the McClellan transformation [38] and the improved McClellan transforma-

tion (McClellan-Hale) techniques [11]. Both sets of migration FIR filters designed with the McClellan transformations were obtained by the 1-D modified projection algorithm in section 3.6. Clearly, all the three responses can accommodate dip angles of up to 65° but Figure 4.9 (a) results in a perfectly circular symmetrical impulse response with less migration noise (dispersion). These match our simulations for designing the 2-D migration FIR filters in the previous subsection. As a consequence, we expect that migrated sections will significantly improve by using such true 2-D migration FIR filters designed using the 2-D modified projection algorithm when compared with the standard McClellan and the standard McClellan-Hale technique at the expense of a higher migration cost. Later on in chapter 6, we are going to introduce a new method to reduce the cost of implementing true 2-D migration FIR filters such as those proposed in this chapter.

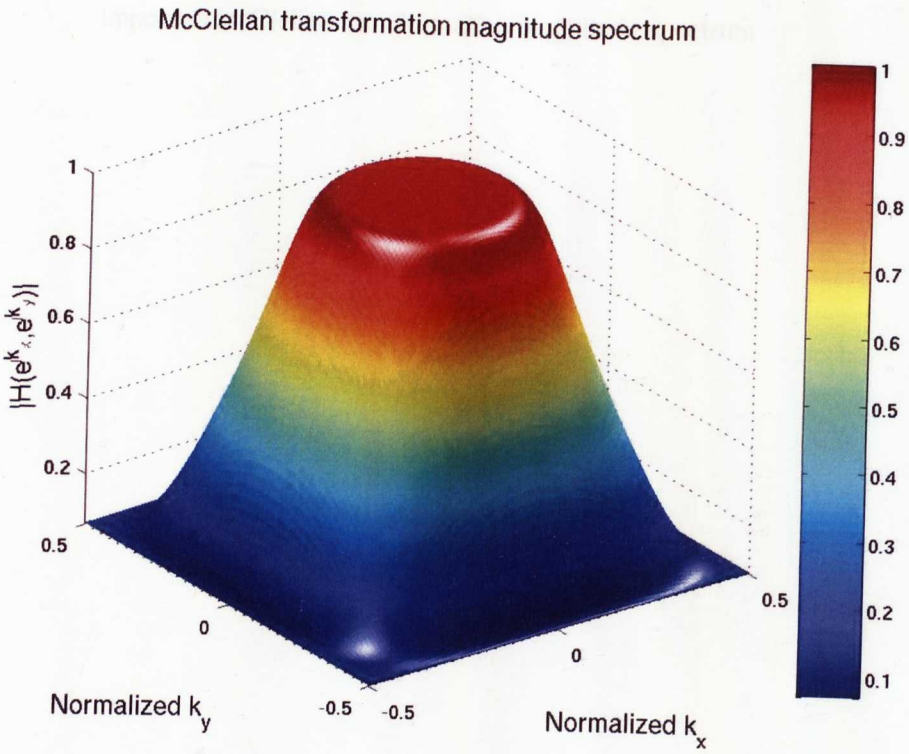

(a)

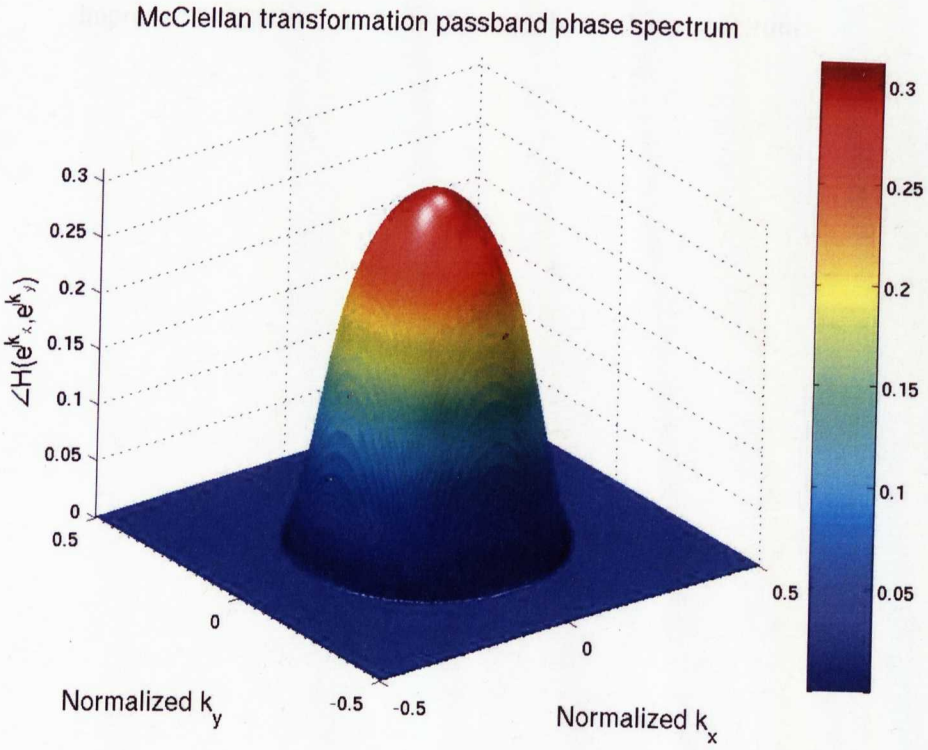

(b)

Figure 4.7: (a) Magnitude response of the McClellan designed 2-D seismic migration filter, (b) Phase response of the McClellan designed 2-D seismic migration filter with $N = 25$, $k_{c_p} = 0.25$, $k_{c_s} = 0.401$, $\delta_p = \delta_s = 10^{-3}$, and $\epsilon = 10^{-14}$ (see section 4.7.1.2).

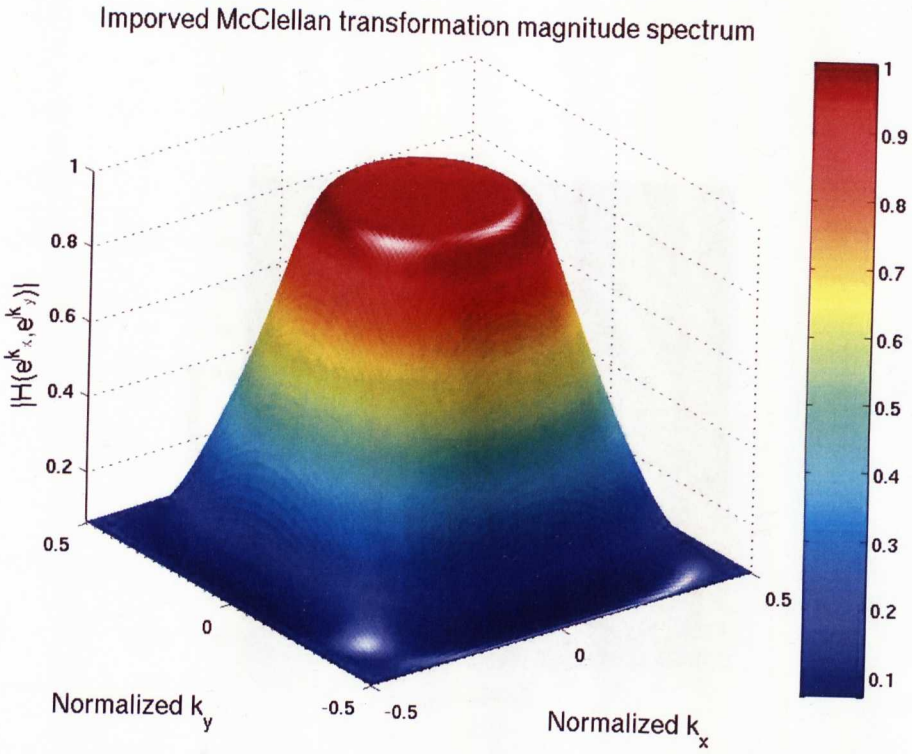

(a)

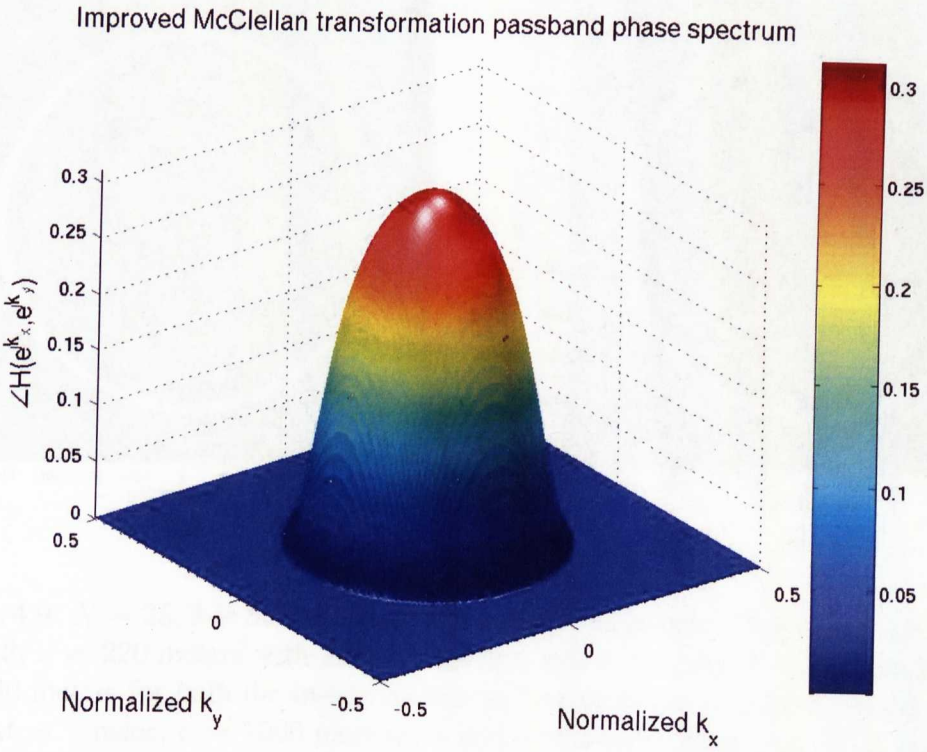

(b)

Figure 4.8: (a) Magnitude response of the improved McClellan designed 2-D seismic migration filter, (b) Phase response of the improved McClellan designed 2-D seismic migration filter with $N = 25$, $k_{c_p} = 0.25$, $k_{c_s} = 0.401$, $\delta_p = \delta_s = 10^{-3}$, and $\epsilon = 10^{-14}$ (see section 4.7.1.2). This shows a better approximation of the 2-D seismic migration FIR filter when compared to the one shown in Figure 4.7 (a). However, we still see an error along the line $k_x \approx k_y$.

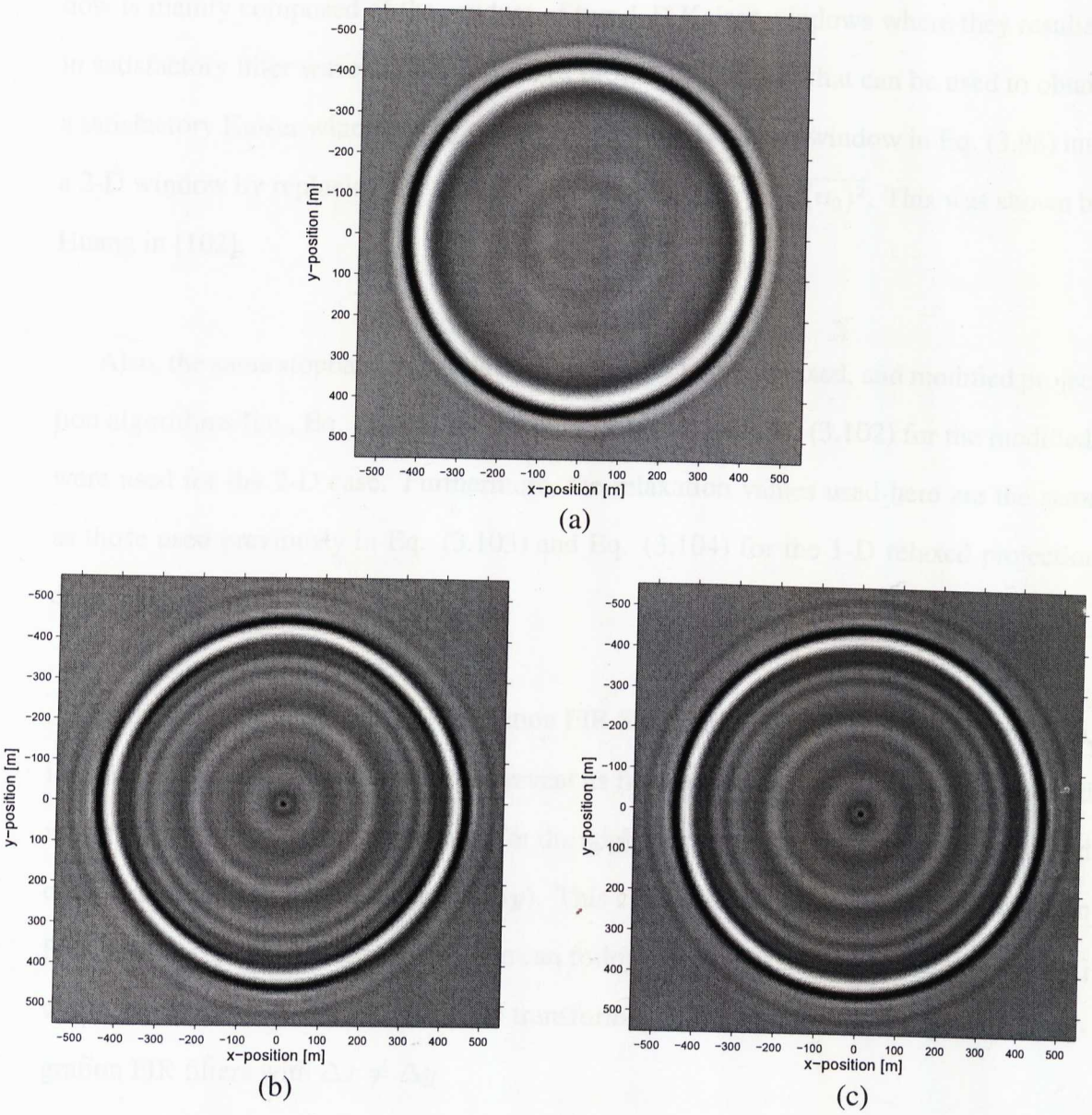

Figure 4.9: $N = 25$, 3-D Seismic migration impulse response 2-D slice (see section 4.7.2) at depth $z = 220$ meters with $\Delta z = 2$ meters, and $\Delta x = \Delta y = 10$ meters for a range of 1100 meters for both the in-line and cross-line sections. The time sampling interval was $\Delta t = 4$ msec, $c = 1000$ meters/sec and a maximum frequency of 45 Hz using (a) true 2-D filters designed using the modified projections with an approximate resulting dip angle of 65°, (b) the McClellan transformation method, and (c) the improved McClellan transformation method. We see that our result in (a) comes with less migration noise and possesses better circular symmetry when we compare with those obtained in (b) and (c).

4.8 Discussion

For the 2-D Kaiser window, we have chosen to use the one given in Eq. (4.19). This window is mainly composed of the product of two 1-D Kaiser windows where they resulted in satisfactory filter wavenumber responses [40]. Another way that can be used to obtain a satisfactory Kaiser window is by transforming the 1-D Kaiser window in Eq. (3.98) into a 2-D window by replacing the spatial index n with $\sqrt{(n_1)^2 + (n_2)^2}$. This was shown by Huang in [102].

Also, the same stopband intervals used for the 1-D pure, relaxed, and modified projection algorithms (i.e., Eq. (3.101) for the pure (relaxed) and Eq. (3.102) for the modified) were used for the 2-D case. Furthermore, the relaxation values used here are the same as those used previously in Eq. (3.103) and Eq. (3.104) for the 1-D relaxed projection design algorithm.

In addition, although our 2-D migration FIR filters suits equally spaced sampled data, i.e., $\Delta x = \Delta y$, however, this will not prevent us from adapting the 2-D pure, relaxed, and modified projection design algorithms for the application to data with different in-line and cross-line sampling intervals ($\Delta x \neq \Delta y$). This can be easily achieved by employing an FFT with $\Delta x \neq \Delta y$. Alternatively, one can follow the work proposed by Levin in [103] where he extended the McClellan-Hale transformation method for the design of 2-D migration FIR filters with $\Delta x \neq \Delta y$.

Finally, it is worth mentioning that in this chapter, the focus was to compare both McClellan transformation designs for designing 2-D seismic migration filters with the proposed 2-D design algorithms based on the pure, relaxed, and modified projections stated respectively in sections 4.4, 4.5, and 4.6. In practice, the 1-D migration FIR digital filters are designed and the structure shown in Figure 4.1 is used along with these pre-designed 1-D filters to realize (implement) the 2-D migration FIR filters [101, 40, 1].

Chapter 6 will show additional experiments with respect to both McClellan transformation techniques from the 2-D FIR filter realization (implementation) point of view [101, 40].

4.9 Conclusion

This chapter has extended the 1-D migration FIR digital filter design algorithms using the pure and relaxed projections onto convex sets to design 2-D migration FIR digital filters. As with the case for the 1-D filters, the 2-D designed filter satisfies all seismic migration filter requirements in addition to possessing perfect circular symmetrical wavenumber responses. In other words, we came up with a robust design algorithm for the 3-D frequency-space explicit depth migration filtering problem.

Based on the simulation results, the 2-D relaxed projection algorithm has significantly reduced the number of iterations by 56.45% when compared to the 2-D pure projection algorithm for the same filter parameters and for the same stopping threshold. Also, the 2-D modified version of the 2-D pure projection was used to eliminate undesirable background artifacts (increase the robustness of migrated sections) on migrated sections where this modification also led to a significant reduction in the number of FFT computations by 95.72% when compared to the 2-D pure design algorithm and by 90.18% when compared to the relaxed design algorithm.

Finally, 3-D seismic migration experiments show that we can use true 2-D seismic migration FIR digital filters designed using the 2-D modified projection algorithm, and this results in less migration (dispersion) noise as well as possessing perfect circular symmetry when compared to standard 2-D migration FIR digital filter design schemes, i.e., the McClellan and the McClellan-Hale transformations.

Chapter 5

The Design of Multi-Dimensional Complex-Valued FIR Digital Filters by the Method of Pure Projections

5.1 Introduction

The design of FIR filters has been a subject of research since the late 1960's, and many design algorithms have been developed since then, [7, 6, 83, 84]. Each technique has its own advantages and disadvantages depending on the application or the required filter design specifications, which could be either time-domain or frequency-domain constraints [7, 83, 21]. In particular, the development of efficient techniques for the design of multi-dimensional (m-D) FIR filters has been drawing the attention of many researchers for quite a time [6].

The algorithms such as the one reported in [48] or in [49] can only address the frequency-domain specifications and results in suboptimal designs. Other methods such as linear programming can satisfy requirements in the frequency-domain as well as the time-space domains [47]. However, this method results in tremendous computational time efforts for the 1-D case and, hence, for the m-D case [47]. Some researchers approach

the problem of designing filters with complex coefficients by expressing the desired phase and magnitude responses as complex Cartesian components and operate on the real and imaginary components independently. Then, the final filter coefficients are formed from the resultant real and imaginary coefficients [7]. Moreover, Chen-Parks [46] approximates the complex-valued response by a real-valued function and the resulting errors in magnitude and group delay are made approximately equiripple. Their method, however, requires large computer memory and the design time increases exponentially with increasing time and frequency grid-density [46, 22]. The generalization of the Remez exchange algorithm to complex-valued FIR filters done by Karam and McClellan [19, 20] is also a kind of development for designing general complex-valued FIR digital filters. All of such methods require filter transformation to design 2-D FIR filters. For the m-D case, it will even be more difficult to directly extend their techniques to the design of m-D complex-valued FIR filters [50, 51].

The theory of VSPMs results in feasible FIR filter designs. More importantly, the designs satisfy the frequency-domain and the time-space domain (refer to chapters 3 and 4). As seen in previous chapters, 1-D and 2-D complex-valued migration FIR digital filters were designed using the theory of VSPM. Such design algorithms can be extended to the multi-dimensional (m-D) case due to the availability of efficient m-D FFT routines (see for example [7, 6]).

In this chapter, a method for the design of multi-dimensional (m-D) complex-valued FIR digital filters using the Pure Projections method, where the resulting frequency responses possess an approximate equiripple nature, will be investigated. This proposed algorithm is a generalization of the one-dimensional (1-D) real-valued FIR filter design case (reported in [21, 22]) as well as to the 1-D and 2-D complex-valued migration FIR digital filters (chapters 3 and 4) to general m-D complex-valued FIR filters. The simulation results illustrate superior designs using pure projections when compared with the complex Remez filter design method previously reported in [20]. More specifically, the

1-D pure design algorithm in section 3.4 is extended to m-D. Furthermore, the constraint set C_1 is changed to include general complex-valued FIR digital filters where seismic migration FIR filters are special case of such filters. Also, C_2 is redefined in a more general approach to suit any pre-defined phase response.

The organization of this chapter is as follows. The problem of designing a complex-valued FIR filter using the pure projection method is shown in section 5.2 with the modifications on C_1 and C_2 to generalize the 1-D pure algorithm given in section 3.4. Section 5.3 presents explicitly the design algorithm of m-D complex-valued FIR filters using the pure projection method. After that, in section 5.4 simulation results are given and section 5.5 discusses some practical aspects of this proposed m-D complex-valued FIR filter design algorithm. Finally, we draw some conclusions in section 5.6.

5.2 Complex-valued FIR Filter Design using the Pure Projection Method

To properly design N-length complex-valued FIR digital filters using pure projection, we need to first define the required filter properties in constraint sets that are closed convex sets. These constraint sets must belong to the set of M-dimensional complex vectors where the dimension M is much greater than the filter length N. More specifically, we want to place some time domain and also frequency domain properties in proper sets which are closed and convex. So we want to design an N-length FIR filter $h[n]$ which is complex-valued. The magnitude spectrum of the discrete time Fourier transform (DTFT) of $h[n]$ must be upper and lower bounded by $1+\delta_p$ and $1-\delta_p$, respectively in the passband. In addition, the stopband magnitude spectrum must be bounded by δ_s. Finally, the phase spectrum must be equal to a pre-defined phase, say $\phi(\omega)$. If these constraint sets are closed convex sets, and happen to intersect, then one can guarantee strong convergence of the algorithm since our space is of finite dimensions. So the following represent the constraint sets.

5.2.1 The constraint set C_1

Let $C_1 = \{\mathbf{h} \in \mathbb{C}^M : h[n] = 0 \text{ for } n \notin S\}$ where S is the set of points on which the filter coefficients of length N are not equal to zero. In words, C_1 is the set of all complex-valued vectors of length M with at most N non-zero filter coefficients.

Convexity of C_1: Let $\mathbf{h}_1, \mathbf{h}_2 \in C_1$, then by the definition of convexity: $\mathbf{h}_3 = \mu\mathbf{h}_1 + (1 - \mu)\mathbf{h}_2$ where $0 \leq \mu \leq 1$. So for $n \notin S$: $h_3[n] = \mu h_1[n] + (1 - \mu)h_2[n]$ which in turn makes $h_3[n]$ equal to 0. Hence, $\mathbf{h}_3 \in C_1$ and, therefore, C_1 is convex.

Closure of C_1: To show that C_1 is a closed set, let $\{\mathbf{h}_n\}$ be a convergent sequence in C_1 where it converges to $\hat{\mathbf{h}}$. We want to show that $\hat{\mathbf{h}} \in C_1$ also. Then

$$\begin{aligned} \|\mathbf{h}_n - \hat{\mathbf{h}}\|^2 &= \sum_{i \in S} |h_n[i] - \hat{h}[i]|^2 + \sum_{i \notin S} |h_n[i] - \hat{h}[i]|^2 \\ &= \sum_{i \in S} |h_n[i] - \hat{h}[i]|^2 + \sum_{i \notin S} |\hat{h}[i]|^2 \\ &\geq \sum_{i \notin S} |\hat{h}[i]|^2. \end{aligned} \tag{5.1}$$

Now by taking the limit as $n \to \infty$, one can obtain $\sum_{i \notin S} |\hat{h_n}[i]|^2 = 0$ which is logically equivalent to saying that:

$$\hat{h}_n[i] = 0 \text{ for } i \notin S. \tag{5.2}$$

Hence, $\hat{\mathbf{h}} \in C_1$ and C_1 is therefore closed.

Projection onto C_1: Since C_1 is closed and convex, then we can derive the projection of an arbitrary vector which belongs to the Hilbert space onto C_1. According to the pure projection theorem, the projection will be unique. Let $\mathbf{x} \in \mathbb{C}^M$ be an arbitrary vector in

the Hilbert space $\mathbb{C}^M$ and let $\mathbf{x} \notin C_1$. Then for $\mathbf{x} \notin C_1$ and $\mathbf{h} \in C_1$:

$$\begin{aligned} \|\mathbf{x}-\mathbf{h}\|^2 &= \sum_{i\in S} |x[i]-h[i]|^2 + \sum_{i\notin S} |x[i]-h[i]|^2 \\ &= \sum_{i\in S} |x[i]-h[i]|^2 + \sum_{i\notin S} |x[i]|^2. \end{aligned} \tag{5.3}$$

However, $\|\mathbf{x}-\mathbf{h}\|^2$ is minimized with respect to $\mathbf{h}$ if

$$h[n] = x[n] \text{ for } n \in S. \tag{5.4}$$

Therefore, the projection onto C_1, i.e., P_{C_1}, can be given by the following relationship:

$$P_{C_1}\mathbf{x} = \begin{cases} x[n], \text{ if } n \in S \\ 0, \text{ if } n \notin S. \end{cases} \tag{5.5}$$

5.2.2 The constraint set C_2

$C_2 = \{\mathbf{h} \in \mathbb{C}^M \text{ with } h[n] \leftrightarrow H(e^{j\omega}) : \angle H(e^{j\omega}) = \phi(\omega)\}$. That is, C_2 is basically the set of all sequences which are complex-valued and whose phase response is constrained to be equal to a pre-defined phase response $\phi(\omega)$. By following the same methodology for deriving the projection onto C_2 in subsection 3.3.2, the projection onto C_2, i.e., P_{C_2} can be given by the following equation:

$$P_{C_2}\mathbf{x} \leftrightarrow \begin{cases} |X(e^{j\omega})| \cos(\theta_x - \phi(\omega)) \exp(j\phi(\omega)), \text{ if } \cos(\theta_x - \phi(\omega)) \geq 0 \\ -|X(e^{j\omega})| \cos(\theta_x - \phi(\omega)) \exp(j\phi(\omega)), \text{ if } \cos(\theta_x - \phi(\omega)) < 0. \end{cases} \tag{5.6}$$

5.2.3 The constraint sets C_3, C_4 and C_5

Define C_3 as the set of complex-valued sequences whose DTFT magnitude spectrum is lower bounded by $1-\delta_p$ in the passband, i.e., $C_3 = \{\mathbf{h} \in \mathbb{C}^M \text{ with } h[n] \leftrightarrow H(e^{j\omega}) : |H(e^{j\omega})| \geq 1-\delta_p \text{ for } \omega \in \Omega_p\}$ where Ω_p is the passband interval which is equal to $[-\omega_p, \omega_p]$, ω_p is the cut-off frequency, and δ_p is the maximum passband allowable tolerance. Also, let $C_4 = \{\mathbf{h} \in \mathbb{C}^M \text{ with } h[n] \leftrightarrow H(e^{j\omega}) : |H(e^{j\omega})| \leq 1+\delta_p \text{ for } \omega \in \Omega_p\}$.

So we can say that C_4 is the set of complex-valued sequences whose DTFT magnitude should not exceed the limit $1 + \delta_p$ in the passband.

Finally, let C_5 be the set of all sequences which are complex-valued and whose DTFT magnitude is bounded by δ_s in the stopband Ω_s where $\Omega_s = [-\pi, -\omega_s) \cap (\omega_s, \pi]$, ω_s is the stopband cut-off frequency and δ_s is the maximum allowable stopband tolerance. So, mathematically, $C_5 = \{\mathbf{h} \in \mathbb{C}^M \text{ with } h[n] \leftrightarrow H(e^{j\omega}) : |H(e^{j\omega})| \leq \delta_s \text{ for } \omega \in \Omega_s\}$.

By following the same methodology developed for the constraint set C_2, one can easily show that C_3, C_4, and C_5 are closed convex sets in $\mathbb{C}^M$. The projection P_{C_3} onto C_3 of an arbitrary vector $\mathbf{x} \in \mathbb{C}^M$, where $\mathbf{x} \notin C_3$, can be written as

$$P_{C_3}\mathbf{x} \leftrightarrow \begin{cases} X(e^{j\omega}), \text{ if } |X(e^{j\omega})| > (1-\delta_p) \text{ for } \omega \in \Omega_p \\ (1-\delta_p)\frac{X(e^{j\omega})}{|X(e^{j\omega})|}, \text{ if } |X(e^{j\omega})| \leq (1-\delta_p) \text{ for } \omega \in \Omega_p \\ X(e^{j\omega}), \text{ otherwise.} \end{cases} \tag{5.7}$$

Also, it can be shown that the projection of an arbitrary vector $\mathbf{x} \in \mathbb{C}^M$, where $\mathbf{x} \notin C_4$, is given by

$$P_{C_4}\mathbf{x} \leftrightarrow \begin{cases} X(e^{j\omega}), \text{ if } |X(e^{j\omega})| < (1+\delta_p) \text{ for } \omega \in \Omega_p \\ -(1+\delta_p)\frac{X(e^{j\omega})}{|X(e^{j\omega})|}, \text{ if } |X(e^{j\omega})| \geq (1+\delta_p) \text{ for } \omega \in \Omega_p \\ X(e^{j\omega}), \text{ otherwise.} \end{cases} \tag{5.8}$$

Finally, the projection of an arbitrary vector $\mathbf{x} \in \mathbb{C}^M$, where $\mathbf{x} \notin C_5$, can be shown to be

$$P_{C_5}\mathbf{x} \leftrightarrow \begin{cases} X(e^{j\omega}), \text{ if } |X(e^{j\omega})| < \delta_s \text{ for } \omega \in \Omega_s \\ -\delta_s\frac{X(e^{j\omega})}{|X(e^{j\omega})|}, \text{ if } |X(e^{j\omega})| \geq \delta_s \text{ for } \omega \in \Omega_s \\ X(e^{j\omega}), \text{ otherwise.} \end{cases} \tag{5.9}$$

5.3 The Pure Projection Design Algorithm for m-D Complex-Valued FIR Filters

Based on Eq. (3.8), the pure projection algorithm for designing 1-D complex-valued FIR digital filters is given by

$$\mathbf{h}_{k+1} = P_{C_1} P_{C_2} P_{C_3} P_{C_4} P_{C_5} \mathbf{h}_k \tag{5.10}$$

where P_{C_1}, P_{C_2}, P_{C_3}, P_{C_4}, and P_{C_5} are given in Eqs. (5.5), (5.6), (5.7), (5.8), and (5.9), respectively, and $\mathbf{h}_0$ is an arbitrary complex-valued vector of dimension M. Now, as mentioned earlier, one of the main advantages of using pure projection to design FIR digital filters is the simplicity of extending the 1-D design algorithm to multi-dimensions. Hence, we are interested in extending the 1-D complex-valued FIR filters design algorithm to m-D, as demonstrated below:

1. Project $\mathbf{h}_k$ onto C_5, that is

$$\mathbf{g}_{1,k} = P_{C_5}\mathbf{h}_k \leftrightarrow \begin{cases} H_k(e^{j\mathbf{\Omega}}), \text{ if } |H_k(e^{j\mathbf{\Omega}})| < \delta_s \text{ for } \mathbf{\Omega} \in \mathbf{\Omega}_s \\ -\delta_s \frac{H_k(e^{j\mathbf{\Omega}})}{|H_k(e^{j\mathbf{\Omega}})|}, \text{ if } |H_k(e^{j\mathbf{\Omega}})| \geq \delta_s \text{ for } \mathbf{\Omega} \in \mathbf{\Omega}_s \\ H_k(e^{j\mathbf{\Omega}}), \text{ otherwise.} \end{cases} \tag{5.11}$$

2. Project $\mathbf{g}_{1,k}$ onto C_4 using

$$\mathbf{g}_{2,k} = P_{C_4}\mathbf{g}_{1,k} \leftrightarrow \begin{cases} G_{1,k}(e^{j\mathbf{\Omega}}), \text{ if } |G_{1,k}(e^{j\mathbf{\Omega}})| < (1+\delta_p) \text{ for } \mathbf{\Omega} \in \mathbf{\Omega}_p \\ -(1+\delta_p)\frac{G_{1,k}(e^{j\mathbf{\Omega}})}{|G_{1,k}(e^{j\mathbf{\Omega}})|}, \text{ if } |G_{1,k}(e^{j\mathbf{\Omega}})| \geq (1+\delta_p) \text{ for } \mathbf{\Omega} \in \mathbf{\Omega}_p \\ G_{1,k}(e^{j\mathbf{\Omega}}), \text{ otherwise.} \end{cases} \tag{5.12}$$

3. Project $\mathbf{g}_{2,k}$ onto C_3 using

$$\mathbf{g}_{3,k} = P_{C_3}\mathbf{g}_{2,k} \leftrightarrow \begin{cases} G_{2,k}(e^{j\mathbf{\Omega}}), \text{ if } |G_{2,k}(e^{j\mathbf{\Omega}})| > (1-\delta_p) \text{ for } \mathbf{\Omega} \in \mathbf{\Omega}_p \\ (1-\delta_p)\frac{G_{2,k}(e^{j\mathbf{\Omega}})}{|G_{2,k}(e^{j\mathbf{\Omega}})|}, \text{ if } |G_{2,k}(e^{j\mathbf{\Omega}})| \leq (1-\delta_p) \text{ for } \mathbf{\Omega} \in \mathbf{\Omega}_p \\ G_{2,k}(e^{j\mathbf{\Omega}}), \text{ otherwise.} \end{cases} \tag{5.13}$$

4. Project $\mathbf{g}_{3,k}$ onto C_2 using

$$\mathbf{g}_{4,k} = P_{C_2}\mathbf{g}_{3,k} \leftrightarrow \begin{cases} |G_{3,k}(e^{j\mathbf{\Omega}})| \cos\left(\theta_{G_{3,k}} - \phi(\mathbf{\Omega})\right) \exp(j\phi(\mathbf{\Omega})) \\ \text{if } \cos\left(\theta_{G_{3,k}} - \phi(\mathbf{\Omega})\right) \geq 0 \\ -|G_{3,k}(e^{j\mathbf{\Omega}})| \cos\left(\theta_{G_{3,k}} - \phi(\mathbf{\Omega})\right) \exp(j\phi(\mathbf{\Omega})) \\ \text{if } \cos\left(\theta_{G_{3,k}} - \phi(\mathbf{\Omega})\right) < 0. \end{cases} \tag{5.14}$$

5. Finally, project $\mathbf{g}_{4,k}$ onto C_1 by

$$\mathbf{h}_{k+1} = P_{C_1}\mathbf{g}_{4,k} = \begin{cases} \mathbf{g}_{4,k}[\mathbf{n}], \text{ for } \mathbf{n} \in \mathbf{S} \\ 0, \text{ otherwise} \end{cases} \tag{5.15}$$

where $\mathbf{\Omega} = (\omega_1, \omega_2, \cdots, \omega_m)$ and $\boldsymbol{n} = (n_1, n_2, \cdots, n_m)$, $\mathbf{S}$ is the m-D finite extent support, $\mathbf{\Omega}_p$ is m-D passband region, and $\mathbf{\Omega}_s$ is m-D stopband region. We are going to use the same stopping criterion reported in [22]. That is, if the error distance is less than or equal to a pre-defined threshold ϵ, i.e., if $\|\mathbf{h}_{k+1} - \mathbf{h}_k\| \leq \epsilon$, then stop the algorithm. Otherwise, repeat steps 1-5.

5.4 Simulation Results

Using the pure projection algorithm given in section 5.3, several examples of 1-D and 2-D complex-valued FIR digital filter design will be illustrated. Recall that M is the dimension of the proper Hilbert space, N is the filter length, δ_p and δ_s are respectively the maximum allowable passband and stopband tolerances (see Figure 5.1), and ϵ is the algorithm stopping threshold. Note that all the simulations are preformed in MATLAB which is installed on a Pentium 4 machine with a processor speed of 2.6 GHz and a RAM of 1GB. Finally, the designed filters are displayed with respect to their normalized angular frequencies.

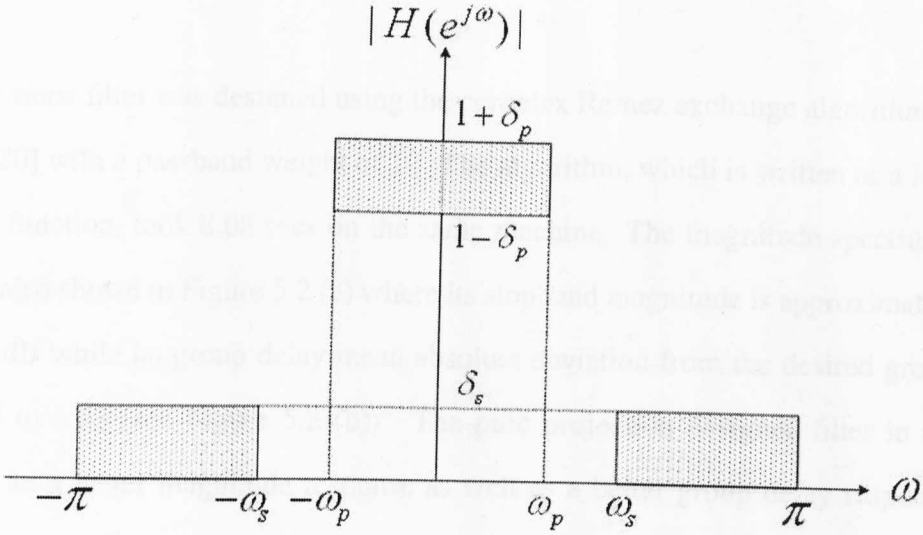

Figure 5.1: Low-pass filter design specifications.

5.4.1 Low Delay Single Passband Filters

Low delay single passband FIR filters are used in many areas of application such as communications [45]. Here, we illustrate the design of two low delay single passband FIR filters: 1-D and 2-D filters designed using pure projection.

5.4.1.1 1-D Low Delay Single Passband Filters

An example of a desired low delay filter can be given by:

$$H_d(e^{j\omega}) = \begin{cases} e^{-j12\omega}, & \text{if } -0.1\pi \leq \omega \leq 0.3\pi \\ 0, & \text{if } -\pi \leq \omega \leq -0.2\pi \ \& \ 0.4\pi \leq \omega \leq \pi \end{cases} \tag{5.16}$$

where $\delta_p = 0.00025$, $\delta_s = 0.025$, $N = 31$, $M = 310$, and with a stopping threshold equal to $\epsilon = 10^{-5}$. In Figure 5.2 (a), the designed magnitude response of the filter shows an approximate equiripple response with a maximum stopband magnitude of -29 dB. The group delay is shown in Figure 5.2 (b) where it corresponds to almost linear-phase characteristics in the passband with a mean absolute deviation from the desired group delay of 4.3993×10^{-2}. The design required 129 iterations to converge (see Figure 5.2 (c)) within

0.54 secs.

The same filter was designed using the complex Remez exchange algorithm reported in [19, 20] with a passband weight of 10. The algorithm, which is written as a MATLAB built-in function, took 8.08 secs on the same machine. The magnitude spectrum of this filter is also shown in Figure 5.2 (a) where its stopband magnitude is approximately equal to -23 dB while its group delay mean absolute deviation from the desired group delay is equal to 5.28 (see Figure 5.2 (b)). The pure projection designed filter in this case resulted in a better magnitude response as well as a better group delay response when compared with those obtained using the complex Remez method. Also, in this case, the pure projection design algorithm required less design running time (saved 93.81% of the design running time) when compared to the complex Remez low delay single passband designed filter.

5.4.1.2 2-D Low Delay Shifted Circularly Symmetric Filters

An example of a 2-D complex-valued FIR low delay filter is designed based on a passband and a stopband circular region. The circular region is centred on $(-0.1\pi, 0.1\pi)$ with a passband radius of 0.3π and a stopband radius of 0.5π. The filter parameters are as follows: $\delta_p = \delta_s = 25 \times 10^{-3}$, for a 19×19 filter, $M = 190 \times 190$, and with a delay of 9 samples. The design took 372 iterations to converge with respect to the distance error threshold $\epsilon = 5 \times 10^{-5}$. Figure 5.3 shows a circularly symmetrical magnitude response of the designed filter (with a maximum stopband magnitude of approximately -32 dB), where it satisfies its required design specifications.

5.4.2 Seismic Migration Filters

Although chapters 3 and 4 presented the design algorithms for designing respectively 1-D and 2-D seismic migration FIR filters using the pure, relaxed and the modified projection algorithms, we show here that the algorithm in section 5.3 is more general where it will include such type of complex-valued FIR filters. We illustrate here two migration filters,

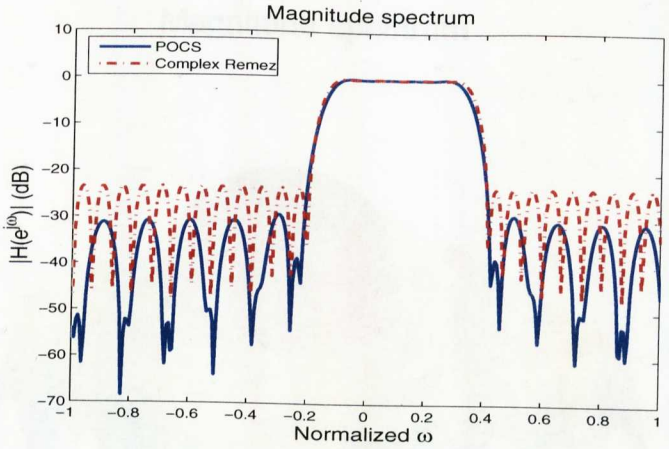

(a)

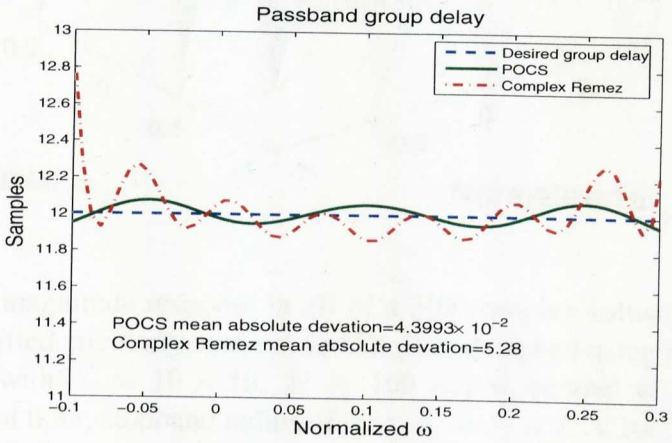

(b)

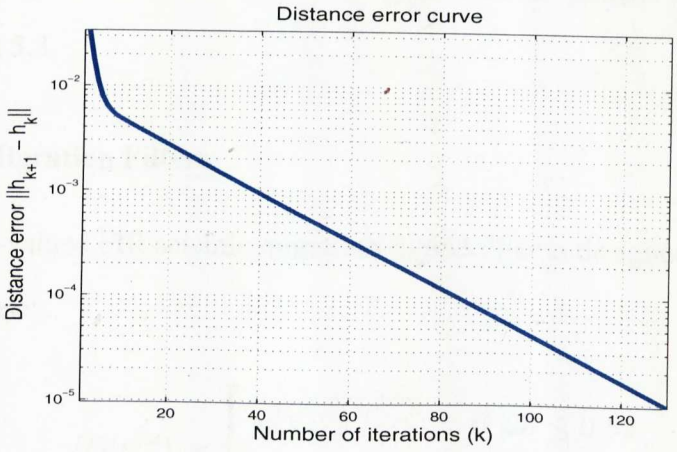

(c)

Figure 5.2: A 1-D complex-valued low delay FIR low-pass filter (see section 5.4.1.1) with $N = 31$, $M = 310$, $\omega_{p_1} = -0.1\pi$, $\omega_{p_2} = 0.3\pi$, $\omega_{s_1} = -0.2\pi$, $\omega_{s_2} = 0.4\pi$ $\delta_p = 0.00025$, $\delta_s = 0.025$, and $\epsilon = 10^{-5}$: (a) magnitude response in dB (pure projection: solid line and Complex Remez: dash-dot line), (b) passband group delay (pure projection (POCS): solid line, Complex Remez: dash-dot line and the Desired Group Delay: dash line), and (c) convergence of the 1-D complex-valued low delay FIR low-pass filter design using pure projection distance error curve.

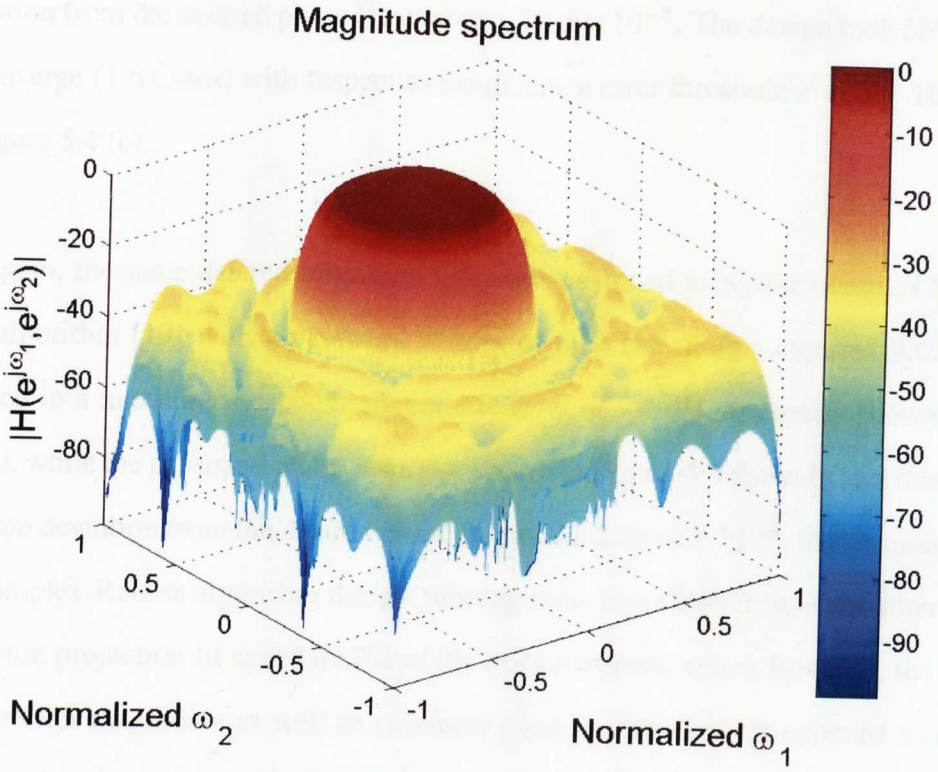

Figure 5.3: The magnitude response in dB of a 2-D complex-valued low delay (a delay of 9 samples) shifted circularly symmetric FIR filter designed using pure projection (see section 5.4.1.2) with $N = 19 \times 19$, $M = 190 \times 190$, centred at $(-0.1\pi, 0.1\pi)$ with passband radius of 0.3π, stopband radius of 0.5π, $\delta_p = \delta_s = 25 \times 10^{-3}$, and $\epsilon = 5 \times 10^{-5}$.

1-D and 2-D complex-valued FIR filters designed with the general m-D pure projection given in section 5.3.

5.4.2.1 1-D Migration Filters

A 1-D complex-valued FIR seismic migration digital filter is designed with the following designed response:

$$H_d(e^{j\omega}) = \begin{cases} e^{j\sqrt{(0.5\pi)^2-\omega^2}}, & \text{if } |\omega| \leq 0.5\pi \\ 0, & \text{if } 0.6\pi \leq |\omega| \leq \pi \end{cases} \tag{5.17}$$

The filter parameters are as follows: $\delta_p = 10^{-3}$, $\delta_s = 0.0025$, $N = 35$, and $M = 350$. Figure 5.4 (a) shows the magnitude response of the designed filter where it has an equiripple response and with a maximum stopband magnitude of -38 dB. Also, Figure 5.4 (b) shows the phase spectrum in the passband for the designed filter where the mean absolute

deviation from the desired phase is equal to 1.7838×10^{-3}. The design took 599 iterations to converge (1.64 secs) with respect to the distance error threshold $\epsilon = 5 \times 10^{-5}$ as seen in Figure 5.4 (c).

Again, the same desired migration filter was designed using the complex Remez design algorithm [19] with a passband weight of 60. The design required 0.62 secs and resulted in a maximum stopband magnitude level of -8 dB, as clearly shown in Figure 5.4 (a), while the passband phase response shown in Figure 5.4 (b) indicates that the mean absolute deviation from the desired phase is equal to 2.9313×10^{-3}. In this case, although the complex Remez algorithm design running time was smaller than the filter designed with pure projection (it saved 62.2% of the design running time), however, the pure projection filter magnitude as well as passband phase response show superior results when compared to those obtained with the complex Remez algorithm.

5.4.2.2 2-D Migration Filters

An example of a 2-D complex-valued FIR seismic migration digital filter is designed based on:

$$H_d(e^{j\omega_1}, e^{j\omega_2}) = \begin{cases} e^{j\sqrt{(0.5\pi)^2-(\omega_1^2+\omega_2^2)}}, & \text{if } \sqrt{\omega_1^2+\omega_2^2} \leq 0.5\pi \\ 0, & \text{if } 0.7\pi \leq \sqrt{\omega_1^2+\omega_2^2} \leq \pi. \end{cases} \tag{5.18}$$

The filter parameters are as follows: $\delta_p = \delta_s = 10^{-3}$, for a 25×25 filter, and $M = 250 \times 250$. The design took 547 iterations to converge with respect to the distance error threshold $\epsilon = 5 \times 10^{-5}$. Figure 5.5 (a) shows a circularly symmetric magnitude response of the designed filter where the maximum stopband magnitude is approximately equal to -50 dB. On the other hand, Figure 5.5 (b) shows the phase spectrum in the passband for the designed filter, which again has circular symmetry.

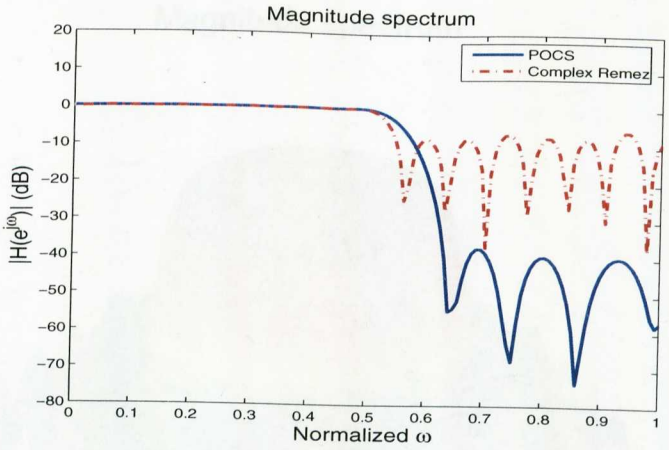

(a)

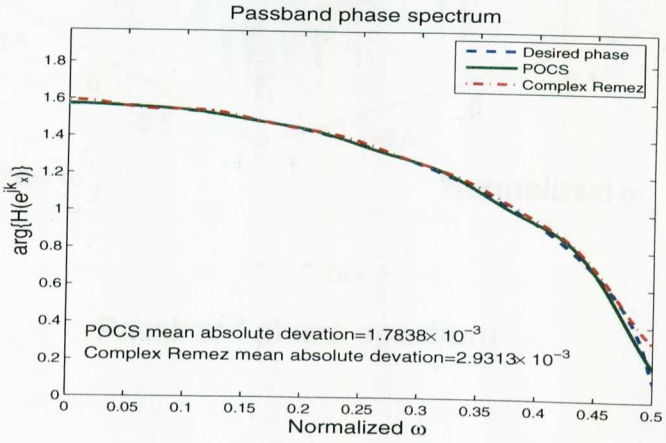

(b)

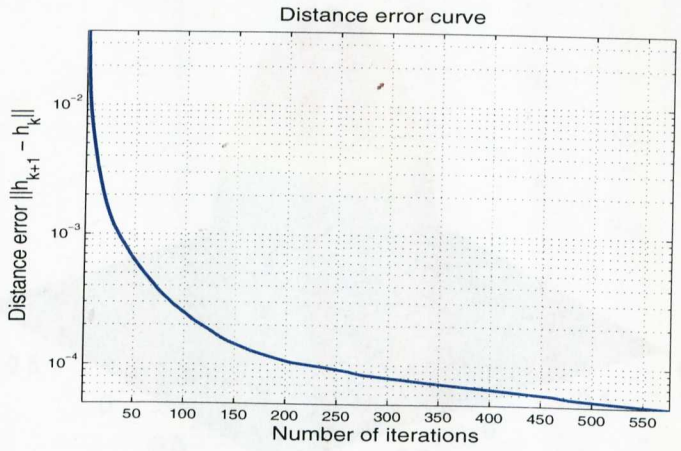

(c)

Figure 5.4: A 1-D complex-valued seismic migration FIR filter (see section 5.4.2.1) with $N = 35$, $M = 350$, $\omega_p = 0.5\pi$, $\omega_s = 0.6\pi$, $\delta_p = 10^{-3}$, $\delta_s = 0.0025$, and $\epsilon = 5 \times 10^{-5}$: (a) its magnitude response in dB (pure projection: solid line and Complex Remez: dash-dot line), (b) its passband phase response (pure projection (POCS): solid line, Complex Remez: dash-dot line and the Desired Passband Phase Response: dash line), and (c) convergence of the 1-D complex-valued seismic migration FIR filter design using pure projection distance error curve.

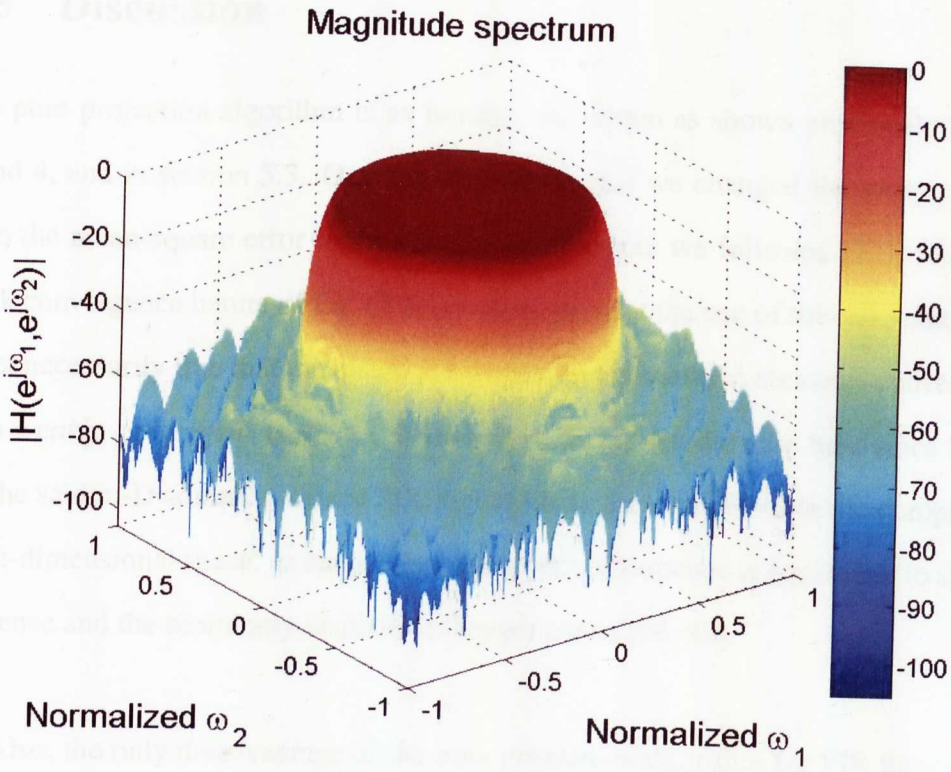

(a)

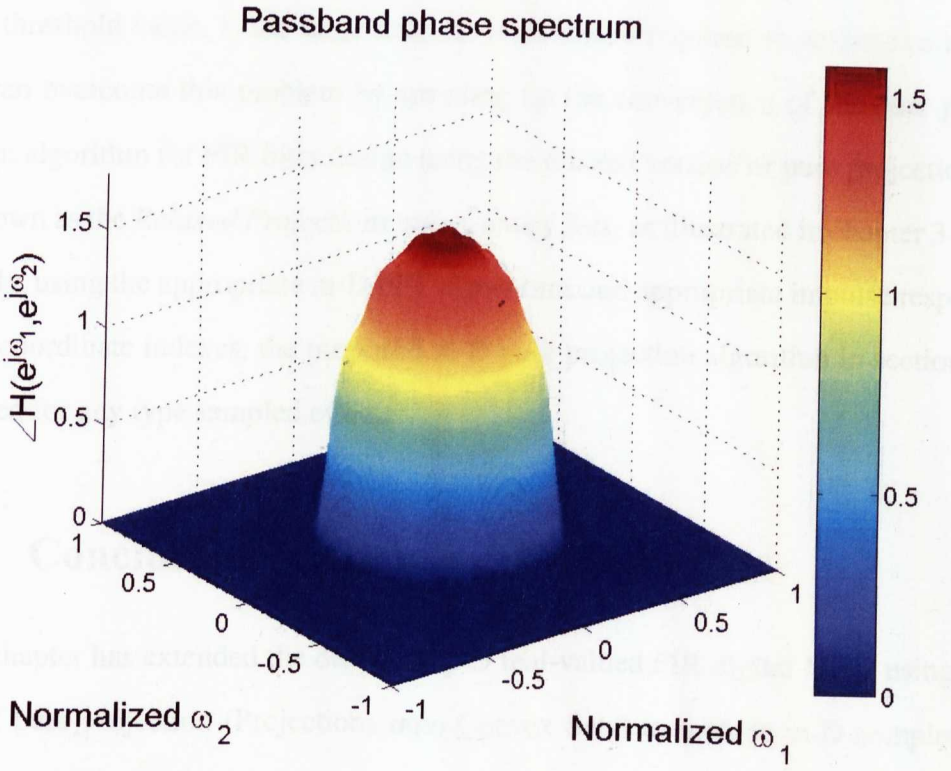

(b)

Figure 5.5: The (a) magnitude response in dB and (b) the passband phase response of a 2-D complex-valued seismic migration FIR filter designed using pure projection with $N = 25 \times 25$, $M = 250 \times 250$, with passband radius of 0.5π, stopband radius of 0.7π, $\delta_p = \delta_s = 10^{-3}$, and $\epsilon = 5 \times 10^{-5}$ (see section 5.4.2.2).

5.5 Discussion

The pure projection algorithm is an iterative algorithm as shown previously in chapters 3 and 4, and in section 5.3. One can also notice that we changed the stopping criterion from the mean-square error to the distance error where we followed [22]. However, the weak convergence nature of Eq. (3.8) seems to prevent the use of this criterion because it is not necessarily true that the distance between two successive elements converge to zero for a *weakly convergent sequence.* Fortunately, this is not the case here since the VSPM for the said m-D complex-valued FIR digital filters are carried out in the complex-valued finite-dimensional space. In such cases, the weak convergence is equivalent to strong convergence and the seemingly obstacle no longer exists [96, 89].

Also, the only disadvantage of the pure projection algorithm for FIR filter design (in the opinion of some filter designers), and depending upon the filter parameters and stopping threshold value, is the large number of iterations required to achieve convergence. We can overcome this problem by speeding up the convergence of the pure projection design algorithm for FIR filter design using the relaxed version of pure projection, which is known as the *Relaxed Projections onto Convex Sets*, as illustrated in chapter 3 and [89]. Finally, using the appropriate m-D FFT algorithms and appropriate impulse response FIR filter coordinate indexes, the proposed m-D pure projection algorithm in section 5.3 can be used for any type sampled of data.

5.6 Conclusion

This chapter has extended the design of 1-D real-valued FIR digital filters using the theory of pure projection (Projections onto Convex Sets) to include m-D complex-valued FIR digital filters. So this newly derived pure projection algorithm for m-D complex-valued FIR filters is more general and can also accommodate m-D real-valued filters. It is also more general in the sense that it includes the migration FIR filters that were previously presented in chapters 3 and 4, respectively. Empirically, the resultant filters possess

an approximate equiripple behavior. For various examples, the simulation results have displayed superior filter designs when using pure projection, when compared with the complex Remez filter design method reported previously in [19, 20].

Chapter 6

Realization of 2-D Migration FIR Digital Filters for 3-D Seismic Volumes Via Singular Value Decomposition

6.1 Introduction

Athough it is considered to be the most expensive seismic data processing step [1], migration is one of the most important processing steps in seismic data processing. Migration filters are used to reposition the seismic energy at the true reflection points and, hence, true geological structures appearing in seismic data are accurately revealed [1, 5, 75].

The frequency-space (or frequency-inline-crossline) ($\omega - x - y$) migration method is considered to be one of the most attractive techniques for performing 3-D seismic migration [1, 13, 12, 14, 10]. The most important feature of such a migration technique is that it can be used for migration of one-way wavefields accurately through heterogeneous media. They also result in stable migration images due to new improvements in the design of these filters as we saw in previous chapters.

To show how much does the $\omega - x - y$ migration method costs, let us consider the following. Recall from chapter 4 that the $\omega - x - y$ migration of a spatially-sampled seismic wavefield $u(x_i, y_j, e^{j\omega_l}, z_k)$ from depth say z_k to $z_{k+1} = z_k + \Delta z$ is performed independently for each frequency ω_l, by a direct 2-D spatial convolution with a designed 2-D migration filter impulse response $h[n_1, n_2]$ using [1, 13, 12, 14]:

$$u(x_i, y_j, e^{j\omega_l}, z_{k+1}) = \sum_{n_1=(-N+1)/2}^{(N-1)/2} \sum_{n_2=(-N+1)/2}^{(N-1)/2} h[n_1, n_2] u(x_{i-n_1}, y_{j-n_2}, e^{j\omega_l}, z_k) \quad (6.1)$$

where $h[n_1, n_2]$ is a non-causal quadrantally symmetrical $N \times N$ (N odd) complex-valued 2-D impulse response, i.e.,

$$h[n_1, n_2] = h[-n_1, n_2] = h[n_1, -n_2] = h[-n_1, -n_2]. \quad (6.2)$$

In this case, the migration (filtering) process is carried over all frequencies ω_l, where $l = 0, \cdots, M-1$ and M, in this case, is the number of frequency samples. A typical $\omega - x - y$ migration process for seismic signals requires a set of 2-D frequency-velocity dependent FIR filters that are designed and stored to migrate the seismic section from one depth level $u(x_i, y_j, e^{j\omega_l}, z_k)$ to the next $u(x_i, y_j, e^{j\omega_l}, z_{k+1})$. Let us assume that the number of samples in both spatial directions (say n_x and n_y) are equal to each other ($n_x = n_y = n_s$). Then for each frequency sample we require n_s^2 convolutions since the convolution migration is performed at each spatial sample location. If we have, for example, 1000 frequency samples, then this results in performing $1000 \times n_s^2$ 2-D convolution processes to get only one depth slice of the final 3-D migrated volume (wavefield). So if one needs 500 depth slices, $500,000 \times n_s^2$ 2-D convolutions are required. Using direct convolution of these 2-D complex-valued $N \times N$ impulse responses, the computational complexity will be $500,000 \times n_s^2 \times N^2$, where $N \times N$ is the FIR filter size in the spatial direction n_1 and n_2. In this application, even by taking advantage of the quadrantally symmetric property of such 2-D impulse responses, the computational complexity will still be high [104, 1, 42, 44].

As shown in chapter 4, different approaches have been proposed to mitigate such expensive 3-D migration processes which rely heavily on direct convolution of 2-D complex-valued FIR filter impulse responses [9]. Most of the present one-dimensional (1-D) migration FIR filter (and filter operators in general) design algorithms cannot be extended to the 2-D case such as the Remez algorithm [19, 21]. Hence, for both reasons, researchers were using approximations of 2-D migration FIR filters based on pre-designed 1-D migration FIR filters which of course comes with a price, i.e., errors in both magnitude response as well as phase response [11].

The first approach (known in the geophysics literature as splitting) is where the migration is performed by splitting the process to alternatively migrate along the in-line and cross-line directions, independently [1, 11], i.e., assuming that the 2-D migration FIR filters are separable. This method is cheap in the sense that its computational complexity is proportional to the used FIR filter length N and is based on the 2-D Fourier transform approximation of the desired migration wavenumber response. It also results in stable migration images. However, this method results in large errors for wavenumber cut-off's in which $k_x \approx k_y \gg 0$. This corresponds to steep dipping at 45° azimuth between the in-line and cross-line directions [11].

The second approach is based on the popular McClellan transformations [37, 38, 10, 11, 39, 40, 6]. This method is based on Chebyshev structures and is very suitable for 2-D FIR filters with a quadrantal symmetry property, like our migration filters. Their cost is proportional to the filter length N, and 1-D filters are needed to obtain the 2-D impulse response, based on a transformation filter as reported in [11]. The transformation results in stable migration images and is best for small wavenumbers - it is exact for $k_x = k_y = 0$ - but exhibits increasing error with increasing wavenumbers where $k_x \approx k_y$. An improved McClellan transformation filter was proposed by Hale in [11] to overcome such wavenumber response errors where the transformation filter (matrix) is larger than the original one (see for example [38, 6]), such that it results in a better approximation

of the circular symmetry property of the 2-D migration wavenumber response. The computational complexity of this improved McClellan transformation filter is higher than the previous McClellan transformation, but it is still proportional to N [11]. None of these transformations yield, however, exactly circularly symmetric migration wavenumber responses.

Thus, there is a need for migrating 3-D seismic data sets with true 2-D migration FIR filters that are cheap to implement, result in stable migrated images, and better approximate circular symmetry with respect to their wavenumber responses. In other words, we want to reduce the cost of the 3-D $\omega - x - y$ migration but, at the same time, we want to obtain accurate migrated volumes in order to allow correct interpretation for such geological maps.

Digital FIR filter realization techniques based on Singular Value Decomposition (SVD) have been proposed for the realization (implementation) of 2-D zero-phase FIR digital filters [105, 106] and, more recently, for 2-D linear-phase FIR digital filters [41]. In both papers, 2-D FIR filters were pre-designed and then realized using the SVD technique for general FIR filters, including symmetrical and anti-symmetrical ones. The SVD realization structure has the following advantages:

- It is suitable for parallel processing such as the case for $\omega - x - y$ migration.
- It is flexible in the sense that we can select the number of realization parallel sections that correspond to the most significant singular values. Hence, this results in a saving in computational complexity at the expense of introducing small errors in the wavenumber response.
- Depending on the number of parallel sections used in the realization, its computational complexity is proportional to the filter's impulse response length N.

Here, in this chapter, we propose implementing pre-designed true 2-D migration FIR digital filters using the method of Singular Value Decomposition (SVD). Such a technique

is very suitable for the $\omega - x - y$ migration method. It is cheap to implement, results in stable migrated volumes, and better approximates circular symmetry with respect to their wavenumber responses when compared to other standard implementations [42, 43, 44].

This chapter is organized as follows. Section 6.2 introduces the concept of SVD realization for 2-D FIR digital filters. Also, the mathematical development for realizing 2-D quadrantally symmetrical complex-valued FIR seismic migration digital filters using SVD is presented. An error analysis, relating to the SVD realization of migration filters, is given in section 6.3. In section 6.4, simulation results are performed to evaluate the accuracy of the 2-D seismic migration FIR filters realized using the proposed SVD scheme. We also show an application of our proposed method to synthetic seismic data. A brief discussion is given in section 6.5. Finally, we conclude this chapter in section 6.6.

6.2 Singular Value Decomposition Realization for the 2-D Migration FIR Impulse Response

Let $h[n_1, n_1]$ be an already designed $N \times N$ quadrantally symmetrical 2-D seismic migration FIR impulse response where $h[n_1, n_1] \in \mathbb{C}^{N \times N}$ for $n_1, n_2 = -(N-1)/2, \cdots, (N-1)/2$ and N is an odd number. Define $\mathbf{A}$ to be an $N \times N$ matrix whose elements represent the quadrantally symmetrical 2-D seismic migration FIR impulse response given by:

$$\mathbf{A} = \{h[n_1, n_1]\}, \text{ for } |n_1, n_2| \leq (N-1)/2. \tag{6.3}$$

6.2.1 Singular Value Decomposition & FIR Filters Realization

In general, the SVD of $\mathbf{A}$ can be written as

$$\mathbf{A} = \mathbf{U}\Sigma\mathbf{V}^* \tag{6.4}$$

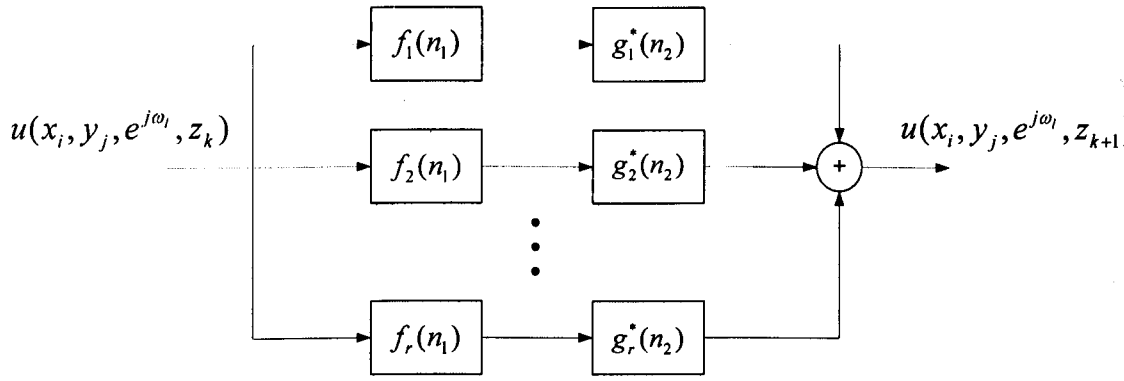

Figure 6.1: SVD based realization structure for a pre-designed 2-D complex-valued migration FIR digital filter. Each branch represents a 2-D sub-filter of which is composed of two cascaded 1-D FIR digital filters.

where $\mathbf{U}$ and $\mathbf{V}$ are unitary matrices, $*$ denotes the complex conjugate transpose, and Σ is a diagonal matrix whose diagonal elements represent the singular values of $\mathbf{A}$, i.e.,

$$\Sigma = \text{diag}(\sigma_1, \sigma_2, \cdots, \sigma_N) \tag{6.5}$$

and $\sigma_1 \geq \sigma_2 \geq \cdots \geq \sigma_N \geq 0$ [107]. Let the rank of $\mathbf{A}$ be $r \leq N$. Hence, $\sigma_{r+1} = \sigma_{r+2} = \cdots = \sigma_N = 0$ and Eq. (6.4) can be rewritten as:

$$\mathbf{A} = \sum_{k=1}^{r} \sigma_k \mathbf{u}_k \mathbf{v}_k^* = \sum_{k=1}^{r} \mathbf{f}_k \mathbf{g}_k^* \tag{6.6}$$

where $\mathbf{u}_k$ and $\mathbf{v}_k$ represent the kth column vectors of $\mathbf{U}$ and $\mathbf{V}$, respectively, and $\mathbf{f}_k = \sqrt{\sigma_k}\mathbf{u}_k$ and $\mathbf{g}_k = \sqrt{\sigma_k}\mathbf{v}_k$. Equation (6.6) suggests that a 2-D complex-valued FIR digital filter can be realized using r parallel 2-D sub-filters where each 2-D sub-filter is composed of a cascade of two N-length 1-D complex-valued FIR digital filters. These 1-D filters have impulse responses given by $f_k(n_1)$ and $g_k(n_2)$. Figure 6.1 demonstrates the SVD based realization structure for the (migration) filtering process where the implementation complexity depends on the value of rank r. The rank r is always equal to $(N+1)/2$ in the case of quadrantally symmetrical impulse responses.

6.2.2 Singular Value Decomposition Realization of Migration FIR Filters

For the analysis given below, we will follow [41]. Define $\mathbf{J}$ to be an $(N-1)/2 \times (N-1)/2$ contra-identity matrix where the contra-diagonal elements are equal to 1 and the remaining elements are zeros (N is an odd positive integer). That is:

$$\mathbf{J} = \begin{bmatrix} 0 & & & & 1 \\ & & & \cdot & \\ & & \cdot & & \\ & \cdot & & & \\ 1 & & & & 0 \end{bmatrix}. \tag{6.7}$$

Since $\mathbf{A} \in \mathbb{C}^{N \times N}$ possesses quadrantal symmetry, then $\mathbf{A}$ can be written as:

$$\mathbf{A} = \begin{bmatrix} \mathbf{A}_1 & \mathbf{a}_1 & \mathbf{A}_1\mathbf{J} \\ \mathbf{a}_2^* & c & \mathbf{a}_2^*\mathbf{J} \\ \mathbf{J}\mathbf{A}_1 & \mathbf{J}\mathbf{a}_1 & \mathbf{J}\mathbf{A}_1\mathbf{J} \end{bmatrix} \tag{6.8}$$

where $\mathbf{A}_1$ is an $(N-1)/2 \times (N-1)/2$ matrix, $\mathbf{a}_1$ and $\mathbf{a}_2$ are $(N-1)/2$-dimensional column vectors, and c is a complex scalar. The matrix $\mathbf{Q} \in \mathbb{C}^{N \times N}$ given by:

$$\mathbf{Q} = \frac{1}{2} \begin{bmatrix} \mathbf{I} + j\mathbf{I} & \mathbf{0} & \mathbf{J} + j\mathbf{J} \\ \mathbf{0} & \sqrt{2} + j\sqrt{2} & \mathbf{0} \\ \mathbf{I} + j\mathbf{I} & \mathbf{0} & -\mathbf{J} + j\mathbf{J} \end{bmatrix} \tag{6.9}$$

is a unitary matrix where $j = \sqrt{-1}$, $\mathbf{I}$ is the identity matrix with the same dimension as $\mathbf{J}$, and $\mathbf{0}$ is a row/column vector of dimension $(N-1)/2$. A unitary matrix $\mathbf{B} \in \mathbb{C}^{N \times N}$

exists, which is mathematically similar to $\mathbf{A}$ and is given by:

$$\begin{aligned}
\mathbf{B} &= \mathbf{Q}\mathbf{A}\mathbf{Q}^* && (6.10)\\
&= \begin{bmatrix} \mathbf{A}_1 + \mathbf{J}\mathbf{A}_1\mathbf{J} & \frac{\sqrt{2}}{2}\mathbf{a}_1 + \frac{\sqrt{2}}{2}\mathbf{J}\mathbf{a}_1 & \mathbf{0} \\ \sqrt{2}\mathbf{a}_2^* & 2c & \mathbf{0} \\ \mathbf{0} & \mathbf{0} & \mathbf{0} \end{bmatrix} && (6.11)\\
&= \begin{bmatrix} \mathbf{B}_1 & \mathbf{0} \\ \mathbf{0} & \mathbf{0} \end{bmatrix} && (6.12)
\end{aligned}$$

where $\mathbf{B}_1$ is an $(N+1)/2 \times (N+1)/2$ matrix. Note that $\mathbf{A}^*\mathbf{A}$ is also unitary and similar to $\mathbf{B}^*\mathbf{B}$ with respect to $\mathbf{Q}$. This implies that $\mathbf{A}^*\mathbf{A}$ and $\mathbf{B}^*\mathbf{B}$ both have the same eigenvalues and, consequently, the same singular values, i.e., the matrices $\mathbf{A}$ and $\mathbf{B}$ are unitarily equivalent [107]. Now, let the SVD of $\mathbf{B}$ be given by:

$$\mathbf{B} = \mathbf{U}_\mathbf{B}\mathbf{\Sigma}_\mathbf{B}\mathbf{V}_\mathbf{B}^* \tag{6.13}$$

where $\mathbf{U}_\mathbf{B}$ and $\mathbf{V}_\mathbf{B}$ are unitary and $\mathbf{\Sigma}_\mathbf{B}$ is a diagonal matrix with singular values in decreasing order. From Eq. (6.12), we can rewrite Eq. (6.13) as:

$$\mathbf{B} = \begin{bmatrix} \mathbf{U}_1 & \mathbf{0} \\ \mathbf{0} & \mathbf{0} \end{bmatrix} \begin{bmatrix} \mathbf{\Sigma}_1 & \mathbf{0} \\ \mathbf{0} & \mathbf{0} \end{bmatrix} \begin{bmatrix} \mathbf{V}_1 & \mathbf{0} \\ \mathbf{0} & \mathbf{0} \end{bmatrix}^* \tag{6.14}$$

and this implies that we can determine the SVD of $\mathbf{B}$, by only computing the SVD of

$$\begin{aligned}
\mathbf{B}_1 &= \mathbf{U}_1\mathbf{\Sigma}_1\mathbf{V}_1^* && (6.15)\\
&= \begin{bmatrix} \mathbf{U}_{11} & \mathbf{b}_1 \\ \mathbf{b}_2^* & U_0 \end{bmatrix} \begin{bmatrix} \mathbf{\Sigma}_{11} & \mathbf{0} \\ \mathbf{0} & \Sigma_0 \end{bmatrix} \begin{bmatrix} \mathbf{V}_{11} & \mathbf{c}_1 \\ \mathbf{c}_2^* & V_0 \end{bmatrix}^* . && (6.16)
\end{aligned}$$

Thus, $\mathbf{A}$ can be expressed as:

$$\begin{aligned} \mathbf{A} &= \mathbf{Q}^*\mathbf{B}\mathbf{Q} && (6.17)\\ &= \mathbf{Q}^*\mathbf{U_B}\mathbf{\Sigma_B}\mathbf{V_B^*}\mathbf{Q} && (6.18)\\ &= \hat{\mathbf{U}}\mathbf{\Sigma_B}\hat{\mathbf{V}}^* && (6.19) \end{aligned}$$

where

$$\begin{aligned} \hat{\mathbf{U}} &= \mathbf{Q}^*\mathbf{U_B} && (6.20)\\ &= \frac{1}{2}\begin{bmatrix} (\mathbf{I}-j\mathbf{I})\mathbf{U}_{11} & (\mathbf{I}-j\mathbf{I})\mathbf{b}_1 & \mathbf{0} \\ (\sqrt{2}-j\sqrt{2})\mathbf{b}_2^* & (\sqrt{2}-j\sqrt{2})U_0 & \mathbf{0} \\ (\mathbf{J}-j\mathbf{J})\mathbf{U}_{11} & (\mathbf{J}-j\mathbf{J})\mathbf{b}_1 & \mathbf{0} \end{bmatrix} && (6.21) \end{aligned}$$

and

$$\begin{aligned} \hat{\mathbf{V}} &= \mathbf{Q}^*\mathbf{V_B} && (6.22)\\ &= \frac{1}{2}\begin{bmatrix} (\mathbf{I}-j\mathbf{I})\mathbf{V}_{11} & (\mathbf{I}-j\mathbf{I})\mathbf{c}_1 & \mathbf{0} \\ (\sqrt{2}-j\sqrt{2})\mathbf{c}_2^* & (\sqrt{2}-j\sqrt{2})V_0 & \mathbf{0} \\ (\mathbf{J}-j\mathbf{J})\mathbf{V}_{11} & (\mathbf{J}-j\mathbf{J})\mathbf{c}_1 & \mathbf{0} \end{bmatrix}. && (6.23) \end{aligned}$$

As expected, only the first $(N+1)/2$ columns of both Eq. (6.21) and Eq. (6.23) are nonzero and they are symmetric. Since both $\hat{\mathbf{U}}$ and $\hat{\mathbf{V}}$ are unitary and both $\mathbf{A}$ and $\mathbf{B}$ have identical singular values, Eq. (6.19) gives a SVD of $\mathbf{A}$. In other words, the SVD of $\mathbf{A}$ can be represented based on Eq. (6.19), where the $\mathbf{u}_k$'s and $\mathbf{v}_k$'s in Eq. (6.6) are replaced respectively with the first $(N+1)/2$ columns of $\hat{\mathbf{U}}$ ($\hat{\mathbf{u}}_k$'s) and $\hat{\mathbf{V}}$ ($\hat{\mathbf{v}}_k$'s), respectively. By doing so, the SVD computations are much simplified and result in less SVD numerical errors.

We now want to discard insignificant singular values and, therefore, reduce the number of parallel sections required to realize our seismic migration 2-D FIR filters. That is,

we want to approximate $\mathbf{A}$ by:

$$\mathbf{A}_K = \sum_{k=1}^{K} \sigma_k \hat{\mathbf{u}}_k \hat{\mathbf{v}}_k^* \sum_{k=1}^{K} = \hat{\mathbf{f}}_k \hat{\mathbf{g}}_k^* \tag{6.24}$$

where $K < (N+1)/2$ (K is the number of used parallel sections). In this case, the number of parallel sections in Figure 6.1 are reduced and this results in significant savings in terms of the computational complexity for obtaining a final seismic image while according to Eq. (6.21) and Eq. (6.23) we guarantee the even symmetry of the 1-D constituent filters to result in an overall desired wavenumber response. Clearly, since the 1-D subfilters are of even symmetry, the number of multiplications per output sample required to realize the 2-D complex-valued migration FIR filter using the SVD realization scheme is $K(N+1)$, where $K < (N+1)/2$.

The number of multiplications per output sample in this case is much less than that needed for direct convolution. Also, we will save in the number of multiplications per output sample even when compared to migration performed via direct convolution, taking into consideration that such FIR filters are of quadrantal symmetry as far as

$$K(N+1) < \frac{(N+1)^2}{4}. \tag{6.25}$$

Similarly, the number of additions per output sample based on the proposed SVD scheme is $2K(N-1)$ since we have K parallel sections and each section is composed of two 1-D even symmetrical FIR filters. As we shall see later on, the savings in this case are significant compared with the number of additions per output sample when using true 2-D convolution (no advantage for the quadrantal symmetry with respect to the number of additions per output sample).

6.3 Error Analysis

In seismic migration, the magnitude and phase responses must satisfy certain conditions as described in [27]. So, it is important to quantify the error due to the reduction in the number of parallel sections used to realize our seismic migration FIR digital filters via the SVD method given in Eq. (6.24), i.e., via discarded singular values. The following analysis states an upper bound for the SVD realization of such a filtering application with respect to the matrix l_2-norm and the Frobenius norms of matrices. The error in the wavenumber response of the realized filter, which is caused by neglecting $((N+1)/2-K)$ smallest singular values can be written as:

$$\begin{aligned} E(e^{jk_x}, e^{jk_x}) &= H(e^{jk_x}, e^{jk_y}) - H_K(e^{jk_x}, e^{jk_y}) \\ &= \sum_{n_2=-(N-1)/2}^{(N-1)/2} \sum_{n_1=-(N-1)/2}^{(N-1)/2} e[n_1, n_2] e^{-j(k_x n_1 + k_y n_2)} \\ &= \mathbf{\Psi}^*(e^{jk_x}) \mathbf{E} \mathbf{\Psi}(e^{jk_y}) \end{aligned} \tag{6.26}$$

where $H(e^{jk_x}, e^{jk_y})$ is the wavenumber response of the pre-designed migration filter, $H_K(e^{jk_x}, e^{jk_y})$ is the wavenumber response of $\mathbf{A}_K = \{h_K[n_1, n_2]\}$ for $|n_1, n_2| \leq (N-1)/2$ (see Eq. (6.24)), $e[n_1, n_2]$ is the error in the impulse response for all values of n_1 and n_2, i.e.,

$$e[n_1, n_2] = h[n_1, n_2] - h_K[n_1, n_2] \tag{6.27}$$

and $\mathbf{E} = \{e(n_1, n_2)\}$ is its impulse response error matrix, and:

$$\mathbf{\Psi}(e^{jk_x}) = [e^{-jk_x(N-1)/2}, \cdots, e^{-jk_x}, 1, e^{jk_x}, \cdots, e^{jk_x(N-1)/2}] \tag{6.28}$$

and finally,

$$\mathbf{\Psi}(e^{jk_y}) = [e^{-jk_y(N-1)/2}, \cdots, e^{-jk_y}, 1, e^{jk_y}, \cdots, e^{jk_y(N-1)/2}]. \tag{6.29}$$

We can now rewrite $\mathbf{E}$ as:

$$\begin{aligned}
\mathbf{E} &= \mathbf{A} - \mathbf{A}_K \\
&= \sum_{k=1}^{(N+1)/2} \sigma_k \hat{\mathbf{u}}_k \hat{\mathbf{v}}_k^* - \sum_{k=1}^{K} \sigma_k \hat{\mathbf{u}}_k \hat{\mathbf{v}}_k^* \\
&= \sum_{k=K+1}^{(N+1)/2} \sigma_k \hat{\mathbf{u}}_k \hat{\mathbf{v}}_k^* \\
&= \mathbf{U_E} \mathbf{\Sigma_E} \mathbf{V_E^*}
\end{aligned} \tag{6.30}$$

where $\mathbf{\Sigma}_E = \text{diag}(\sigma_{K+1}, \cdots, \sigma_{(N+1)/2}, 0, \cdots, 0)$, $\mathbf{U_E}$ and $\mathbf{V_E}$ are complex-valued unitary matrices of dimension $N \times N$. By substituting Eq. (6.30) into Eq. (6.26) and taking the absolute value of the result, we obtain:

$$|E(e^{jk_x}, e^{jk_x})| = |\mathbf{\Psi}^*(e^{jk_x}) \mathbf{U_E} \mathbf{\Sigma_E} \mathbf{V_E^*} \mathbf{\Psi}(e^{jk_y})|. \tag{6.31}$$

Now, using the Cauchy-Schwartz inequality and since $\mathbf{U_E}$ and $\mathbf{V_E}$ are unitary, we can show that the upper bound of the absolute wavenumber response error with respect to the matrix Frobenius norm is:

$$\max_{-\pi \le k_x, k_y \le \pi} |E(e^{jk_x}, e^{jk_x})| \le N[\sum_{k=K+1}^{(N+1)/2} \sigma_k^2]^{1/2}. \tag{6.32}$$

A much tighter bound can be found based on the matrix l_2-norm and is given by:

$$\max_{-\pi \le k_x, k_y \le \pi} |E(e^{jk_x}, e^{jk_x})| \le N\sigma_{K+1}. \tag{6.33}$$

For this geophysical application, Eqs. (6.32) and (6.33) quantify the magnitude wavenumber response error introduced using the proposed SVD realization method with $K < (N+1)/2$.

It is difficult, however, to analytically find an upper bound for the error incurred by the phase response of the SVD realized migration filter. However, based on empirical results, the circular symmetry of the wavenumber phase response is always achieved when

discarding insignificant singular values. As we are going to show in simulations, one possible way to relate the phase error with the singular values is by plotting the relationship between the number of parallel sections used, the total energy used per number of used parallel sections, and the corresponding phase response error.

6.4 Simulation Results

The following simulations are divided into two subsections. The first subsection deals with the accuracy of implementing 2-D complex-valued migration FIR filters using the SVD realization method presented in section 6.2.2 and given by Eq. (6.24). Also, this realization is compared with the original and the improved McClellan transformation realization schemes reported in [11] in terms of the realized filters' wavenumber responses, the passband and stopband maximum and mean absolute wavenumber errors and, finally, the computational complexity. The second subsection is concerned with applying the realized 2-D complex-valued migration FIR filters using our proposed SVD realization scheme on synthetic seismic data volumes and again comparing with those migrated sections using the original and the improved McClellan transformations given in [11].

6.4.1 Accuracy of the 2-D Migration FIR Digital Filters Realized Via SVD

The main objective of this section is to subjectively and objectively evaluate our proposed realization scheme for the migration filters and to compare it with the bench mark realizations heavily used in practice in terms of the wavenumber responses and the computational complexity. For this, a 25×25 complex-valued seismic migration FIR filter was designed (as the case in [14]) using the 2-D modified projections method described in section 4.6 for $\Delta z = 2$ m, $\Delta x = \Delta y = 10$ m, $\Delta t = 0.004$ seconds, $\omega_o = 50\pi$ radians/sec, and a velocity $c_o = 1000$ m/s, to give a normalized cut-off wavenumber of $k_{c_p} = 0.25$.

6.4.1.1 Realization of 2-D Seismic Migration FIR Digital Filters Via SVD

Figures 6.2 (a) and (b) show respectively the magnitude response and the phase response of the pre-designed 2-D migration FIR filter with the above-mentioned parameters. The 2-D FIR filter impulse response matrix is then transformed to be of the form of Eq. (6.12) and then decomposed to give the resultant $\mathbf{B}_1$ matrix based on Eq. (6.14). The rank of the impulse response matrix of this filter is of full rank, i.e., $\text{rank}(\mathbf{B}_1) = 13$. That is, the number of parallel sections that can be used to correctly implement such filters is equal to 13 sections. However, Figure 6.3 suggests that we can implement such a filter matrix with a reduced number of parallel sections (see Figure 6.1) by discarding the insignificant singular values according to Eq. (6.24) (where we can see that 4 or 5 parallel sections are sufficient to realize our migration filter). This is because most of the energy is concentrated in the first few singular values. The selection can be quantitatively dependent upon a threshold, say γ, in accordance with either Eq. (6.33) or Eq. (6.32).

In Figure 6.4, the passband and stopband maximum absolute wavenumber errors are plotted against the number of parallel sections used (or the number of used singular values). As expected, both curves are always less than the matrix l_2-norm bound curve as given by Eq. (6.33) as well as less than the matrix Frobenius norm bound curve as given by Eq. (6.32). Also, we can clearly see that as we use more parallel sections (incorporate more singular values into the approximation), then the approximation error will decrease. However, this will be at the expense of increasing both the number of multiplications and additions per output sample. The passband and stopband errors when using 5 parallel sections are less by 15 dB on average when compared to the errors introduced by using 4 parallel sections. Now, in order to quantify the passband phase error incurred due to the use of Eq. (6.24), we calculated the maximum as well as the root-mean-squared (RMS) passband phase errors (for different numbers of used parallel sections and total used energy per realization) for our SVD realized filter as shown in Figure 6.5. It is evident from the figure that both errors will approach zero as we use more parallel sections. For $K = 5$, both the maximum and RMS passband phase errors are almost identical and very close to

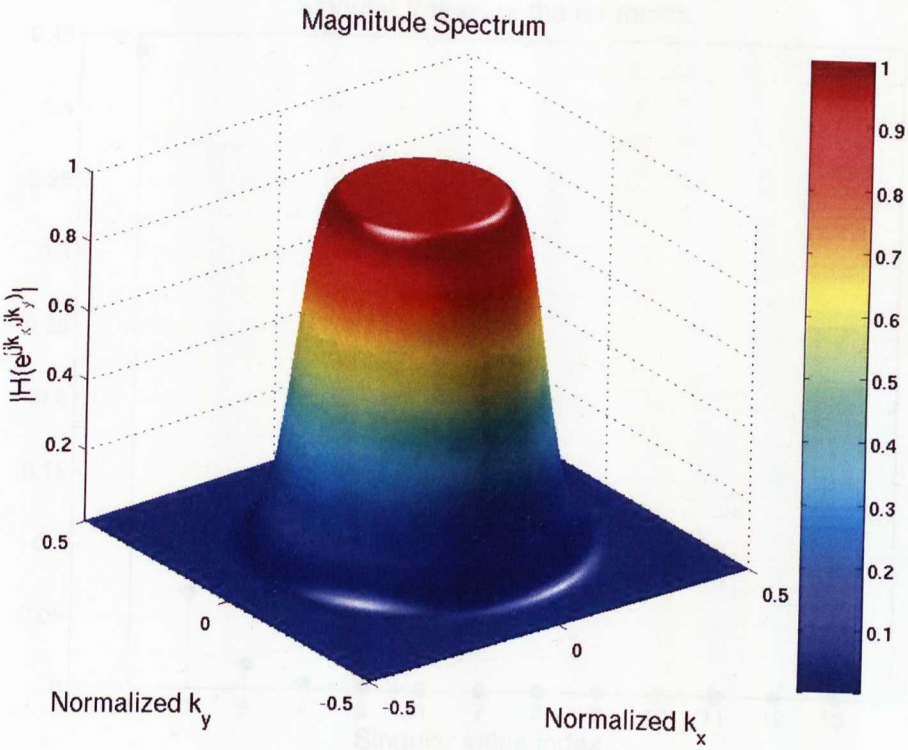

(a)

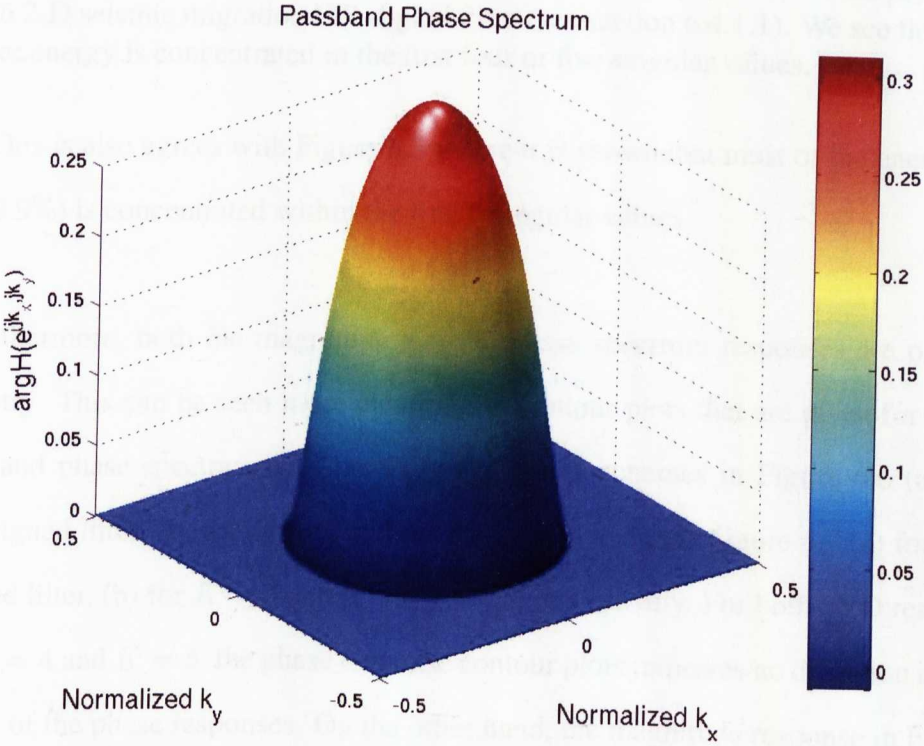

(b)

Figure 6.2: A 25×25 2-D seismic migration FIR digital filter (see section 6.4.1.1) with a cut-off $k_{c_p} = 0.25$. (a) Pre-designed magnitude spectrum, and (b) Pre-designed phase spectrum.

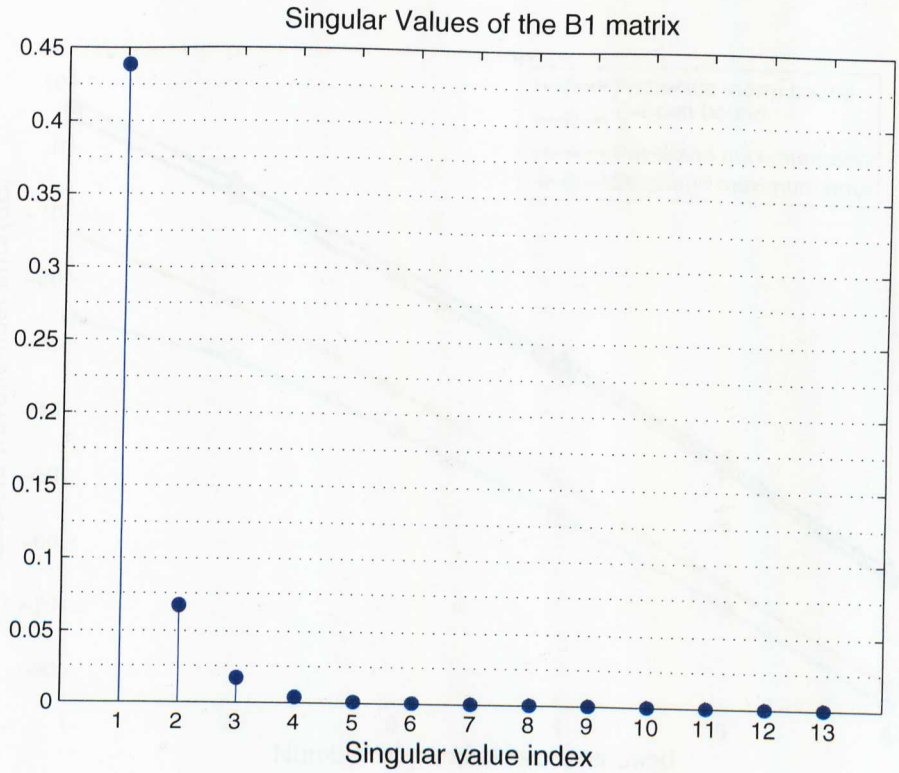

Figure 6.3: Singular values of the matrix $\mathbf{B}_1$ (see equation Eq. (6.16)) for the pre-designed 25×25 2-D seismic migration FIR digital filter (see section 6.4.1.1). We see that most of the filter energy is concentrated in the first four or five singular values.

zero. This is also agrees with Figure 6.3 where it is shown that most of the energy (more than 99.9%) is concentrated within the first 5 singular values.

Furthermore, both the magnitude and the phase spectrum responses are of circular symmetry. This can be seen more clearly with contour plots that are given for the magnitude and phase spectra using the SVD realization schemes in Figure 6.6 (a) for the pre-designed filter, (b) for $K = 4$ and (c) for $K = 5$ and also Figure 6.7 (a) for the pre-designed filter, (b) for $K = 4$ and (c) for $K = 5$, respectively. For both SVD realizations with $K = 4$ and $K = 5$, the phase response contour plots indicates no deviation in the circularity of the phase responses. On the other hand, the magnitude response in Figure 6.6 (c) for $K = 5$ is subjectively better (circularly symmetry) when compared to Figure 6.6 (b) for $K = 4$. Also, Figure 6.8 and Figure 6.9 show the magnitude and phase wavenumber responses for our 2-D FIR filter realized using the proposed SVD with $K = 3$ and $K = 4$, respectively. It is clear from both figures that both wavenumber phase responses

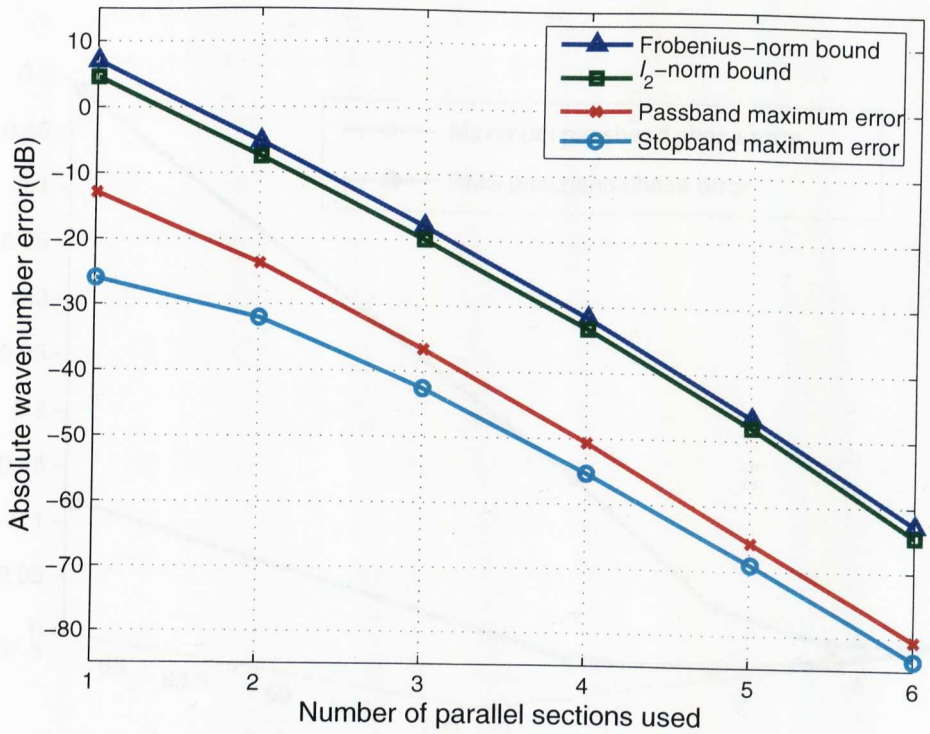

Figure 6.4: Maximum absolute wavenumber error bounds and within the passband and the stopband for the SVD realized pre-designed 25×25 2-D seismic migration FIR digital filter (see section 6.4.1.1) with respect to the number of parallel sections used (i.e., the number of singular values).

possess circular symmetry. Unlike the magnitude wavenumber response in Figure 6.9 (a), the migration using the filter with the magnitude wavenumber response in Figure 6.8 (a), however, will affect the stability of the migration process since it has magnitude response values $\gg 1$. Hence, in overall, using five parallel sections in this case is the best choice. Therefore, we realized our 2-D seismic migration FIR filters with only 5 parallel sections out of 13. Finally, Figures 6.10 (a) and (b) show the magnitude and the phase spectra of the SVD realized version of the pre-designed 2-D FIR filter with 5 parallel sections.

6.4.1.2 Comparisons with the McClellan Transformations

To compare the SVD realization with the standard realizations used for this geophysical application, a 1-D complex-valued FIR seismic migration filter was pre-designed using the method of modified projections given in section 3.6 with the same filter parameters

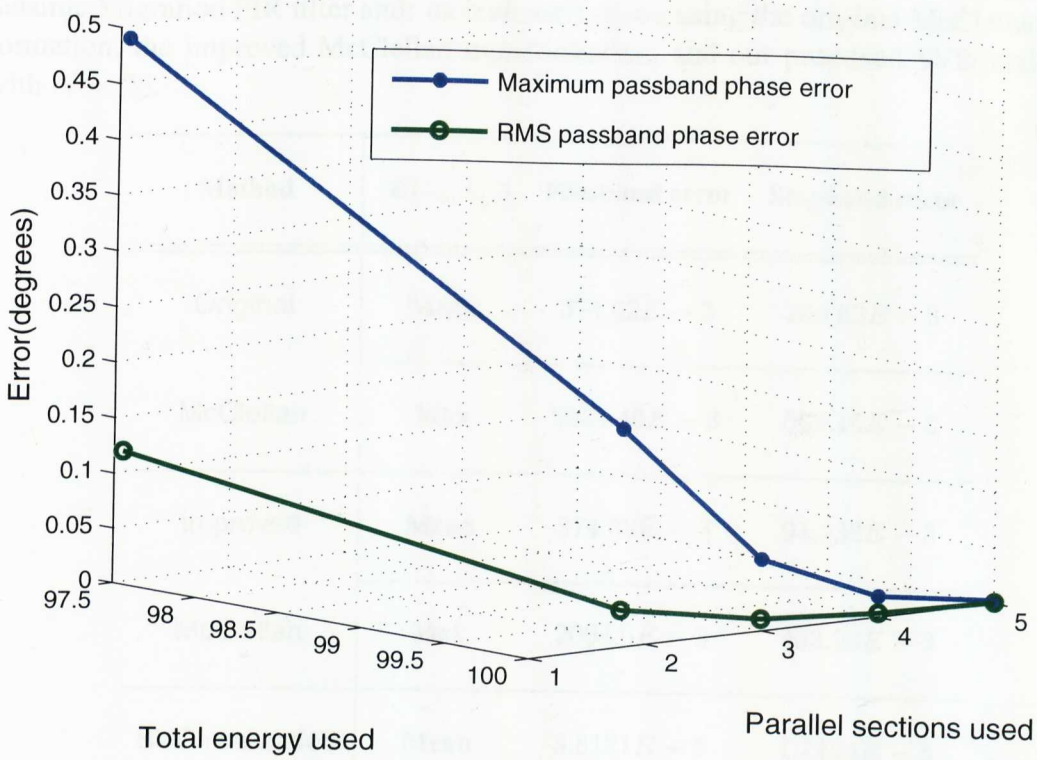

Figure 6.5: Maximum and root-mean-squared phase errors within the passband for the SVD realized pre-designed 25×25 2-D seismic migration FIR digital filter (see section 6.4.1.1) with respect to the number of parallel sections used (i.e., the number of singular values) as well as the total used energy.

described earlier. This 1-D filter is then transformed into a 2-D filter by the McClellan transformation and its improved version reported in [11] (refer to section 4.2 and Figure 4.1). Figure 6.6 (d) and Figure 6.7 (d) show contour plots of the McClellan transformed filter magnitude and phase response while Figure 6.6 (e) and Figure 6.7 (e) show the magnitude and phase response contour plots for the improved McClellan transformed filter. In both cases, the circularity of the contours in both the magnitude and the phase responses for both McClellan transformation results deteriorate rapidly as k_x and k_y increase, although the improved results possess less errors when compared to the original McClellan transformation. This is unlike our proposed SVD realization method were we do obtain an almost perfect circular symmetry in both the magnitude and the phase responses as can be seen in Figures 6.6 (b) and (c) and Figures 6.7 (b) and (c).

Table 6.1: Comparison of the mean and maximum absolute errors within the passband and stopband wavenumber responses (see section 6.4.1.2) between the pre-designed 2-D Seismic Migration FIR filter and: its realized version using the original McClellan transformation, the improved McClellan transformation, and our proposed SVD realization with $N = 25$.

Method	$\lvert E(k_x, k_y)\rvert$	**Passband error**	**Stopband error**
Original	**Mean**	$374.62E-3$	$100.62E-3$
McClellan	**Max**	$2004.46E-3$	$502.15E-3$
Improved	**Mean**	$374.38E-3$	$94.236E-3$
McClellan	**Max**	$2004.6E-3$	$463.23E-3$
SVD realization	**Mean**	$3.8121E-5$	$1.1194E-5$
with $K = 5$	**Max**	$0.51789E-3$	$0.35336E-3$

Table 6.1 compares the three realizations, namely, the McClellan method, the improved McClellan method and our SVD method with $K = 5$ in terms of the passband and stopband maximum and mean absolute wavenumber errors. As we can see from Table 6.1, the SVD realization with 5 parallel sections presents the realization with the lowest significant passband as well as stopband maximum and mean absolute wavenumber errors and, therefore, out-performs both McClellan realizations.

Finally, Tables 6.2 and 6.3 respectively compare the number of multiplications and additions both per output sample between various realization schemes, including our proposed SVD method. It is clear from both tables that the original McClellan transformation is the cheapest among all of these schemes including our proposed SVD ($K = 5$) technique. In terms of the number of multiplications per output sample, the proposed SVD

Table 6.2: Comparison between the number of multiplications per output sample required to realize a 2-D complex-valued FIR seismic migration filter (see section 6.4.1.2) using the direct 2-D convolution with quadrantal symmetry, the original McClellan transformation, the improved McClellan transformation, and our proposed SVD realization with $N = 25$.

Method	**Multiplications per output sample**	**Savings compared with true convolution**
2-D convolution with symmetry	$(\frac{N+1}{2})^2 = 169$	-
McClellan	$5(\frac{N-1}{2}) + 1 = 61$	63.91%
Improved McClellan	$8(\frac{N-1}{2}) + 1 = 97$	42.6%
SVD ($K = 5$)	$K(N+1) = 130$	23.08%

($K = 5$) technique, however, is more economical than the true 2-D convolution with quadrantal symmetry (saved 23.08%). Also, in terms of the number of additions per output sample, our proposed SVD ($K = 5$) method saved 61.54% when compared with 2-D direct convolution. It is worth mentioning that although our proposed SVD realization method (depending on K) might be more expensive than the McClellan transformations, it results in much better circularly symmetrical magnitude and phase responses and comes with insignificant wavenumber errors. This consequently results in superior 3-D migration results when compared to 3-D migration based on both McClellan transformations as we shall see in 6.4.2.

6.4.2 3-D Seismic Migration Impulse Response Tests

To test our SVD realized migration filters for the so called *3-D Seismic Migration Impulse Responses* [1], a synthetic seismic volume was created. It is basically composed of zero amplitude traces containing one zero-phase Ricker wavelet centred at 0.512 second located at the $x = y = 0$ seismic trace. In this experiment, a set of 25×25 2-D seis-

Table 6.3: Comparison between the number of additions per output sample required to realize a 2-D complex-valued FIR seismic migration filter (see section 6.4.1.2) using the direct 2-D convolution with quadrantal symmetry, the original McClellan transformation, the improved McClellan transformation, and our proposed SVD realization with $N = 25$.

Method	**Additions per output sample**	**Savings compared with true convolution**
2-D convolution with symmetry	$N^2 - 1 = 624$	-
McClellan	$9(\frac{N-1}{2}) - 2 = 106$	83.01%
Improved McClellan	$12(\frac{N-1}{2}) - 2 = 142$	77.24%
SVD ($K = 5$)	$2K(N-1) = 240$	61.54%

mic migration FIR digital filters were designed using the method of modified projections (section 4.6) and stored with the same filter parameters as mentioned earlier. The range of in-line and cross-line sections was 1100 meters. Also, for this experiment, the maximum angular frequency used was 90π radians/sec. These 2-D designed filters were then used to perform 3-D migration (using the scheme in Figure 6.11) based on true 2-D convolution (taking into account the quadrantal symmetry of such filters) and based on our SVD derived realization scheme given by Eq. (6.24) with $K = 3$, 4 and 5 (all based on the migration scheme in Figure 6.11). A 2-D slice of the migrated volume at $z = 220$ meters is shown in Figure 6.12 (a) using true direct convolution, and using our SVD realization scheme with (b) $K = 3$, (c) $K = 4$ and (d) $K = 5$. Subjectively, the slice of the migrated volume via SVD realization with $K = 5$ in Figure 6.12 (d) is the best among the other two migrated volumes with the SVD realization with $K = 3$ (see Figure 6.12 (b)) and with $K = 4$ (see Figure 6.12 (c)). Finally, the signal to noise ratio (SNR) is computed with respect to the original migrated slice in Figure 6.12 (a) for those in Figures 6.12 (b), (c), and (d). Again, the migration via SVD realization with $K = 5$ gave the highest SNR

which is equal to 11.1296 dB when compared with $K = 3$ (SNR=-0.8722 dB) and with $K = 4$ (SNR=4.9115 dB). This is an expected result, due to the simulations performed previously in subsection 6.4.1.1.

The same input seismic section described above was migrated using both the McClellan and the improved McClellan transformation schemes. A set of 25-tap 1-D migration FIR digital filters were pre-designed (using the modified projections in section 3.6) and stored in order to perform such an experiment again with the same filter parameters as in 6.4.1. Figures 6.13 (c) and (d) show the same 2-D slice of the 3-D migrated section at $z = 220$ meters with SNR's equal to -2.8654 dB and -3.4829 dB, respectively.

Although the improved McClellan slice given in Figure 6.13 (d) has a better response when compared to the migrated section slice in Figure 6.13 (c) using the original McClellan method, both methods result in poor migrated images when compared to the SVD realized migrated section with $K = 5$ (Figure 6.13 (b)). The differences can be seen clearly where the McClellan transformation migration impulse responses are not perfect circles and they also possess poor SNR values. This is justified by reconsidering the simulation results shown in subsection 6.4.1.2.

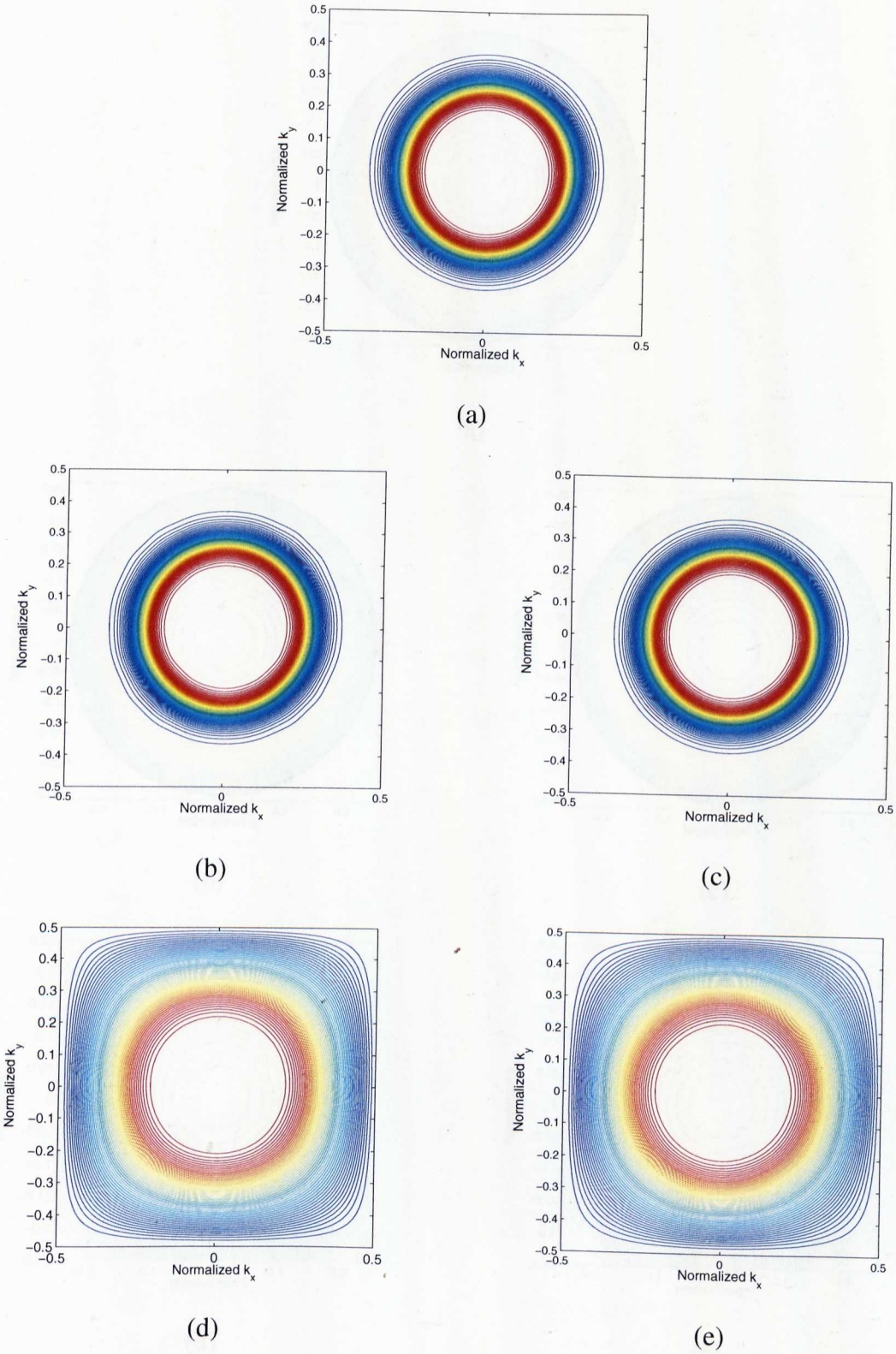

Figure 6.6: A 25×25 2-D seismic migration FIR digital filter (see sections 6.4.1.1 and 6.4.1.2) (with a cut-off $k_{c_p} = 0.25$) showing contour plots of the magnitude spectrum for the (a) Pre-designed, (b) SVD realized with $K = 4$, (c) SVD realized with $K = 5$, (d) Original McClellan transformation method, and (e) Improved McClellan transformation method.

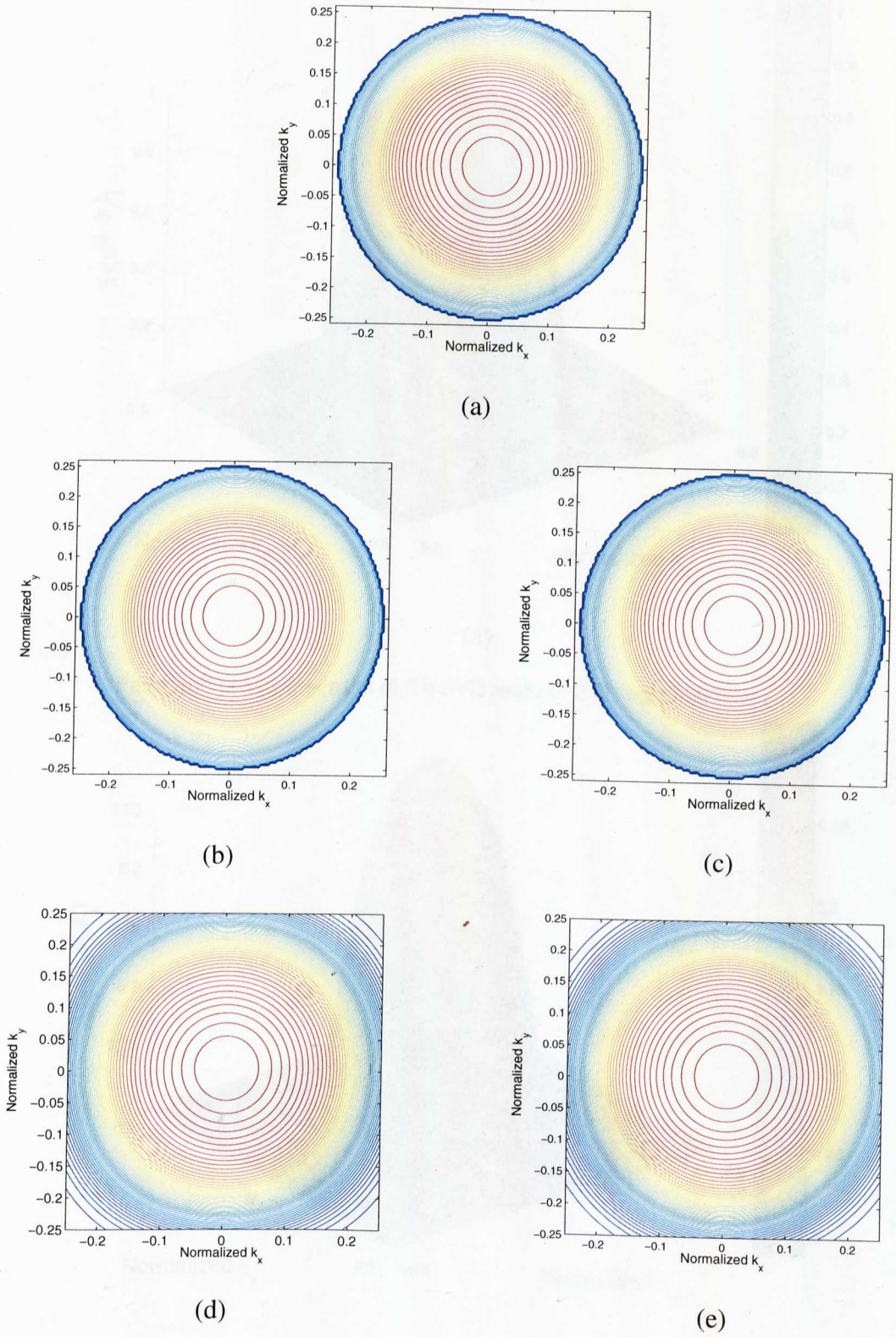

Figure 6.7: A 25×25 2-D seismic migration FIR digital filter (see sections 6.4.1.1 and 6.4.1.2) (with a cut-off $k_{c_p} = 0.25$) showing contour plots of the phase spectrum for the (a) Pre-designed, (b) SVD realized with $K = 4$, (c) SVD realized with $K = 5$, (d) Original McClellan transformation method, and (e) Improved McClellan transformation method.

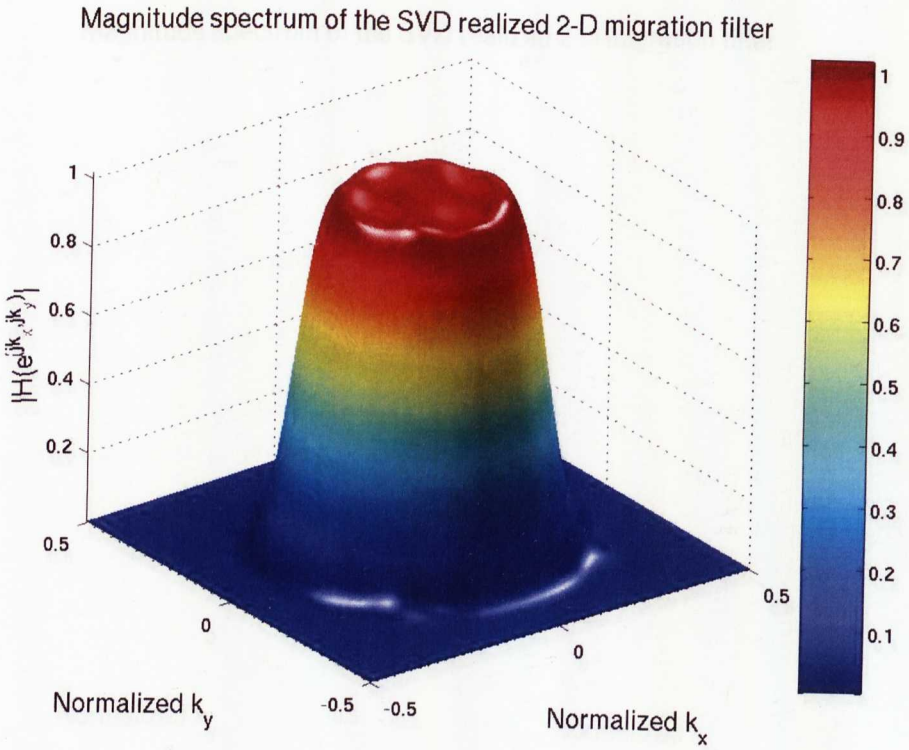

(a)

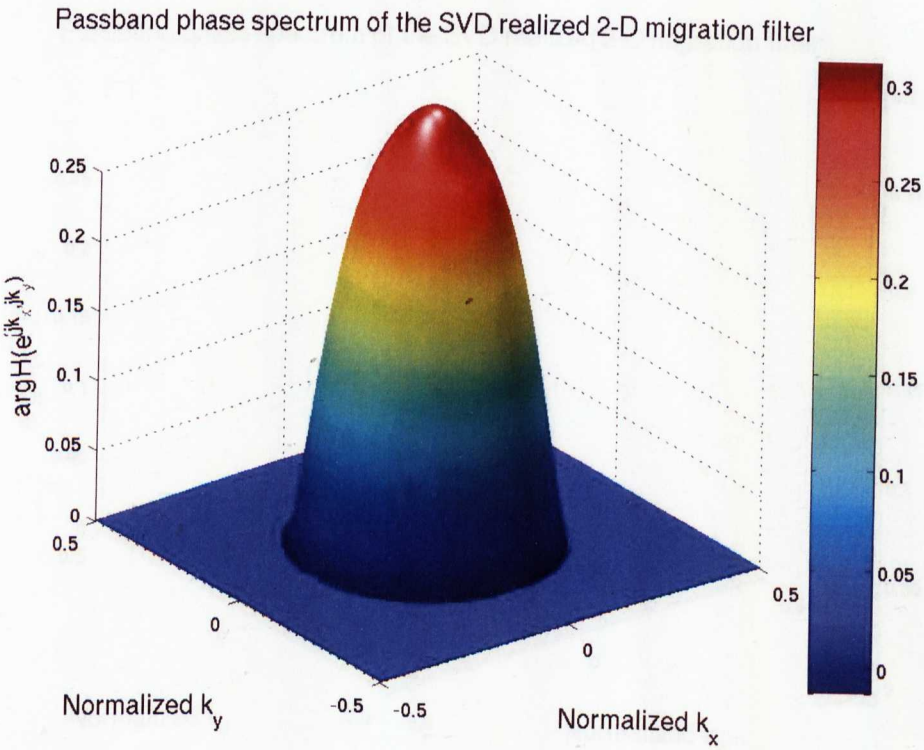

(b)

Figure 6.8: A 25×25 2-D seismic migration FIR digital filter (see section 6.4.1.1) with a cut-off $k_{c_p} = 0.25$. (a) SVD realized magnitude spectrum ($K = 3$), and (b) SVD realized phase spectrum ($K = 3$). In this case, it is clear that the magnitude wavenumber response will affect the migration process stability since it has values $\gg 1$.

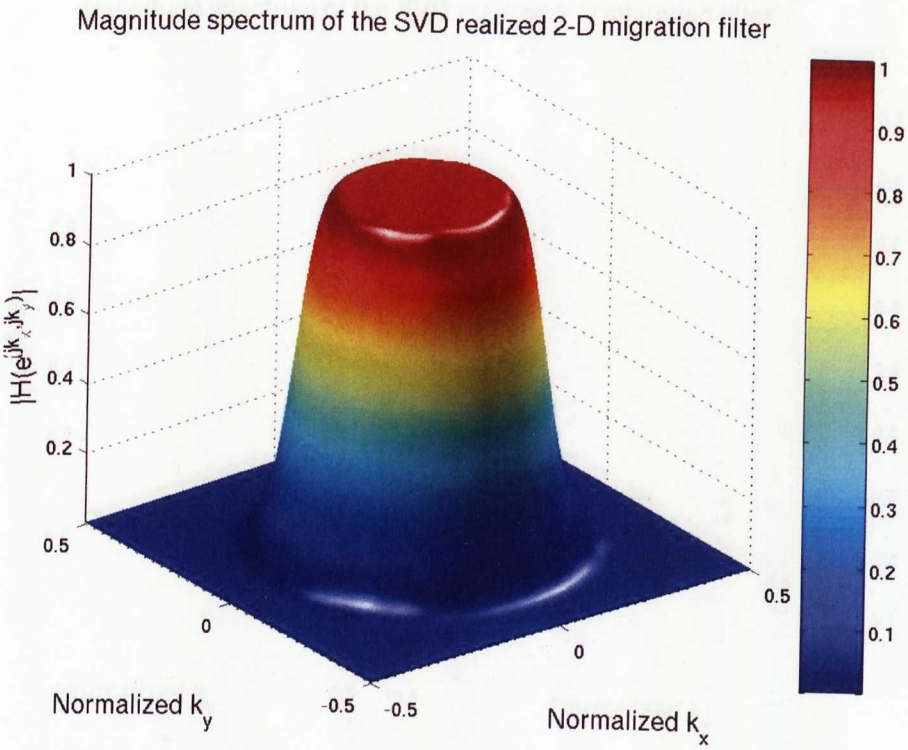

(a)

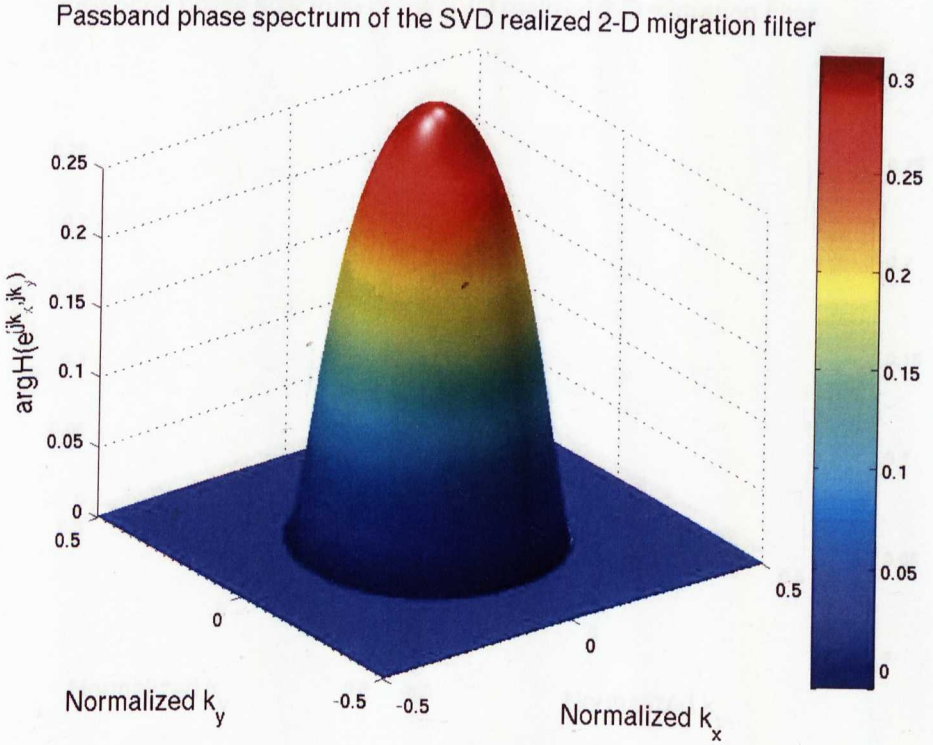

(b)

Figure 6.9: A 25×25 2-D seismic migration FIR digital filter (see section 6.4.1.1) with a cut-off $k_{c_p} = 0.25$. (a) SVD realized magnitude spectrum ($K = 4$), and (b) SVD realized phase spectrum ($K = 4$).

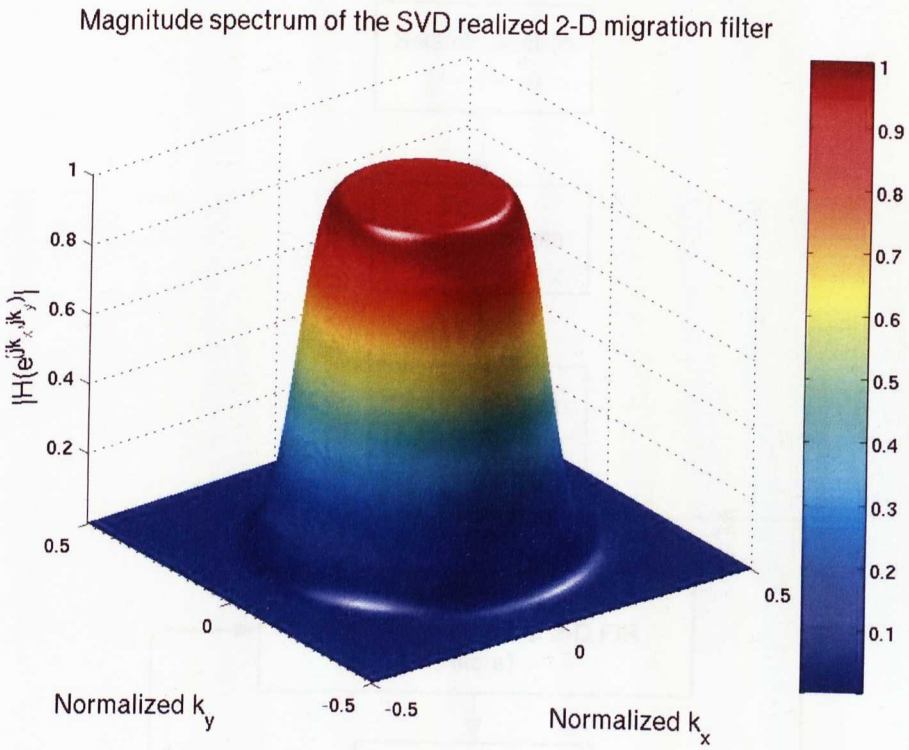

(a)

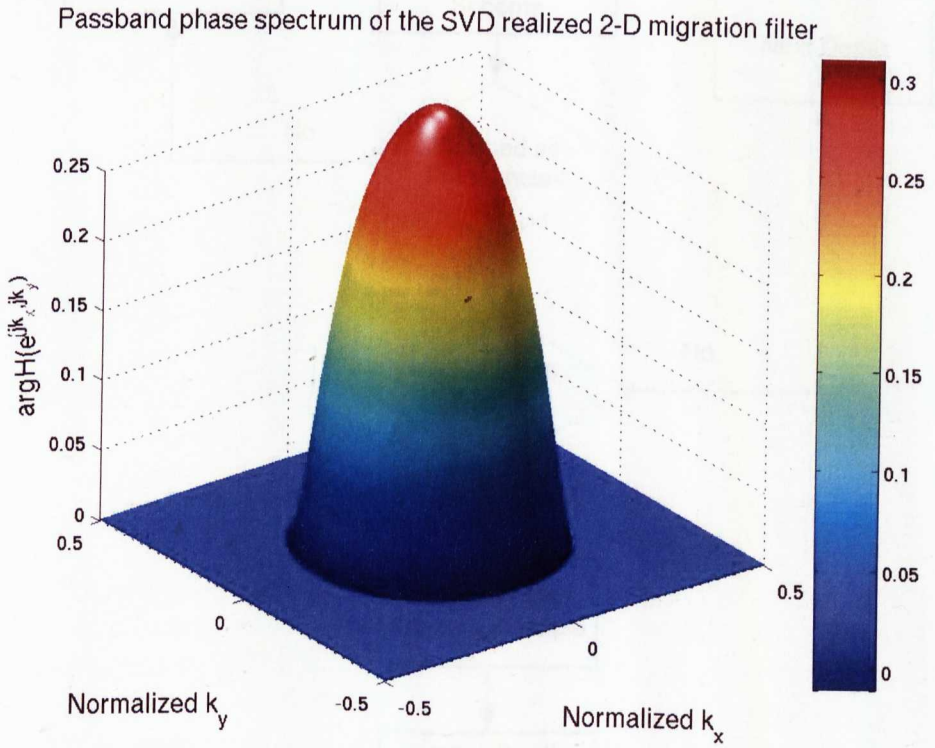

(b)

Figure 6.10: A 25×25 2-D seismic migration FIR digital filter (see section 6.4.1.1) with a cut-off $k_{c_p} = 0.25$. (a) SVD realized magnitude spectrum ($K = 5$), and (b) SVD realized phase spectrum ($K = 5$). Based on previous figures, this wavenumber response results in a better realization choice, where all the 2-D migration FIR filter requirements are satisfied.

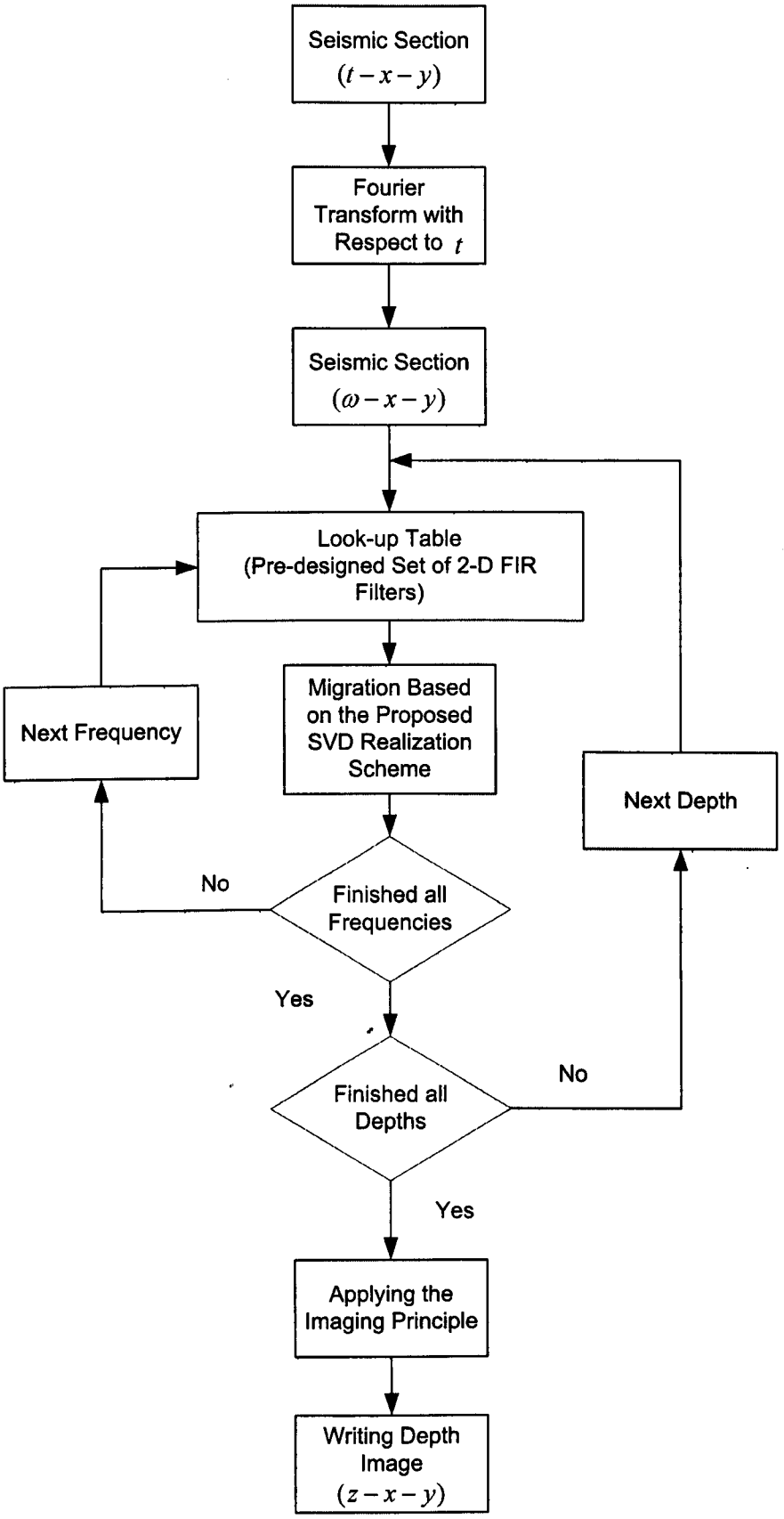

Figure 6.11: Diagram illustrating the explicit depth 3-D $\omega - x - y$ post-stack migration process which is based on using the 2-D FIR filters realized (implemented) via SVD (see section 6.4.2).

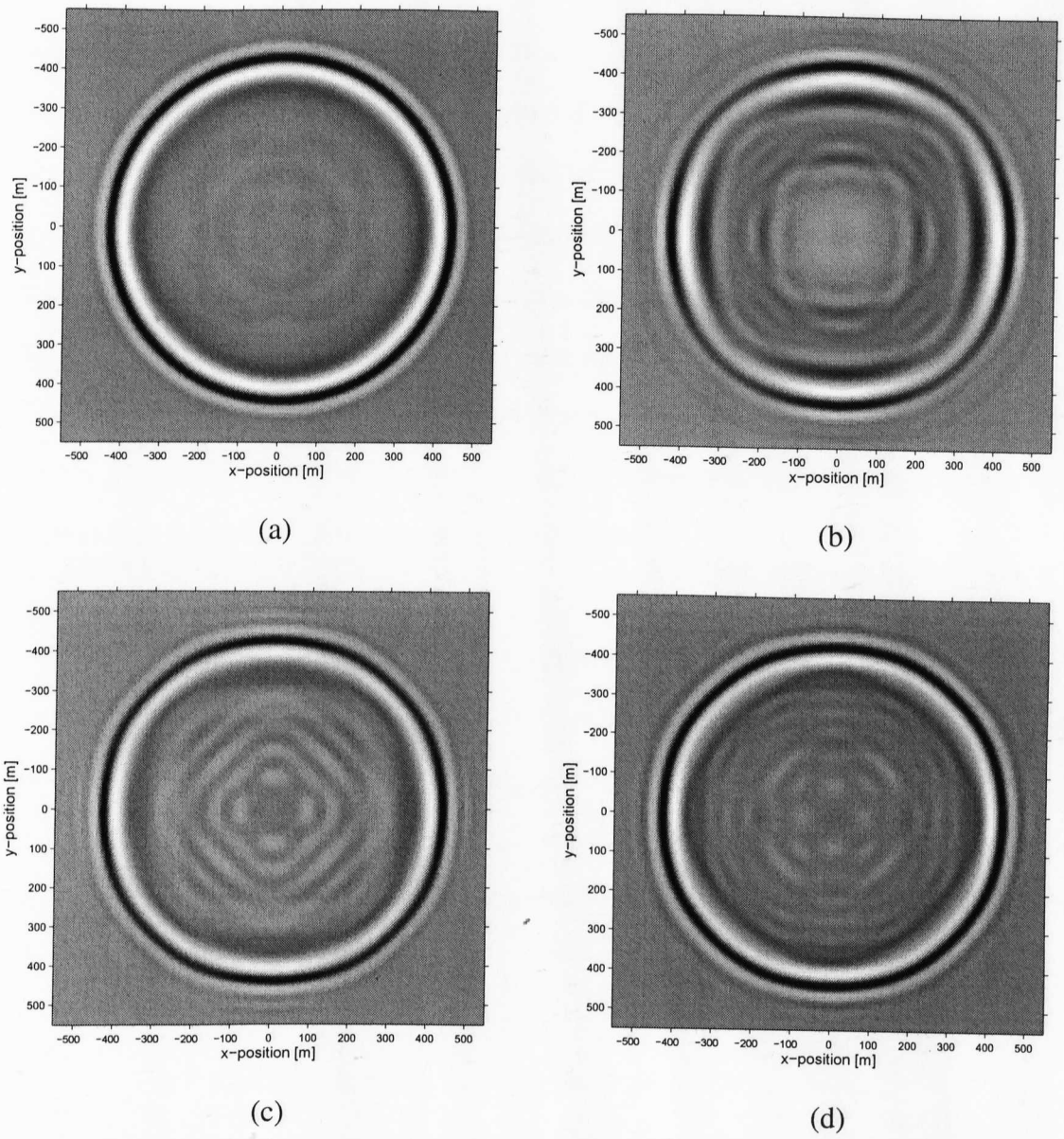

Figure 6.12: 3-D Seismic migration impulse response 2-D slice (see section 6.4.2) at depth $z = 220$ meters with $\Delta z = 2$ meters, and $\Delta x = \Delta y = 10$ meters for a range of 1100 meters for both the in-line and cross-line sections. The time sampling interval was $\Delta t = 4$ msec, $c = 1000$ meters/sec and a maximum frequency of 45 Hz using (a) direct convolution, and our proposed SVD realization scheme with (b) $K = 3$ and SNR= -0.8722 dB, (c) $K = 4$ and SNR= 4.9115 dB, and (d) $K = 5$ and SNR= 11.1296 dB.

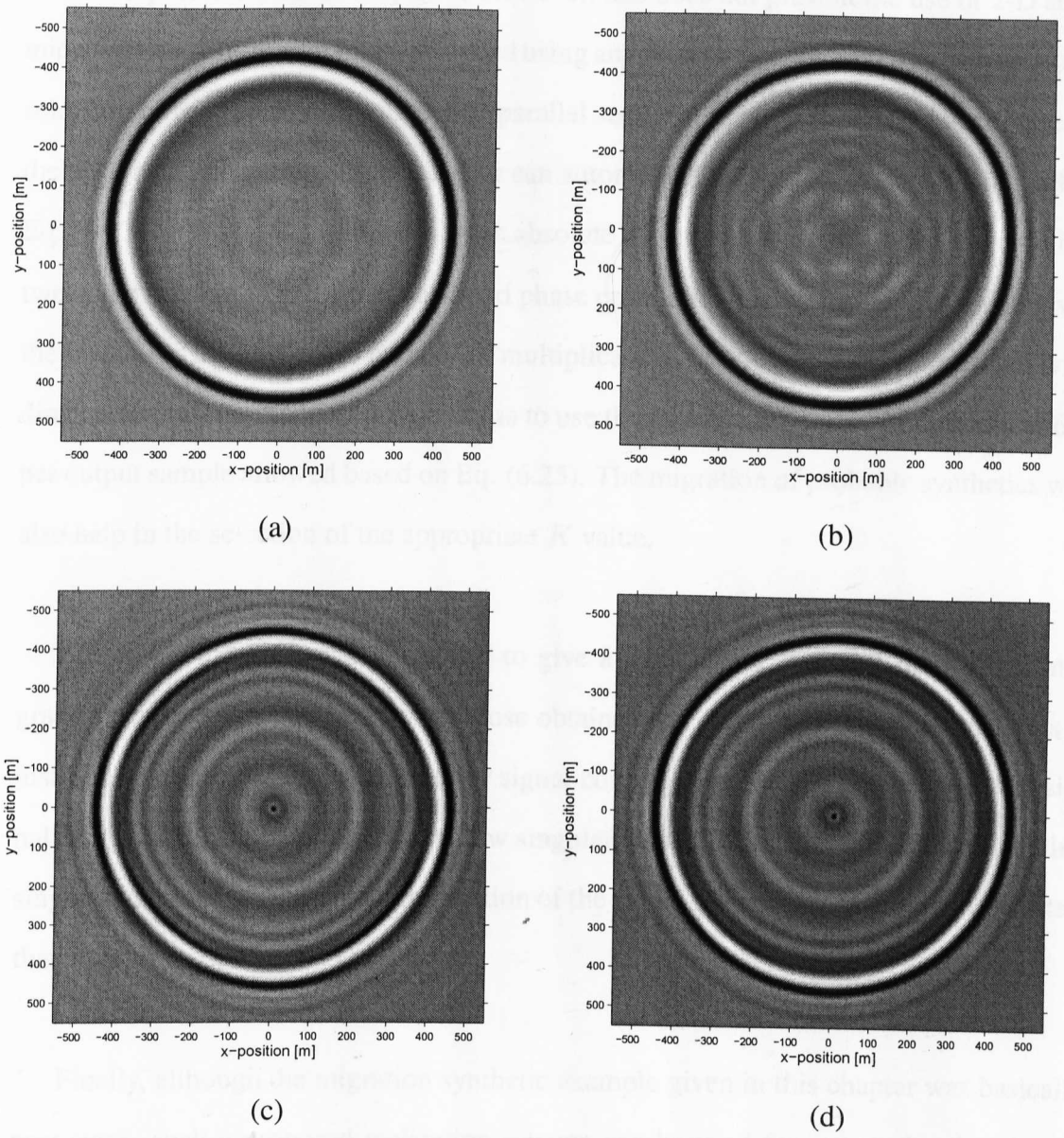

Figure 6.13: 3-D Seismic migration impulse response 2-D slice (see section 6.4.2) at depth $z = 220$ meters with $\Delta z = 2$ meters, and $\Delta x = \Delta y = 10$ meters for a range of 1100 meters for both the in-line and cross-line sections. The time sampling interval was $\Delta t = 4$ msec, $c = 1000$ meters/sec and a maximum frequency of 45 Hz using (a) direct convolution, (b) our proposed SVD realization scheme with $K = 5$ and SNR= 11.1296 dB, (c) the original McClellan transformation method with SNR= -2.8654 dB, and (d) the improved McClellan transformation method with and SNR= -3.4829 dB.

6.5 Discussion

All the pre-designed 2-D seismic migration FIR digital filters were designed using the method reported earlier in chapter 4. However, this does not prevent the use of 2-D seismic migration FIR digital filters designed using any filter design method. Furthermore, the selection of the appropriate number of parallel sections, namely K, will be the choice of the designer. For example, the designer can automate the selection by considering either Eq. (6.33) or Eq. (6.32) which deal with absolute wavenumber error bounds, the ratio between the maximum and RMS passband phase error, and, finally, Eq. (6.25) which gives the bound for the maximum number of multiplications per output sample compared with direct convolution. Another possibility is to use the maximum number of multiplications per output sample allowed based on Eq. (6.25). The migration of probable synthetics will also help in the selection of the appropriate K value.

Moreover, the SNR was computed to give a quantitative figure of the realized migration results when compared with those obtained via direct 2-D convolutions. This is justified since the SVD can be used for signal compression [108] where most of the signal energy is concentrated in the first few singular values. Thus, discarding the remaining singular values results in an approximation of the signal (in our case is the 2-D FIR filter) that is decomposed via SVD.

Finally, although the migration synthetic example given in this chapter was basically post-stack, such a proposed realization scheme can be used for pre-stack migration of rectangularly sampled data sets. If the pre-stacked data are irregularly sampled (as is usually the case), it will then be required to rectangularly resample such data prior to applying our proposed SVD realization.

6.6 Conclusion

We have presented a novel application of singular value decomposition (SVD) for realizing 2-D quadrantally symmetrical complex-valued seismic migration FIR digital filters which are used for the expensive application of 3-D explicit depth $\omega - x - y$ migration. In order to simplify the SVD computations for such an impulse response structure, we applied a special matrix transformation on the migration filter impulse responses where the wavenumber phase response is guaranteed to be retained.

This SVD realization saved 23.08% of the number of multiplications per output sample when compared to direct implementation with symmetry via true 2-D convolution. Also, the SVD realization saved 61.54% of the number of additions per output sample when compared to direct implementation with symmetry via true 2-D convolution. This came with almost negligible wavenumber errors. In addition, both wavenumber magnitude and phase responses possess circular symmetry unlike migration FIR filters realized with the previously reported McClellan and the improved McClellan transformations for such geophysical applications.

Finally, we demonstrated our work by applying such SVD realized 2-D seismic migration FIR filters to synthetic seismic sources. We showed subjectively and objectively that seismic migration via our proposed SVD realization scheme is out-performing migration results via other standard methods used for such an application like the McClellan and the improved McClellan realizations. This was clearly seen in terms of the wavenumber responses, the maximum and mean passband and stopband absolute wavenumber errors, and the computational complexity (see sections 6.4.1.2 and 6.4.2).

Chapter 7

Migration Experiments on the Two-Dimensional SEG/EAGE Salt Model

7.1 Introduction

One of the challenges that faces the seismic industry is to migrate (image) beneath salt bodies or domes [109, 1]. Structurally contoured with high velocities salt domes act as sonic lenses that disperse seismic energy in haphazard ways. As was described in chapter 2, various migration techniques exist which try to overcome these salt related problems of velocity and structure. The Gulf of Mexico is one of the areas which contains such structures. It has become a standard procedure to test any newly developed migration algorithms that are expected to deal with such challenging structures on the so called *SEG/EAGE Salt Model* [110, 111, 112, 109, 113]. The SEG/EAGE Salt Model shown in Figure 7.1, is a 3-D model, and was defined in October 1993 by representatives from major oil companies operating in the Gulf of Mexico in addition to many independents and oil service contractors [110, 111, 112, 109, 113]. Maps describing the model were generated in November 1993 and the model was constructed in December 1993 at the Nancy School of Geology, Nancy, France. A preliminary velocity grid was avail-

able in March 1994. In August 1994, the SEG/EAGE modelling committee decided to convert the model metric coordinates to be compatible with the Overthrust model. A final velocity grid was made available in September 1994 (see [110, 111, 112, 113] and http://research.seg.org/3dmodel/salthome/intro.html). This model was built to address data quality issues which are encountered around the types of salt features found in the coast of the US Gulf.

The resulting modified projections (modified POCS) 1-D migration FIR filters derived and described in section 3.6 are applied to a 2-D slice from the challenging 3-D SEG/EAGE Salt model. This 2-D section was used to generate a zero-offset section using the method of finite differences [3]. By migrating this 2-D zero-offset section, we can easily assess our FIR filters designed using the modified projection algorithm and compare the result with other well known post-stack migration methods. Hence, the migrated result is compared with images obtained via migration FIR filters based on the modified Taylor series [12], and with other standard techniques such as the Phase Shift Plus Interpolation (PSPI) [28], and the Split-Step (SS) Fourier methods [29, 3] (both were briefly described in chapter 2). The modified projection algorithm provides very stable depth filters (extrapolators). As we shall see later in this chapter, the resulting migrated section is of comparable quality to the expensive PSPI result, and visibly out-performs the other two techniques [30, 31].

We start this chapter by performing some preliminarily experiments (section 7.2) based on the given zero-offset and velocity model of the 2-D SEG/EAGE model. These experiments evaluate the accuracy of the designed filters and provide prior information that assists the interpretation of the obtained migrated images of the 2-D SEG/EAGE data set. Finally, the chapter ends with a brief discussion and conclusion in section 7.3.

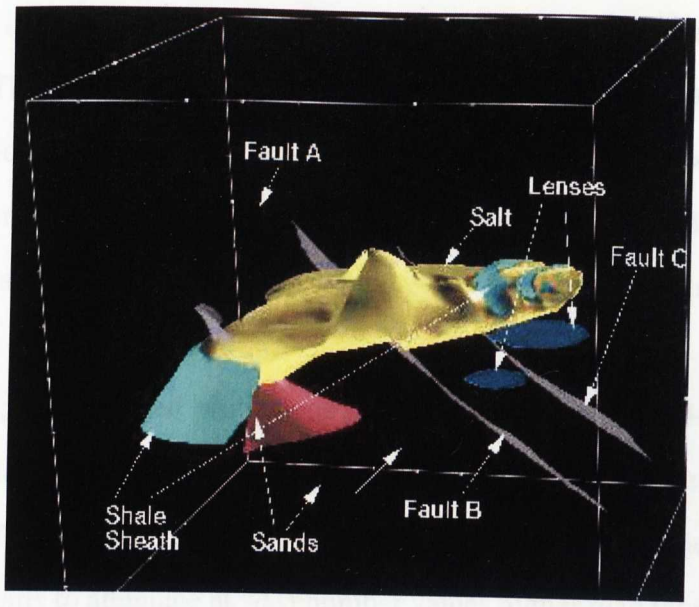

Figure 7.1: This is a 3-D perspective of the SEG/EAGE Salt Model. The model contains various challenging geological structures such as sand bodies, salt sill, different faults, etc. The model was designed to test migration (pre/post-stack) algorithms in different geological settings. Finally, the velocities which are surrounding the salt body are typical of Gulf of Mexico sediments (courtesy of http://www.ees4.lanl.gov/image-seg).

7.2 Post-Stack Migration of the 2-D SEG/EAGE Salt Model

This section presents various simulation experiments. The first three subsections provide prior information of how the migration of the 2-D SEG/EAGE Salt Model would look like based on its required seismic migration FIR filters parameters. Note that all of such experiments are performed using MATLAB on a Pentium IV machine with 1GB of RAM on a Linux based OS.

7.2.1 Accuracy of the 1-D Seismic Migration FIR Filters

First we compare the accuracy of the 1-D seismic migration FIR filters (extrapolators) designed using the proposed modified projection algorithms (with $\epsilon = 10^{-15}$) reported in chapter 3 with the modified Taylor series method (with 8 derivative terms) reported in [12], the complex Remez exchange algorithm (with a passband weight=80) reported in [19, 20]. All filters were designed with an FIR filter length $N = 25$, and a passband wavenumber cut-off $k_{c_p} = 0.25$. The magnitude response for both the modified Taylor series method and the modified projections method have a flatter amplitude within the

passband. That is, the designs result in much less ripple when compared to the complex Remez result. This can be clearly seen in Figure 7.2 (a) where the passband magnitude response error for the modified projections and the modified Taylor series methods are very close to zero. In other words, the modified projections and modified Taylor series filters results in a more stable migration compared with the complex Remez method.

Furthermore, the modified projections designed migration FIR filter accommodates higher propagation angles when compared to the modified Taylor series and the complex Remez filters. This is seen in Figure 7.2 (a) where the modified projections magnitude response error starts to attenuate at wavenumber values higher than those of the other two filters. Figure 7.2 (b) shows the passband phase response error for all designed filters.

The passband phase response error indicates that both the modified projections and the modified Taylor series phase response errors are smaller than the phase response error of the complex Remez method. In fact, the passband phase error related to the complex Remez technique is very high and this would result (as we are going to see later) in positioning seismic events incorrectly. Finally, Table. 7.1 compares the CPU time for designing all the above mentioned techniques where the modified projections technique required the minimum design timing. This also shows that we can save in design time compared with the other two techniques.

7.2.2 2-D Impulse Responses

For 2-D extrapolation impulse response, the synthetic seismic section used here is a zero section with the zero-offset trace containing only 25 Hz three zero-phase Ricker wavelets centred at 0.3, 0.6, and 0.9 seconds. The depth interval $\Delta z = 4$ meters, and lateral sampling interval $\Delta x = 20$ meters for a range of 1600 meters. The time sampling interval is $\Delta t = 2$ msec, a velocity $c = 750$ meters/sec and we have a maximum frequency of 45 Hz. Based on that, we designed a set of 25-tap 1-D filters using the modified projections, the modified Taylor series, and the complex Remez methods. Figure 7.3 (a) shows the 2-D

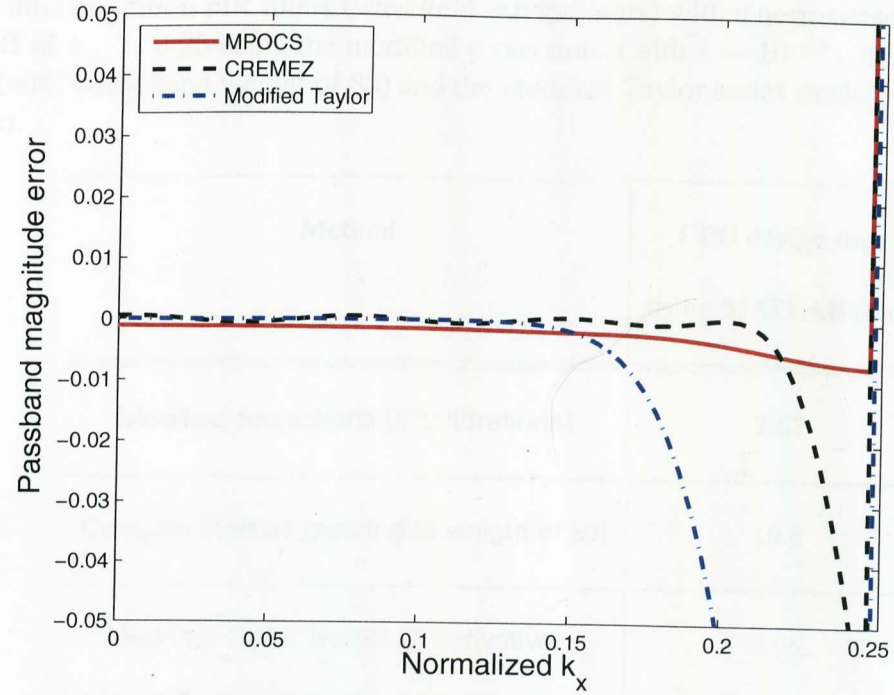

(a)

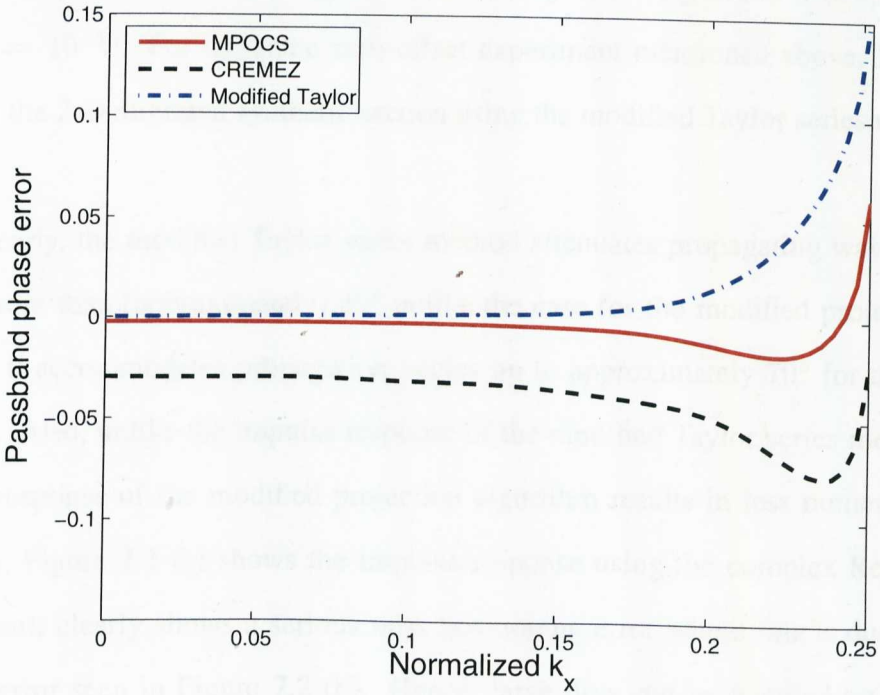

(b)

Figure 7.2: The designed 1-D migration FIR filters (see section 7.2.1) using the modified projections (solid-line), the modified Taylor series (dash-dotted line), and the complex Remez exchange (dashed line) algorithms with $N = 25$, and $k_{c_p} = 0.25$, (a) Magnitude response error within the passband, and (b) Phase response error within the passband.

Table 7.1: Comparison of CPU design time (see section 7.2.1) for designing a 25-tap 1-D seismic migration FIR filters (wavefield extrapolators) with a normalized wavenumber cut-off of $k_{c_p} = 0.25$ using the modified projections (with $\epsilon = 10^{-15}$), the complex Remez (with a passband weight of 80) and the modified Taylor series methods (8 derivative terms).

Method	**CPU design time using MATLAB (sec.)**
Modified projections (679 iterations)	2.67
Complex Remez (passband weight of 80)	10.8
Modified Taylor Series (8 derivatives)	2.95

migrated synthetic section using the modified projections algorithm with $\delta_p = \delta_s = 10^{-3}$, and $\epsilon = 10^{-15}$. For the same zero-offset experiment mentioned above, Figure 7.3 (b) shows the 2-D migrated synthetic section using the modified Taylor series method.

Clearly, the modified Taylor series method attenuates propagating waves having angles more than (approximately) 45° unlike the case for the modified projection method where it accommodates propagation angles up to approximately 70° for the same filter length. Also, unlike the impulse response of the modified Taylor series method, the impulse response of the modified projection algorithm results in less numerical artifacts. Finally, Figure 7.3 (c) shows the impulse response using the complex Remez method. The result clearly shows a serious miss-positioning error where this is due to the large phase error seen in Figure 7.2 (b). Hence, large dips can be handled by the modified projection filters. Also, compared with both the modified Taylor and the complex Remez seismic impulse responses, the impulse response of the modified projection filters results in less dispersion noise and a correct positioning of the impulse responses.

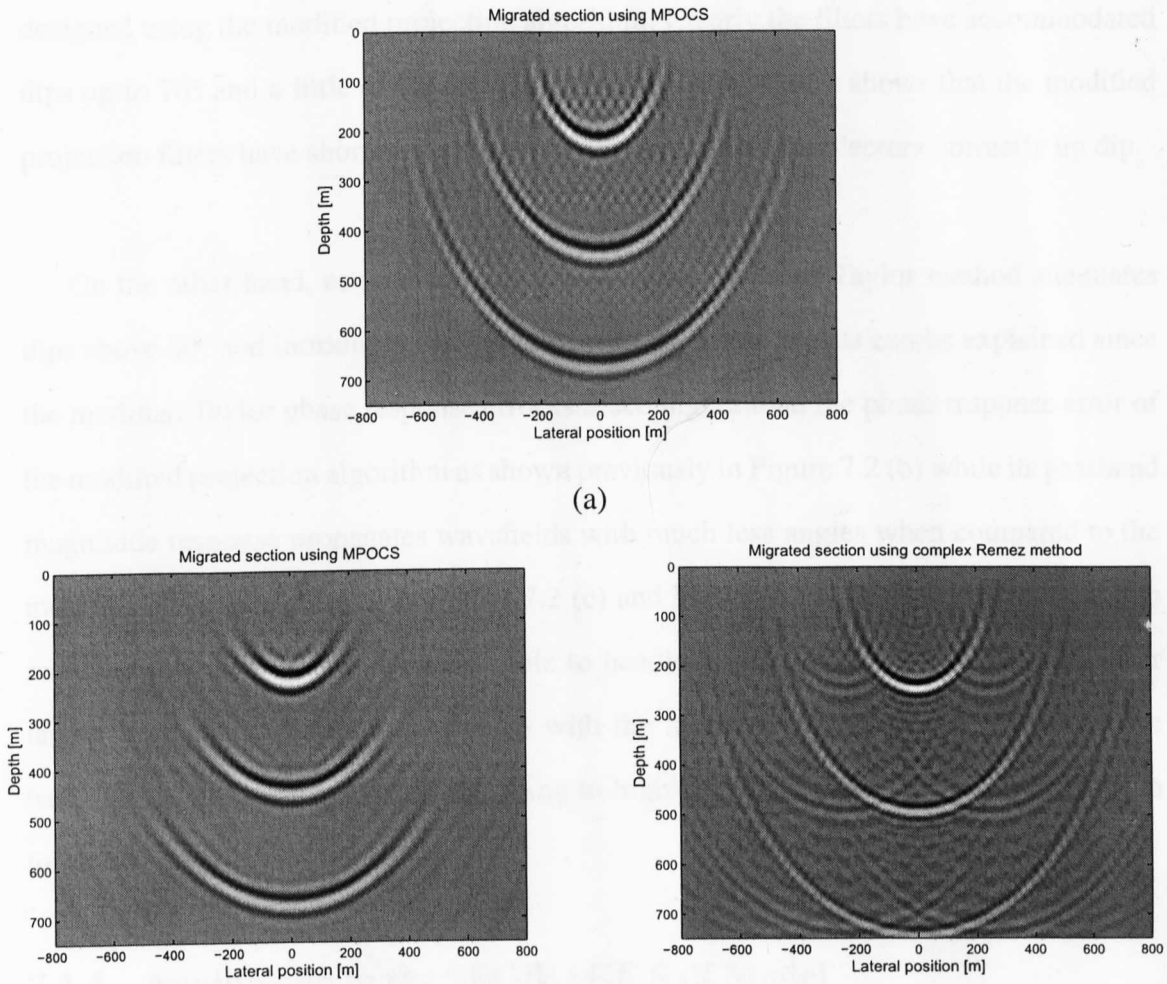

Figure 7.3: 2-D Impulse response sections (see section 7.2.2) with $\Delta z = 4$ meters, $\Delta x = 20$ meters, $\Delta t = 2$ msec, $c = 750$ meters/sec, and we have used a maximum frequency of 80 Hz using (a) the modified projections algorithm where the filter's parameters are $\delta_p = \delta_s = 10^{-3}$, and $\epsilon = 10^{-15}$ for $N = 25$ with an approximate resulting dip angle of 70°, (b) the modified Taylor series method where $N = 25$ with an approximate resulting dip angle of 45°, and (c) the complex Remez method where $N = 25$ with an approximate resulting dip angle of 70°.

7.2.3 2-D Dip Accuracy and Stability

The same set of filters designed using the modified projection algorithm and the modified Taylor series method for the impulse response experiments in the previous subsection are used to migrated a synthetic time-space seismic section shown in Figure 7.4 (a). This section contains dips with angles: $0^o, 30^o, 50^o, 60^o, 70^o$ and 80°. It is constructed based on a Ricker wavelet input with a dominant frequency of 15 Hz and with a time duration of 0.2 seconds. Figure 7.4 (b) shows the migrated section using the migration FIR filters

designed using the modified projection algorithm. Clearly the filters have accommodated dips up to 70° and a little of the 80° dip. Also, the same figure shows that the modified projection filters have shortened and moved the synthetic dip reflectors correctly up dip.

On the other hand, as seen in Figure 7.4 (c), the modified Taylor method attenuates dips above 50° and introduces background artifacts. These results can be explained since the modified Taylor phase response error is much higher than the phase response error of the modified projection algorithm as shown previously in Figure 7.2 (b) while its passband magnitude response propagates wavefields with much less angles when compared to the modified projection filter as in Figure 7.2 (c) and Figure 7.3 (a) and (b). Therefore, the modified projection filters are again able to handle large dips and are more stable over larger propagation distances compared with the modified Taylor filters. Note that we have used a nonlinear gray scale mapping to highlight the background artifacts for both migrated images.

7.2.4 Application to the SEG/EAGE Salt Model

The main objective here is to subjectively evaluate our modified projection seismic migration FIR filters designed in the previous subsections for post-stack migration. Figure 7.5 represents the SEG/EAGE salt velocity model reported by [110, 111, 112, 109, 113]. The salt body is embedded in sediments with smoothly varying velocities. The velocity model is composed of 1024 traces where each trace contains 1048 depth samples. A zero-offset section of the SEG/EAGE salt velocity model was generated based on finite differences [3]. It is composed of 1024 traces and the time record was up to 6 seconds (3001 time samples per trace).

7000 frequency-velocity dependent filters were designed with the same filter parameters given in the previous subsections with a total filter length of 25 coefficients but only 13 coefficients were stored and used due to their symmetry property. Here, we display only offsets ranging from $3,000$ m up to $17,000$ m and a time interval from 0 up to 5 sec

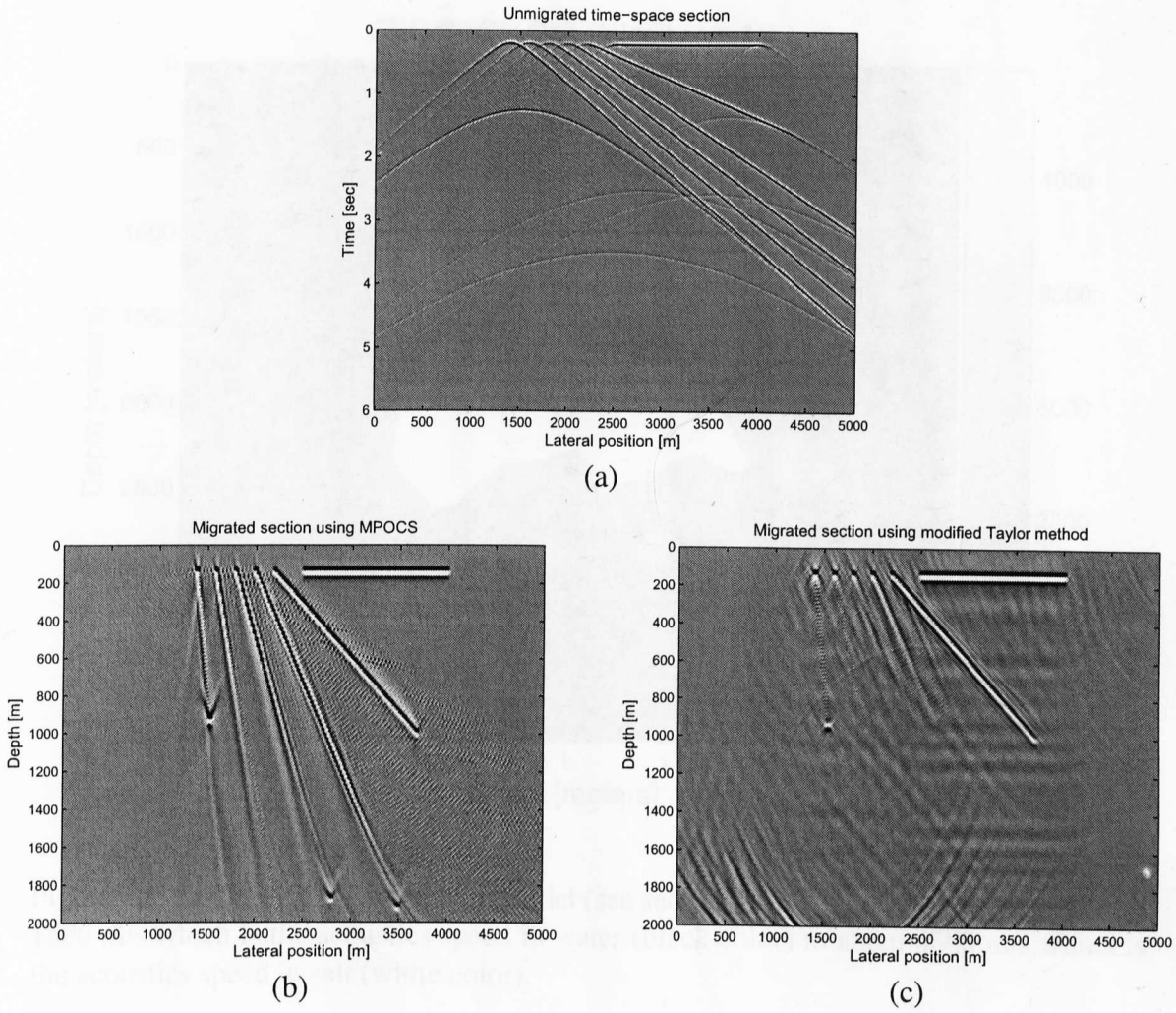

Figure 7.4: (a) A 2-D synthetic time-space section containing dipping events with angles $0^o, 30^o, 50^o, 60^o, 70^o$ and 80° (see section 7.2.3). This section is constructed based on a Ricker wavelet input with a dominant frequency of 15 Hz and with a time duration of 0.2 seconds. Migration of the 2-D synthetic time-space section containing dipping events with angles $0^o, 30^o, 50^o, 60^o, 70^o$ and 80° using (b) the modified projections algorithm with $N = 25$, and (c) the modified Taylor series method with $N = 25$.

(depth interval from 0 up to 4000 m). A MATLAB MEX[1] file was written to implement the post-stack explicit depth extrapolation process as reported in [13, 12, 1] where the filters are implemented in a spatially varying convolution in order to accommodate lateral velocity variations [13]. This was earlier described in chapter 2 (see Figure 2.24 which illustrates the $\omega - x$ post-stack migration algorithm and Figure 2.23 (b) for the concept of

[1]MEX-files (MEX stands for MATLAB Executable) are dynamically linked subroutines produced from C or Fortran source code that, when compiled, can be run from within MATLAB in the same way as MATLAB M-files or built-in functions. For more details see http://www.mathworks.com.

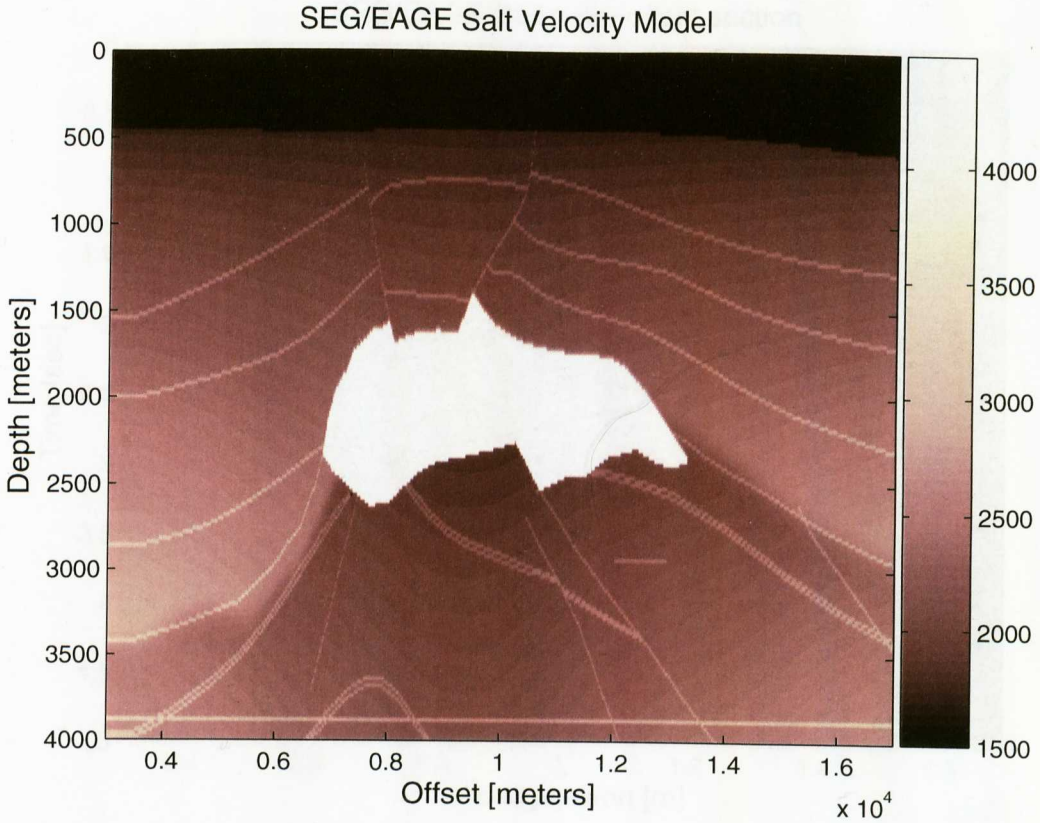

Figure 7.5: SEG/EAGE Salt velocity Model (see section 7.2.4). The velocities range from 1500 m/s which is the acoustics speed in water (black color) to about 4500 m/s which is the acoustics speed in salt (white color).

spatially varying migration filtering process).

Figure 7.7 shows migration results obtained by explicit depth extrapolation using operators designed with (a) the modified projection algorithm (MPOCS), and (b) the modified Taylor series method (MTaylor). For both results, we applied a 0.006 (1/m) cut-off high pass wavenumber depth filter per seismic trace in order to enhance the overall display of the results. The modified projection result (Figure 7.7 (a)) has presented a better overall image of the SEG/EAGE salt model compared with the one obtained using the modified Taylor filters (Figure 7.7 (b)). This is seen clearly in areas that are difficult to migrate, i.e., beneath the salt dome and at reflectors with steep dips. This matches with the synthetics results shown in Figure 7.3 (a) and (b), and Figure 7.4. For comparison, Figure 7.8 shows migration sections produced by other standard techniques, namely, (a) the split-step Fourier method with 2048 FFT points [29, 3] and (b) the Phase Shift Plus

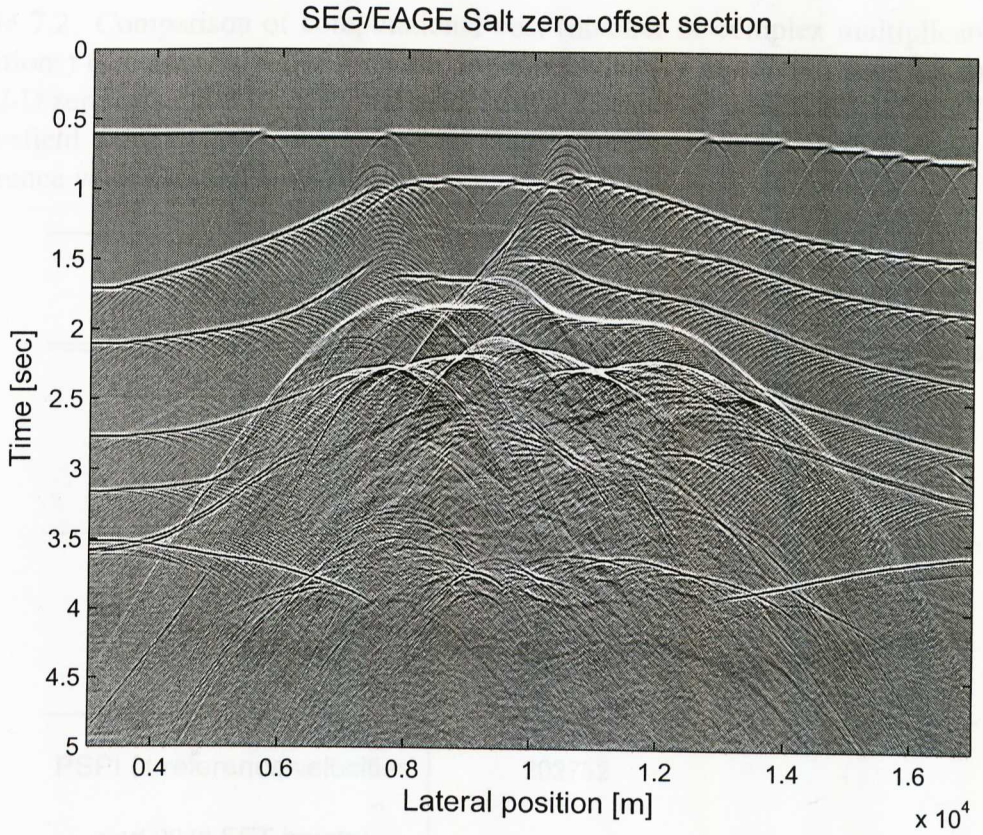

Figure 7.6: The time-space zero-offset section of the SEG/EAGE Salt Model which is generated based on finite differences (see section 7.2.4). This data set serves to assess the structural migration capabilities of different post-stack migration algorithms (see for example [3]).

Interpolation (PSPI) technique with 4 reference velocities and 2048 FFT points[2][28]. Although the PSPI is a very expensive method, it produces the best quality image. This is clearly seen at areas beneath the salt dome and at steep dip reflectors. It thus serves as an overall quality control. Table. 7.2 shows the cost of all the compared migration schemes for a single angular frequency at a given depth slice. Clearly, the most expensive is the PSPI (refer to Eqs. (2.21) and (2.23)). All migrated results at the sediments above the salt dome as well as within the salt dome are clearly imaged.

To highlight differences, however, Figures 7.9, 7.10, 7.11 contain zoom-ins on structurally difficult areas (respectively, different dips, steep dips and sub-salt structures). As anticipated, the PSPI technique produces the best migration result, although the explicit

[2]Both the SS and PSPI results were generated using the Colorado School of Mines Seismic Un*x package at http://www.cwp.mines.edu/cwpcodes/.

Table 7.2: Comparison of computational cost (number of complex multiplications and additions) (see section 7.2.4) for each angular frequency at a depth slice for migrating the 2-D zero-offset SEG/EAGE salt model using 25-tap 1-D seismic migration FIR filters (wavefield extrapolators), the Split-Step Fourier method and the PSPI method (with 4 reference velocities and 2048 FFT points).

Method	**Computational cost**	**Savings w.r.to PSPI**
$\omega - x$ (25-taps)	37888	81.31%
Split-Step Fourier (2048 FFT points)	101376	50%
PSPI (4 reference velocities and 2048 FFT points)	202752	-

wavefield extrapolation using the modified projection design algorithm yields a migrated section of comparable quality. Both strong dips and sub-salt structures are imaged clearly for those obtained using the modified projection and the PSPI methods. In other words, the modified projection and PSPI approaches visibly out-perform the other two techniques. Therefore, besides obtaining a much better quality image than the split-step Fourier method and the modified Taylor filters, by using 25-tap explicit depth migration FIR filters designed using the modified projections, a comparable image overall image with the expensive PSPI method was obtained.

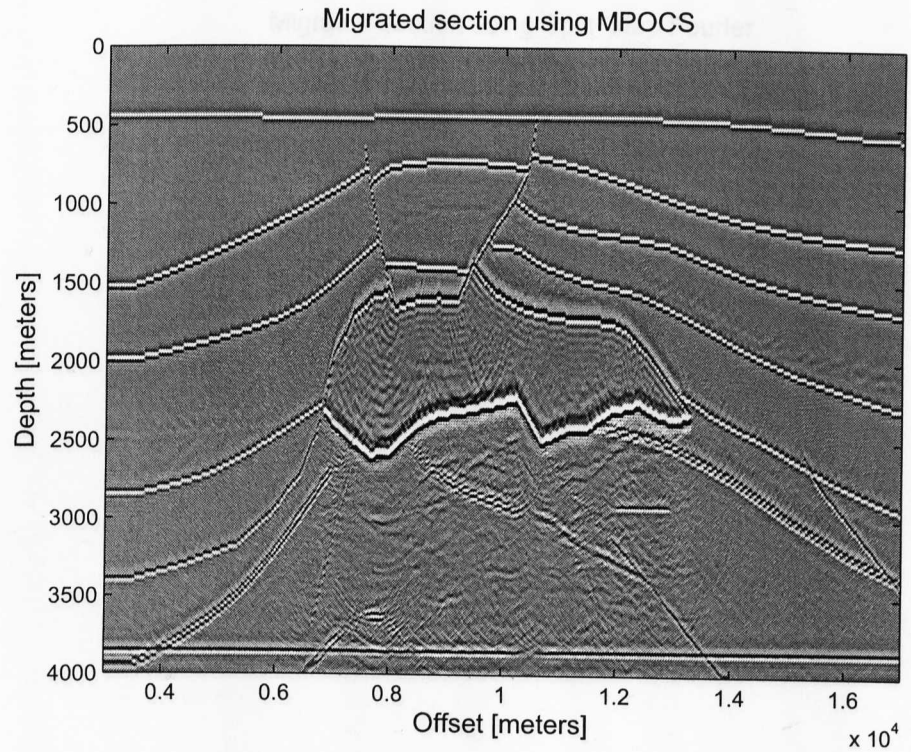

(a)

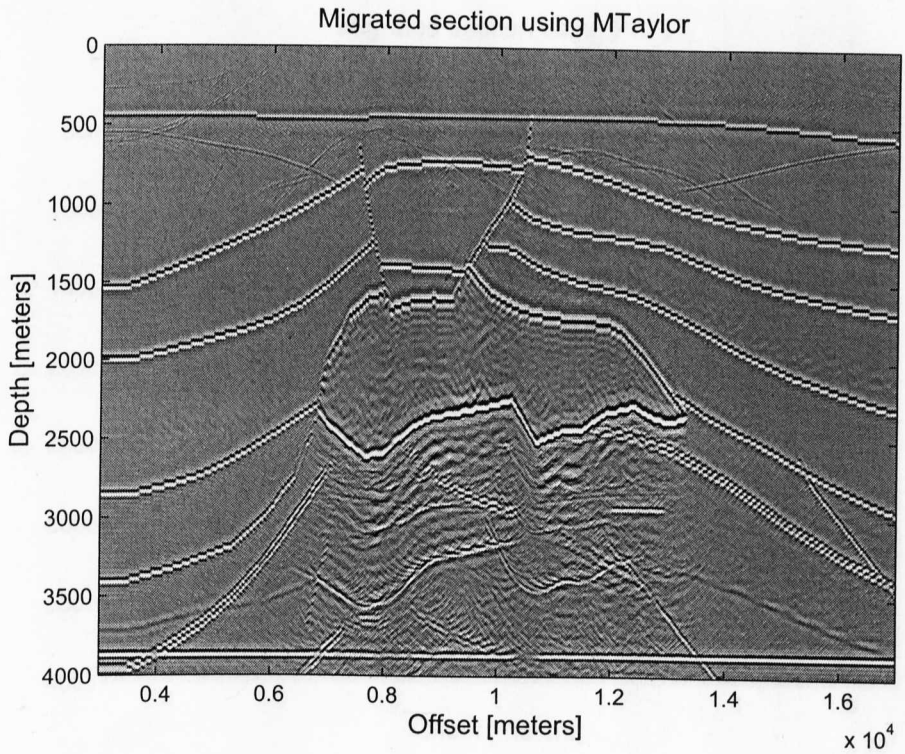

(b)

Figure 7.7: Migrated SEG/EAGE Salt model (see section 7.2.4) via (a) the modified projections method, and (b) the modified Taylor series method.

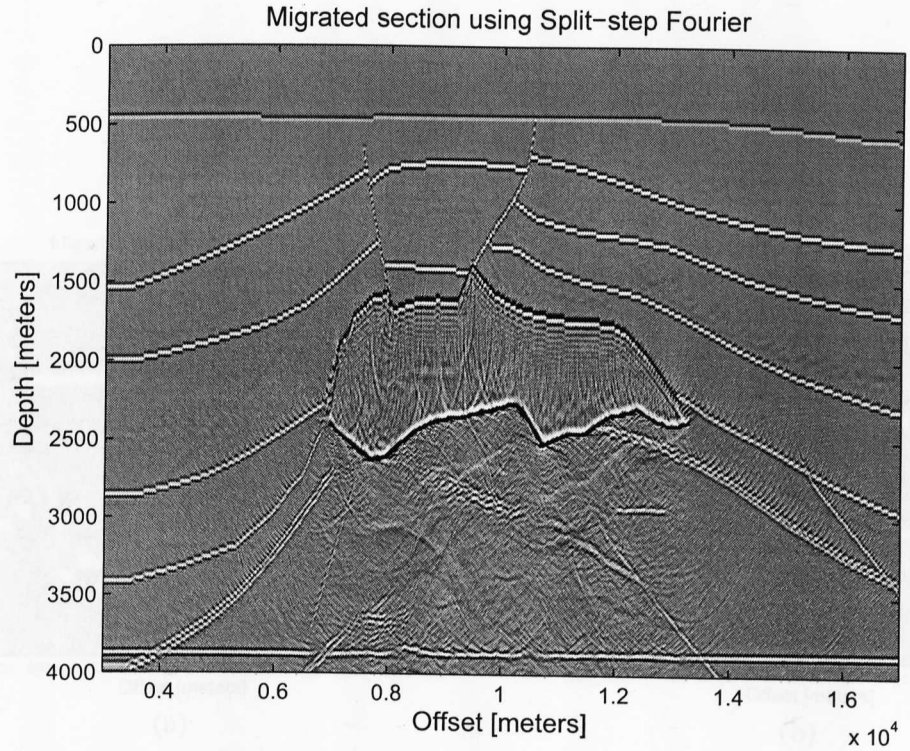

(a)

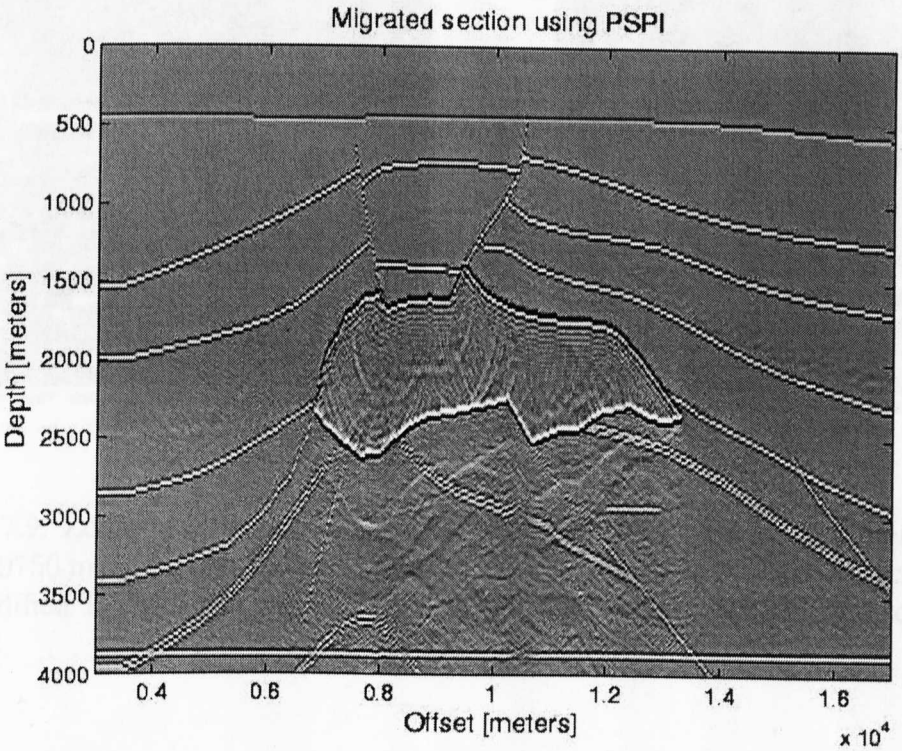

(b)

Figure 7.8: Migrated SEG/EAGE Salt model (see section 7.2.4) via (a) the Split-Step method, and (b) the PSPI method.

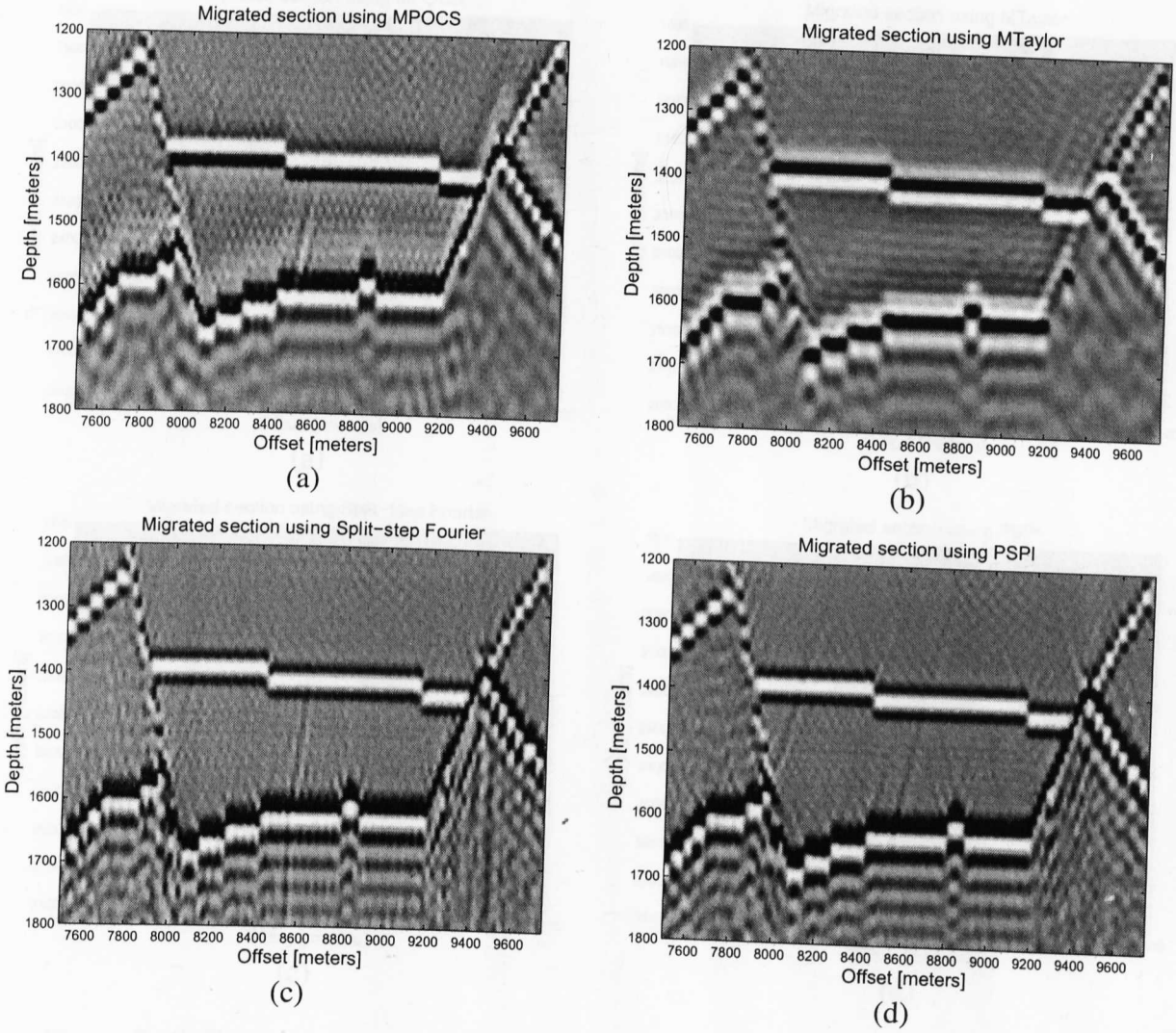

Figure 7.9: Zoom-in on an area with different dips (see section 7.2.4): (lateral position 7500 : 9750 m, and depth 1200 : 1800 m) via (a) the modified projections technique, (b) the modified Taylor series method, (c) the Split-Step Fourier method, and (d) the PSPI method.

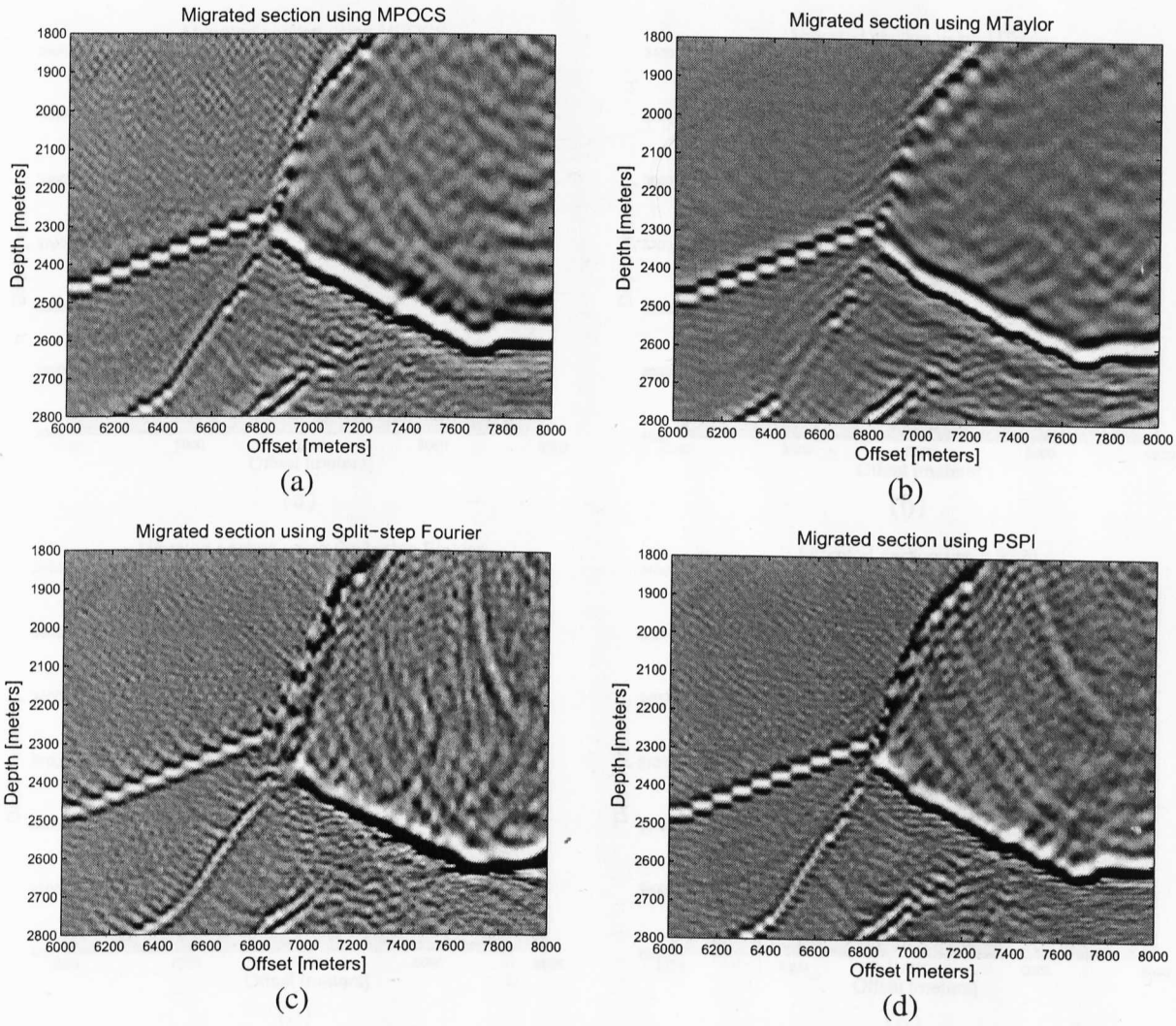

Figure 7.10: Zoom-in on an area with steep dips (see section 7.2.4): left flank of the salt model (lateral position 6000 : 8000 m, and depth 1800 : 2800 m)via the (a) modified projections technique, (b) the modified Taylor series method, (c) the split-step Fourier method, and (d) the PSPI method. The modified projections technique provides stable results even in the presence of steep dips using only 25 filter coefficients.

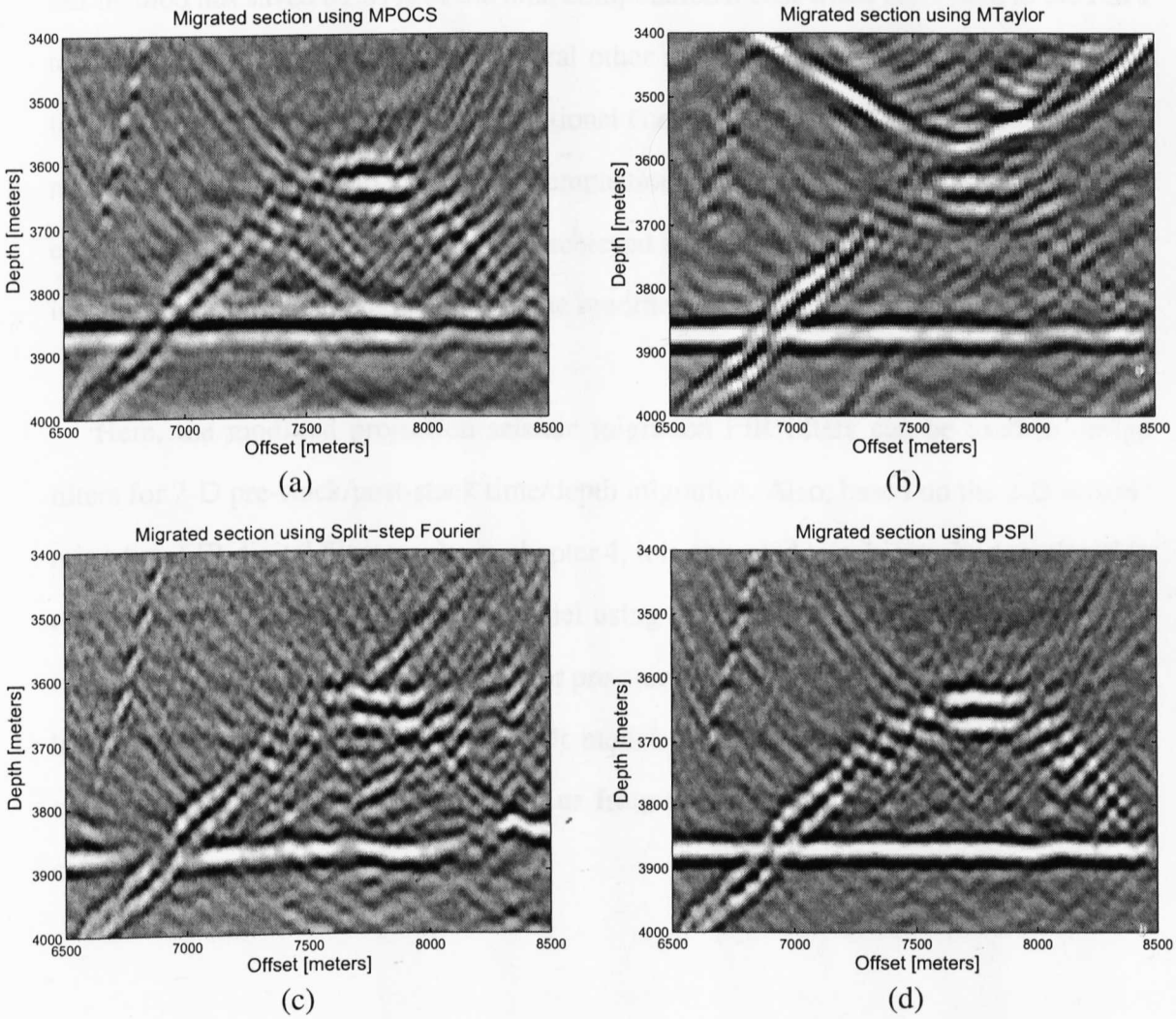

Figure 7.11: Zoom-in on a structurally challenging sub-salt area (see section 7.2.4) (lateral position 6500 : 8500 m, and depth 3400 : 4000 m) via the (a) modified projections technique, (b) the modified Taylor series method, (c) the split-step Fourier method, and (d) the PSPI method. The modified projections technique provides again stable results.

7.3 Discussion & Conclusion

A 2-D post-stack depth migration of the challenging SEG/EAGE Salt model using migration FIR filters designed with the modified projections scheme compared favourably with the computationally expensive Phase Shift Plus Interpolation (PSPI) method where our method has saved 81.31% of the total computational cost when compared to the PSPI technique. Also, it out-performed several other standard techniques such as the modified Taylor method at the same computational cost as well as the Split-Step Fourier (SS) method with savings of 40.65% of the compuational cost. Hence, stable and short length explicit depth extrapolation can even be achieved in structurally challenging areas involving steep dips or underneath salt using the modified projection FIR migration filters.

Here, the modified projection seismic migration FIR filters can be used to design filters for 2-D pre-stack/post-stack time/depth migration. Also, based on the 2-D seismic migration FIR digital filter results in chapter 4, it is expected to achieve similar migration results on the 3-D SEG/EAGE Salt model using the 2-D modified projection algorithm (section 4.6) where it can be also used for pre-stack/post-stack time/depth migration. The lack of 3-D zero-offset SEG/EAGE Salt model data as well as the relevant advanced computational facilities have prevented us from applying our 2-D filters as reported in chapter 4.

Chapter 8

Conclusion and Further Work

In this thesis, we have derived new 1-D and 2-D complex-valued seismic migration FIR digital filter design algorithms (chapters 3 and 4) using the method of Vector Space Prjections (VSPM)s. In general, these 1-D and 2-D design algorithms satisfy the explicit depth frequency-space migration problem. They are used for the post-stack migration of 2-D and 3-D seismic data sets, respectively.

To be more precise, we derived such FIR filter design algorithms based on the pure and the relaxed projections theorems where we demonstrated that, for the same filter design parameters and algorithm stopping thresholds, the relaxed version of the pure design algorithm results in significant savings in filter design time. To obtain a more robust design, we modified the pure design algorithm and called it the modified projection algorithm. This modified algorithm also provided a significant saving in terms of the filter design time even when compared with the relaxed projection method. We achieved better filter design characteristics with the 1-D and 2-D pure, relaxed and modified projection algorithms than other previously reported methods for the frequency-space explicit depth migration FIR filters.

These sets of 1-D and 2-D migration FIR digital filters, which are derived based on the VSPMs, serve as kernels for pre-stack time/depth migration. Therefore, they can be applied for pre-stack depth migration. The simplicity of the VSPM algorithms and

robustness of their designed migration FIR filters encourage us to further use them for pre-stacked data sets. This is because the pre-stack depth migration is nowadays becoming a more important seismic data processing step in the seismic industry [114, 115, 116], although it is an expensive migration scheme as mentioned earlier in the thesis.

The VSPM used to design our filters has the freedom to incorporate other constraints into the design algorithm (see chapter 1 and [89]). Therefore now-including constraints, while performing migration, the effect of data acquired in non-flat surfaces is of important further investigation [117]. Alternatively, we can add a constraint to limit the total average noise power passing through the stopband (evanescent) region of the designed filters [89]. By doing so, we expect to enhance the overall SNR of the migrated sections, especially, during pre-stack migration.

Moreover, there exist nowadays 3-D seismic data which is acquired based on hexagonal grids in the in-line and cross-line $(x - y)$ plane [23]. The frequency-wavenumber response of a 3-D seismic data set can be approximated by a domain bounded by two cones [118]. So in the spatial wavenumber domain- i.e., for each frequency slice, the 2-D wavenumber spectra are circularly band limited. Mersereau [119, 6] has proved that the optimal sampling scheme for such band limited signals are hexagonal grids. So the use of hexagonal grid sampling in 3-D processing data is thus an important issue to consider.

As the case for the acquisition of 3-D data on hexagonal sampling grids [23], processing of such hexagonally sampled data sets is an advantageous economic alternative because it needs 13.4% fewer sample points as compared to rectangular grids [119, 6, 118]. Hence, the design of 2-D migration FIR digital filters whose coefficients are matching such hexagonal configurations is a further important research issue to consider. This, in turn, also gives savings in terms of the expensive migration computational effort since less data samples need to be processed. When using the VSPM method in this case, in addition to fixing a proper indexing scheme, a 2-D FFT for hexagonally sampled data

sets is required to successfully design such 2-D complex-valued FIR filters. Hence, this attracts us for future investigations.

We also applied our migration filters designed using the VSPMs on the most challenging data set used to assess any post-stack migration method (chapter 7). That is, we applied them to the 2-D zero-offset SEG/EAGE model. We showed that our proposed migration FIR digital filters achieved superior migrated images when compared to the SEG/EAGE data set migrated using other previously proposed frequency-space migration FIR filters as well as other standard migration methods. Also, when compared to the most satisfactory, expensive, and accurate method (i.e., the Phase-Shift Plus Interpolation (PSPI) method), we obtained a comparable migrated image via our filters with about 18.69% of the total computational cost required for the same image obtained using the PSPI method. Similar work can be done to the 3-D zero-offset SEG/EAGE model. However, a cluster or a supercomputer must be used to migrate such a 3-D data set. In the future, we can benefit from the work done previously in [16, 15, 17] to apply our 2-D migration FIR filters to such a massive 3-D volume.

Not only that, but due to the extensive cost of the 3-D migration process, in chapter 6, we have also proposed a novel application of Singular Value Decomposition (SVD) theory to cheaply implement the 2-D complex-valued migration FIR digital filters. This came in trade-off negligible wavenumber errors. We applied a matrix transformation on the 2-D complex-valued migration FIR filter impulse responses to simplify the SVD computations and reduce the SVD numerical computation errors. Such a cheap implementation showed satisfactory filter wavenumber responses which follow with the 2-D migration FIR filter requirements. Consequently, we obtained better 3-D migrated volumes when compared to those obtained via the up-to-date used implementation schemes for such a geophysical application, namely, the McClellan transformations.

Although we assumed that our migration FIR filter size is of $N \times N$, i.e., the impulse response matrix is square, we can still realize the 2-D migration FIR filters whose impulse responses are of rectangular matrices based on SVD. We also might be interested in hardware implementation of the SVD realization method using parallel DSP chips for migrating 3-D seismic data sets. Similarly to the 3-D migration of the SEG/EAGE salt model, it is important to test the proposed SVD realization method on such an important model. Such migration results can help the geophysicists to select the optimal number of parallel SVD sections to accurately migrate that challenging 3-D model. All of these ideas stimulate our enthusiasm for further research developments on this important subject.

Finally, encouraged by the availability of multi-dimensional (m-D) Fast Fourier Transform (FFT) algorithms, we extended the 1-D and 2-D complex-valued migration FIR digital filter design algorithms to a more general class of m-D complex-valued FIR digital filters in chapter 5. This was done by modifying one of the proposed constraint sets for the 1-D and 2-D complex-valued migration FIR digital filter design problem using VSPMs. Empirical results demonstrated that our m-D FIR filter design algorithm results in equiripple FIR filter responses. In addition, we showed that our designs outperformed the work reported in [19, 20] in terms of the magnitude and phase responses using the same FIR filter parameters. Depending on the appropriate FFT algorithm and coordinate indexes, such a newly derived m-D complex-valued FIR digital filter design algorithm can be used for any data (real/complex) sampled with any regular form. Thus, by considering other DSP applications, we will further elaborate on such proposed pure projection algorithm for designing m-D complex-valued FIR digital filters with other sampling schemes.

List of Publications

Published

1. W. Mousa, D. C. McLernon, & S. Boussakta, "The Design of M-D Complex-Valued FIR Digital Filters Using POCS", *Accepted to appear in the 14th EURASIP European Signal Processing Conference (EUSIPCO'06), 2006.*

2. W. Mousa, M. Van Der Baan, D. C. McLernon, & S. Boussakta, "Explicit Wavefield Extrapolation Using Projections Onto Convex Sets with Application to the SEG/EAGE Salt Model", *Accepted to appear in the 68th EAGE Conference & Exhibition, 2006.*

3. W. Mousa, S. Boussakta, D. C. McLernon, "Realization of 2-D Seismic Migration FIR Digital Filters for 3-D Seismic Volumes via Singular Value Decomposition", *Accepted to appear in the IEEE Intr. Conf. on Acoustics, Speech, and Signal Processing (ICASSP'06), 2006.*

4. W. A. Mousa, D. McLernon, S. Boussakta, & M. Van der Baan, "The Design of Wavefield Extrapolators Using Projections Onto Convex Sets", *Proceedings of the 75th Society of Exploration Geophysicists (SEG) 2005 Annual Meeting.*

5. W. A. Mousa, S. Boussakta, & D. McLernon, "Design of Complex-valued Seismic Migration FIR Digital Filters Using Pure & Relaxed Projections", *Proceedings of the 13th EURASIP European Signal Processing Conference (EUSIPCO'05), 2005.*

6. W. A. Mousa, S. Boussakta, & D. McLernon, "Design of Complex-valued Seismic Migration FIR Digital Filters Using Vector Space Projection Methods", *IEEE Intr. Conf on Image Processing. (ICIP'05), vol. 2, pp.:189 - 192, 2005.*

7. W. Mousa, S. Boussakta, D. C. McLernon, & M. Van Der Baan, "Implementation of 3-D Wavefield Extrapolation Using Singular Value Decomposition", *Accepted to Appear in Proceedings of the 76th Society of Exploration Geophysicists (SEG) 2006 Annual Meeting.*

8. W. Mousa, S. Boussakta, M. Van Der Baan, & D. C. McLernon, "Designing Stable Operators for Explicit Depth Extrapolation of 3-D Wavefields Using Projections Onto Convex Sets", *Accepted to Appear in Proceedings of the 76th Society of Exploration Geophysicists (SEG) 2006 Annual Meeting.*

Submitted

1. W. Mousa, D. C. McLernon, & S. Boussakta, "The Design of M-D Complex-Valued FIR Digital Filters Using POCS", *Submitted to the IEEE trans. on Circuits & Systems-I (TCAS I).*

2. W. Mousa, S. Boussakta, D. C. McLernon, & M. Van Der Baan, "Implementation of 2-D Seismic Migration FIR Digital Filters for 3-D Seismic Volumes Using Singular Value Decomposition", *Submitted to IEEE trans. on Signal Processing (SP).*

3. W. Mousa, M. Van Der Baan, S. Boussakta, & D. C. McLernon, "Designing Stable Operators For Explicit Depth Extrapolation of 2-D Wavefields Using Projections Onto Convex Sets", *Submitted to the SEG Journal of Geophysics.*

4. W. Mousa, S. Boussakta, & D. C. McLernon, "Seismic Migration Complex-Valued FIR Digital Filter Design using Vector Space Projection Methods", *Submitted to the IEEE trans. on Geosciences & Remote Sensing (TGRS).*

References

[1] Öz. Yilmaz, editor. *Seismic Data Analysis: Processing, Inversion, and Interpretation of Seismic Data.* Society of Exploration Geophysicists, 2nd edition, 2001.

[2] D. Forel, T. Benz, and W. D. Pennington. *Seismic Data Processing with Seismic Un*x: A 2-D Seismic Data Processing Primer.* Society of Exploration Geophysicists (SEG), 2005.

[3] R. J. Ferguson and G. F. Margrave. Planned seismic imaging using explicit, one-way operators. *Geophysics*, 70(5):101–109, 2005.

[4] R. P. Bording and L. R. Lines. *Seismic Modeling and Imaging with Complete Wave Equation.* SEG, 2004.

[5] P. Kearey, M. Brooks, and I. Hill. *An Introduction to Geophysical Exploration.* Blackwell Science, 3rd edition, 2002.

[6] D. E. Dudgeon and R. M. Mersereau. *Multidimensional Digital Signal Processing.* Prentice-Hall, 1984.

[7] V. K. Madisetti and D. B. Williams, editors. *The Digital Signal Processing Handbook.* CRC Press and IEEE Press, 1998.

[8] B. Buttkus. *Spectral Analysis and Filter Theory in Applied Geophysics.* Springer, 2000.

[9] J. W. Thorbeck and A. J. Berkhout. 3-D recursive extrapolation operators: an overview. *Geophysics Extended Abstracts*, 1994.

[10] L. J. Karam and J. H. McClellan. Efficient design of digital filters for 2-D and 3-D depth migration. *Signal Processing, IEEE Transactions on*, 45(4):1036–1044, April 1997.

[11] D. Hale. 3-D migration via McClellan transformation. *Geophysics*, 56:1778 – 1785, 1991.

[12] D. Hale. Stable explicit depth extrapolation of seismic wavefields. *Geophysics*, 56:1770 – 1777, 1991.

[13] O. Holberg. Towards optimum one-way wave propagation. *Geophysical Prospecting*, 36:99–114, 1988.

[14] J. Thorbecke. *Common Focus Point Technology*. PhD thesis, Delft University of Technology, 1997.

[15] D. Bhardwaj, S. Yerneni, and S. Phadke. Parallel computing in seismic data processing. pages 279–285. 3rd International Petroleum Conf. and Exhibition (PETROTECH-99), 1999.

[16] D. Bhardwaj, S. Yerneni, and S. Phadke. Efficient parallel I/O for seismic imaging in a distributed computing environment. pages 105–108. 3rd conference and exposition on Petroleum and Geophysics (SPG 2000), 2000.

[17] S. Phadke, R. Rastogi, S. Yerneni, and S. Chakraborty. Parallel distributed seismic imaging algorithms on PARAM 10000. 4th conference and exposition on Petroleum and Geophysics (SPG 2002), 2002.

[18] R. Soubaras. Explicit 3-D migration using equiripple polynomial expansion and Laplace synthesis. *Geophysics*, 61(5):1386–1393, 1996.

[19] L. J. Karam and J. H. McClellan. Complex Chebyshev approximation for FIR filter design. *IEEE Trans. on Circuits and Systems*, 42(3):207 – 216, March 1995.

[20] L. J. Karam and J. H. McClellan. Chebyshev digital FIR filter design. *Signal Processing*, 76:17 – 36, 1999.

[21] A. E. Çetin, O. N. Gerek, and Y. Yardimci. Equiripple FIR filter design by the FFT algorithm. *Signal Processing Magazine, IEEE*, Vol.14:60–64, Mar 1997.

[22] K. C. Haddad, H. Stark, and N. P. Galatsanos. Constrained FIR filter design by the method of vector space projections. *IEEE Trans. on Circuits and Systems*, 47(8):714 – 725, August 2000.

[23] A. Özbek, L. Hoteit, and G. Dumitru. 3-D filter design on a hexagonal grid with application to point-receiver land acquisition. *SEG 2004 Expanded Abstracts*, 2004.

[24] W. A. Mousa, S. Boussakta, and D. C. McLernon. Design of complex-valued seismic migration fir digital filters using vector space projection methods. *Proceedings of the IEEE Intr. Conf on Image Processing. (ICIP'05)*, 2:189–192, 2005.

[25] W. A. Mousa, S. Boussakta, and D. C. McLernon. Design of complex-valued seismic migration fir digital filters using pure & relaxed projections. *Proceedings of the 13th EURASIP European Signal Processing Conference (EUSIPCO'05)*, 2005.

[26] W. A. Mousa, S. Boussakta, and D.C. McLernon. Seismic migration complex-valued FIR digital filter design using vector space projection methods. *Submitted to IEEE Trans. on Geosciences and Remote Sensing*, 2006.

[27] W. A. Mousa, D. C. McLernon, S. Boussakta, and M. Van Der Baan. The Design of Wavefield Extrapolators Using Projections Onto Convex Sets. *SEG 2005 Expanded Abstracts*, 2005.

[28] J. Gazdag and P. Sguazzero. Migration of seismic data by phase shift plus interpolation. *Geophysics*, 49:124–131, 1984.

[29] P. L. Stoffa, J. T. Fokkema, R. M. de Luna Freire, and W. P. Kessinger. Split-step Fourier migration. *Geophysics*, 55:410–421, 1990.

[30] W. A. Mousa, M. Van Der Baan, D. C. McLernon, and S. Boussakta. Explicit wavefield extrapolation using projections onto convex sets with application to the

SEG/EAGE salt model. *Accepted to appear in the 68th EAGE Conference & Exhibition*, 2006.

[31] W. A. Mousa, M. Van Der Baan, S. Boussakta, and D.C. McLernon. Designing stable operators for explicit depth extrapolation of 2-d wavefields using projections onto convex sets. *Submitted to the SEG Journal of Geophysics*, 2006.

[32] C. L. Liner. *Elements of 3-D Seismology*. PennWell, 1999.

[33] G. J. Baeten, V. Belougne, L. Combee, E. Kragh, J. Orban, A. Özbek, and P. Vermeer. Acquisition and processing of point receiver measurements in land seismic. *SEG 2000 Expanded Abstracts*, 2000.

[34] G. Blacquiere and L. Ongkiehong. Single sensor recording: Antialias filtering, perturbations and dynamic range. *SEG 2000 Expanded Abstracts*, 2000.

[35] P. Christie, D. Nichols, A. Özbek, T. Curtis, L. Larson, A. Strudley, R. Davis, and M. Svendsen. Raising the standards of seismic data quality. *Oilfield Review*, pages 16–31, 2001.

[36] W. A. Mousa, S. Boussakta, M. Van der Baan, and D. C. McLernon. Designing stable operators for explicit depth extrapolation of 3-D wavefields using projections onto convex sets. *Accepted to Appear in the SEG 2006 International Exposition & Seventy-Sixth Annual Meeting Proceedings*, 2006.

[37] W. F. Mecklenbräuker and R. M. Mersereau. McClellan transformations for two-dimensional digital filtering: I-design. *IEEE Trans. on Circuits and Systems*, 23(7):405–414, July 1976.

[38] J. McClellan and D. S. K. Chan. A 2-D FIR filter structure derived from the Chebyshev recursion. *IEEE Trans. on Circuits and Systems*, 24(7):372–378, July 1977.

[39] A. H. Kayran and R. A. King. Design of recursive and nonrecursive fan filters with complex transformation. *IEEE Trans. on Circuits and Systems*, 30(12):849 – 857, Dec. 1983.

[40] W. Lu and A. Antoniou. *Two-Dimensional Digital Filters*. Marcel Dekker Publisher, 1st edition, 1992.

[41] Wei-Ping Zhu, M. Omair Ahmad, and M. N. S. Swamy. Realization of 2-D linear-phase FIR filters by using the singular valued decomposition. *IEEE Trans. on Signal Processing*, 47(5):1349–1358, May 1999.

[42] W. A. Mousa, S. Boussakta, and D. C. McLernon. Realization of 2-D seismic migration fir digital filters for 3-D seismic volumes via singular value decomposition. *Accepted to appear in the IEEE Intr. Conf. on Acoustics, Speech, and Signal Processing (ICASSP'06)*, 2006.

[43] W. A. Mousa, S. Boussakta, D. C. McLernon, and M. Van der Baan. Implementation of 3-D wavefield extrapolation using singular value decomposition. *Accepted to Appear in the SEG 2006 International Exposition & Seventy-Sixth Annual Meeting Proceedings*, 2006.

[44] W. A. Mousa, S. Boussakta, D.C. McLernon, and M. Van Der Baan. Implementation of 2-D seismic migration fir digital filters for 3-D seismic volumes using singular value decomposition. *Submitted to IEEE Trans. On Signal Processing*, 2006.

[45] S. C. Chan and K. M. Tsui. On the design of real and complex FIR filters with flatness and peak error constraints using semidefinite programming. volume 3, pages III: 125–128. International Symposium on Circuits and Systems (ISCAS'04), 2004.

[46] X. Chen and T. Parks. Design of FIR filters in the complex domain. *IEEE Trans. on Acoustics, Speech, and Signal Processing*, 35(2):144 – 153, Feb. 1987.

[47] A. Biasiolo, G. Cortelazzo, and G. A. Mian. Computer aided design of multidimensional FIR filters for video applications. *IEEE trans. on Consumer Electronics*, 35(3):290–296, August 1989.

[48] T. Sekiguchi and S Takahasi. Mcclellan transformations for multidimensional FIR digital filters with complex coefficients. *Electronics and Communications in Japan*, 72(4):79–93, 1989.

[49] L. J. Karam. On the design of multidimensional FIR filters by transformation. In *Proceedings of IEEE Int. Conf. on Acoustics, Speech, and Signal Processing (ICASSP)*, volume 3, pages 2157–2160, 1997.

[50] W. A. Mousa, D. C. McLernon, and S. Boussakta. The design of M-D complex-valued fir digital filters using POCS. *Accepted to appear in the 14th EURASIP European Signal Processing Conference (EUSIPCO'06)*, 2006.

[51] W. A. Mousa, D.C. McLernon, and S. Boussakta. The design of M-D complex-valued fir digital filters using POCS. *Submitted to IEEE Trans. on Circuits & Systems (TCAS-I)*, 2006.

[52] S. Boussakta, O. Al-Shibami, M. Aziz, and A. G Holt. 3-D vector radix algorithm for the 3-D new Mersenne number transform. *IEE Proc.-Vis: Image & Signal Processing*, 148(2):115–125, April 2001.

[53] S. Boussakta, O. Al-Shibami, and M. Aziz. Radix 2 x 2 x 2 algorithm for the 3-D discrete Hartley transform. *IEEE Trans. on Signal Processing*, 49(12):3145–3156, Dec. 2001.

[54] A. S. Spanias, S. B. Jonsson, and S. D. Stearns. Transform methods for seismic data compression. *IEEE Tran. on Geosciences and Remote Sensing*, 29(3):407–416, May 1991.

[55] A. Özbek. Adaptive beamforming with generalized linear constrains. *Geophysics Extended Abstracts*, 2000.

[56] A. Özbek. Multichannel adaptive interface canceling. *Geophysics Extended Abstracts*, 2000.

[57] X. Miao and S. Cheadle. Noise attenuation with wavelet transform. *SEG 1998 Expanded Abstracts*, 1998.

[58] T. J. Ulrych, M. D. Sacchi, and J. M Graul. Signal and noise separation: Art and science. *Geophysics*, 64:1648 – 1656, Sept.- Oct. 1999.

[59] L. Duval and T. Rosten. Filter bank decomposition of seismic data with application to compression and denoising. *SEG 2000 Expanded Abstracts*, 2000.

[60] Qiansheng Cheng, Rong Chen, and Ta-Hsin Li. Simultaneous wavelet estimation and deconvolution of reflection seismic signals. *IEEE Transactions on Geoscience and Remote Sensing*, 34(2):377 – 384, March 2001.

[61] K. Berkner and Jr. Wells, R.O. Wavelet transforms and denoising algorithms. *Conference Record of the Thirty-Second Asilomar Conference on Signals, Systems and Computers*, 2:1639 – 1643, Nov. 1998.

[62] Rongfeng Zhang and Tadeusz J. Ulrych. Physical wavelet frame denoising. *Geophysics*, 68(1):225–231, Jan 2003.

[63] J. E. Womack and J. R. Cruz. Seismic data filtering using a gabor representation. *IEEE Tran. on Geosciences and Remote Sensing*, 32(2):467–472, March 1994.

[64] A. F. Linville and R. A. Meek. A procedure for optimally removing localized coherent noise. *Geophysics*, 60(1):191 – 203, Jan.-Feb. 1995.

[65] B. Duquet and K. J. Marfurt. Filtering coherent noise during prestack depth migration. *Geophysics*, 64(4):1054 – 1066, July-Aug. 1999.

[66] S. Treitel, J. L. Shanks, and C. W. Fraster. Some aspects of fan filtering. *Geophysics*, XXXII:789 – 800, 1967.

[67] M. Z. Mulk, K. Obata, and K. Hirano. Design of fan filters. *IEEE Trans. on Acoustics, Speech, and Signal Processing*, 31(6):1427 – 1434, Dec. 1983.

[68] D. W. McCowan, P. L. Stoffa, and J. B. Diebold. Fan filters for data with variable spatial sampling. *IEEE Trans. on Acoustics, Speech, and Signal Processing*, 32(6):1154 – 1159, Dec. 1984.

[69] R. Ansari. Efficient IIR and FIR fan filters. *IEEE Trans. on Circuits and Systems*, 34:941 – 945, August 1987.

[70] R. H. Bamberger and M. J. T Smith. A filter bank for the directional decomposition of images: Theory and design. *IEEE Tran. on Signal Processing*, 40(4):882–893, December 1992.

[71] E. A. Robinson. *Migration of geophysical data.* Intr. Human Resources Development Corporation, 1983.

[72] J. F. Claerbout. *Imaging the Earth's Interior.* Blackwell, 1984.

[73] P. M. Shearer. *Introduction to Seismology.* Cambridge Uni. Press, 1999.

[74] J. A. Scales. *Theory of Seismic Imaging.* Samizdat Press, 1997.

[75] G. Garibotto. 2D recursive phase filters for the solution of two-dimensional wave equations. *IEEE Trans. on Acoustics, Speech, and Signal Processing*, 27(4):367 – 373, Aug. 1979.

[76] J. Gazdag. Wave equation migration with the phase-shift method. *Geophysics*, 43:1342–1351, 1978.

[77] R. H. Stolt. Migration by Fourier transform. *Geophysics*, 43(1):23–48, 1978.

[78] A. A. Dubrulle and J. Gazdag. Migration by phase shift-an algorithmic description for array processors. *Geophysics*, 44(10):1661–1666, 1979.

[79] A. J. Berkhout. Wavefield extrapolation techniques in seismic migration, a tutorial. *Geophysics*, 46(12):1638–1656, 1981.

[80] J. T. Etgen. Stability of explicit depth extrapolation through laterally-varying media. *SEG 1994 Expanded Abstracts*, 1994.

[81] Samuel H. Gray, John Etgen, Joe Dellinger, and Dan Whitmore. Seismic migration problems and solutions. *Geophysics*, 66(5):1622–1640, 2001.

[82] A. J. Berkhout. *Seismic Migration: Imaging of Acoustic Energy by Wave Field Extrapolation*, volume A. Theoretical Aspects. Elsvier Scientific Publishing Company, 2nd edition, 1982.

[83] A.V. Oppenheim and R.W. Schafer. *Discrete-time signal processing*. Prentice Hall, Englewood Cliffs, NJ, 1989.

[84] L. B. Jackson. *Digital Filters and Signal Processing*. Kluwer Academic Publisher, 3rd edition, 1996.

[85] J. W. Thorbeck, K. Wapenaar, and G. Swinnen. Design of one-way wavefield extrapolation operators, using smooth functions in WLSQ optimization. *Geophysics*, 69(4):1037–1045, 2004.

[86] L. M. Bregman. Finding the common point of convex sets by the method of successive projections. *Dokl. Akad. Nauk. USSR*, 162(3):487–490, 1965.

[87] L. G. Gubin, B. T. Polyak, and E. V. Raik. The method of projections for finding the common point in convex sets. *USSR Compu. Math. Phy.*, 7(6):1–24, 1967.

[88] E. Hermanowicz and M. Blok. Iterative technique for approximate minimax design of complex digital fir filters. *7th IEEE International conference on Electronics, Circuits and Systems*, 1:83–86, 2000.

[89] H. Stark and Y. Yang. *Vector Space Projections: a numerical approach to Signal and Image processing, Neural nets, and Optics*. John Wiley and Sons Publisher, 1st edition, 1998.

[90] A. Levi and H. Stark. Signal restoration from phase by projections onto convex sets. In *Proceedings of IEEE Int. Conf. on Acoustics, Speech, and Signal Processing (ICASSP)*, 1983.

[91] M. Sezan. An overview of convex projections theory and its application to image recovery problems. *Ultramicroscopy*, 40:55–67, 1992.

[92] K. C. Haddad, H. Stark, and N. P. Galatsanos. Design of digital linear-phase FIR crossover systems for loudspeakers by the Method of Vector Space Projections. *IEEE Trans. on Signal Processing*, 47(11):3058–3066, November 1999.

[93] P. Oskoui-Fard and H. Stark. Tomographic image reconstruction using the theory of convex projections. *IEEE Trans. on Medical Imaging*, 7(1):45–58, March 1988.

[94] S. Oh, R. J. Marks, and L. E. Atlas. Kernel synthesis for generalized time-frequency distributions using the method of alternating projections onto convex sets. *IEEE Trans. on Signal Processing*, 42(7):1653–1661, July 1994.

[95] I. Th. Bjarnason and W. Menke. Application of the pocs inversion method to cross-borehole imaging. *Geophysics*, 58(7):941–948, July 1993.

[96] E. Kreyszig. *Introductory Functional Analysis with Applications*. John Wiley and Sons, 1978.

[97] K. Sydsaeter and P. Hammond. *Essential Mathematics for Economic Analysis*. Prentice Hall, 2001.

[98] A. Levi and H. Stark. Image restoration by the method of generalized projections with application to restoration from magnitude. *JOSA A*, 1(9), September 1984.

[99] A. Antoniou. *Digital Filters: Analysis, Design, and Applications*. McGraw-Hill, 1993.

[100] D. Williamson. *Discrete-time Signal Processing*. Springer, 1999.

[101] W. F. Mecklenbräuker and R. M. Mersereau. McClellan transformations for two-dimensional digital filtering: II-implementation. *IEEE Trans. on Circuits and Systems*, 23(7):414–422, July 1976.

[102] T. S. Huang. Two-dimensional windows. *IEEE trans. on Audio Electroacoust.*, 20:88–89, March 1972.

[103] S. Levin. $\Delta x \neq \Delta y$ in 3D depth migration via McClellan transformations. *Geophysical Prospecting*, 52:241–246, 2004.

[104] M. Reshef and D. Kessler. Practical implementation of three-dimensional poststack depth migration. *Geophysics*, 54(3):309–318, March 1989.

[105] Wu-Sheng Lu, Hui-Ping Wang, and A. Antoniou. Design of two-dimensional FIR digital filters by using the singular-value decomposition. *IEEE Trans. on Signal Processing*, 37(1):35–46, January 1990.

[106] Wu-Sheng Lu, Hui-Ping Wang, and A. Antoniou. Design of two-dimensional digital filters using singular-value decomposition and balanced approximation method. *IEEE Trans. on Signal Processing*, 39(10):2253–2262, October 1991.

[107] L. N. Trefethen and D. Bau. *Numerical Linear Algebra*. Siam, 1997.

[108] M. Kirby. *Geometric Data Analysis*. John Wiley & Sons, INC., 2001.

[109] M. J. O'Brien and S. H. Gray. Can we image beneath salt? *The Leading Edge*, 15(1):17–22, Jan. 1996.

[110] Progress report from the SEG/EAGE 3-D modeling committee. *The Leading Edge*, 13(2):110–112, 1994.

[111] F. Aminzadeh, N. Burkhard, L. Nicoletis, F. Rocca, and K. Wyatt. SEG/EAGE 3-D modeling project: 2nd update. *The Leading Edge*, 13(9):949–952, 1994.

[112] F. Aminzadeh, N. Burkhard, T. Kunz, L. Nicoletis, and F. Rocca. 3-D modeling project: 3rd report. *The Leading Edge*, 14(2):125–128, 1995.

[113] F. Aminzadeh, N. Burkhard, J. Long, T. Kunz, and P. Duclos. Three dimensional SEG/EAGE models-an update. *The Leading Edge*, 15(2):131–134, Feb. 1996.

[114] Lawrence M. Gochioco and Matthew Brzostowski. An introduction to this special section—migration. *The Leading Edge*, 24(6):601–601, 2005.

[115] D. Bevc and B. Biondi. Which depth imaging method should you use? A road map through the maze of possibilities. *The Leading Edge*, 24(6):602–606, 2005.

[116] S. Pharez, N. Jones, V. Dirks, S. Zimine, H. Prigent, K. Ibbotson, and J-P. Gruffeille. Prestack wave-equation migration as a routine production tool. *The Leading Edge*, 24(6):608–613, 2005.

[117] M. Reshef. Depth migration from irregular surfaces with depth extrapolation methods. *Geophysics*, 56(1):119–122, Jan. 1991.

[118] V. Bardan. A hexagonal sampling grid for 3D recording and processing of 3D seismic data. *Geophysical Prospecting*, 45:819 – 830, 1997.

[119] R. M. Mersereau. The processing of hexagonally sampled two-dimensional signals. *Proceedings of the IEEE*, 67(6):930–949, June 1979.